Design of Induction Machines for Traction Applications

by

Marné Botha

Thesis presented in partial fulfilment of the requirements for the degree of Master of Engineering (Electrical) in the Faculty of Engineering at Stellenbosch University

Supervisor: Dr. R-J. Wang

March 2020

Declaration

By submitting this thesis electronically, I declare that the entirety of the work contained therein is my own, original work, that I am the sole author thereof (save to the extent explicitly otherwise stated), that reproduction and publication thereof by Stellenbosch University will not infringe any third party rights and that I have not previously in its entirety or in part submitted it for obtaining any qualification.

Date: .March 2020

Abstract

Design of Induction Machines for Traction Applications

MC. Botha

Department of Electrical and Electronic Engineering,
University of Stellenbosch,
Private Bag X1, Matieland 7602, South Africa.

Thesis: MEng (Electrical)

March 2020

Over the past few years, electric vehicles have gained popularity due to environmental driven aspirations of industrialized countries to ban fossil-fuel cars. In synergy with an agenda for renewable energy, electrified transportation is seen as a key component for a sustainable future. The aim of this thesis was to formulate a design strategy for induction motors for traction applications, with emphasis on a wide flux weakening range. An analytical model was derived to generate an initial design according to required specifications. The performance accuracy of the analytical model was closely aligned with commercial software packages such as ANSYS RMxprt. The initial design was optimized through a non-gradient based genetic algorithm. The optimized design was then further refined for manufacturability and adapted to reduce harmonic copper losses at high frequencies. The traction motor was built and tested, with measured performance matching well with expected results. The prototype motor performance validated the legitimacy of the suggested design strategy. The design strategy was then used to develop a theoretical model of a larger traction motor for locomotive applications. Additionally, the design approach was adapted to implement voltage management with the aim of reducing manufacturing costs of larger traction motors. The adapted strategy was tested with the design of an additional traction motor and proved to be a less expensive alternative.

Uittreksel

Ontwerp van Induksie Motors vir Traksie Toepassings

("Design of Induction Machines for Traction Applications")

MC. Botha

Departement van Elektries en Elektroniese Ingenieurswese,
Universiteit van Stellenbosch,
Privaatsak X1, Matieland 7602, Suid Afrika.

Tesis: MIng (Elektries)

Maart 2020

In vorige jare het elektriese voertuie populêr geraak weens omgewings aspirasies van eerste wêreld lande om petrol aangedrewe motors te verbied. Behalwe vir hernubarie energie, word elektries aangedrewe vervoer gesien as sleutelkomponent vir 'n volhoubare toekoms. Die doel van hierdie tesis is om 'n ontwerpstrategie vir induksiemotors te formuleer, met klem op 'n breë vloed verminderings interval. 'n Analitiese model was ontwerp wat oorspronklike ontwerpe genereereer volgens die vereiste prestasie. Die resultate van die anlitiese model het goed saamgestem met kommersiële sagteware pakkette soos ANSYS RMxprt. Die oorpsonklike model was geoptimiseer deur 'n Genetiese Algoritme. Die geoptimiseerde model was minimaal aangepas om die vervaardigings proses te vergemaklik, maar ook om Koper harmoniek verliese te verminder teen hoër frekwensies. Die prototipe was vervaardig en getoets met resultate wat die verwagte prestasie goed reflekteer. Die akkurate toets resultate van die prototipe motor het die geldigheid van die voorgestelde ontwerpsproses bevestig. Hierdie ontwerpsproses was toe geïmplemeteer om 'n groter induksiemotor toereties te ontwerp vir lokomotiewe toepassings. Die strategie was ook aangepas om spannings-bestuur te implementeer met die doel om die motor grootte te verminder. Die aangepaste strategie was suksesvol met die teoretiese ontwerp van 'n groter traksie motor. Met motor grootte wat verwant is aan vervaardigingskoste, is die aangepaste strategie 'n goedkoper alternatief vir groot traksie motors.

Acknowledgements

I would like to acknowledge and thank the following people for their contribution to this project:

- Prof. Rong-Jie Wang for his continuous guidance and support throughout the duration of the project. Your knowledge in this field of research is immense and I am grateful to have learned under your supervision.
- Dr. Stiaan Gerber who assisted me with SEMFEM throughout the duration of the project. I am thankful for all the help provided.
- Mr. Petzer and the workshop team who aided with assembly, wiring and testing of the prototype motor. Your team is highly professional and I thoroughly enjoyed spending time in the workshop.
- Mr. Des Smith who inserted the stator windings of the prototype motor. An excellent and accurate job was done.
- Family and friends for their continued support and encouragement during my time at university. I am grateful to be surrounded by a network of inspiring individuals who always challenge me to reach my full potential.

List of publications

The following publication(s) can be viewed in Appendix G:

T.M. Masuku, R.J. Wang, M.C. Botha, S. Gerber, "Design Strategy of Traction Induction Motors," *in Proceedings of the 27th Southern African Universities Power Engineering Conference, (SAUPEC)*, Bloemfontein, 2019, pp. 316-321.

Contents

List of Figures

List of Tables

Nomenclature

Acronyms

AC	Alternating Current
CPSR	Constant Power Speed Range
DC	Direct Current
EMF	Electromotive Force
EV	Electric Vehicle
FEM	Finite Element Method
FFT	Fast Fourier Transform
GA	Genetic Algorithm
IGBT	Insulated-Gate Bipolar Transistor
MMF	Magnetomotive Force
NEMA	National Electrical Manufacturers Association
PEC	Power Electronics Converter
PF	Power Factor
PWM	Pulse Width Modulation
QN	Quasi Newton
RCL	Rotor Copper Losses
SCL	Stator Copper Losses
SEM	Stellenbosch Electrical Machines
SLSQP	Sequential Least Squares Quadratic Programming
VFD	Variable Frequency Drive

Constants

$g =$	$9.81\,\mathrm{m/s^2}$
$\mu_0 =$	$4\pi \times 10^{-7}\,\mathrm{H/m}$
$\pi =$	3.14

Greek Symbols

α_i	pole spanning coefficient	[ ]

β_s	skin effect coefficient	[ ]
ΔT_{cs}	temperature differential between conductor and slot wall	[K]
ΔT_{fa}	temperature differential between frame and ambient air	[K]
η_n	efficiency	[ ]
η_{fin}	fin efficiency	[ ]
λ	stack aspect ratio	[ ]
λ_b	rotor slot permeance coefficient	[ ]
λ_{dr}	rotor differential permeance coefficient	[ ]
λ_{ds}	stator differential permeance coefficient	[ ]
λ_{ec}	end connection coefficient	[ ]
λ_{end}	stator end-coil permeance coefficient	[ ]
λ_{er}	end dring permeance coefficient	[ ]
λ_{ins}	insulation thermal conductivity	[K/W]
λ_r	rotor slot permeance coefficient	[ ]
λ_s	stator permeance coefficient	[ ]
λ_{skew}	rotor skew permeance coefficient	[ ]
λ_{ss}	stator slot permeance coefficient	[ ]
λ_{zr}	rotor zig-zag permeance coefficient	[ ]
λ_{zs}	stator zig-zag permeance coefficient	[ ]
ω_b	base angular speed	[rad/s]
ω_m	maximum angular speed	[rad/s]
ϕ	magnetic flux	[Wb]
ρ_{Co}	copper resistivity at temperature	[Ω]
τ	magnetic pole pitch	[ ]
τ_r	stator slot pitch	[ ]
τ_s	stator slot pitch	[ ]
ε_{fin}	fin effectiveness	[ ]

Variables

a_1	current paths in parallel	[m]
a_p	conductors in parallel	[m]
A_b	rotor bar area	[m^2]
A_{Co}	magnetic wire cross section	[m^2]
A_{er}	end ring cross sectional area	[m^2]
A_{fin}	fin area	[m^2]
A_{frame}	frame area	[m^2]
A_{ls}	lateral slot area	[m^2]

A_{nofin}	original surface area without the addition of fins	[m^2]
A_p	cross sectional insulation paper area	[m^2]
A_s	cross sectional electrical steel area	[m^2]
A_{su}	useful slot area	[m^2]
A_{sur}	surface area of stator	[m^2]
A_{unfin}	surface area between fins	[m^2]
b_{r0}	rotor slot opening width	[m]
b_{r1}	rotor slot notch width	[m]
b_{r2}	rotor slot width	[m]
b_{s0}	stator slot opening width	[m]
b_{s1}	stator slot notch width	[m]
b_{s2}	stator slot width	[m]
b_{tr}	rotor tooth thickness	[m]
b_{ts}	stator tooth thickness	[m]
B_{cr}	rotor core flux density	[T]
B_{cs}	stator core flux density	[T]
B_g	air gap flux density	[T]
B_{tr}	rotor tooth flux density	[T]
B_{ts}	stator tooth flux density	[T]
C_0	Esson's Constant	[ ]
C_ω	Constant power speed range ratio	[ ]
d_{Co}	wire gauge diameter	[m]
D_{er}	end ring outer diameter	[m]
D_{is}	stator inner diameter	[m]
D_{os}	stator outer diameter	[m]
D_{re}	rotor outer diameter	[m]
D_{shaft}	shaft diameter	[m]
f	frequency	[Hz]
F_m	magnetization MMF	[A·t]
F_{mcr}	rotor core MMF	[A·t]
F_{mcs}	stator core MMF	[A·t]
F_{mg}	air gap MMF	[A·t]
F_{mtr}	rotor tooth MMF	[A·t]
F_{mts}	stator tooth MMF	[A·t]
g	air gap length	[m]
G_{t1}	stator tooth weight	[Kg]

G_{tr}	rotor tooth weight	[Kg]
G_{y1}	stator yoke weight	[Kg]
h	fin height	[m]
h_{air}	air convection coefficient	[W/m^{2}K]
h_{cr}	rotor core height	[m]
h_{cs}	stator core height	[m]
h_{r0}	rotor slot opening height	[m]
h_{r1}	rotor slot notch height	[m]
h_{r2}	rotor slot height	[m]
h_{s0}	stator slot opening height	[m]
h_{s1}	stator slot notch height	[m]
h_{s2}	stator slot height	[m]
H_{cr}	rotor core field intensity	[A/m]
H_{cs}	stator core field intensity	[A/m]
H_{tr}	rotor tooth field intensity	[A/m]
H_{ts}	stator tooth field intensity	[A/m]
i_{LR}	locked/rated current ratio	[ ]
I_n	rated current	[A]
I_{oA}	no-load current	[A]
I_{er}	end ring current	[A]
I_{LK}	starting current	[A]
I_μ	magnetization current	[A]
I_n	rated current	[A]
J_b	rotor bar current density	[A/mm^2]
J_{er}	end ring current density	[A/mm^2]
J_{cos}	stator current density	[A/mm^2]
k_{cond}	slot conductivity coefficient	[W/m^{2}K]
k_p	insulation paper conductivity coefficient	[W/m^{2}K]
k_s	electrical steel conductivity coefficient	[W/m^{2}K]
K_c	Carters coefficient	[ ]
K_f	form factor	[ ]
K_s	saturation factor	[ ]
K_{fill}	slot fill factor	[ ]
K_E	EMF coefficient	[ ]
K_{Fe}	lamination thickness	[m]
K_I	ratio between rotor and stator tooth MMF	[ ]

K_{shw}	stator slot height to width ratio	[ ]
K_r	skin effect resistance coefficient	[ ]
K_{st}	stator tooth saturation coefficient	[ ]
K_{q1}	winding zone factor	[ ]
K_{w1}	stator winding factor	[ ]
K_{y1}	chording factor	[ ]
l_{er}	end ring segment length	[m]
l_c	coil length	[m]
	equivalent fin length	[m]
l_{end}	end connection coil length	[m]
l_p	radial length of insulation paper	[m]
l_s	radial length of stator yoke	[m]
L	stack length	[m]
L_{sc}	stator leakage inductance	[H]
m	electrical phases	[ ]
	fin specific variable	[ ]
n_b	base rotational speed	[rpm]
n_m	maximum rotational speed	[rpm]
n_r	rated rotational speed	[rpm]
n_s	conductors per slot	[ ]
p	magnetic poles	[ ]
p_{core}	core losses	[W]
p_{fw}	friction and winding losses	[W]
p_{rcl}	rotor copper poles	[ ]
p_{scl}	stator winding losses	[W]
p_{stray}	stray losses	[W]
p_1	magnetic poles pairs	[ ]
P_{in}	input power	[W]
P_n	rated output power	[W]
P_{out}	output power	[W]
q	slots per pole constant	[ ]
q_1	slots per pole per phase	[ ]
Q_r	number of rotor slots	[ ]
Q_s	number of stator slots	[ ]
R_{be}	rotor bar / end ring equivalent resistance	[Ω]
R_{paper}	convectional thermal resistance of convection	[K/W]

R_{1eq}	equivalent stator resistance	[Ω]
R_{paper}	thermal resistance of insulation paper	[K/W]
R_s	stator phase resistance	[Ω]
R_{paper}	thermal resistance of electrical steel	[K/W]
S	slip	[ ]
S_n	rated slip	[ ]
S_{gap}	apparent air gap power	[ ]
t	fin thickness	[m]
t_{bk}	breakdown/rated torque ratio	[ ]
t_{ins}	insulation thickness	[m]
t_{lr}	locked/rated torque ratio	[ ]
T_{air}	ambient air temperature	[K]
T_b	torque at base speed	[N·m]
T_{bk}	breakdown torque	[N·m]
T_{bp}	peak torque at base speed	[N·m]
T_{Co}	copper temperature	[K]
T_m	torque at maximum speed	[N·m]
T_{mp}	peak torque at maximum speed	[N·m]
T_n	rated torque	[N·m]
T_{sur}	stator surface temperature	[K]
T_w	winding temperature	[K]
V_{1eq}	equivalent stator voltage	[V]
V_L	line voltage	[V]
V_m	maximum supply voltage	[V]
V_{ph}	phase voltage	[V]
W_1	number of turns per phase	[ ]
X_{1eq}	equivalent leakage reactance	[Ω]
X_2	referred rotor leakage reactance	[Ω]
X_{be}	rotor bar leakage reactance	[Ω]
X_m	magnetization inductance	[Ω]
X_{sl}	rotor leakage reactance	[Ω]
X_{sl}	stator phase leakage reactance	[Ω]
y	coil pitch	[ ]

Chapter 1

Introduction

This chapter presents the background of traction motors, their current status, classification and design challenges. The formulation of the research problem and the research methodology in context with this thesis are also described. In conclusion of this chapter, an overview of each subsequent chapter is included.

1.1 Background

Since its invention in the 1830s, electrical machines have made key contributions to industrial developments world wide. It can be said that electrical motors are the backbone of the modern era. Since it was introduced, thousands of pioneering researchers and engineers have made significant improvements and various adoptions for specific applications. One of these applications is traction drives such as being utilized in electrically powered vehicles, locomotives and mine trucks.

The first electric vehicle (EV) made its debut in the United States of America in the late nineteenth century. Although it was rather described as an electrified wagon, it sparked major interest. It was estimated that by 1910, EVs accounted for a third of all vehicles in New York [1]. From the 1920s a decline in popularity of EVs took place due to the discovery, cheap extraction and mass availability of crude oil. By 1935 EVs were no longer economically produced due to the success of internal combustion engines.

In recent years, EVs and hybrid vehicles have been developed at an excessive rate as a solution for energy and environmental problems. Many countries have aspirations to ban fossil-fuel cars in the future: Norway by 2025, China by 2030, France by 2040 and the United Kingdom by 2050 [2]. EVs are regarded as a key part for a sustainable future. At the beginning of this century low energy densities and the prolonged charging time of batteries were the main reasons why EVs lost its competitive edge against combustion engines. With

major recent technological improvements in battery development and optimal energy management, the future looks bright for electrified transportation systems.

1.1.1 Classification of traction motors

Typical characteristics that are required from a motor for traction applications are as follows: high reliability and robustness, a wide constant power speed range (CPSR), high efficiency over wide speed ranges and a high power density [3]. There are a variety of motor technologies that conform to these requirements and can thus be used for traction drive applications. These motors include, but aren't limited to:

- Permanent magnet brushless DC motor;
- Brushed DC motor;
- Permanent magnet synchronous motor;
- Switched reluctance motor;
- Reluctance synchronous motor;
- Induction motor.

For traction applications such as in EVs and electrical trains, the squirrel cage induction motor is widely used due to its wide constant power speed range, good overload capability and high efficiency. In addition, it is highly reliable, cheap to manufacture, robust and easy to maintain. Although the operating principle is the same, the design of a traction induction motor is significantly different to that of a conventional induction motor. Conventional induction motors are generally designed and optimized for single point operation at rated speed. However, for traction induction motors performance characteristics are considered at multiple operating points. This is to establish a wide flux weakening range, as well as to achieve high efficiency throughout the flux weakening range.

1.2 Problem statement

The aim of this thesis is to formulate a design approach of induction machines for heavy traction applications with emphasis on a wide constant power speed range. Induction motors are cheap, robust and easy to construct. They were not favoured for traction applications before the advent of variable frequency drives, which allowed variable speed applications. When investigating vehicle

drive cycles across various terrains, a wide constant power speed range is an essential traction motor performance characteristic. The proposed design approach will investigate to what extent a wide CPSR can be achieved by refining general induction motor design theory for traction applications. This will be applied in the derivation of physical motor dimensions from desired machine specifications to achieve rated performance.

A small prototype motor will be optimally designed, built and tested experimentally to validate the applied design approach. Finally, a large traction induction motor will be optimally designed and analysed for heavy rail applications. The research will mainly be focussed on three-phase squirrel cage induction motor technology.

1.3 Research aims and methodology

Electric vehicles represent one of the most promising solutions to energy security world wide and reducing emissions [4]. As mentioned above, induction motors are very attractive solutions to traction drive applications such as in electric vehicles and locomotives.

The design of an induction motor for traction applications is significantly different from that of the conventional induction motor. For an induction motor to be deemed suitable for traction drives a set of requirements have to be met:

- High reliability and robustness;
- Wide constant power speed range;
- High efficiency over wide speed ranges and;
- High power density.

The research methodology employed in this thesis is to formulate and test a holistic design strategy; which entails the design and optimisation of a traction induction motor that conforms to the above conditions. The following steps will be taken to accomplish the aim of this project:

1. A literature review will be completed to gain knowledge on the current state of technology in traction drives.
2. An investigation will commence thereafter on general induction machine operating principles and design methodology.
3. An analytical model will be derived to calculate machine dimensions and specifications according to rated conditions.

4. The initial analytically generated design will further be optimized.

5. A small prototype motor will be designed and tested to evaluate the design approach.

6. Insights gained through the design and experimental evaluation of the prototype motor will aid in the design and optimization of a larger traction motor.

1.4 Layout of thesis

The basic layout for the remainder of the thesis is as follows:

In Chapter 2 the basic theory for the traction induction motor design is presented necessary for the design of a traction motor.

In Chapter 3 the design specifications of a prototype motor and analytical model are presented. The aim of the analytical model is to calculate machine parameters and dimensions for given machine specifications.

In Chapter 4 different optimization algorithms are discussed and how the design will benefit from these algorithms respectively. The initial design achieved by the analytical model will be optimized and the results will further be documented in this chapter. The motor will be tested for manufacturability and refined if required.

In Chapter 5 the construction of a prototype motor is presented. This involves the mechanical design, construction and assembly. In addition, the test results of the prototype induction motor will be presented. The performance and operating regions will be discussed in detail to determine whether the design procedure was successful.

In Chapter 6 the design of a larger traction motor following the same or adapted design approach used for the prototype motor, will be documented.

In Chapter 7, conclusions pertaining to the content of the entire thesis will be presented. From these, recommendations and improvements will be proposed for future research in this field of work.

Chapter 2

Design aspects of traction induction motors

This section will present the design theory of induction machines and how it will be applied for heavy traction applications.

2.1 Brief history of induction machines

After Farady revealed the electromagnetic induction law in 1831 and Maxwell developed the laws of electricity in 1860, the theoretical foundation of a induction machine was established. The induction machine has two founders: Galileo Ferraris (1885) and Nicola Tesla (1887) [5]. Both their inventions were supplied with a 2-phase AC (Alternating Current) power source. Therefore, the 1-1' and 2-2' winding configuration was applied as seen in Figure 2.1.

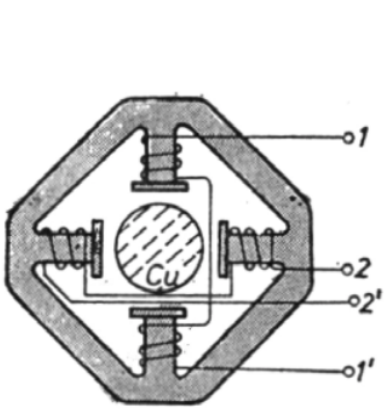

(a) Ferraris' induction motor (1885).

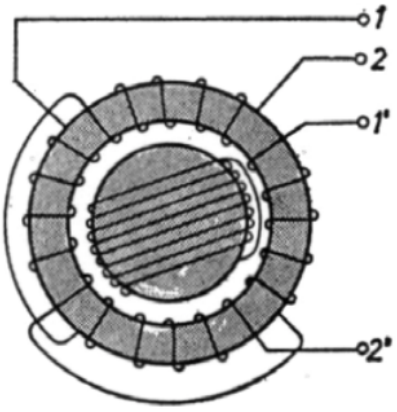

(b) Tesla's induction motor (1887).

Figure 2.1: Earliest induction motors [5].

During the 1880s, Dolivo Dobrovolsky succeeded in delivering 3-phase power to induction machines from power grids over long distances. He was also the inventor of the wound rotor, single and double-cage rotors used in modern times [5]. In the early 1900s, induction machines were used industrially, but soon got replaced by DC machines. The induction machine made a remarkable comeback in the 1980s with the addition of insulated-gate bipolar transistors (IGBT) and pulse width modulation (PWM) inverters. This allowed for wider supply frequencies and thus made the induction motor suitable for variable speed drive applications.

At the beginning of the 21st century, approximately 60 % of all power consumed around the world were due to motor loads. From these motor loads, more than 90 % are induction motors [6]. This is a good reflection of the continuous research conducted in this field for an ever expanding technological era where motor drives become more advanced and specialized for various applications. Although modern induction machines have better performance and advanced topologies than a century ago, the principle behind an induction motor has remained the same throughout the years. A rotating magnetic field is produced by a multiphase AC stator winding. This rotating magnetic field induces voltages that produces currents in the rotor windings. An interaction exists between the stator produced magnetic field and the induced rotor magnetic field which results in torque production [5, 7].

2.2 Classification of induction motors

As can be seen from Figure 2.2, induction motors can be divided into two main categories: single-phase and three-phase. Single-phase induction motors can be further divided into four categories: split phase, capacitor start, capacitor-start-capacitor-run and shaded pole. Three-phase induction motors can be divided into two categories: squirrel cage rotor and slip ring or wound rotor [8].

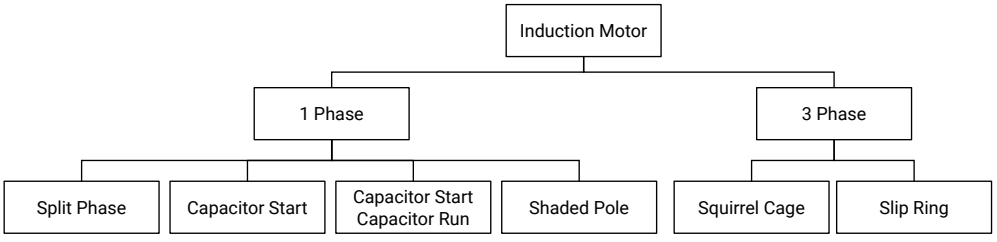

Figure 2.2: Different types of induction machines.

2.3 Three-phase induction motors

Due to the fact that three-phase AC current can transfer more power at lower cost compared to single-phase AC current, it is used as the industry standard in power intensive environments. Therefore, the focus of this thesis will be on three-phase AC induction machines. As mentioned in the previous section, three-phase induction motors can be divided into two sub-categories due to their rotor construction. These are wound rotors and squirrel-cage rotors. Both these significantly different rotors have the same stator construction.

2.3.1 Wound rotor

Just as in the stator, a wound-rotor has its own set of three-phase windings. These windings are connected by brushes to slip rings on the shaft. This rotor configuration allows examination of rotor currents and rotor resistance. The latter allows adjustment of the machine's torque-speed characteristics and are usually applied for high starting torque applications. Unfortunately, wound-rotors are expensive and require a considerable amount of maintenance and their applications are rather limited [9]. An example of a wound-rotor induction machine can be seen in Figure 2.3.

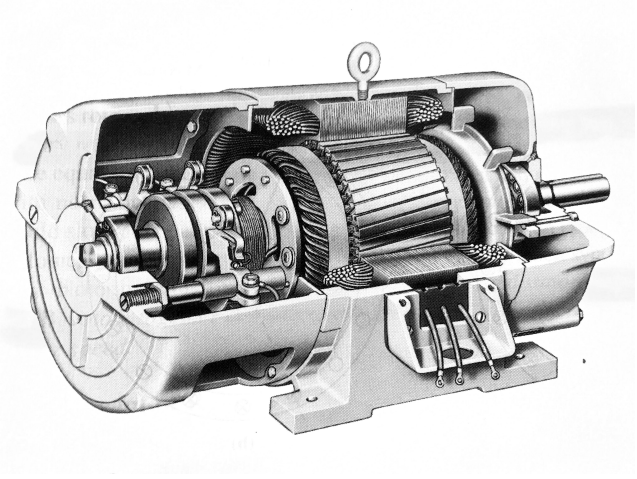

Figure 2.3: Section view of a small wound-rotor induction motor [9].

2.3.2 Squirrel-cage rotor

Squirrel-cage rotors consist of a series of conducting rotor-bars which are placed in slots along the outer diameter of the rotor. These conducting bars are shorted at both ends by end-rings. An example of a squirrel cage induction motor can be seen in Figure 2.4. The scope of this thesis will focus on three-phase squirrel cage induction motors for traction applications. They are known

to be reliable, robust, cheap and efficient [10]. There are four different methods of construction for a squirrel cage rotor: aluminium die-cast, copper die-cast, fabricated aluminium and fabricated copper.

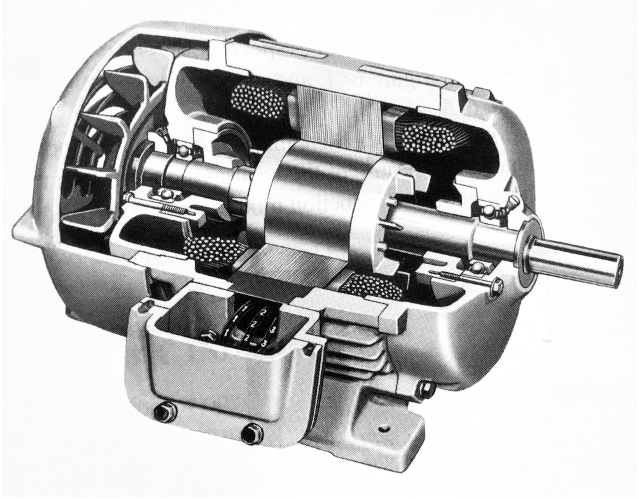

Figure 2.4: Section view of a small squirrel cage induction motor [9].

2.3.2.1 Aluminium die-cast:

This method of construction has been in use since the 1930s and is unchanged since its inception. Due to technological advancements in the casting field, a wide range of rotor sizes can be casted successfully. Since Aluminum can shrink as much as 6 % upon cooling, care should be taken regarding mould sizes and tolerances. An uneven distribution of material in the cast can cause an unwanted increase in rotor resistance and subsequently an increase in bar temperature. If the manufacturer successfully complies with modern die cast practices, it should have the same level of reliability of fabricated rotor bars [11].

2.3.2.2 Copper die-cast:

Copper has a superior electrical conductivity over aluminium and is better suited for rotors in induction motors. The casting process of copper is very similar to aluminium. The manufacturing process has additional challenges which were only met in recent years. These challenges include consistency of the cast clamp pressure and shot pressure at predetermined temperatures. This is to ensure that the cast material is homogeneous and to avoid porosity. If the process is not carefully controlled, cast material will not be evenly

distributed and blow-holes can appear in the material. This can result in increased resistance, uneven temperature distribution and decreased efficiency of the motor. With higher temperatures and pressures required for copper castings, increased costs are eminent. Table 2.1 gives a comparison between the two casting processes. Similar quality as in aluminium castings can be achieved, but this process requires larger initial capital investment [11]. It is estimated that highly efficient motors with copper rotors have a payback period of four months due to the energy saved [12].

	Aluminium	**Copper**
Temperature [°C]	650	1050
Shot pressure [MPa]	13.8	44.8
Clamp pressure [MPa]	16.5	53.8

Table 2.1: Comparison of aluminium and copper casting requirements [11].

2.3.2.3 Aluminium fabricated:

The main advantage of fabricated aluminium rotor bars over aluminium cast rotors is the cost. Further, most manufacturers have a finite set of cast sizes available. Depending on the quantity required, it's more expensive to cast and use tooling techniques to achieve a desired dimension. For industrial use, a break-even calculation can be made regarding the cost of creating custom moulds and the payback period. The main difference in construction between aluminium and copper fabricated rotors is that the former is welded and the latter is brazed for structural integrity.

2.3.2.4 Copper fabricated:

This is the oldest rotor manufacturing technique dating back to the 1920s. This construction method can be used for rotors of any size, but is more expensive and unattractive for small machines. For an aluminium rotor to achieve similar efficiencies such as in copper rotor motors, the length of an aluminium rotor has to be increased between 20 % and 50 %. This has an increase in the amount of electrical steel laminations required. Due to a limited budget and a single rotor needed for experimental purposes of this thesis, the rotor will be constructed with fabricated copper bars.

2.3.3 Equivalent circuit

As mentioned earlier, the working principle of an IM is such that voltages and currents are produced in the rotor from the three phase stator windings. This

action is similar to that of a transformer and thus, the equivalent circuit of an IM can be derived from it. The stator side of the circuit is identical to that of a transformer containing a resistance R_1 and leakage reactance X_1. Due to the high reluctance of the air-gap, a high magnetizing current is needed to achieve a specified flux value. As a result, the magnetization reactance X_m will be smaller than that of a transformer [9].

The main difference between the equivalent circuit of an IM and a transformer is due to the effects of a varying rotor frequency on the induced rotor voltage and rotor impedance. The magnitude and frequency of the induced voltage on the rotor is proportional to the connected load and thus relates to the slip S. Slip is known as the difference between the synchronous speed and mechanical speed of the motor at a given time. For a transformer, the secondary currents, voltages and impedances are referred to the primary side through a turns ratio. For squirrel cage IM, the turns ratio is practically impossible to determine. Luckily, when referring the secondary side to the primary side of the IM, the referred reactance X_2 and resistance R_2 can be measured experimentally. After simplifying the effect of slip on rotor induced voltages and reactance, the referred and final equivalent per phase circuit of the IM can be seen in Figure 2.5.

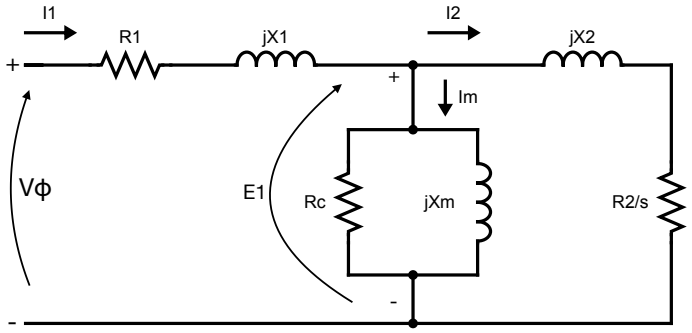

Figure 2.5: Equivalent circuit of an induction motor.

The variables I_1, I_m and I_2 represent the stator phase current, magnetization current and induced rotor current, respectively. The induced and referred voltage on the rotor is represented by E_1. Lastly, the core losses (eddy and hysteresis) is represented by R_c. Parameters related to starting torque are R_1, R_2 and X_2; to pull-out torque are X_1 and X_2; and for rated torque R_2 [13].

2.3.4 Machine losses

It is estimated that within the industrial sector of the United States, more than 70 % of the power consumed is from electrical motors [12]. There are

thus major economical benefits in understanding machine losses and how to create efficient motors. A power-flow diagram can be seen in Figure 2.6 indicating how energy enters and dissipates though motor operation.

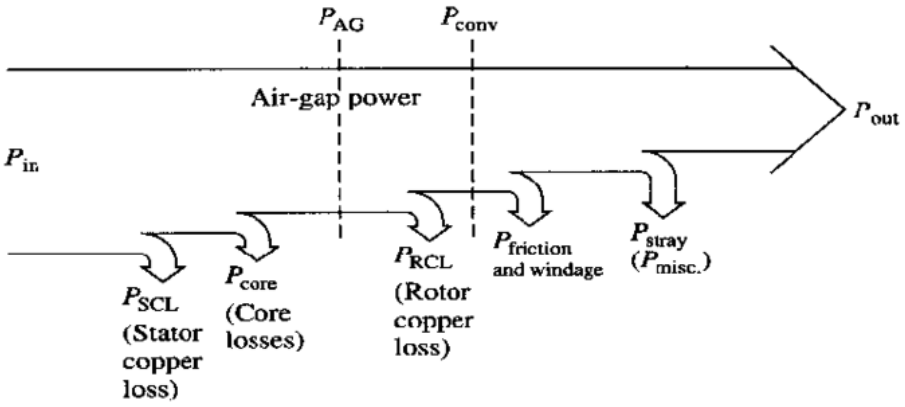

Figure 2.6: Power-flow diagram of an induction motor [9].

The diagram starts with electrical energy entering the motor in the form of three-phase voltages and currents. Conductor losses occur in the stator copper windings, P_{SCL}. These losses are also known as ohmic losses due to the $P \propto I^2R$ relationship. Magnetic or iron losses such as hysteresis and eddy current losses are grouped together as core losses, P_{core}. The remaining power is transferred to the rotor across the air-gap and is known as the air-gap power, P_{AG}. Further conductor losses occur in rotor copper windings and are indicated by P_{RCL}. The remaining power is converted to mechanical energy and is given by P_{conv}. Mechanical losses include friction and windage losses, P_{fw}, as well as stray losses, P_{misc}. Stray losses are difficult to determine due to the machine's stack aspect ratio and winding configuration. The remaining power is the output power received by the load.

Motor losses can be reduced by the optimization of machine characteristics such motor geometry, winding configurations and aspect ratios. Further efficiency improvements can be made by utilization of low loss materials and reduction of mechanical losses.

2.4 Power and torque characteristics of traction motors

Traction motors are mostly used for propulsion systems such as electric vehicles (EVs) and load carrying applications. Induction motors are widely accepted as traction motor of choice due to its good constant power speed range (CPSR)

[14]. In EV applications, the power and torque characteristics of a traction motor has a big influence on the motor's acceleration, grade ability and maximum speed [4]. A well designed traction drive motor has three distinguishable operating regions: a constant torque, constant power region and reduced power as seen in Figure 2.7. These regions will be discussed briefly below.

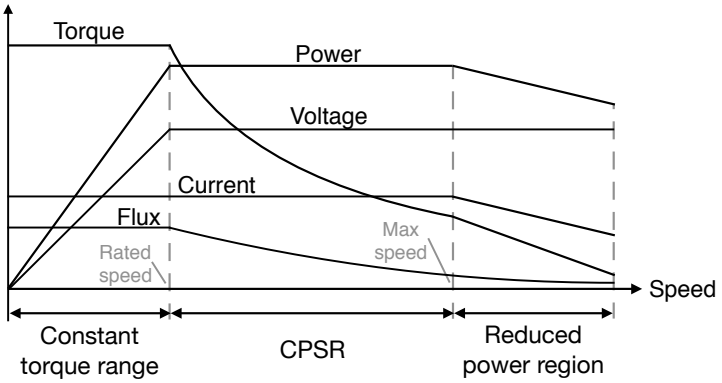

Figure 2.7: Torque-speed characteristics of a traction motor.

2.4.1 Constant torque

In this region a constant torque is maintained by increasing the supply voltage and frequency at a fixed ratio while the current and flux remains constant. The voltage/frequency ratio is maintained until the rated voltage value is achieved at base speed. Once base speed is surpassed, the voltage remains fixed while the frequency continues to increase within the CPSR. Additionally, in the constant torque region the output power increases linearly with supply voltage.

2.4.2 Constant power

This region is entered once the the supplied voltage and frequency ratio is broken. Thus, the supply frequency continues to increase while the supply voltage remains fixed. The air-gap flux reduces inversely proportional to the increasing supply frequency while the machine current remains constant. Thus, the decrease in torque appears as seen in Figure 2.7. In EV applications an extended constant power region is important for initial acceleration and cruising operation. For a traction motor design to be deemed suitable, it should have a constant power region of approximately three times its base or rated speed [5].

2.4.3 Reduced power

In this region the torque, as well as the output power reduces due to the increased influence of back electromotive force (Back-EMF). The machine operates at pull-out or breakdown slip in order to maximize the output torque. As a result, the current decreases, output power reduces and machine operation is unstable.

2.5 Motor overload capability

Traction motors are often subjected to heavy traction duty, which requires them to handle excessive loads. This causes premature wear and damage to both mechanical and electrical components of the motor [15]. Induction motors can be overloaded by more than four times their rated operating conditions [16]. This makes the induction motor well suited for traction drive applications.

2.6 Design considerations

This section will describe and discuss important design considerations of a traction induction motor.

2.6.1 Main dimensions

An important design consideration regarding the main dimensions, as seen in Figure 2.8, is the relationship between the stator outer diameter D_{out} and the stack length L.

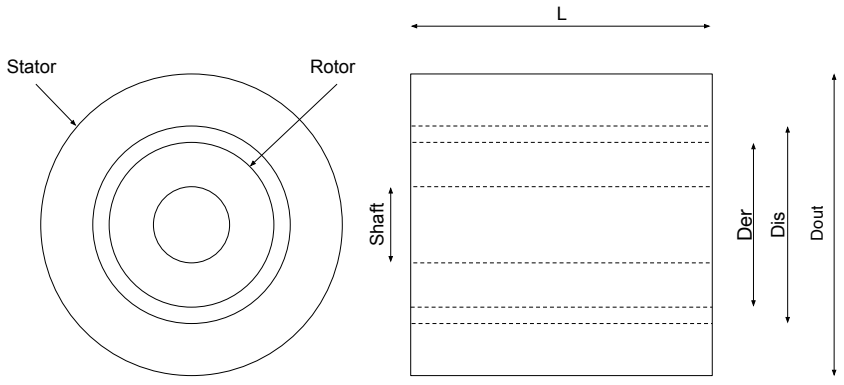

Figure 2.8: Main induction machine dimensions.

This relationship can further be adapted as the relationship between the pole pitch (arc length) and the stack length given by [17]:

$$\left(\frac{\pi D_{out}}{pL}\right) \tag{2.1}$$

where p is the number of magnetic poles in the machine. This relationship determines the general shape of the motor. The shape can vary from a wide, but short disc shape to a long cylindrical form. The variations in shape have an influence on the machine's performance and are summarized in Table 2.2.

Table 2.2: Pole pitch and stack length ratio influence on performance [17].

Performance	$\left(\frac{\pi D_{out}}{pL}\right)$
Well rounded design	1.0 - 1.1
High power factor	1.0 - 1.3
High efficiency	1.4 - 1.6
Minimum overall cost	1.5 - 2.0

It should be mentioned that the information presented in Table 2.2 predominantly apply to large sized machines. For smaller machines such as a 3 kW machine, a smaller ratio tends to have a better performance in terms of efficiency and power factor. This is especially the case for traction induction motors.

2.6.2 Stator design

The stator is the stationary portion of a rotating electrical machine. From Figure 2.8 the stator can be viewed as the outer portion which consists of a stack electrical steel laminations and a set of insulated electrical windings placed inside machined slots. The electrical steel serves as a magnetic path for interaction between stator and rotor magnetic fields. The core consists of laminations to reduce eddy current losses. Further, the electrical windings are designed to withstand thermal loading of the motor. The remainder of this sub-section discusses considerations when designing the stator of a traction induction motor.

2.6.2.1 Delta vs wye connection

The phase connection chosen for an induction motor is related to the allowable turns per coil. As machine size increases, the amount of turns per coil decreases generally. Therefore, larger machines results in restricted options for phase belt connections. It should also be noted that the phase connection

has an influence on the third harmonic flux modulation. For a delta connection and sinusoidal voltage supply, the third harmonic of flux cannot exist, as well as its induced voltage resulting in marginally reduced core losses [5]. The maximum line current is greater for a delta connection compared to a wye connection. This results in a higher winding temperature for delta phase connections [18].

Further, a combination of the two winding methods known as delta-wye can be used. This is often used to reduce the starting current or increase the constant power speed range of the machine. If the winding connection is switched from delta to wye the phase voltage across the winding will decrease from V_L to $\frac{V_L}{\sqrt{3}}$, causing the starting current to be reduced by the same ratio [9].When the machine is operating in the constant power region and the winding connection is switched from wye to delta, the speed range can be increased by as much as three times within the region [5].

2.6.2.2 Selection of the number of stator slots

The number of stator slots has an impact on the operation, cost and weight of the motor. To increase the overload capability traction induction motors are often designed with relatively high number of stator slots. However, there are also some disadvantages associated with a high number of stator slots as summarized in Table 2.3 [17].

Table 2.3: Trade-off for higher amount of stator slots.

Advantages	Disadvantages
Higher overload capacity	Increased cost
Reduced leakage reactance	Increased iron losses
Reduced tooth pulsation losses	Increased magnetization current
	Poor cooling
	Reduced efficiency

To avoid an increase in leakage reactance, the slots/pole/phase ratio should generally be more than or equal to two. Both integral and fractional slot windings should adhere to this ratio.

2.6.2.3 Stator slot types

The two most commonly used stator slots for traction applications in induction motors are semi-closed slots and open slots. These slots can be seen in Figure 2.9. The differences between these slots are described below:

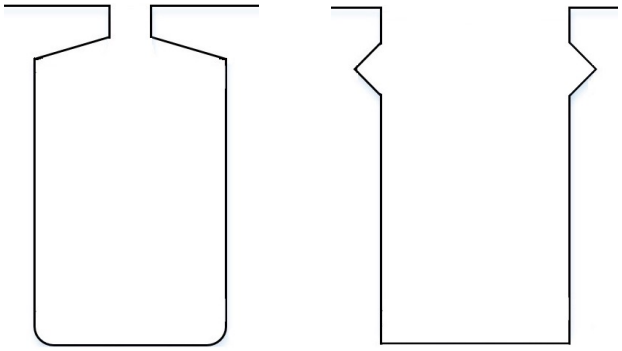

(a) Semi-closed slot. (b) Open slot.

Figure 2.9: Most common induction motor slots.

Semi-closed slot

From Figure 2.9a it can be seen that the slot width is much wider than the slot opening. A result of this is a more expensive winding procedure.The semi-closed slot consists of wound coils and is mostly used for induction motors with a voltage rating lower than 3 kV [19].

Open slot

The open slot has an uniform slot width with a small wedge placed inside a notch to secure the form-wound coils. Due to the slot opening and width being the same, it makes the winding process easier and cheaper when compared to a semi-closed slot. The gap between the tightly fit wedge and the air-gap creates an additional ventilation path and has heat transfer advantages. This configuration is mostly used in larger machines such as 75 KW or higher when the rated voltage is 3 kV and above [19, 20].

Performance dependence on slot shape

The main difficulties involved when designing for a wide flux weakening range are:

- Reducing the leakage inductance;
- Reducing the skin effect and;
- High efficiency throughout the flux weakening range.

How these aspects influence performance through slot shape design are discussed as listed in Sections 2.7.1, 2.8.2 and 2.8.4 respectively. A rectangular slot is sufficient to address the design challenges mentioned above. In addition, its simplicity and ease of manufacturing aided in the decision.

2.6.2.4 Stator winding

Stator windings are generally constructed from enamelled copper wire for its superior conductivity. These windings are spatially distributed within the stator slots to achieve sinusoidal current linkage. The rest of this sub-section describes stator windings and how it can be manipulated to achieve desired performance.

Form-wound vs random-wound coils

The physical appearance of the two winding configuraions can be compared and viewed in Figure 2.10. Form-wound coils consist of rectangular wire. This rectangular shape is constructed in a shaping machine and dimensioned according to the configuration it will occupy in its slot. The winding process begins with the looping of the wire. Several wires in parallel creates a turn. These turns are always arranged in precise location with respect to each other. When inserting, these coils are kept in place by slot wedges. When there is no definite arrangement between turns at insertion, the winding configuration is called random. Random windings are cheaper and generally used in smaller machines [21].

The biggest advantage of random-wound coils over form-wound coils is the lower cost and ease of mechanized construction due to its cylindrical shape. It should be noted that the life expectancy of random-wound coils are drastically reduced under non-linear loads and severe weather conditions. The primary advantage of form-wound coils are due to its uniform copper fill construction and thus better fill factor. As a result, form windings have uniform temperature distribution which minimizes the chance of a localized hotspot. Due to the cylindrical wire shape and configuration of random-wound coils, resin builds up unevenly and creates unpredictable localized hotspots.

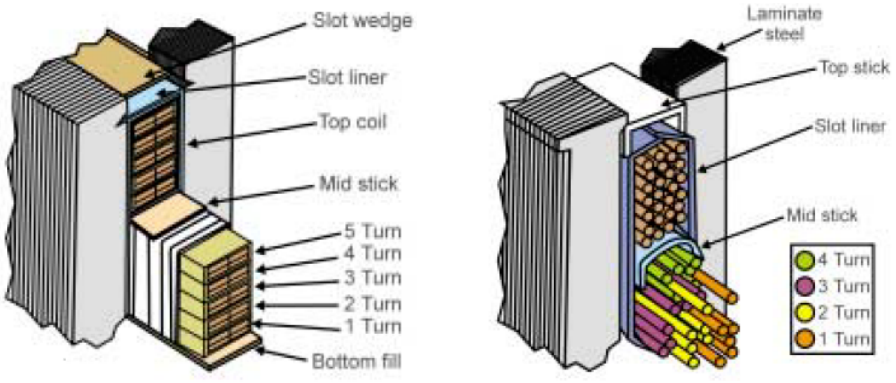

(a) Form-wound coil. (b) Random-wound coil.

Figure 2.10: Form- and random-wound coil comparison [21].

Short-pitched winding

A coil span can be defined as the peripheral distance between two coil sides of a coil. Pole pitch can be described as the centre to centre distance of two adjacent poles and is generally expressed in terms of the number of slots on the periphery or electrical degrees. If the coil span is equal to the pole pitch, the armature winding is called a full pitched winding. If the coil span is less than the pole pitch, the armature winding is known as a short-pitched or fractional-pitched winding [22]. This fraction is known as the winding factor or chording factor. This concept can be visualized in Figure 2.11:

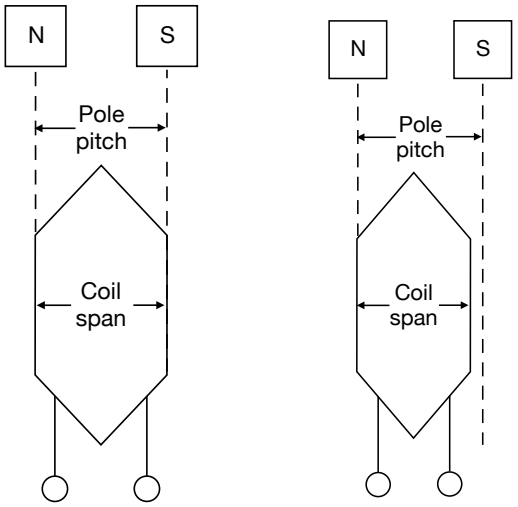

(a) Full-pitch. (b) Short-pitch.

Figure 2.11: Full and Short pitched coil comparison.

Some of the advantages regarding short pitched winding include [23]:

- The amount of copper required for the end connection winding is reduced when compared to full pitch winding.
- It improves the waveform of the generated EMF by reducing harmonic distortion.
- Due to the elimination of high frequency harmonics, hysteresis losses and eddy currents are reduced, resulting in an increase of efficiency of the motor.

The primary disadvantage of short pitched coils is the reduction in generated EMF. To counter this effect, more coil turns are required to produce similar

voltages of a full pitched coil.This increase in coil turns aren't significant compared to the shortening of the end connections, thus the material consumption will always be less for a short pitch winding.

Winding layers

Conventional induction machines generally have single layer or double-layer winding configurations. In double layer windings, the amount of coils equal the amount of slots due to each slot accommodating two coil sides. This method is mostly used in larger or mass produced machines due to being the cheaper winding process. Further, fractional slot windings can be realized through this method. In single layer windings, the amount of coils are equal to half the amount of slots due to each slot consisting of one coil side. The primary advantage of single layer winding is quieter machine operation, reduced tooth losses and less ampere-turns required to produce a desired air-gap flux density. This winding method is mostly used in small machines. A visual representation of both winding methods can be seen in Figure 2.12.

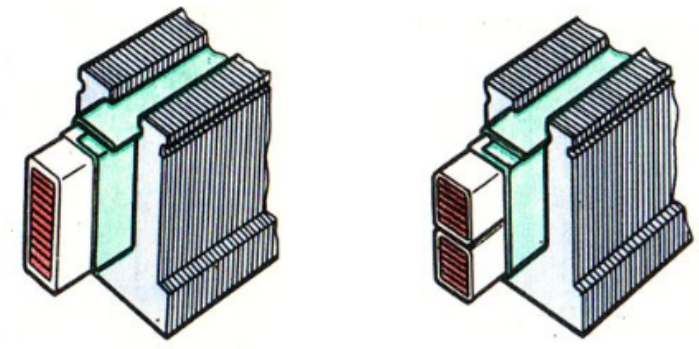

(a) Single layer winding. (b) Double-layer winding.

Figure 2.12: Single and double-layer winding comparison.

2.6.3 Rotor design

As displayed in Figure 2.8, the rotor is the inner and moving portion of an induction motor. It consists of slotted steel laminations and a set of windings within its slots. Two types of rotors were discussed in section 2.3 with squirrel cage rotors being the preferred option.

The rotor design has a major influence on the motor efficiency and power factor at all operating conditions. The remainder of this section will present important considerations for the the design of a rotor for traction applications.

2.6.3.1 Rotor slots

The rotor slots are generally semi-closed or closed with a small gap that leads to the outer surface. Because of the smoothness of the air-gap, a closed slot rotor will have a lower magnetization current and quieter operation. Although this sounds promising, the motor will have a reduced overload capability and an increased leakage reactance [17]. For traction applications a semi-closed slot is more advantageous due to its higher overload capability. More detailed considerations regarding the design of a semi-closed slot will be presented in the following chapter.

2.6.3.2 Number of slots selection

Although the amount of stator slots is an important design consideration, the ratio between stator and rotor slots is crucial to prevent disturbances during operation. Thus, a careful selection of rotor slots Q_r with respect to stator slots have to be made. The most common disturbances of poor stator and rotor slot combinations are summarized hereafter.

- **Crawling:** The rotating magnetic field within the air-gap generated from the three-phase power supply is generally non-sinusoidal and contains harmonics. These harmonics that are present in the flux wave have a magnificent impact on the torque-speed characteristics of the motor. Additionally, If a 7^{th} order harmonic is present, the motor will have a undesired tenancy of running at a seventh of its rated speed [19, 20].
- **Cogging:** This is when the rotor remains stationary and refuses to start due to magnetic locking. This occurs when the amount of rotor and stator teeth are equal. When all the rotor and stator slots are aligned, the reluctance of the magnetic path is a minimum and the rotor remains stationary [19, 20].

The following conditions, as well as Figure 2.13 can be used as a guideline for rotor and stator slot combinations. Table 2.4 depicts conditions that should be complied with in order to avoid unwanted operating behaviour.

Table 2.4: Boundary conditions to avoid unwanted motor behaviour [19, 20].

Unwanted behaviour	Boundary condition
Cogging and crawling	$Q_s \neq Q_r$ and $(Q_s - Q_r) \neq \pm 3p$
Hooks and cusps in torque characteristics	$Q_r \neq \pm p, \pm 2p, \pm 5p$
Noisy operation	$(Q_s - Q_r) \neq \pm 1, \pm 2, (\pm p \pm 1), (\pm p \pm 2)$

All the clear spaces in Figure 2.13 are safe tooth combinations. The '-' indicates harmful torques in counter current braking, 'x' indicates harmful mechanical

vibrations, '○' represents harmful synchronous torques at standstill while the '+' refers to harmful torques at positive speeds. However, if the design isn't under strict limits compromises can be made with the combination selection.

		Number of pole pairs $p = 1$										Number of pole pairs $p = 2$									
	Tens of rotor	Ones of rotor slot number Q_r										Ones of rotor slot number Q_r									
Q_s	slot number	0	1	2	3	4	5	6	7	8	9	0	1	2	3	4	5	6	7	8	9
24	1	−	×	○	×	+	×	−	×	○	×	−	×	○	×	+	×	+	×		×
	2	+	×	−	×	○	×	+	×	−	×	−	×	−	×	○	×	+	×	+	×
	3	○	×	+	×	−	×	○	×	+	×		×	−	×		×	○	×		×
36	1	−	×	○	×	+	×	−	×	○	×		×	○	×		×	∓	×	○	×
	2	+	×	−	×	○	×	+	×	−	×	±	×		×	○	×		×	+	×
	3	○	×	+	×	−	×	○	×	+	×		×	−	×	−	×	○	×	+	×
	4	−	×	○	×	+	×	−	×	○	×	+	×		×	−	×		×	○	×
	5	+	×	−	×	○	×	+	×	−	×		×	+	×		×	−	×		×
48	1	−	×	○	×	+	×	−	×	○	×		×	○	×		×	+	×		×
	2	+	×	−	×	○	×	+	×	−	×	−	×	−	×	○	×	+	×	+	×
	3	○	×	+	×	−	×	○	×	+	×		×	−	×		×	○	×		×
	4	−	×	○	×	+	×	−	×	○	×	+	×		×	−	×	−	×	○	×
	5	+	×	−	×	○	×	+	×	−	×	+	×	+	×		×	−	×		×
	6	○	×	+	×	−	×	○	×	+	×	○	×		×	+	×		×	−	×

Figure 2.13: Safe rotor and stator slot combinations [20].

2.6.4 Rotor Shaft

There exists two design approaches for the calculation of minimum shaft diameter for safe machine operation according to [24]. These methods are based on resistance of torsional deflection and transmission of torque. These two approaches can be combined into the following equation in order to determine the minimum diameter of shaft with a keyway:

$$D_{min} = \sqrt[3]{\frac{1.33 \times 10^6 \times P_{out}}{n_m}} \text{ [mm]} \tag{2.2}$$

where D_{min} is the minimum shaft diameter, P_{out} is rated output power and n_m the maximum speed in rpm. Minimum shaft diameters can also be found in induction motor catalogues with sample shaft sizes and its resulting allowable maximum torque.

2.6.5 Air-gap

As can be seen from Figure 2.8, the air-gap is the space between the outer surface of the rotor and the inner surface of the stator. It has a large effect

on important machine characteristics such as the power factor, overload capability, magnetizing current, cooling, noise and balanced magnetic pull. These are important characteristics when designing a traction induction motor, as they differ from the conventional IM. The air-gap influences the mentioned characteristics as follows:

- **Power factor:** A relationship exists where the product of the air-gap length and the flux density is proportional to the MMF needed to transmit flux though the air-gap. Thus, an increased air-gap results in an increased MMF, which results in a high magnetizing current. This eventually leads to a poor power factor.
- **Overload capability:** For a larger air-gap a reduction in leakage flux exists, hence a reduced leakage reactance. This leads to an increase in overload capacity.
- **Magnetizing current:** The air-gap forms the non-magnetic component of the magnetic equivalent circuit. Due to it being connected magnetically in series the magnetic flux flows through the air-gap. A large air-gap increases the magnetizing current and lowers the achievable flux density [25].
- **Cooling:** The flow of air through the air-gap can be classified as internal forced convection. The outer diameter and thickness of the air-gap is directly related to the amount of heat transferred [26].
- **Noise:** The air-gap plays a role in the magnitude of the noise generated from magnetic origin. Periodic force waves are generated within the air-gap resulting in marginal deformation of the stator core and excitation of the surrounding air. This is how the acoustic noise is generated [27]. This noise can be reduced by increasing the air-gap length or reducing the magnetic flux density in the air-gap.
- **Unbalanced magnetic pull:** This comes as a result of a non-uniform air-gap. This leads to the bending motion of the stator that further results in structure-borne acoustic noise. In addition, torque ripple is caused by this effect. These effects are reduced with a uniform and larger air-gap length.

To summarize the information stated above, Table 2.5 can be used in the selection of air-gap size by comparing the advantages and disadvantages of larger air-gap lengths.

Due to the magnetization current, power factor and efficiency being important design parameters for traction induction machines, a minimum air-gap length

Table 2.5: Large air-gap length selection.

Advantages	Disadvantages
Increased overload capability	Increased magnetization current
Better cooling	Reduced power factor
Noise reduction	Reduced efficiency
Reduced tooth pulsations	
Reduced unbalanced magnetic pull	

can be established by the following empirical equation [5]:

$$g = \left(0.1 + 0.02\sqrt[3]{P_n}\right) \cdot 10^{-3}\,[\text{m}] \tag{2.3}$$

where P_n is the rated power of a 4-pole induction motor.

2.6.6 Magnetic loading

The flux density throughout the core of the motor should be monitored throughout the design process. To avoid heavy saturation, the flux density should be kept below a well defined maximum. Generally, the maximum flux density occurs in the rotor and stator teeth. Smaller machines (below 75 kW) have more prominent tapered teeth which increases the probability of saturation at the tooth tips. As machine sizes increase, the tapering of teeth becomes less significant. This allows bigger machines to have larger slot fill factors. Table 2.6 can be used as a benchmark when considering flux densities for machine design:

Table 2.6: Suggested motor flux densities [19].

Flux density [T]	Value
Rotor yoke	1.0 - 1.6
Rotor tooth	1.5 - 2.2
Air-gap	0.7 - 0.9
Stator tooth	1.4 - 2.1
Stator yoke	1.4 - 1.7

2.6.7 Electric loading

The steady state current density value is limited by the motor's ability to dissipate heat. The more effective of a cooling method implemented, the higher allowable current densities can be safely designed for. This is presented in

Table 2.7. It is also advised for traction drive applications that the current densities of the rotor should generally be less than that of the stator.

Table 2.7: Impact of cooling on electric loading [19].

Cooling method	Current density [A/mm^2]
None	6.0
Forced external cooling over surface	7.0 - 9.0
Forced external through vents in stator	14.0 - 15.0
Liquid cooling through vents in stator	>20.0

2.7 Design for wide constant power speed range

As mentioned earlier in section 2.4 and depicted in Fig. 2.7, the power and torque characterteristics of a traction induction motor is what sets it apart from normal induction motors. A well designed traction drive has a CPSR defined as ω_m/ω_b as illustrated in Fig. 2.14 of 3 or greater [5]. Thus, the maximum speed ω_m achieved in the constant power region should at least be 3 times greater than the base speed ω_b. Because a design evolves around the base speed ω_b and the maximum constant power speed ω_m is a result thereof, it is important to establish a relationship between the two. This relationship is key to ensure that the design specifications at both speeds can be satisfied. The maximum torque of an $m-$phase, $p-$pole pair induction motor can be derived from a per-phase Thevenin equivalent circuit and expressed as [5, 28, 29]:

$$T' = \frac{p}{2\pi f} \cdot \frac{mV_{1eq}^2}{2\left(R_{1eq} + \sqrt{R_{1eq}^2 + (X_{1eq} + X_2)^2}\right)} \tag{2.4}$$

where V_{1eq}, R_{1eq}, X_{1eq} and X_2 are equivalent stator voltage, resistances, leakage reactance and referred rotor leakage reactance, respectively. Taking R_{1eq} as negligible and V_{1eq} as constant under flux weakening operation. Eq. (2.4) can be written as:

$$T' = K \cdot \left(\frac{V_{1eq}}{f}\right)^2 \tag{2.5}$$

where $K = mp/[8\pi^2(L_{1eq} + L_2)]$ and L_{1eq} and L_2 are equivalent stator leakage and referred rotor leakage inductances. Since the frequency, $f \propto \omega$ (electrical angular speed) and V_{1eq} is constant Eq. (2.5) can be written as:

$$T' \approx K_1 \frac{1}{\omega^2} \tag{2.6}$$

where K_1 is a constant. The relation between the maximum torques at the base and maximum speeds, ω_b and ω_m, is thus:

$$T'_b \cdot \omega_b^2 = T'_m \cdot \omega_m^2 \tag{2.7}$$

Under constant power P, the rated operational torques at the base and maximum speed, T_b and T_m, are related by:

$$P_{out} = \omega_b T_b = \omega_m T_m \tag{2.8}$$

At the maximum speed, the maximum torque must exceed the rated operating torque by a factor κ_m, such that:

$$T'_m = \kappa_m T_m \tag{2.9}$$

From Eq. (2.7) – (2.9), the ratio between the maximum torque and the rated operational torque at the base speed, κ_b, can be derived:

$$T'_b = \kappa_b T_b \tag{2.10}$$

$$T'_b = \frac{\omega_m}{\omega_b} \kappa_m T_b \tag{2.11}$$

$$\implies \kappa_b = \frac{\omega_m}{\omega_b} \kappa_m \tag{2.12}$$

Eq. (2.12) can be incorporated into the initial design steps to optimize a suitable maximum torque in order to realize the required CPSR for the induction motor.

2.7.1 Reduction of leakage inductance

The most common method of achieving a higher breakdown torque comes from decreasing the leakage inductance. The stator and rotor leakage inductances are given by [5]:

$$L_{sl} = 2\mu_0 L_i \cdot n_s^2 p_1 q_1 \left(\lambda_{ss} + \lambda_{za} + \lambda_{ds} + \lambda_{end}\right) \tag{2.13}$$

and

$$L_{rl} = 4m_1 \frac{(W_1 K_{w1})^2}{Q_r} \times 2\mu_0 L_i \left(\lambda_b + \lambda_{er} + \lambda_{zr} + \lambda_{dr} + \lambda_{skew}\right) \tag{2.14}$$

with

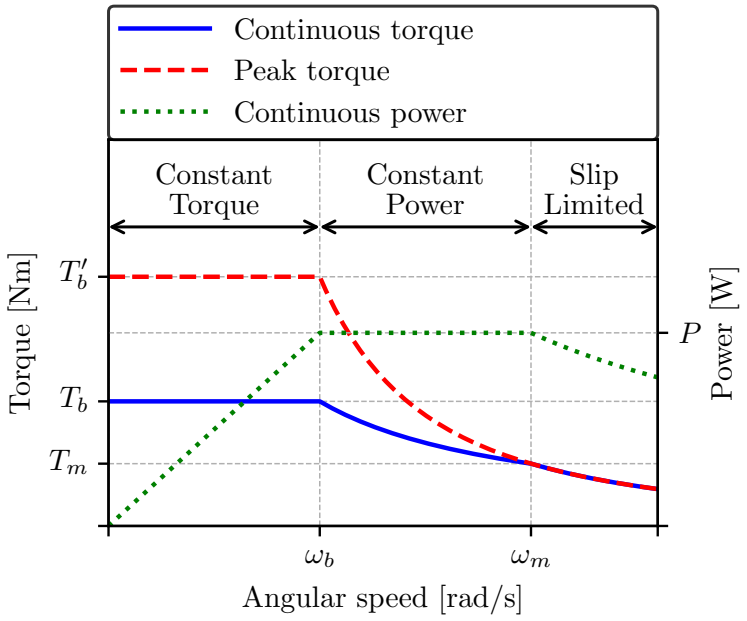

Figure 2.14: Output torque and power characteristics with flux weakening.

n_s = conductors per slot
m_1 = number of phases
q_1 = slots per pole per phase
W_1 = number of turns per phase
λ_{ss} = stator slot permeance coefficient
λ_{zs} = stator zig-zag permeance coefficient
λ_{ds} = stator differential permeance coefficient
λ_{end} = stator end-coil permeance coefficient
λ_b = rotor slot permeance coefficient
λ_{er} = end ring permeance coefficient
λ_{zr} = rotor zig-zag permeance coefficient
λ_{dr} = rotor differential permeance coefficient
λ_{skew} = rotor skew permeance coefficient

As can be seen in these expressions, each is loaded with parameters which cannot be neglected in any thorough analysis. Both these equations are valid for open and semi-closed slots, which will be implemented for the thesis. An in-depth sensitivity analysis of how geometrical variables influence rotor and stator leakage inductance is no easy task. This is mainly done iteratively through finite element methods and differs from motor types and applications. However, the main geometrical dimensions that have an influence on rotor and stator leakage inductance respectively are:

- Amount of pole pairs;
- Stator inner diameter;

- Stator slots per pole per phase;
- Stator and rotor slot aspect ratio;
- Stator and rotor rated torque current density;
- Rotor slots per pole pair;
- Air-gap flux density;
- Stack length per pole pitch ratio and;
- Slot tooth to width ratio.

Generally, when the main design objectives are efficiency, breakdown torque and minimal motor volume, a 4-pole motor is most beneficial. A compromise exists for both the rotor and stator where an increase in the number of slots per pole per phase reduces leakage inductance, but simultaneously increases stray losses.

2.7.2 Design towards an even wider CPSR with voltage management

It is now known that to achieve a wide CPSR a machine is required that is capable of producing:

$$\frac{T_{bk}}{T_n} = \frac{\omega_m}{\omega_b} = C_\omega \tag{2.15}$$

with both the breakdown torque to rated torque ratio and maximum speed to base speed ratio equalling a CPSR ratio. This can be achieved through leakage flux management or voltage management methods as discussed for the remainder of this section.

2.7.2.1 Higher voltage per phase

Generally, once the rated speed is achieved, the phase voltage is at its maximum rated value and remains constant through the CPSR. An alternative approach is to design the IM at a lowered rated phase voltage to allow a continuous steady rise through the CPSR as seen in Figure 2.15. This will however result in a larger rated current and thus increased inverter costs. Literature exists for the calculation of the inverter current increase, but will not be derived for the purpose of this thesis. It should be noted that this method does not suppose overrating, just a design adjustment for the lower rated voltage at base speed.

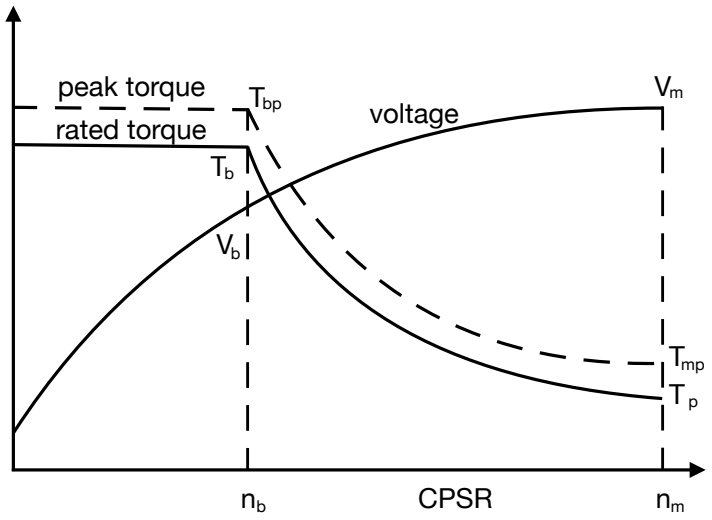

Figure 2.15: Continued increase in voltage for CPSR.

2.7.2.2 Switching winding phase connection

For a large CPSR ratio of more than 4, the above mentioned methods are not generally sufficient. Changing the stator phase connection from wye (Y) to delta ($\triangle$) during machine operation results in a sudden increase of phase voltage by $\sqrt{3}$. The influence on the torque-speed characteristics can be seen in Figure 2.16.

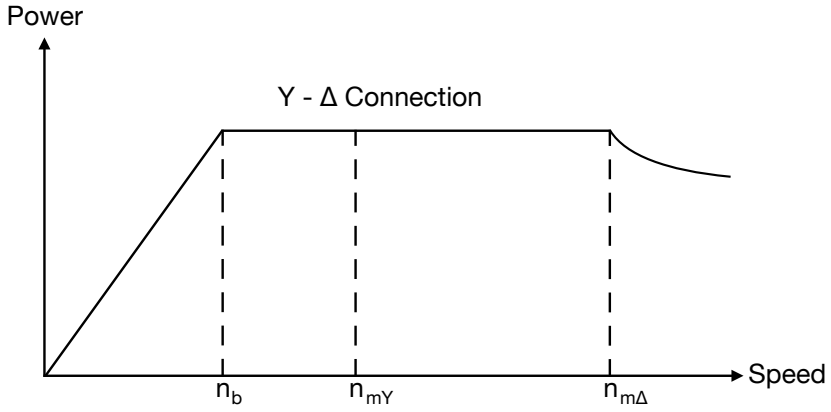

Figure 2.16: Extended CPSR by switching winding phase connection from Y to Δ.

This switch is completed smoothly through a magnetic switch via the power electronics converter (PEC) and can be done during operation. To build on this method an even wider CPSR can be achieved through a winding tap. In this process the amount of turns per phase are reduced via an additional

switch at high speeds. This reduction in turns per phase results in a reduction of stator winding resistance, as well as the total leakage inductance. Thus achieving a higher breakdown torque.

2.7.2.3 Inverter pole switching

Through this method the amount of poles can be reduced at a ratio of 2:1, thus increasing the CPSR by a factor of 2. This can be achieved through two twin half-rating inverters or a single PEC in combination with two three-phase switches connected to different pole count winding configurations.

2.8 The design of an induction motor with variable frequency drive

As the rotor tangential speed increases to between 60 m/s and 80 m/s, mechanical constraints become dominant and rotor design becomes critical. Generally for high speed applications, solid rotors with copper bars are mostly considered. The challenge of traction drive applications with a wide CPSR is that the size of IM increases with high torque requirements, but for high speed applications smaller machine sizes are advantageous. Despite international efforts in previous years, the numerical design of a traction IM with variable speed capability did not realize in widely accepted methodologies [5].

What follows as the remainder of this section can be seen as small steps towards a daring goal. The design algorithms developed for constant $\left(\frac{V}{f}\right)$ are applicable for variable speed drive design. The main issues involved in the design of variable speed IM drives are as follow:

- Power and voltage derating;
- Reducing skin effect;
- Reduction of torque pulsations and;
- Increased efficiency.

2.8.1 Power and voltage derating

An induction motor generally forms part of a variable speed drive assembly such as seen in Figure 2.17. For variable frequency drives (VFD's), there is a power electronics converter placed between the IM and power grid.

The PEC, which manipulates the harmonics of a voltage or current source type IM, in combination with the PWM control strategy is used to achieve speed

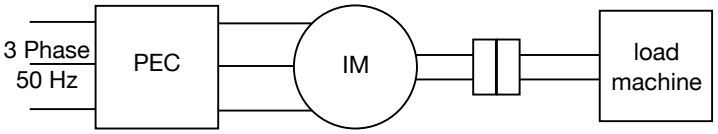

Figure 2.17: Variable speed drive assembly for IM.

control. Each type of PEC has its very own harmonics and respective voltage drop. Recently, both these indexes have been reduced. The IM motor has to be designed with a voltage derating considered of between 5 % to 10 %. This means that the motor design should be performed at a rated voltage V_m which is less than the AC power grid voltage V_g:

$$V_m = V_g \left(1 - v_{derating}\right) \tag{2.16}$$

Power derating has an influence on the design approach when Esson's constant is determined. Esson's constant is a volume utilization factor which provides a torque-to-volume design ratio. When power derating is evident, Esson's constant can be adapted as follows for variable V/f supply:

$$C_0' = C_0 \left(1 - p_{derating}\right), \text{ with } p_{derating} \approx (0.08 - 0.12) \tag{2.17}$$

Although this may seem as quite an empirical approach, it is only implemented in the initial sizing process. Once the sizing is completed, the voltage drops in the PEC, as well as the time harmonics and windings losses can be determined iteratively until refinements are done [5].

2.8.2 Reducing skin effect

For variable speed drive design, starting torque and current constraints are not as relevant due to the variable voltage and frequency. However, for traction and wide-constant-power-speed-range applications, a high breakdown torque is required. This can be a challenging task without increasing the machine geometry. The skin effect in winding losses is related to conductor size and position within slots, as well as the supply frequency. The rotor and stator skin effect is to be reduced at fundamental frequency initially, where after its influence has to be checked and limited from the PEC.

The skin effect is most evident in the rotor cage, therefore the solution will involve rotor bar analysis. Further, the rotor slot shape has an effect as well. For round and rectangular slots, the analysis procedure is simplified. Generally, the maximum slot depth is related to motor peak torque requirements. Reduction in rotor bar skin effect can be achieved with shallower slots. Thus, for a given stator diameter a longer stack length is required. This results in reduced leakage inductance and larger breakdown torque. When slot depth

reduction is not possible, a wound rotor is suggested. To reduce end ring skin effect, a compromise exists. By placing the end rings further away from the stack a reduction of skin effect is achieved. Replacing aluminium with copper will reduce bar resistance at a larger skin effect. Therefore, reducing the copper bar size until equivalent aluminium resistance is achieved will result in reduced leakage inductance and increased breakdown torque. In reality a round bar is rather impractical for large IMs. In most cases rectangular slots with a height to width ratio of ≤ 3 is acceptable. In well designed IMs the skin effect is negligible at fundamental frequencies of less than 100 Hz [5].

2.8.3 Reduction of torque pulsations

The source of torque pulsations can be categorized into two groups: the interaction between air-gap magnetic permeance space harmonics with stator MMF harmonics and voltage time harmonics produced by the PEC. Space harmonics torque pulsations are produced by synchronous parasitic torques. This is highly dependant on stator and rotor slot ratio, slot opening to air-gap length ratio, air-gap to pole pitch ratio and the level of saturation in the core. However, this is only valid at slip values of $S \geq 0.7$.

Just as for constant voltage and frequency supply drives, the same constraints regarding rotor and stator slot combinations apply as discussed in Section 2.6.3.1. Slot openings tend to amplify parasitic synchronous torques for $Q_r > Q_s$, therefore the general design rule for variable V and f drives are $Q_r < Q_s$ without cage skewing considered. Stator winding overlapping or chording will magnificently reduce parasitic torque. It is essential to have slot openings that reduce parasitic currents without increasing the leakage inductance [5].

2.8.4 Increased efficiency

Its seems obvious that to achieve a more efficient motor a reduction in machine losses is required. Lower values of flux and current densities lead to larger, but more efficient motors in general. This is why larger or more efficient machine are regularly considered for variable voltage and frequency applications. Achieving good efficiency is not always an easy task, but a few design considerations below can be used as guideline [5]:

- As briefly discussed in Section 2.6.2.2, a large number of slots/pole/phase is required to reduce first order harmonics.
- A relationship $0.8 \times Q_s < Q_r < Q_s$ should be adhered to reduce inter bar current losses by reducing leakage flux.
- For $Q_r < Q_s$ skewing is insignificant and can be eliminated.

- Usage of thin laminations (± 0.1 mm) is recommended for supply frequencies above 300 Hz to reduce core losses.
- The air-gap size can be marginally increased to reduce core and rotor cage losses without compromising power factor and efficiency significantly.

2.9 Rotor slot design

The main reason why permanent magnet motors are preferred over induction motors for traction applications is due to higher efficiencies and power densities. For induction motors, the time harmonic of the supply voltage causes harmonic secondary copper losses in the rotor conductors near the surface. These losses are a result of the harmonic characteristic of the air-gap flux density. A solution to this reduced efficiency was proposed in [30]. For square rotor slots, the default slot configuration is given in Figure 2.18a, while the suggested solutions are given in Figures 2.18b and 2.18c.

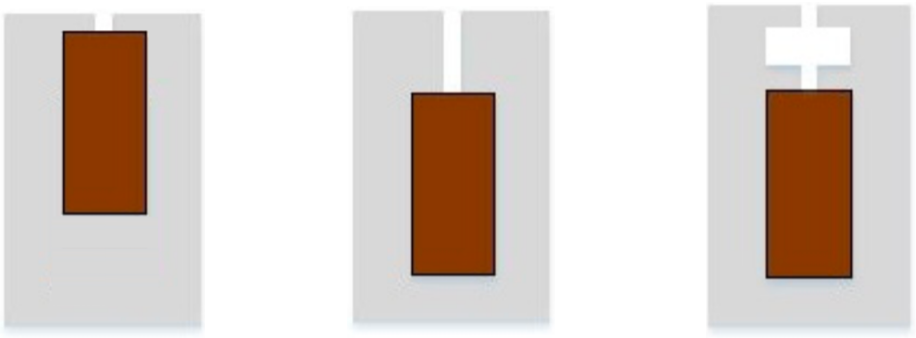

(a) Design A. (b) Design B. (c) Design C.

Figure 2.18: Rotor slot configurations for reduced secondary harmonic losses.

For Design B, by placing the conductor deeper and thus further away from the air-gap, the harmonic secondary copper losses can be expected to reduce. This however will increase the leakage inductance on the upper portion of the slot and reduce the much desired breakdown torque of a traction motor. This reduction in breakdown torque can be countered with a slot configuration as seen in Figure 2.18c. This configuration reduces harmonic secondary copper losses without significantly increasing rotor leakage inductance. The devised rotor slots are beneficial for the design of a traction motor and was tested in a FEM software package on a generic IM for confirmation. To isolate the harmonic secondary copper losses in the rotor bars during a simulation, the motor should run at synchronous speed under no load. Therefore, no currents can be induced in the rotor bars and ultimately the torque will be zero. The

only losses occurring will be due to the magnetic field generated from the stator. The results are visible in Table 2.8:

Table 2.8: Comparison of simulated core and harmonic secondary copper losses among different rotor designs.

Slot	A	B	C
Harmonic secondary copper losses [W]	22.7	10.6	9.2
Core losses [W]	37.7	38.5	39.0
Total [W]	60.4	49.1	48.2

Although the core losses marginal increased from Design A to Design C, the harmonic secondary copper losses were reduced by more than 50 %. The total harmonic losses decreased with 20 %. This confirms the increased efficiency from the suggested rotor slot configurations and can ultimately be implemented in a final design.

2.10 Design summary

This chapter briefly discussed important design considerations for a traction induction motor. The information obtained throughout the chapter will be implemented in the design strategy for traction motors. A high level design of this strategy can be seen in Fig. 2.19 and will broadly represent the remaining chapters of this dissertation. The high level summary of the individual steps throughout the process is given below:

- **Step 1:** The desired machine specifications are finalized which will serve as an input for the analytical model to follow.
- **Step 2:** An analytical model is used to generate a complete set of geometrical dimensions from the desired motor specifications. During this process, the generated geometric dimensions are tested and validated to comply with electric and magnetic loadings during machine operation. The main objective of the analytical model is to instantly generate a set geometrical dimensions that will give fairly accurate desired motor performance. The analytical model will be implemented using Matlab scripts.
- **Step 3:** The final design generated through the analytical model will be termed as the Matlab model.
- **Step 4:** The Matlab model performance will be verified within the RMxprt software package. This will ensure a clear understanding of technical design characteristics.

- **Step 5:** Once the Matlab model is verified within RMxprt and any differences in performance justified, the slightly adapted design will be termed as the Initial Design. The initial design will be used for optimization purposes.

- **Step 6:** The Initial design is optimized within an extension of RMxprt known as the RMxprt Optimetrics package. The optimization duration will be relatively quick due to reduced population size and initial dimensions being close to convergence values.

- **Step 7:** The optimized model from the RMxprt Optimetrics package will be termed as the Base Design.

- **Step 8:** The Base Design will be tested in a 2D FEM environment to confirm motor performance. The FEM packages that will be used for comparison are Maxwell 2D and SEMFEM.

- **Step 9:** If the FEM comparison is satisfactory and the results are similar, the Base Design model will be known as the Confirmed Design.

- **Step 10:** Once Step 9 is reached, some experimental fine tuning can commence. The influence on performance of the refined design are expected to be marginal, but beneficial.

- **Step 11:** After fine tuning, a Final Design is reached. The mechanical design of the motor can commence for construction and testing.

This design strategy will be implemented and verified for a traction induction motor. The process will be documented throughout the dissertation where after conclusions will be made on its effectiveness.

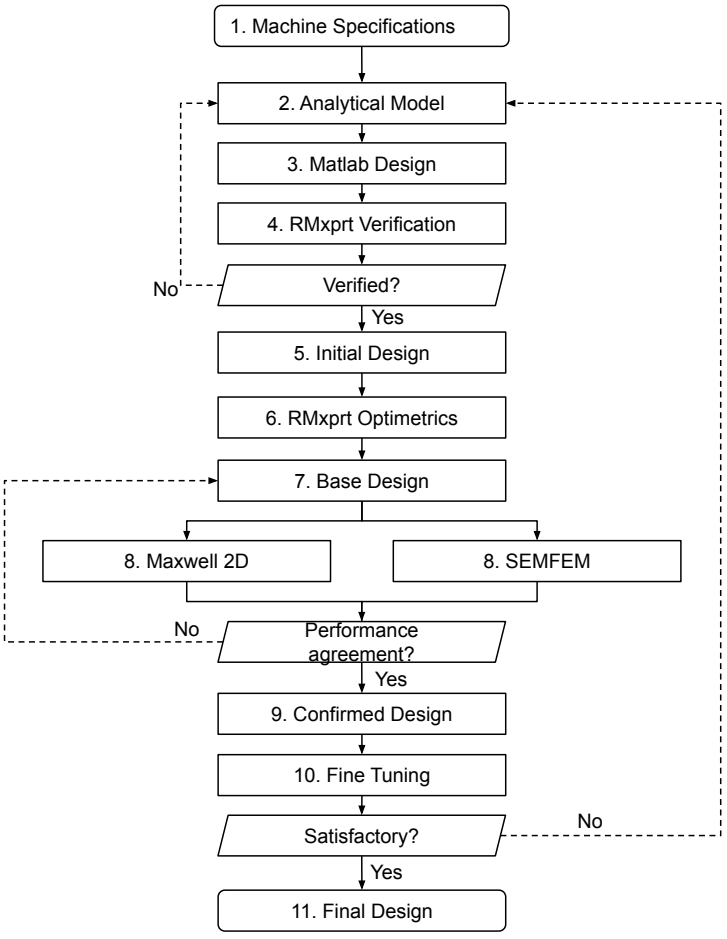

Figure 2.19: High level process flow diagram of the design strategy.

Chapter 3

Design process and analytical model

The design process of an induction motor is rather complex. It is an iterative process which entails the careful consideration of various parameters for a quality design. The design of a high efficiency traction motor is a mixture of art and science. Design optimization will be discussed at a later stage. This chapter will describe each phase of the design process, as well as important design considerations.

3.1 Design specifications

As mentioned in Chapters 1 and 2, the design of a small traction induction motor is needed for this project. This, as well as the remaining design specifications can be seen below:

- Rated power: $P_n = 3\,\text{kW}$;
- Base speed: $n_b = 1000\,\text{rpm}$;
- Line supply voltage: $V_l = 380\ \text{V}$;
- Number of phases: $m = 3$;
- Phase connection: star;
- Target power factor: $\text{PF} = 0.75$;
- Target efficiency: $\eta_n = 0.85$;
- Locked/rated torque ratio: $t_{LR} = 2.0$;
- Locked/rated current ratio: $i_{LR} = 6.0$ and;
- Breakdown/rated torque ratio: $t_{BK} = 3.0$.

For the design of a 3 kW traction motor, the given efficiency and power factor are reasonable. The emphasis of the design is to achieve a minimum CPSR of three. As mentioned in Section 2.7, a breakdown/rated torque ratio is related to the maximum/rated speed ratio. Thus, this ratio will serve as guide to achieve the required CPSR.

3.2 Design approach

A high level process flow diagram which represents each step in the analytical model can be seen in Fig. 3.1. The analytical model is adapted from a general design approach in [5] for traction applications.

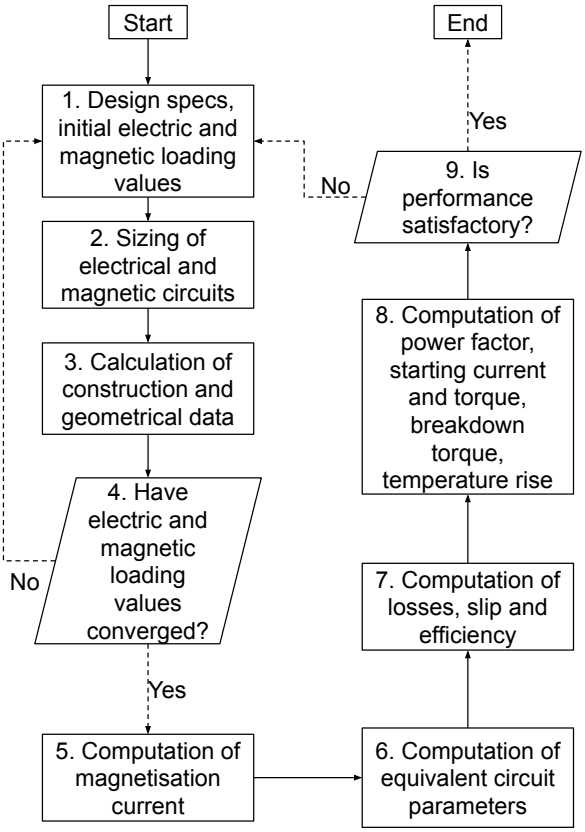

Figure 3.1: Flow chart of the design process [5].

From Fig. 3.1, the design process starts at step (1) on the flow chart with design specifications and assigned values of current and flux densities. In steps (2) and (3), the main dimensions such as stator bore diameter D_{is}, stator outer diameter D_{out}, stack length and slots sizes are determined after rotor and stator currents are calculated. The calculated stator winding wire thick-

ness is also given. In step (4), the actual current and flux densities are verified.

If the results on the magnetic saturation coefficient for both the stator and the rotor have not converged, the process restarts at (1). This is an iterative process whereby both stator and rotor tooth flux values are adjusted until sufficient convergence is obtained.

If the magnetic saturation of both the rotor and the stator teeth are satisfactory, step (5) can commence. In this step the magnetization current is calculated followed by the calculation of equivalent circuit parameters in step (6). The rated slip S_n, losses and efficiency are calculated in step (7). In step (8) the locked rotor current and torque, breakdown torque, power factor as well as the operating temperature of the machine is calculated.

The machine performance is reviewed in step (9) and if found unsatisfactory, the process returns to step (1). If the process is to be restarted, a new set of current and flux densities, as well as a new stack aspect ratio is chosen for another iteration. The inner/outer stator diameter ratio can be adjusted as well. If the performance is satisfactory, the design can further be optimized and fine tuned for best possible performance.

3.3 Analytical model

This section dedicated to explain the basic design theory and equations used in the analytical model.

3.3.1 Main dimensions of stator core

The concept used for the design and determination of the initial machine parameters is the ${D_{is}}^2 L$ output coefficient method [5]. Based on this method, the inner diameter of the stator D_{is} is given by:

$$D_{is} = \sqrt[3]{\frac{2p_1}{\pi\lambda}\frac{p_1}{f}\frac{S_{gap}}{C_o}} \tag{3.1}$$

with the apparent air-gap power given by:

$$S_{gap} = \frac{K_E P_n}{\eta_n PF} \tag{3.2}$$

and the stack aspect ratio:

$$\lambda = L\left(\frac{2p_1}{\pi D_{is}}\right) = \frac{L}{\tau} \tag{3.3}$$

where p_1 is the number of pole pairs, K_E the EMF coefficient, C_o Esson's constant and τ the pole pitch. The stack aspect ratio is the relationship between the length of a a machine and its pole pitch. The first step to determine the main dimensions of the stator core is to choose a reasonable stack aspect ratio from Table 3.1.

Table 3.1: Stack aspect ratio.

$2p_1$	2	4	6	8
λ	0.6 - 1.0	1.2 - 1.8	1.6 - 2.2	2.0 - 3.0

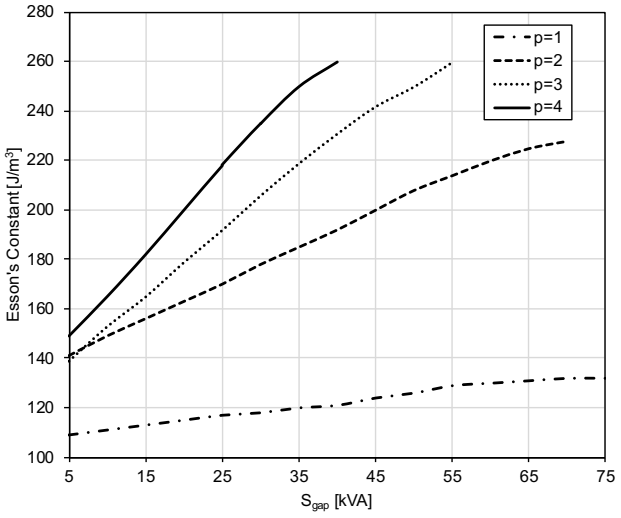

Figure 3.2: Esson's constant versus apparent air-gap power.

The EMF coefficient is given by $K_E = 0.98 - 0.005p_1$, while Esson's constant C_o can be determined from Figure 3.2 with S_{gap} known. With all the variables known for Eq. (3.1), D_{is} can be calculated. As a result, the calculation of the stack length L and pole pitch τ follows. The number of slots per pole $3q$ can be calculated with $q = 3$ or $q = 2$. With $q = 3$, the slot pitch τ_s can be calculated as:

$$\tau_s = \frac{\tau}{3q} \tag{3.4}$$

The larger value for q results in improved performance due to reduced space field harmonics and a decrease in machine losses. From the optimal lamination concept, ideal ratios between inner and outer stator diameter are given in Table 3.2. This allows the calculation of the the stator outer diameter D_{out}.

Table 3.2: Inner/outer stator diameter relationship.

$2p_1$	2	4	6	8
$\frac{D_{is}}{D_{out}}$	0.54 - 0.58	0.61 - 0.63	0.68 - 0.71	0.72 - 0.74

The air-gap length g can be calculated from:

$$g = 0.1 + 0.012{P_n}^{1/3} \text{ for } 2p_1 \geq 2 \tag{3.5}$$

This is an initial estimate and might have to be altered due to manufacturing restrictions at a later stage. Too small air-gap can result in large air-gap field harmonics which leads to additional losses. If the air-gap is too large, it can lead to a reduced efficiency and power factor. Air-gap length influence on performance is discussed in Section 2.6.5.

3.3.2 Stator winding

The number of stator slots N_s can be calculated with:

$$N_s = 2p_1qm \tag{3.6}$$

With the coil pitch given by y and pole pitch by τ, the chording ratio is given with $\frac{y}{\tau}$. Thus, for any double-layer winding where $y < \tau$, fractional pitch coils exist. This chorded coil ratio will be implemented and represented fractionally throughout the analytical model. The winding distribution factor K_{q1} is given by:

$$K_{q1} = \frac{\sin\frac{\pi}{6}}{q\sin\left(\frac{\pi}{6q}\right)} \tag{3.7}$$

The chording factor K_{y1} is given by:

$$K_{y1} = \sin\frac{\pi}{2}\frac{y}{\tau} \tag{3.8}$$

The stator winding factor K_{w1} is a product of the winding distribution factor and the pitch factor:

$$K_{w1} = K_{q1} \cdot K_{y1} \tag{3.9}$$

The number of turns per phase W_1 is related to the pole flux ϕ:

$$\phi = \alpha_i \tau L B_g \tag{3.10}$$

Assuming a reasonable value of the tooth saturation factor $1 + K_{st}$, the flux density shape factor α_i and form factor k_f can be read from Figure 3.3. A

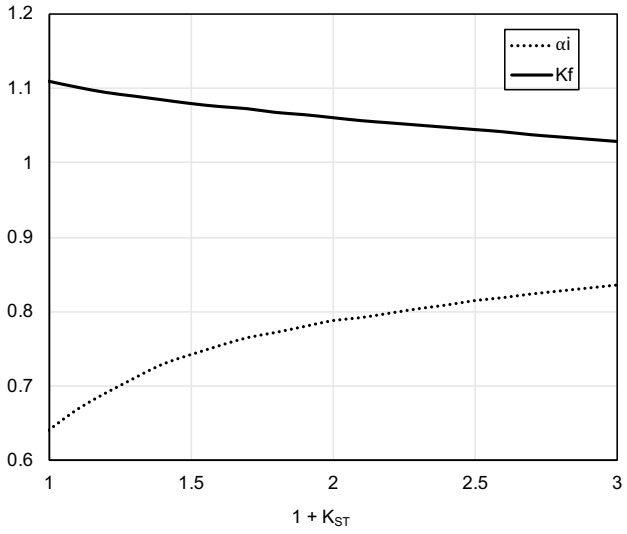

Figure 3.3: The pole spanning coefficient α_i and form factor k_f versus tooth saturation.

reasonable air-gap flux density value can be determined from the number of pole pairs:

$$B_g = (0.65 - 0.78)\text{T for } 2p_1 = 4 \tag{3.11}$$

From Eq. (3.15) and Figure 3.3 all the unknowns have been determined to calculate ϕ. Therefore, the initial number of turns per phase $W_{1(initial)}$ can now be calculated as:

$$W_{1(initial)} = \frac{K_E V_{1ph}}{4K_f K_{w1} f \phi} \tag{3.12}$$

With the number of current paths in parallel given by a_1, the number of conductors per slot is:

$$n_s = \frac{a_1 W_{1(initial)}}{p_1 q} \tag{3.13}$$

Once calculated, n_s should be rounded to the nearest even number because there are two distinct coils per slot for double layer winding. Consequently the actual number of turns per phase can be calculated as $W_1 = p_1 q n_s$. The air-gap flux density can now be recalculated by multiplying the original B_g value with the turns ratio $\frac{W_1}{W_{1(initial)}}$. The rated current is calculated as follows:

$$I_n = \frac{P_n}{\eta_n PF\sqrt{3}V_1} \tag{3.14}$$

Once again, the number of pole pairs determines the range in which initial reasonable current densities can be selected from:

$$J_{cos} = (4.0 - 7.0)\text{A/mm}^2 \text{ for } 2p_1 = 2, 4 \tag{3.15}$$

The magnetic wire cross section A_{Co} is given by:

$$A_{Co} = \frac{I_n}{J_{cos} a_1} \tag{3.16}$$

With gauge diameter d_{Co}:

$$d_{Co} = \sqrt{\frac{4A_{Co}}{\pi}} \tag{3.17}$$

If $d_{Co} > 1\,\text{mm}$ in lower power induction machines, conductors can be used in parallel making $a_p = 2$ and the new d_{Co} value:

$$d_{Co} = \sqrt{\frac{4A_{Co}}{\pi a_p}} \tag{3.18}$$

A standard magnetic wire table can be used to determine minimum wire insulation.

3.3.3 Stator slot sizing

The useful slot area A_{su} is a function of the previously calculated number of turns per slot n_s, number of parallel paths a_p and the wire diameter d_{Co}. Generally for a round wire and a motor of less than 10 kW a fill factor K_{fill} of 0.4 can be used. For motors larger than 10 kW a conservative fill factor of 0.45 can be assumed. The useful slot area A_{su} can be calculated as:

$$A_{su} = \frac{\pi {d_{Co}}^2 a_p n_s}{4K_{fill}} \tag{3.19}$$

As mentioned earlier, square or trapezoidal slots are ideal for traction drive applications and will thus be implemented in this analytical model. Figure 3.4 indicates how geometrical dimensions are labelled for implementation in the analytical model.

There exists some typical values for variables b_{s0}, h_{s0} and h_{s1}, such as $b_{s0} = 2 - 4\,\text{mm} \leq 8 \times g$, $h_{s0} = 0.5 - 1\,\text{mm}$ and $h_{s1} = 1 - 4\,\text{mm}$, where g is the air-gap length and τ_s the stator slot pitch. Assuming that all the air-gap flux passes through the teeth, the following relationship may be obtained:

$$b_{ts} \approx \frac{B_g \tau_s}{B_{ts} K_{Fe}} \tag{3.20}$$

Taking $K_{Fe} \approx 0.5$ for 0.5 mm thick laminations and choosing a reasonable tooth flux density B_{ts} as seen in Table 2.6, the stator tooth thickness b_{ts} can

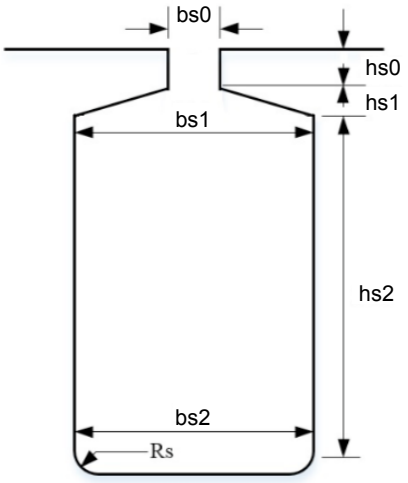

Figure 3.4: Stator slot geometrical dimensioning.

be determined. From Figure 3.4, for trapezoidal stator slots the height variable h_{s1} is set to zero. The upper slot width is calculated as:

$$b_{s1} = \frac{\pi \left(D_{is} + 2h_{s0} + 2h_{s1}\right)}{N_s} - b_{s1} \tag{3.21}$$

where D_{is} is the stator inner diameter. The lower and upper slot width ratio is $K_{wr} \approx 1.5$. The lower slot width can be calculated from:

$$b_{s2} = b_{s1} K_{wr} \tag{3.22}$$

With both the upper and lower slot width known, the slot height h_{s2} is given by:

$$h_{s2} = \frac{2A_{su}}{b_{s1} + b_{s2}} \tag{3.23}$$

The next objective is to calculate the tooth saturation factor $1 + K_{st}$. This can be done after the assumption that the rotor and stator tooth saturation are similar. It is calculated by:

$$1 + K_{st} = 1 + \frac{F_{mts} + F_{mtr}}{F_{mg}} \tag{3.24}$$

Making an assumption that Carters coefficient $K_c = 1.2$, the air-gap MMF F_{mg} is:

$$F_{mg} \approx K_c g \frac{B_g}{\mu_0} \tag{3.25}$$

With B_{ts} known, the magnetic field intensity can be retrieved from Figure 3.5 which is required to calculate the stator tooth MMF with:

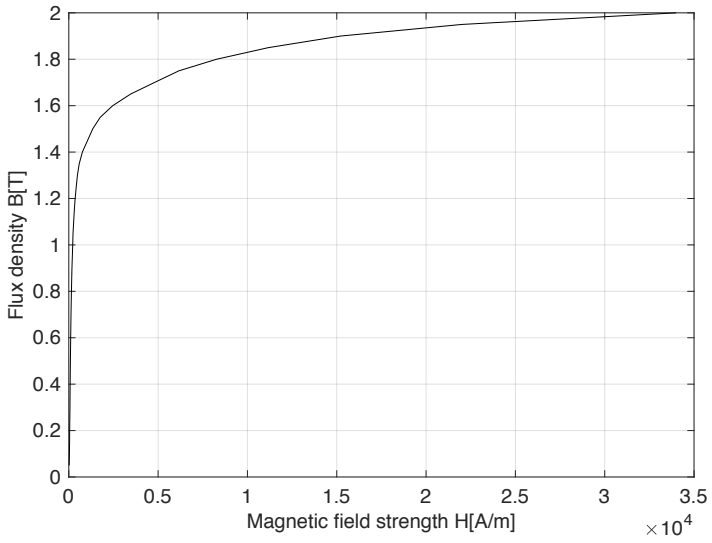

Figure 3.5: Lamination magnetization curve.

$$F_{mts} = H_{ts}\left(h_{s2} + h_{s0} + h_{s1}\right) \tag{3.26}$$

Thus, the stator tooth MMF can now be calculated:

$$F_{mtr} = K_{st}F_{mg} - F_{mts} \tag{3.27}$$

When comparing F_{mts} and F_{mtr}, the values should be close to each other. If $F_{mtr} \ll F_{mts}$, it implies that for the initial tooth saturation factor $(1 + K_{st})$, a reduced air-gap flux density B_g is required. The whole design procedure should restart from Eq. (3.10). Alternatively, the tooth saturation factor can be iteratively reduced until convergence is reached. If $F_{mtr} \approx F_{mts}$, the design process can continue. The stator yoke or back core iron height h_{cs} can be determined next:

$$h_{cs} = \frac{D_{out} - (D_{is} + 2(\,h_{s0} + h_{s1} + h_{s2}\,))}{2} \tag{3.28}$$

With h_{cs} known, the back core flux density can be verified:

$$B_{cs} = \frac{\phi}{2Lh_{cs}} \tag{3.29}$$

When comparing B_{cs} with reasonable flux density values such as presented in Table 2.6 and similar values aren't achieved, it can be solved with one of the following methods:

- Increase the stator outer diameter until a reasonable B_{cs} value is achieved.

- Restart the design process with a larger stack aspect ratio which will eventually result in a larger b_{cs} and smaller B_{cs}.
- For applications where efficiency isn't of utmost importance, the current density can be increased in order to reduce the slot height h_{s2}.

3.3.4 Rotor slots

The rotor slot design process starts with selecting an adequate amount rotor slots relative to the stator slots. This was discussed in Section 2.6.3.1 and can be used as guideline. The rotor bar current can be calculated from:

$$I_b = K_I \frac{2mW_1K_{w1}}{Q_r} I_n \tag{3.30}$$

The K_I variable is the ratio between the rotor tooth MMF and the stator tooth MMF. In general the rotor tooth MMF is slightly less, thus K_I can be calculated by:

$$K_I = 0.8 \cos \phi_n + 0.2 \tag{3.31}$$

All the variables from Eq. (3.30) are now known and the rotor bar current can be calculated. For a high efficiency design, a rotor bar current density is assumed to be slightly less than that of stator winding (e.g. $J_b \approx 3.5\text{A/mm}^2$). Therefore the rotor slot area can be calculated from:

$$A_b = \frac{I_b}{J_b} \tag{3.32}$$

with the end ring current I_{er}:

$$I_{er} = \frac{I_b}{2 \sin \frac{\pi p_1}{Q_r}} \tag{3.33}$$

The end ring current density is generally between 75 % to 80 % of the rotor bar current density. With $J_{er} = 0.75 \cdot J_b$, the end ring cross sectional area is:

$$A_{er} = \frac{I_{er}}{J_{er}} \tag{3.34}$$

The rotor slot sizing can continue based on the variables defined in Figure 3.6. The rotor slot pitch τ_r can be calculated as:

$$\tau_r = \frac{\pi \left(D_{is} - 2g\right)}{Q_r} \tag{3.35}$$

With a reasonable rotor tooth flux density B_{tr} assumption from Table 2.6, an estimation of rotor tooth width can determined from:

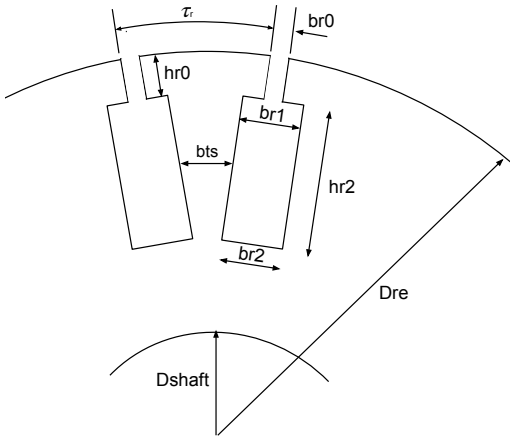

Figure 3.6: Rotor slot geometrical dimensions.

$$b_{tr} \approx \frac{B_g}{K_{Fe} B_{tr}} \tau_r \tag{3.36}$$

The rotor outer diameter is can easily be calculated by:

$$D_{re} = D_{is} - 2g \tag{3.37}$$

As mentioned in Section 2.6, it's generally safe to have a rotor slot height to width ratio K_{rhw} of approximately 3 to reduce skin effect. With this initial assumption made, the slot width b_{r1} can be calculated as:

$$b_{r1} = \sqrt{\frac{A_b}{K_{rhw}}} \tag{3.38}$$

Width the IM being designed with rectangular slots, the lower slot width $b_{r2} = b_{r1}$. The slot height h_{r2} can be determined by:

$$h_{r2} = b_{r1} K_{rhw} \tag{3.39}$$

With an initial B_{tr} assumed, the magnetic field strength H_{tr} can be found from Figure 3.5. The rotor teeth MMF can be evaluated as follows:

$$F_{mtr} = H_{tr} \left(h_{r2} + h_{r0} \right) \tag{3.40}$$

When comparing this result with the initial rotor tooth MMF calculated in Eq. (3.27), a difference of less than 25 % is required in order to continue with the design process. There are multiple ways to address this problem:

- If the initial F_{mtr} is too large, the given tooth saturation factor $(1 + K_{st})$, should be increased. This is a good solution when the PF constraint is not too high.

- For a large initial F_{mtr}, the same efficiency can be maintained by increasing the stator outer diameter.Thus, the whole design process restarts at Eq. (3.1).
- If initial F_{mtr} is too small, the B_{tr} should be increased. Thus, the design process returns to Eq. (3.36).
- Alternatively, the tooth saturation factor $(1 + K_{st})$ should be increased and the design process restarts at Eq. (3.10).

The rotor yoke or back core height h_{cr} can be calculated after a reasonable design flux density value B_{cr} is chosen from Table 2.6. The rotor back core height h_{cr} is:

$$h_{cr} = \frac{\phi}{2LB_{cr}} \tag{3.41}$$

Thus, the maximum allowable shaft diameter can easily be calculated with:

$$D_{shaft} \leq D_{is} - 2g - 2(h_{r0} + h_{r2} + h_{cr}) \tag{3.42}$$

The minimum shaft diameter can be calculated with Eq. (2.2) as discussed in Section 2.6.4. The end ring outer diameter D_{er} generally between 3 mm to 4 mm smaller when compared to the rotor outer diameter D_{re}. The end ring height b as seen from Figure 3.7 can be calculated as follows:

$$b = (h_{r2} + h_{r0}) \tag{3.43}$$

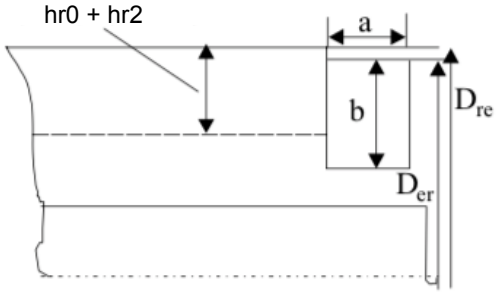

Figure 3.7: End ring cross section [5].

Lastly, the end ring width a can be calculated with:

$$a = \frac{A_{er}}{b} \tag{3.44}$$

3.3.5 Magnetization current

In order to calculate the magnetization current, the magnetization MMF has to be determined first and is given by:

$$F_m = 2\left(K_c g\frac{B_g}{\mu_0} + F_{mts} + F_{mtr} + F_{mcs} + F_{mcr}\right) \tag{3.45}$$

Initially a value of Carters coefficient K_c for Eq. (3.25) was assumed. All variables are now known to recalculate K_c as follows:

$$K_{c1} = \frac{\tau_s}{\tau_s - \left(\frac{{b_{s0}}^2}{5g + b_{s0}}\right)} \tag{3.46}$$

$$K_{c2} = \frac{\tau_r}{\tau_r - \left(\frac{{b_{r0}}^2}{5g + b_{r0}}\right)} \tag{3.47}$$

The total Carter coefficient is given by:

$$K_c = K_{c1}K_{c2} \tag{3.48}$$

With B_{cs} and B_{cr} known, their respective magnetic field strength values H_{cs} and H_{cr} can be retrieved from Figure 3.5. The back core MMF values can be calculated with:

$$F_{mcs} = C_{cs}\frac{\pi(D_{out} - h_{cs})}{2p_1}H_{cs}B_{cs} \tag{3.49}$$

and

$$F_{mcr} = C_{cr}\frac{\pi(D_{shaft} + h_{cr})}{2p_1}H_{cr}B_{cr} \tag{3.50}$$

with both

$$C_{cs,r} = 0.88 \times e^{-0.4{B_{cs,r}}^2} \tag{3.51}$$

After plugging Eqs. (3.48 - 3.50) into Eq. (3.45), the magnetization MMF F_m can be determined. The total saturation factor K_s can be calculated with:

$$K_s = \frac{F_m}{2Fmg} - 1 \tag{3.52}$$

The magnetization current I_μ is:

$$I_\mu = \frac{\pi p_1(F_m/2)}{3\sqrt{2}W_1K_{w1}} \tag{3.53}$$

3.3.6 Resistances and inductances

The phase resistance for the stator is given by:

$$R_s = \rho_{Co}\frac{l_c W_1}{A_{Co} a_1} \tag{3.54}$$

The total coil length l_c of a complete turn includes the core length $2L$, as well as the end connection length $2l_{end}$:

$$l_c = 2(L + l_{end}) \tag{3.55}$$

Although the end connection length depends on the number of poles, the shape of the coils, the number of layers and the coil span y, empirical formulas exist. For $2p_1 = 2$:

$$l_{end} = 2y - 0.02 \text{ mm} \tag{3.56}$$

The chording factor β is given by $\frac{y}{\tau}$, with τ being the pole pitch. Therefore y can easily be calculated with:

$$y = \beta\tau \tag{3.57}$$

With y known, l_{end} can be determined. The Copper resistivity $(\rho_{Co})_{20\,^\circ C}$ at $20\,^\circ C = 1.78 \cdot 10^{-8}\,\Omega$m. Therefore a new resistivity at assumed operating temperature can be calculated with:

$$(\rho_{Co})_{Assumed} = (\rho_{Co})_{20^\circ C}\left(1 + \frac{T_{CoAssumed} - 20\,^\circ C}{273}\right)\ \Omega\text{m} \tag{3.58}$$

Therefore, the stator phase resistance can now be determined in Eq. (3.54). The next step is to calculate the rotor bar and end ring equivalent resistance R_{be}:

$$R_{be} = (\rho_{Co})_{Assumed}\left[\frac{L}{A_b}K_r + \frac{l_{er}}{2A_{er}\sin\left(\frac{\pi P_1}{Q_r}\right)^2}\right] \tag{3.59}$$

The end ring segment length l_{er} can be calculated with:

$$l_{er} = \frac{\pi(D_{er} - b)}{Q_r} \tag{3.60}$$

The skin effect resistance coefficient for rectangular rotor bars can be simplified as follow:

$$K_r = \xi\frac{(\sinh 2\xi + \sin 2\xi)}{(\cosh 2\xi - \cos 2\xi)} \approx \xi \tag{3.61}$$

with

$$\xi = \beta_s h_{r2} \sqrt{S} \tag{3.62}$$

where S is the slip frequency and the skin effect coefficient:

$$\beta_s = \sqrt{\frac{\omega_b \mu_0}{2(\rho_{Co})_{20\,^\circ C}}} \tag{3.63}$$

Therefore, all the variables are known to calculate R_{be}. The rotor cage resistance reduced to the stator R'_r can now be calculated:

$$(R'_r)_{S1} = \frac{4m_1}{Q_r}(W_1 K_{w1})^2 R_{be} \tag{3.64}$$

The next step is to calculate the stator phase leakage reactance X_{sl}:

$$X_{sl} = 2\mu_0 \omega_b L \frac{{W_1}^2}{P_n q}(\lambda_s + \lambda_{ds} + \lambda_{er}) \tag{3.65}$$

The following parameters: λ_s, λ_{ds} and λ_{ec} are slot differential and end connection coefficients of which each has to be calculated separately:

$$\lambda_s = \left(\frac{h_{s2}}{3b_{s1}} + \frac{h_{s0}}{b_{s0}}\right) \cdot \left(\frac{1+3\beta}{4}\right) \tag{3.66}$$

$$\lambda_{ds} = \frac{0.9\tau_s q^2 {K_{w1}}^2 C_s \gamma_{ds}}{K_c g(1+K_{st})} \tag{3.67}$$

with

$$C_s = 1 - 0.033\frac{{b_{s0}}^2}{g\tau_s} \tag{3.68}$$

and for $q = 3$:

$$\begin{aligned} \gamma_{ds} &= (0.18 sin\phi_1 + 1.24) \cdot 10^{-2} \\ \phi_1 &= \pi(6\beta - 5.5) \end{aligned} \tag{3.69}$$

For double-layer windings, the specific geometric coefficient for end connections λ_{ec} is:

$$\lambda_{ec} = 0.34\frac{q}{L}(l_{end} - 0.64\beta\tau) \tag{3.70}$$

All the variables are now known to calculate the stator phase leakage reactance X_{sl} from Eq. (3.65). Next the rotor bar leakage reactance X_{be} will be calculated:

$$X_{be} = 2\pi f_1 \mu_0 L(\lambda_r K_X + \lambda_{dr}\lambda_{er}) \tag{3.71}$$

where λ_r, λ_{dr} and λ_{er} is the rotor slot, rotor differential and end ring permeance coefficients respectively. For rectangular rotor slots:

$$\lambda_r = \frac{h_{r2}}{3b_{r1}} + \frac{h_{r0}}{b_{r0}} \tag{3.72}$$

The rotor differential permeance coefficient is:

$$\lambda_{dr} = \frac{0.9\tau_r\gamma_{dr}}{K_c g}\left(\frac{Q_r}{6p_1}\right)^2 \tag{3.73}$$

with

$$\gamma_{dr} = 9\left(\frac{6p_1}{Q_r}\right)\cdot 10^{-2} \tag{3.74}$$

The end ring permeance coefficient is given by:

$$\lambda_{er} = \frac{2.3(D_{er}-b)}{4Q_r L\sin\left(\frac{\pi P_n}{Q_r}\right)^2}\cdot\log\frac{4.7(D_{er}-b)}{b+2a} \tag{3.75}$$

The skin effect coefficient K_x for leakage reactance is:

$$K_x = \frac{3}{2\xi}\frac{(\sinh 2\xi - \sin 2\xi)}{(\cosh 2\xi - \cos 2\xi)} \approx \frac{3}{2\xi} \tag{3.76}$$

Therefore, all the variables are now known and the equivalent rotor bar leakage reactance X_{be} from Eq. (3.71) can be calculated. The rotor leakage reactance X_{rl} becomes:

$$X_{rl} = 4m\frac{(W_1 K_{w1})^2}{Q_r}\cdot X_{be} \tag{3.77}$$

For rated speed or slip S_n, both the skin and leakage saturation effects may be eliminated $K_x = K_r = 1$. With this adjustment, $(R_{be})_{Sn}$, $(R'_r)_{Sn}$,$(X_{be})_{Sn}$ and $(X_{rl})_{Sn}$ can easily be determined. The magnetization inductance X_m is given by:

$$X_m = \sqrt{\left(\frac{V_{ph}}{I_\mu}\right)^2 - {R_s}^2} - X_{sl} \tag{3.78}$$

3.3.7 Losses and efficiency

Efficiency is defined as the ratio of output power to input power:

$$\eta = \frac{P_{out}}{P_{out} + \sum \text{losses}} \tag{3.79}$$

With the aid of the power flow diagram in Figure 2.6, the summation of losses are:

$$\sum \text{losses} = p_{scl} + p_{rcl} + p_{fw} + p_{stray} + p_{core} \tag{3.80}$$

where p_{scl} represents the stator winding losses:

$$p_{scl} = 3R_s {I_n}^2 \tag{3.81}$$

and p_{rcl} the rotor cage losses:

$$p_{rcl} = 3(R_r)_{Sn} I_{rn}^2 = 3(R'_r)_{Sn} {K_I}^2 {I_n}^2 \tag{3.82}$$

The friction and winding losses are given by the following empirical formula:

$$p_{fw} = 0.012 \times P_n \text{ for } p_1 = 2 \tag{3.83}$$

Generally, the stray losses are given by the following equation:

$$p_{stray} = 0.01 \times P_n \tag{3.84}$$

The core losses P_{core} consists of fundamental p_{c1} and harmonic p_{c2} losses respectively. The fundamental core losses only occurs in the teeth and yoke (p_{t1}, p_{s1}) of the stator for slip frequencies below 4 Hz. The stator teeth fundamental losses can be given by:

$$p_{t1} \approx K_t p_{10} \left(\frac{f_1}{50}\right)^2 {B_{ts}}^{1.7} G_{t1} \tag{3.85}$$

where p_{10} is the specific losses in W/Kg at 50 Hz and 1 Tesla. In this case, p_{10} will be between 2 and 3 W/Kg. K_t accounts for the core loss augmentation as a result of mechanical machining. It is related to the quality of the material and cutting tools used. A factor of $K_t = 1.7$ will be used. G_{t1} represents the stator tooth weight:

$$G_{t1} = \gamma_{iron} \cdot N_s \cdot b_{ts}(h_{s2} + h_{s0}) \cdot L \cdot K_{Fe} \tag{3.86}$$

where γ_{iron} represents the sheet metal density. With B_{ts} and f_1 known, p_{t1} can be calculated. Similarly, the stator yoke fundamental losses is given by:

$$p_{y1} = K_y p_{10} \left(\frac{f_1}{50}\right)^2 {B_{cs}}^{1.7} G_{y1} \tag{3.87}$$

with K_y, similar to K_t is factored in due to the influence of machining. The weight of the stator yoke G_{y1} is:

$$G_{y1} = \gamma_{iron} \frac{\pi}{4} \left[{D_{out}}^2 - (D_{out} - 2h_{cs})^2\right] L K_{Fe} \tag{3.88}$$

All variables are now known to calculate p_{y1}. Therefore, the fundamental iron losses is given by:

$$p_{c1} = p_{t1} + p_{t2} \tag{3.89}$$

The harmonic or tooth flux pulsation core losses p_{c2} consists of the main stray loss components and is given by:

$$p_{c2} = 0.5 \cdot 10^{-4} \left[\left(Q_r \frac{f_1}{p_1} K_{ps} B_{ps} \right)^2 G_{ts} + \left(N_s \frac{f_1}{p_1} K_{rs} B_{pr} \right)^2 G_{tr} \right] \tag{3.90}$$

where:

$$\begin{aligned} K_{ps} &\approx \frac{1}{2.2 - B_{ts}} \\ K_{pr} &\approx \frac{1}{2.2 - B_{tr}} \end{aligned} \tag{3.91}$$

and

$$\begin{aligned} B_{ps} &\approx (K_{c2} - 1) B_g \\ B_{pr} &\approx (K_{c1} - 1) B_g \end{aligned} \tag{3.92}$$

The rotor teeth weight G_{tr} can be calculated with:

$$G_{tr} = \gamma_{iron} \cdot L \cdot K_{Fe} \cdot Q_r \cdot h_{r2} \cdot b_{tr} \tag{3.93}$$

All the unknowns have now been determined to calculate p_{c2}. Therefore the total core losses can now be determined as:

$$p_{core} = p_{c1} + p_{c2}. \tag{3.94}$$

With all the losses now known, the efficiency η can be calculated with Eq. (3.79). If the desired efficiency is not achieved, the geometry can be slightly adjusted by increasing the stator bore diameter and using a smaller current density.

3.3.8 Operation characteristics

The active no-load current I_{0a} is given by the no-load losses as:

$$I_{0a} = \frac{p_{core} + p_{fw} + 3{I_\mu}^2 R_s}{3\frac{V_1}{\sqrt{3}}} \tag{3.95}$$

The rated operating slip S_n is:

$$S_n = \frac{p_{rcl}}{P_n + p_{rcl} + p_{fw} + p_{stray}} \tag{3.96}$$

The rated shaft torque T_n can be calculated as:

$$T_n = \frac{P_n}{2\pi \frac{f_1}{p_1}(1 - S_n)} \tag{3.97}$$

The breakdown torque T_{bk} is:

$$T_{bk} = \frac{3p_1}{2\omega_b} \cdot \frac{{V_{ph}}^2}{\left[R_s + \sqrt{{R_s}^2 + (X_{sl} + (X_{rl})_{Sn})^2}\right]} \tag{3.98}$$

The starting current with $S = 1$ is:

$$I_{LR} = \frac{V_{ph}}{\sqrt{(R_s + (R'_r)_{s1})^2 + (X_{sl} + X_{rl})^2}} \tag{3.99}$$

The starting torque is given by:

$$T_{LR} = \frac{3(R'_r)_{S1} \cdot {I_{LR}}^2}{\omega_b} P_n \tag{3.100}$$

For the design specifications a desired PF, locked rotor torque ratio t_{LR}, locked rotor current ratio i_{LR} and breakdown torque ratio t_{BK} was given. These variables can be determined as follow:

$$PF = cos\phi_n = \frac{P_n}{3V_{ph}I_n\eta_n} \tag{3.101}$$

$$t_{BK} = \frac{T_{bk}}{T_n} \tag{3.102}$$

$$t_{LR} = \frac{T_{LR}}{T_n} \tag{3.103}$$

$$i_{LR} = \frac{I_{LR}}{I_n} \tag{3.104}$$

3.3.9 Temperature rise

Although any electromagnetic design has to be thermally valid, this section will briefly investigate the winding temperature. The temperature differential ΔT_{cs} between the conductors and slot walls have to be determined. This is followed by the calculation of the frame temperature rise ΔT_{fa} with respect to the ambient air:

$$\Delta T_{cs} \approx \frac{p_{scl}}{k_{cond}A_{ls}} \tag{3.105}$$

$$\Delta T_{fa} \approx \frac{\sum \text{losses}}{k_{cond}A_{frame}} \tag{3.106}$$

For IM with self ventilators placed outside the motor, the air convection coefficient $h_{air}[\text{W/m}^2\text{K}]$ can be calculated with:

$$h_{air} = 50; \text{ for } 2p_1 = 4 \tag{3.107}$$

The slot insulation thermal conductivity λ_{ins} with an estimated insulation thickness t_{ins} allows the calculation of the conductivity coefficient k_{cond}:

$$k_{cond} = \frac{\lambda_{ins}}{t_{ins}} \tag{3.108}$$

The lateral area of the stator slot A_{ls} is given by:

$$A_{ls} \approx (2h_{s2} + b_{s2})L \cdot Q_s \tag{3.109}$$

The frame area A_{frame} is given by:

$$A_{frame} = \pi D_{out}(L + \tau) \tag{3.110}$$

All the variables are now known to calculate ΔT_{cs} and ΔT_{fa}. Assuming an ambient temperature T_{air} of 40 °C, the winding temperature can be calculated with:

$$T_w = T_{air} + \Delta T_{cs} + \Delta T_{fa} \tag{3.111}$$

3.4 Analytical model results

An analytical design model based on the theory described in the previous sections was implemented in Matlab. The detailed results can be viewed in Appendix A.1.

As mentioned in Section 2.10, the main objective of the analytical model was to generate an initial design that will give fairly accurate desired motor performance. For the remainder of this section, a summary of the geometrical dimensions will be given, electric and magnetic loadings will be discussed and the accuracy of the model will be investigated.

3.4.1 Initial set of geometrical dimensions

Table 3.3 presents all the geometrical variables required for optimization in the following chapter. The ANSYS RMxprt software package allows a basic 2D graphical representation of the designed model. The geometry of the design can be seen in Figure 3.8.

3.4.2 Electric and magnetic loading

Table 3.4 gives an indication of the electric and magnetic loading values used in the analytical model. These values where initially assumed, but iteratively adjusted until stator tooth and rotor tooth EMF values converged. All the design values are within the recommend ranges as discussed in Sections 2.6.6 and 2.6.7.

Table 3.3: Analytical model generated geometrical dimensions.

General	Description	Value [mm]
L	Stack length	153.1
g	Air-gap width	0.65
D_{shaft}	Shaft diameter	30.0
Stator	**Description**	**Value [mm]**
D_{out}	Outer diameter	190.0
D_{is}	Inner diameter	108.3
h_{s0}	Slot opening height	1.0
h_{s2}	Slot height	22.4
b_{s0}	Slot opening width	3.5
b_{s1}	Slot lower width	4.1
b_{s2}	Slot upper width	6.1
h_{cs}	Yoke height	17.4
Rotor	**Description**	**Value [mm]**
h_{r0}	Rotor slot opening height	2.5
h_{r2}	Slot height	11.0
b_{r0}	Slot opening width	1.0
b_{r1}	Slot upper width	3.7
b_{r2}	Slot lower width	3.7

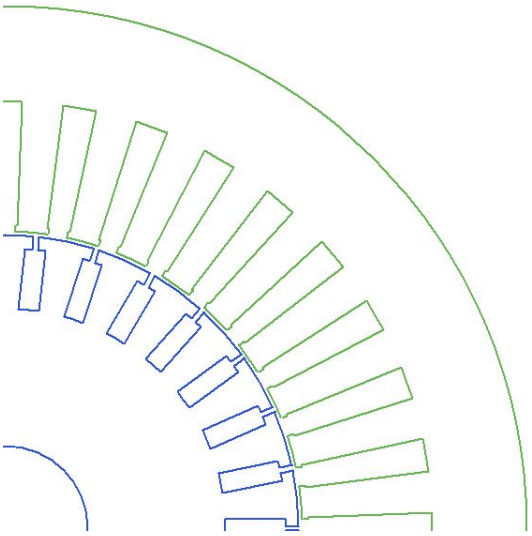

Figure 3.8: Visual representation of Matlab analytical model.

Table 3.4: Analytical model electrical and magnetic loading.

Flux density [T]	Design value	Recommended
Stator teeth	1.6	1.4 - 2.1
Stator yoke	1.7	1.4 - 1.7
Air-gap	0.7	0.7 - 0.9
Rotor teeth	1.6	1.5 - 2.2
Rotor yoke	1.4	1.0 - 1.6
Current density [A/mm^2]	Design value	Recommended
Stator slot	4.1	< 6
Rotor bar	3.4	< 7

3.4.3 Accuracy comparison

The required design specifications was indicated in Section 3.1. The traction motor was designed for a rated power of 3 kW at a rated speed of 1000 rpm. A comparison between the target and achieved design specifications at rated conditions can be seen in Table 3.5. The achieved results were reasonably close to the target results.

Table 3.5: Comparison between target and achieved specifications.

Characteristic	Target	Achieved
Efficiency %	85.0	83.4
Power factor %	75.0	76.4
Breakdown/Rated Torque ratio	3.0	2.9
Locked/Rated Torque ratio	2.0	1.8
Locked/Rated current ratio	6.0	4.8

In Table 3.6, the performance characteristics achieved by the analytical model is compared with the results from ANSYS RMxprt. This software requires a user to supply geometrical dimensions as inputs where-after it generates motor performance information. It can be seen from Table 3.6 that the performance results are reasonably accurate. The biggest difference in performance is ≈ 6.7 % for breakdown torque. This is due to marginal differences in slot-shape coefficients and leakage inductances.

Table 3.6: Analytical model operation characteristics comparison.

Characteristic	Matlab	RMxprt
Rated shaft torque [Nm]	29.6	29.3
Breakdown torque [Nm]	85.2	79.5
Starting torque [Nm]	52.5	55.5
Efficiency %	83.4	82.5
Power factor %	76.4	75.7

3.5 Analytical model summary

From Section 6.3, it can be concluded that the analytical model gave fairly accurate results. The geometrical results presented in Table 3.3 can now be optimized for improved performance. The aim of the optimization will be to reach the required target performance. An increase in efficiency and breakdown/rated torque ratio is desired. Due to the calculated initial geometrical dimension and gained knowledge regarding population size, the optimization can be expected to reach convergence quite easily. The optimization process will be discussed in Chapter 4.

Chapter 4

Design optimization

4.1 Introduction

In this chapter the geometrical dimensions which were generated through the analytical model and verified in RMxprt will be optimized. The optimization will be conducted within the RMxprt Optimetrics module. The optimized model performance will be confirmed and finalized within two FEM packages known as Maxwell 2D and SEMFEM. Once the performance is confirmed, the design will be experimentally fine tuned for increased performance. By the end of the chapter a final design will be achieved that will be built and tested experimentally.

4.2 RMxprt optimetrics

Within ANSYS RMxprt there exists an extension known as the Optimetrics module. This module adds optimization capabilities through various optimization algorithms to RMxprt. The available optimization algorithms include the Genetic Algorithm (GA), Quasi Newton (QN) and Pattern Search. The Optimetrics module incorporates single point optimization. In other words, motor performance is only optimized at a single operating point. As discussed in Section 2.7, a wide CPSR relates to the breakdown/rated torque ratio. Therefore, the torque characteristics will serve as important optimization constraints optimization for the design of the traction motor. The available optimization algorithms within the Optimetrics module are discussed below:

4.2.1 Quasi Newton

The Quasi Newton (QN) optimization algorithm is derived from Newton's method. It is an iterative and gradient based method for finding the roots of a twice differentiable function. The solutions include minima, maxima or saddle points. The method aims to find the roots of a function from a stationary

point by converging through a sequence known as Taylor series expansion. It involves the implementation of the Jacobian Matrix in search for zero's or the Hessian matrix in finding extrema. For the QN method, the Hessian matrix does not have to be computed. The QN algorithm makes use of the secant method for root finding of multi dimensional problems.

4.2.2 Pattern Search

The pattern search optimization algorithm does not require a gradient. Therefore, it can be used in applications where the design function is not differentiable. It aims to find a solution with the smallest error value in a multidimensional analysis of space possibilities. It is however not an iterative method that converges to the best solution. Generally, it is only implemented in scenarios where useful approximations are required.

4.2.3 Genetic algorithm

The GA is a heuristic non-gradient based optimization approach inspired by biological processes such as mutation, cross-over and natural selection. GA maintains a population of chromosomes, or rather, a set of potential solutions for a specific problem. The concept is such that through evolution an optimal solution will be found after succesive generations [31]. GA is powerful and generates high-quality optimization and solutions to problems that are hard to solve by conventional optimization techniques Therefore, GA will be used within RMxprt Optimetrics as optimization algorithm of choice.

4.3 Set-up of design variables

For the optimization process to be successful, care should be taken regarding variable mapping and sizing constraints. All the variables generated in Table 3.3 will be considered to define slot and overall motor dimensions during the optimization process. The way in which the stator and rotor slot variables are geometrically defined in RMxprt Optimetrics is given again in Figure 4.1 for convenience. It should be noted that h_{s1}, h_{r1}, Rs and Rr are set to zero for the proposed rectangular slots and will be neglected for the remainder of this chapter.

4.3.1 Slot sizing constraints

To ensure geometric valid designs regarding rotor and stator slot size optimization, the slots are defined through trigonometry with radial position and pitch taken into account. This can be visualized in Figure 4.2.

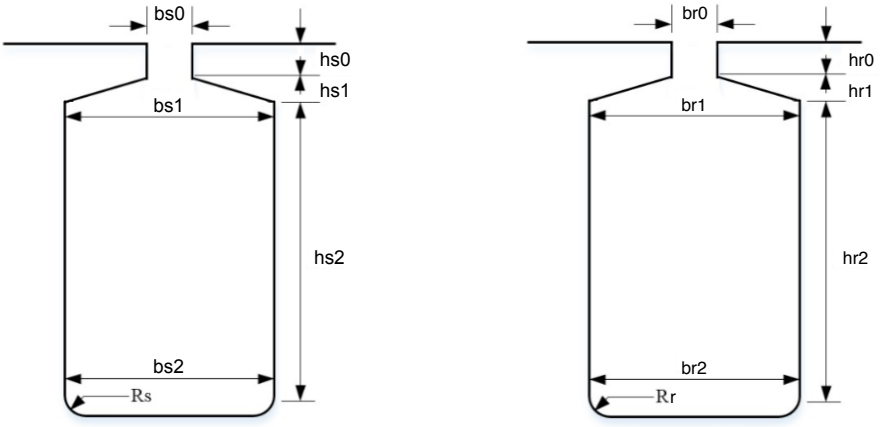

(a) Stator slot.

(b) Rotor slot.

Figure 4.1: Defining variables of stator and rotor slots for 3 kW motor.

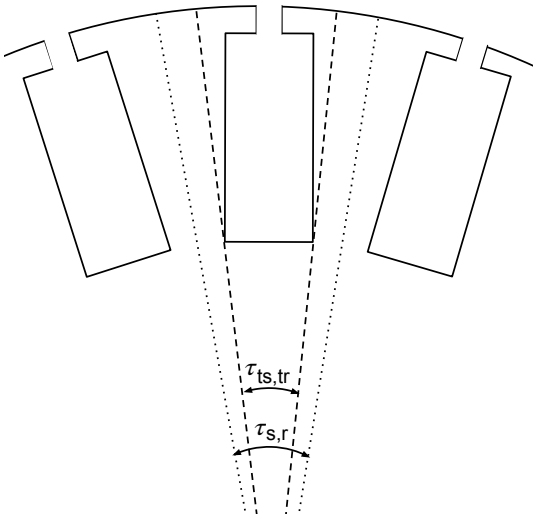

Figure 4.2: Slot width to pitch ratio.

4.3.1.1 Slot width

For both the rotor and the stator slots, the tooth width to slot pitch relationship $k_{s,r}$ exists respectively:

$$k_{s,r} = \frac{\tau_{ts,tr}}{\tau_{s,r}} \tag{4.1}$$

where $\tau_{ts,tr}$ is the slot width pitch of the stator and rotor respectively. The variables $\tau_{s,r}$ are the slot pitch of the stator and rotor respectively. Rearranging and simplifying both the slot pitches can be represented with:

$$\tau_{s,r} = \frac{2\pi k_{s,r}}{Q_{s,r}} \tag{4.2}$$

By limiting the variable $k_r < 1$ during the optimization process, the risk of generating a geometric invalid solution is avoided. The optimal rotor slot width is then iteratively determined by the following equation:

$$b_{r2} = 2\tan\left(\frac{\tau_{tr}}{2}\right)\left(\frac{D_{out}}{2} - h_{cs} - h_{s2} - h_{s0} - g - h_{r0} - h_{r2}\right) \tag{4.3}$$

Similar to the rotor, by limiting $k_s < 1$ during optimization the optimal stator slot width is determined by:

$$b_{s1} = 2\tan\left(\frac{\tau_{ts}}{2}\right)\left(\frac{D_{out}}{2} - h_{cs} - h_{s2}\right) \tag{4.4}$$

4.3.1.2 Slot opening

For both the rotor and the stator, the winding should withstand centrifugal forces and remain fixed within each slot. This is ensured by introducing a ratio between the slot opening and slot width as follows:

$$k_{bs,br} = \frac{b_{s0,r0}}{b_{s1,r1}} \tag{4.5}$$

By limiting $k_{bs,br} < 1$, semi-closed slots are ensured. This ratio further ensures valid geometric solutions during each optimization iteration.

4.3.2 Variable mapping

The process of variable mapping is used to relate geometric variables. The aim is to minimize the total amount of variables used in an optimization process which will increase the optimization speed. This is done by effectively defining main geometrical dimensions through a summation of minimum required sub-variables. For the design of the traction motor the stator outer diameter, as well as the air-gap length remained fixed at 190 mm and 0.65 mm respectively. Further, a minimum shaft diameter is also calculated as discussed in Section 2.6.4. This allows geometrical optimization to be constrained between the fixed stator outer diameter and shaft diameter. The geometric dimensions are mapped in Table 4.1.

4.4 Optimization formulation

The objective function for the optimization is given in Eq. (4.6) below:

$$Minimize: \quad F(\mathbf{X}) = \sum_i [w_i G_i(X)] \tag{4.6}$$

Table 4.1: Geometric variable mapping of 3 kW traction motor.

Dimensions	Design Variable(s)
Stack length	L
Air-gap length	g (Fixed)
Shaft diameter	D_{shaft} (Fixed)
Stator	**Design Variable(s)**
Outer diameter	D_{out} (Fixed)
Inner diameter	$D_{out} - 2(h_{cs} + h_{s2} + h_{s0})$
Slot opening height	h_{s0}
Slot height	h_{s2}
Slot opening width	$k_{bs}b_{s1}$
Slot lower width	b_{s1}
Slot upper width	$2\tan\left(\frac{\tau_{ts}}{2}\right)\left(\frac{D_{out}}{2} - h_{cs} - h_{s2}\right)$
Yoke height	h_{cs}
Rotor	**Design Variable(s)**
Outer diameter	$D_{out} - 2(h_{cs} + h_{s2} + h_{s0} + g)$
Slot opening height	h_{r0}
Slot height	h_{r2}
Slot opening width	$k_{br}b_{r2}$
Slot upper width	b_{r2}
Slot lower width	$2\tan\left(\frac{\tau_{tr}}{2}\right)\left(\frac{D_{out}}{2} - h_{cs} - h_{s2} - h_{s0} - g - h_{r0} - h_{r2}\right)$
Yoke height	$\frac{D_{out}}{2} - \frac{D_{shaft}}{2} - h_{cs} - h_{s2} - h_{s0} - g - h_{r0} - h_{r2}$

where X is the set of design variables, w_i is a set of weighting functions and G_i is a set of penalty functions for constraints. With each optimization iteration motor performance is calculated, as well as the deviation from the design constraints. The assigned penalties are directly related to the size of the constraint deviation. The weighting function for each constraint was chosen as unity. The optimization constraints and boundaries can be seen in Sections 4.4.1 and 4.4.2 respectively.

4.4.1 Optimization constraints

The constraints considered at a base speed of 1000 rpm for the design of a traction motor:

$$P_{\text{out}} = 3\,\text{kW} \tag{4.7}$$
$$\eta \geq 85\,\% \tag{4.8}$$
$$\text{PF} \geq 75\,\% \tag{4.9}$$
$$T_{\text{bk}} \geq 100\,\text{Nm} \tag{4.10}$$
$$T_{\text{n}} \geq 30\,\text{Nm} \tag{4.11}$$

where P_{out} is the output power, η is the efficiency, PF is the power factor, T_{bk} is the breakdown torque and T_{n} is the rated torque. It should be noted that a CPSR of 3 is realised through this optimization method by having a breakdown/rated torque ratio of 3 or more.

4.4.2 Optimization boundaries

The boundaries on geometrical variables for the optimization process can be seen in Table 4.2. Due to the fixed shaft diameter and stator outer diameter, the optimization had less freedom for variables defined in a radial manner. To avoid an invalid solution, the sum of radial defined variables $h_{cs}, h_{s2}, h_{s0}, g, h_{r0}$ and h_{r2} should be less or equal to the difference between D_{out} and D_{shaft}. Therefore, the upper and lower boundary for each of these variables, as well as L were chosen as 20 % of the original value. Invalid solutions regarding slot widths were prevented through ratio's as discussed in Section 4.3.1.

4.4.3 Stator and rotor winding configuration

For the optimization process, the number of stator winding layers, parallel branches, fill factor and coil pitch remains fixed at 2, 1, 40 % and 8 respectively. However, variables such as conductors per slot, number of wire strands and wire thickness are automatically adjusted according to required performance specifications as slot shapes iteratively changes during the optimization process. For the rotor, the end bar length and end ring width remains fixed at 15 mm and 25 mm respectively, while the end ring height is calculated by multiplying slot height with an optimal ratio of between 1.1 and 1.3.

4.5 Optimization results

This section contains the results of the RMxprt Optimetrics optimization. A geometric comparison is given in Section 4.5.1 and a performance comparison in Section 4.5.3. The performance of the optimized design gets verified in Section 4.5.4 through FEM in Maxwell 2D. Finally, in Section 4.6 a performance comparison is made between two FEM packages: Maxwell 2D and SEMFEM.

Table 4.2: The Matlab generated set of geometrical dimensions with optimization boundaries.

General	Description	Lower [mm]	Matlab [mm]	Upper [mm]
L	Stack length	122.4	153.1	184.0
g	Air-gap length	-	0.65	-
D_{shaft}	Shaft diameter	-	30.0	-
Stator	Description	Lower [mm]	Matlab [mm]	Upper [mm]
D_{out}	Outer diameter	-	190.0	-
h_{s0}	Slot opening height	0.8	1.0	1.2
h_{s2}	Slot height	18.0	22.4	27.0
k_s	Pitch ratio	0.1	0.4	0.9
k_{bs}	Slot width ratio	0.1	0.8	0.9
b_{s0}	Slot opening width	2.1	3.5	3.7
b_{s1}	Slot lower width	1.9	4.1	5.8
b_{s2}	Slot upper width	4.9	6.1	7.2
h_{cs}	Yoke height	13.9	17.4	20.9
Rotor	Description	Lower [mm]	Matlab [mm]	Upper [mm]
h_{r0}	Slot opening height	2.0	2.5	3.0
h_{r2}	Slot height	8.8	11.0	13.2
k_r	Pitch ratio	0.1	0.4	0.9
k_{br}	Slot width ratio	0.1	0.3	0.9
b_{r0}	Slot opening width	0.8	1.0	1.2
b_{r1}	Slot upper width	1.7	3.7	5.0
b_{r2}	Slot lower width	1.7	3.7	5.0

4.5.1 Geometric comparison

The optimized motor geometry will be analysed and discussed in this subsection. Figure 4.3 serves as a visual comparison between the original and optimized model. The optimized geometry variables is given in Table 4.3.
Figures 4.3a and 4.3b represent a section view of the original Matlab analytical model and the RMxprt Optimetrics model respectively. Although the presented drawings are not on identical scales, Table 4.3 can be used as reference. The optimized model has a shallower rotor slot opening and thinner stator slot opening. The smaller a motor's leakage reactance, the higher breakdown torque it is capable of achieving. Therefore, a better breakdown torque can be expected. These predictions will have to be confirmed. Further, the rotor and stator slots have marginally larger area's, which will slightly increase efficiency.

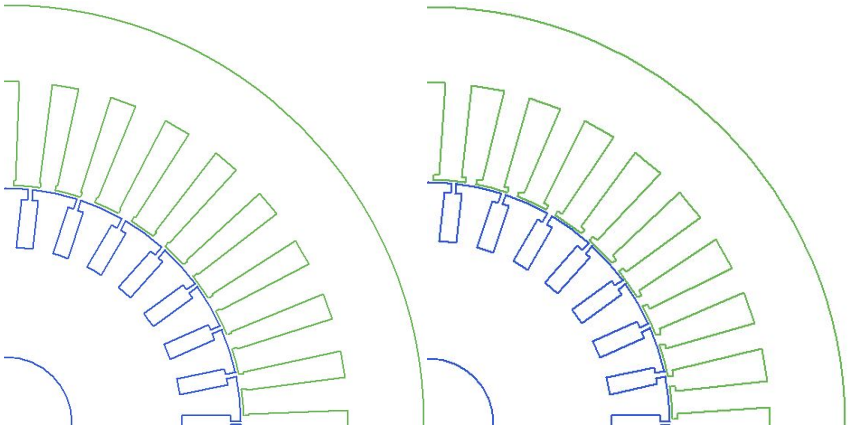

(a) Matlab analytical model. (b) RMxprt Optimetrics.

Figure 4.3: Visual comparison between the original Matlab analytical model and the RMxprt optimetrics model.

Table 4.3: Geometrical comparison of the initial Matlab analytical model and RMxprt Optimetrics model.

General	Description	Matlab [mm]	Optimetrics [mm]
L	Stack length	153.1	168.2
g	Air-gap width	0.65	0.65
D_{shaft}	Shaft diameter	30.0	30.0
Stator	Description	Matlab [mm]	Optimetrics [mm]
D_{out}	Outer diameter	190.0	190.0
D_{is}	Inner diameter	108.3	111.5
h_{s0}	Slot opening height	1.0	1.0
h_{s2}	Slot height	22.4	20.9
b_{s0}	Slot opening width	3.5	2.5
b_{s1}	Slot lower width	4.1	4.8
b_{s2}	Slot upper width	6.1	7.4
h_{cs}	Yoke height	17.4	17.4
Rotor	Description	Matlab [mm]	Optimetrics [mm]
h_{r0}	Slot opening height	2.5	2.3
h_{r2}	Slot height	11.0	11.1
b_{r0}	Slot opening width	1.0	1.1
b_{r1}	Slot upper width	3.7	3.9
b_{r2}	Slot lower width	3.7	3.9
h_{cr}	Yoke height	25.0	26.7

4.5.2 Winding information of optimized motor

A summary of the optimized stator and rotor winding parameters can be seen in Table 4.4. The stator and rotor resistance and inductance values, which was determined analytically within RMxprt, will be imported into FEM packages such as Maxwell 2D and SEMFEM for verification of the traction motor performance.

Table 4.4: General stator and rotor winding data.

Stator winding	Value
Terminal resistance per phase	1.926 Ω
End leakage inductance per phase	1.400 mH
Turns per phase	192
Number of parallel branches	1
Number of conductors per slot	32
Coil pitch	8
Fill factor	37.3%
Rotor winding	**Value**
End resistance between adjacent conductors	2.991 $\mu\Omega$
End inductance between adjacent conductors	3.080 nH
End length of bar	15 mm
Height of end ring	17.4 mm
Width of end ring	25 mm

4.5.3 Performance comparison

The pre-verified performance of the optimized model is given in Table 4.5. The performance complies well with the optimization constraints as discussed in Section 4.4.1. Besides the rated torque constraint, all other optimization constraints were met. As mentioned in Section 2.7, a well designed traction motor has a CPSR of 3 or greater. Further, the output power should remain at the required power output throughout the whole CPSR. This was achieved and can be seen in Figure 4.4. From the figure it can be seen that a maximum speed of 2962 rpm was achieved which is 1.3 % within the target speed of 3000 rpm. A CPSR of 2.9 was achieved and is acceptable. These results are preliminary and will have to be verified by a FEM package such as Maxwell 2D.

4.5.4 Maxwell 2D verification

The Maxwell 2D FEM package was used to verify the optimized design through a transient response at 1000 rpm and 3000 rpm respectively. Figure 4.5 shows

Table 4.5: RMxprt optimetric pre-verified performance results.

Characteristic at 1000 rpm	Matlab model	Optimized model
Output power [kW]	3.0	3.0
Efficiency %	82.5	85.1
Power factor %	75.7	75.0
Starting torque [Nm]	55.5	81.0
Output torque [Nm]	29.3	28.4
Breakdown torque [Nm]	79.3	100.2
Breakdown/Rated Torque ratio	2.7	3.5
Characteristic at 3000 rpm	Matlab	RMxprt Opt
Output power [kW]	3.0	3.0
Output torque [Nm]	9.6	9.7

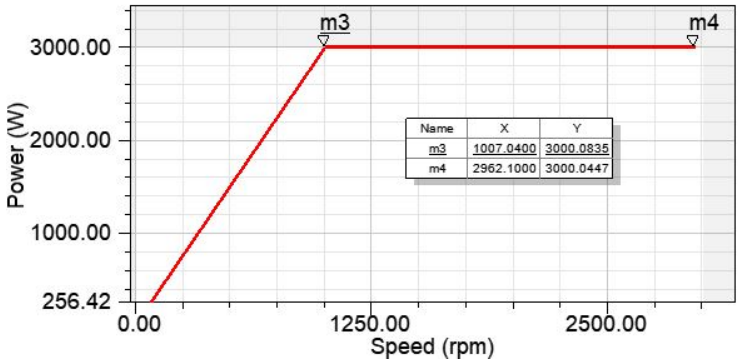

(a) Output power.

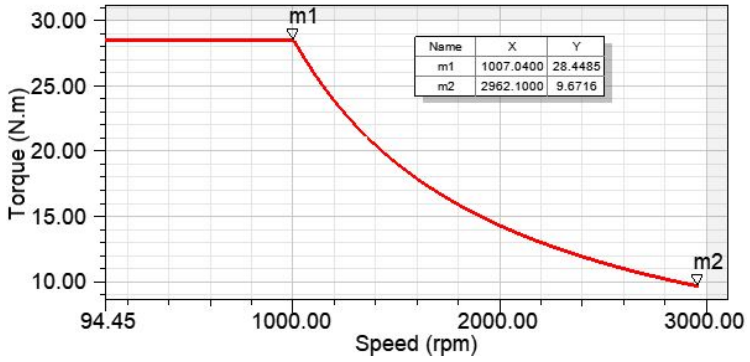

(b) Output torque.

Figure 4.4: Power and torque characteristics for the CPSR.

the Maxwell 2D model. The magnetic and electric loading characteristics are visually represented in Appendix C.1. For the remainder of this section a comparison will be made between the RMxprt Optimetrics model and the Maxwell

2D FEM model. If the results are reasonably close, it can be concluded that a successful design approach was used.

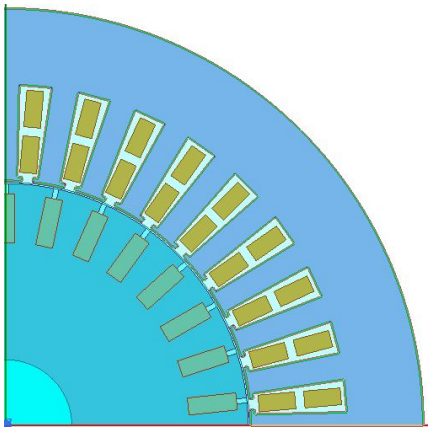

Figure 4.5: Maxwell 2D FEM model.

4.5.4.1 Output power

The analytical result from Figure 4.4a can be verified with a transient analysis in Maxwell 2D. The results can be seen in Figure 4.6. The average output power is 3012 W at both 1000 rpm and at 3000 rpm. The output power at rated speed and maximum speed is within 1 % of the required 3 kW specification. Therefore, it can be concluded that Maxwell 2D results verify the RMxprt results and partly verify that a CPSR of 3 was achieved. These results correspond to traction motor characteristics as discussed in Sections 2.4 and 2.7. To fully validate the successful design of a wide flux weakening range, the output torque results have to be investigated.

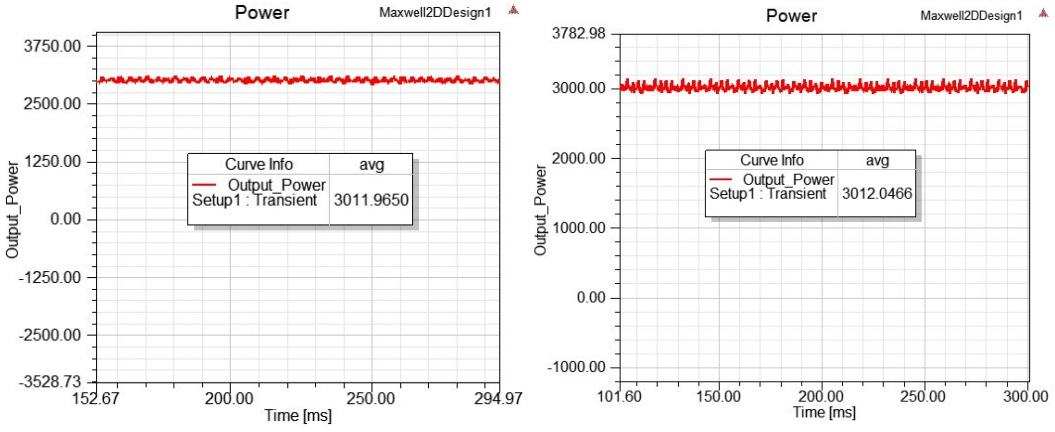

(a) output power at 1000 rpm. (b) output power at 3000 rpm.

Figure 4.6: Maxwell 2D transient power analysis.

4.5.4.2 Output torque

As discussed in Sections 2.4 and 2.7, a top design criteria for a traction motor is a wide flux weakening range. This allows a more gradual decrease in output torque throughout the required CPSR. From Figure 4.4a, an output torque of 28.5 Nm at rated speed and 9.7 Nm at maximum speed was achieved. Similar as in Section 4.5.4.1, the results have to be verified with two FEM transient plots at rated and maximum speed. The Maxwell 2D results of the torque characteristics can be seen in Figure 4.7.

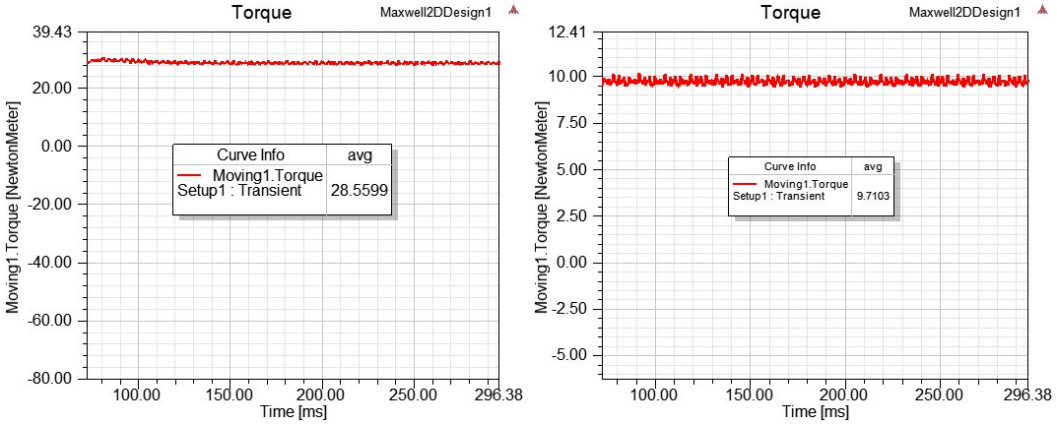

(a) Output torque at 1000 rpm. (b) Output torque at 3000 rpm.

Figure 4.7: Maxwell 2D transient torque analysis.

From Figure 4.7, it can be seen that an output torque of 28.6 Nm was achieved at a rated speed of 1000 rpm. At a maximum speed of 3000 rpm an output torque of 9.7 Nm was achieved. Therefore, the torque characteristics achieved is within 1 % of the analytical results and thus verifies that a wide flux weakening range was achieved.

4.5.4.3 Efficiency

The Maxwell 2D FEM result can be seen in Figure 4.8. An efficiency of 87.8 % was achieved. This difference of 3 % when compared to the result from Table 4.5 can be attributed to the windage, friction and stray losses, which was not accounted for in Maxwell 2D.

4.5.4.4 Power factor

Maxwell 2D does not give the motor power factor as a default output variable. However, the instantaneous current, flux and voltage values are available. As a result, a dq0 transformation can be used to model the power factor and validate the RMxprt result. The power factor was calculated as follows [28]:

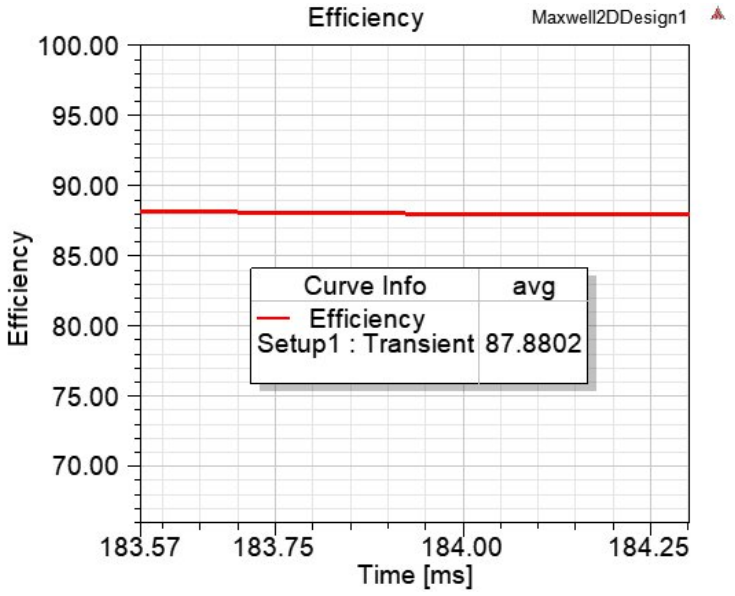

Figure 4.8: Maxwell 2D FEM efficiency.

$$S_d = \frac{2}{3} \cdot [S_a cos(\omega t) + S_b cos(\omega t - 120^o) + S_c cos(\omega t + 120^o)] \tag{4.12}$$

$$S_q = \frac{2}{3} \cdot [-S_a sin(\omega t) - S_b sin(\omega t - 120^o) - S_c sin(\omega t + 120^o)] \tag{4.13}$$

where S represents a stator quality to be transformed. For this application, it represents instantaneous current and voltage values. The a, b and c subscripts represent the stator phase quantities, while the d and q subscripts represent the direct and quadrature axes.

Once the transformation is complete, the current and voltage transformation angles, α_{dq} and β_{dq}, can be calculated to determine the power factor:

$$\alpha_{dq} = tan^{-1}\left(\frac{I_d}{I_q}\right) \tag{4.14}$$

$$\beta_{dq} = tan^{-1}\left(\frac{V_d}{V_q}\right) \tag{4.15}$$

$$PowerFactor = \cos\left(\alpha_{dq} - \beta_{dq}\right) \tag{4.16}$$

From Figure 4.9 the achieved results can be seen. The achieved PF is 73.6 %, which is 1.4 % lower than the optimized model in Table 4.5. Therefore, the achieved PF is acceptable and satisfactory.

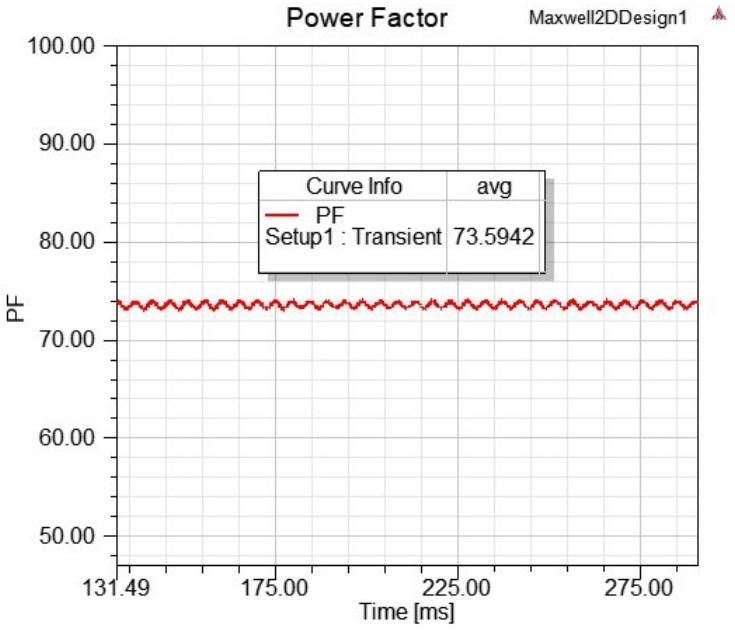

Figure 4.9: Maxwell 2D power factor.

4.5.4.5 Maxwell 2D conclusion

From all the results presented in Section 4.5.4 it can be concluded that the optimized performance is verified. A CPSR of 2.9 was achieved which is reasonably close to the desired target of 3 and is deemed acceptable. The FEM results of Maxwell 2D will be confirmed through SEMFEM and is presented in Section 4.6.

4.6 SEMFEM verification

The aim of this section is to compare the transient analysis of Maxwell 2D with SEMFEM for the optimized design. The SEMFEM version of the optimized model is represented in Figure 4.10. The magnetic loading can be seen in Appendix C.2. The FEM performance comparison is given in Table 4.6 for the optimized design.

The biggest difference for the FEM comparison is 2.1 % for the PF. This is within acceptable margins and validates Maxwell 2D. It can be concluded that the suggested design approach is capable of generating a traction motor with acceptable performance.

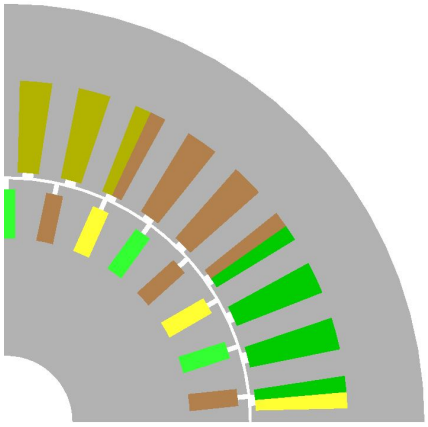

Figure 4.10: Maxwell 2D FEM model.

Table 4.6: FEM performance comparison between the Maxwell 2D model and the SEMFEM for the optimized model.

Characteristic at 1000 rpm	Maxwell 2D	SEMFEM
Output power [kW]	3.0	3.0
Efficiency %	87.9	87.5
Power factor %	73.6	75.2
Output torque [Nm]	28.6	29.2
Characteristic at 3000 rpm	Maxwell 2D	SEMFEM
Output power [kW]	3.0	3.0
Output torque [Nm]	9.7	9.8

4.7 Fine tuning of optimized design

For manufacturability the optimized design had to be slightly adapted due to reduced costs, fixed material sizes, ease of assembly and experimental purposes. These geometric changes are only marginal and a comparison between the optimized and fine tuned design will be made to discover if any significant performance changes occur. These changes are discussed in Sections 4.7.1 and 4.7.2

4.7.1 Geometrical changes

A geometric comparison between the optimized and adapted design is given in Table 4.7. For general motor sizing, the stack length was reduced to 160 mm which is a 5 % reduction in length. With the stator outer diameter remaining fixed, the stack aspect ratio remains approximately identical and no major performance characteristic changes will occur. The stator slot size changes marginally. The slot opening was increased to ease the winding installation.

Although this might negatively influence air-gap flux harmonics it improves manufacturability of the windings. The winding characteristics remained identical. The rotor slot size was marginally adjusted to fit the closest available copper bars on the market. The rotor slot opening height was slightly increased for the experimental slot designs as discussed in Section 4.7.2.

Table 4.7: Geometrical comparison between the optimized and adapted design.

General	Description	Optimized [mm]	Adapted [mm]
L	Stack length	168.2	160.0
g	Air-gap length	0.65	0.65
D_{shaft}	Shaft diameter	30.0	30
Stator	Description	Optimized [mm]	Adapted [mm]
D_{out}	Outer diameter	190.0	190
h_{s0}	Slot opening height	1.0	1.0
h_{s2}	Slot height	20.9	22.5
b_{s0}	Slot opening width	2.5	4.0
b_{s1}	Slot lower width	4.8	5.0
b_{s2}	Slot upper width	7.4	7.0
h_{cs}	Yoke height	17.4	17.2
Rotor	Description	Optimized [mm]	Adapted [mm]
h_{r0}	Slot opening height	2.3	2.5
h_{r2}	Slot height	11.1	10.0
b_{r0}	Slot opening width	1.1	1.2
b_{r1}	Slot upper width	3.9	3.5
b_{r2}	Slot lower width	3.9	3.5

4.7.2 Rotor slot profile

As discussed in Chapter 2.9, changing the rotor slot such as Design C in Figure 2.18c it is proven through FEM analysis to increase efficiency by reducing harmonic copper losses. Due to RMxprt Optimetrics not accounting for harmonic secondary copper losses during optimization, the slot shape of Design C will be implemented in the adapted design. The final design or prototype motor can be seen in Figure 4.11 with the changes implemented.

4.7.3 Winding information of prototype motor

Due to stator and rotor winding information being altered due to the minor changes of the stator and rotor slots, updated winding information is given in

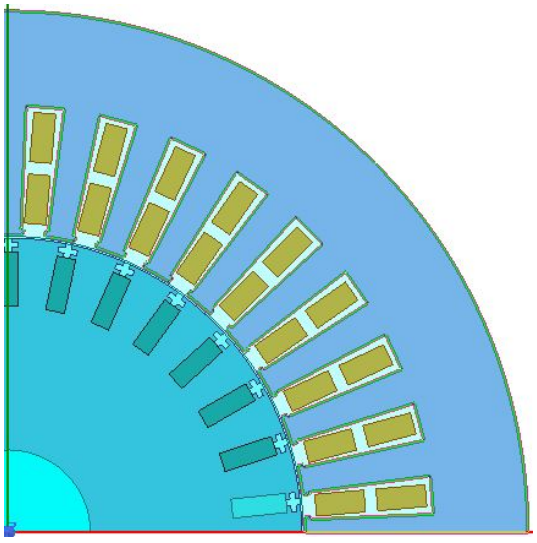

Figure 4.11: Final design of the traction motor.

Table 4.8. The rotor and stator winding resistance and inductance parameters are once again included into Maxwell 2D to verify motor performance. The remaining information is given for construction purposes.

Table 4.8: General stator and rotor winding data.

Stator winding	Value
Terminal resistance per phase	1.979 Ω
End leakage inductance per phase	1.700 mH
Turns per phase	204
Number of parallel branches	1
Number of conductors per slot	34
Coil pitch	8
Fill factor	37.4 %
Rotor winding	**Value**
End resistance between adjacent conductors	2.243 μΩ
End inductance between adjacent conductors	3.894 nH
End length of bar	15 mm
Height of end ring	16.25 mm
Width of end ring	25 mm

4.7.4 Prototype performance

To understand how the geometrical changes influenced motor performance, a FEM simulation was completed in Maxwell 2D which will be used for com-

parison. The power, torque, efficiency and power factor results are presented in Sections 6.6.1.1, 6.6.1.2 and 6.6.1.3 respectively. The comparison will be presented in Section 4.7.5.

4.7.4.1 Power

The power characteristics for the prototype motor are given in Figures 4.12 and 4.13. It can be seen that the output power remained at 3 kW throughout the flux weakening range. The markers at every 500 rpm in Figure 4.12 will be used as reference when compared the measured results of the prototype motor.

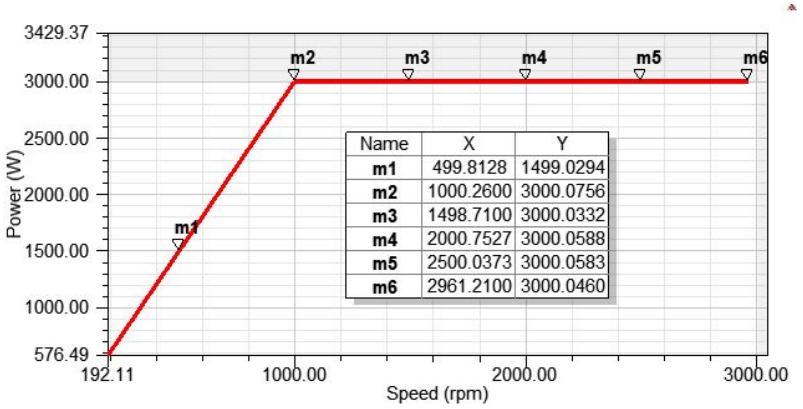

Figure 4.12: RMxprt power-speed curve during the CPSR.

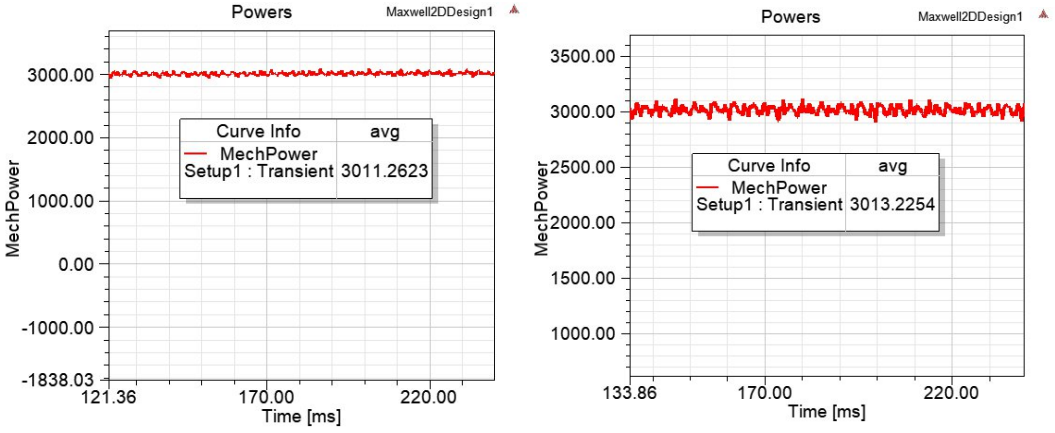

(a) Output power at 1000 rpm.

(b) Output power at 3000 rpm.

Figure 4.13: Maxwell 2D transient power analysis of prototype motor.

4.7.4.2 Torque

The torque characteristics for the prototype motor are given in Figure 4.15. The results look reasonable and similar to what is expected. Similar to that of Figure 4.14, the markers in Figure 4.14 will be used as reference when compared to the measured results of the prototype motor.

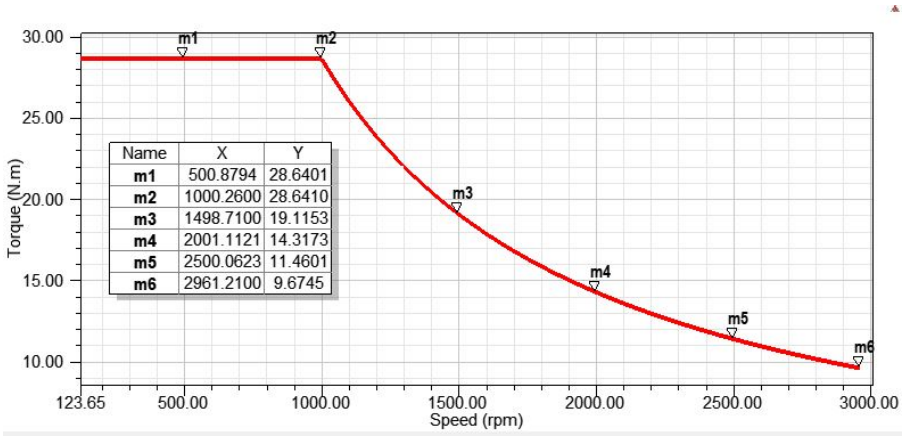

Figure 4.14: RMxprt torque-speed curve during the CPSR.

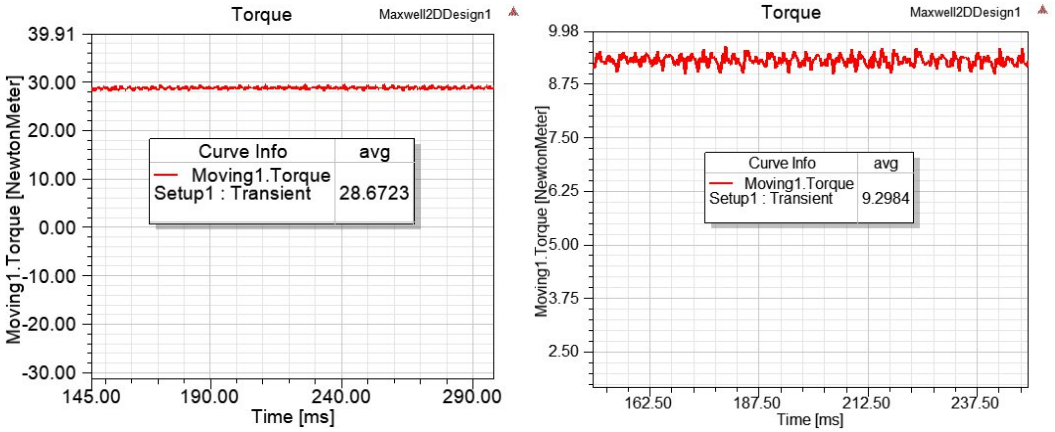

(a) Output torque at 1000 rpm.

(b) Output torque at 3000 rpm.

Figure 4.15: Maxwell 2D transient torque analysis of prototype motor.

4.7.4.3 Efficiency and power factor

The efficiency and power factor are given in Figure 4.16. The performance comparison will be presented in the following section.

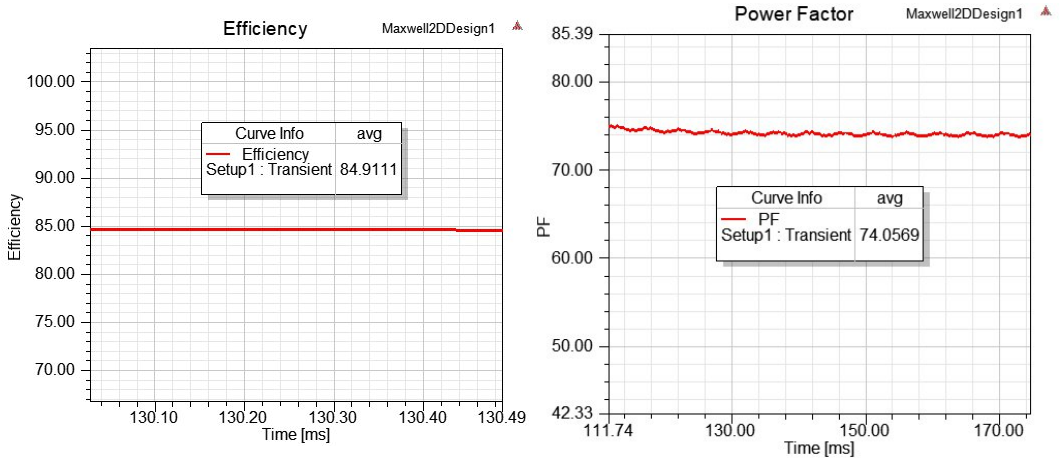

(a) Efficiency at 1000 rpm.

(b) PF at 1000 rpm.

Figure 4.16: Maxwell 2D transient analysis of efficiency and power factor of the prototype motor.

4.7.5 Performance comparison

The FEM performance comparison for the optimized model and the prototype model to be built and tested is given in Table 4.9. The complete design sheet comparison is available in Appendix B.1. The power and torque characteristics at both base and maximum speed remained similar. The power factor increased slightly by 0.5 %. However, the efficiency reduced by approximately 3 %. Although this is not ideal, it is still deemed as acceptable performance for a traction motor. A compromise is made between manufacturability and performance.

Table 4.9: Maxwell 2D performance comparison between the optimized model and the prototype model.

Characteristic at 1000 rpm	Optimized	Prototype
Output power [kW]	3.0	3.0
Efficiency %	87.9	84.9
Power factor %	73.6	74.1
Output torque [Nm]	28.6	28.7
Characteristic at 3000 rpm	**Optimized**	**Prototype**
Output power [kW]	3.0	3.0
Output torque [Nm]	9.7	9.3

4.7.6 Magnetic and electric loading

The magnetic and electric loading for the prototype motor is given in Table 4.10. All the values are reasonably close or within the recommend range which indicates a quality design. The flux lines, flux density and current density during transient analysis can be viewed in Figure 4.17.

Table 4.10: Prototype electrical and magnetic loading.

Flux density [T]	Design value	Recommended
Stator teeth	1.4	1.4 - 2.1
Stator yoke	1.3	1.4 - 1.7
Air-gap	0.8	0.7 - 0.9
Rotor teeth	1.5	1.5 - 2.2
Rotor yoke	0.5	1.0 - 1.6
Current density [A/mm^2]	Design value	Recommended
Stator slot	6.4	< 7
Rotor bar	5.8	< 6

4.8 Optimization summary

The aim of this chapter was to finalize a traction motor design that could be built and tested. This was achieved by optimizing the model generated by the analytical model through a non-gradient search based algorithm known as the GA. Due to the CPSR being related to torque characteristics, the torque constraints played an important role in achieving the objective CPSR of 3. However, due to manufacturing limitations, cost and availability of specific material sizes required the design had to be optimally fine-tuned. Marginal changes were made to increase manufacturability and to accommodate fixed material sizes locally available within a time constraint. This was done without sacrificing optimal performance to a major extent with a comparison given. In addition, an experimental rotor slot shape was introduced due to its perceived benefits. The performance of the prototype motor is acceptable for a traction motor and will therefore be built and tested to verify the results.

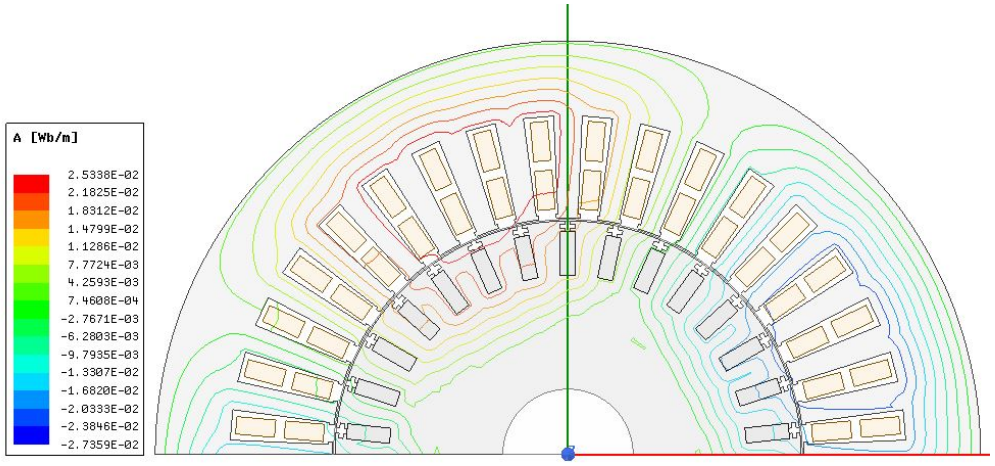

(a) Flux lines.

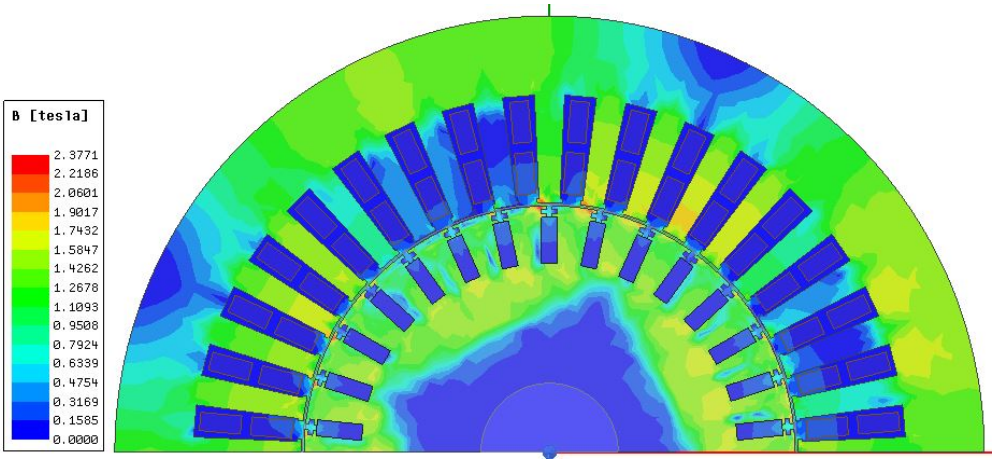

(b) Flux density.

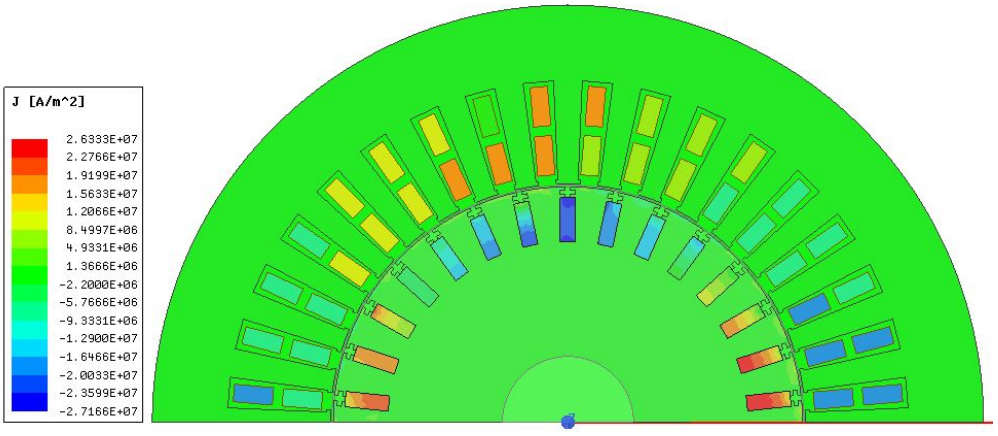

(c) Current density.

Figure 4.17: Magnetic and electric characteristics during transient analysis of prototype design.

Chapter 5

Mechanical design and testing of a prototype motor

5.1 Introduction

A design strategy for traction motors was used to develop a prototype motor as discussed in Chapters 1 - 4. The developed prototype traction motor will be constructed and experimentally evaluated. This chapter aims to discuss the mechanical design and assembly, as well as the testing of the prototype motor.

5.2 Mechanical design

The prototype traction motor incorporated a frameless design. These designs are becoming more popular due to reduction in torsional losses and a decrease in weight, thus creating higher torque densities. Further, the frameless motor leads to greater design flexibility [32], [33]. The finned stator design was adapted for increased heat transfer. An isometric and section-view of the frameless designed traction motor can be seen in Figure 5.1. It should be noted that these drawings do not include stator windings. The complete drawing pack with part labels can be viewed in Appendix D.

5.2.1 Assembly and construction

To visualize and understand how the different components integrate and connect to each other, the assembly will be explained first. The motor core consists of eight slots aligned in the axial direction and tangent to the outer surface of the stator. A detailed view of these slots can be seen in Fig. 5.8. It was found that costs could be reduced by the inclusion of the rectangular cutaway which allows continuous laser cutting motion. The stator core is compressed between two inner end-plates via four threaded rod and nut assemblies. Its further held in position between two outer end-plates via four threaded rod, nut and bush

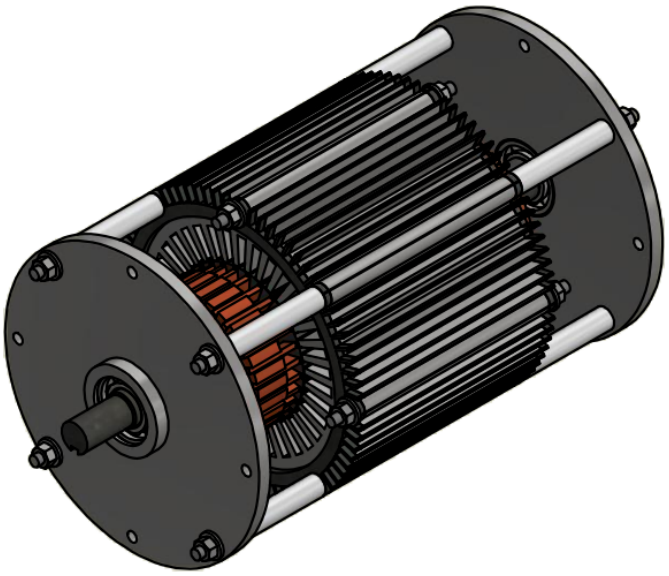

(a) Prototype motor isometric view.

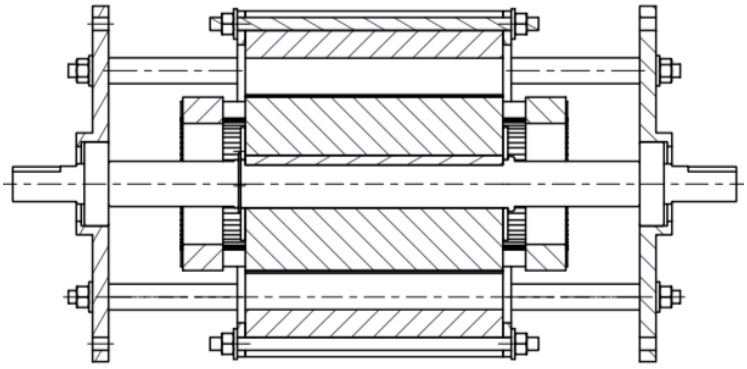

(b) Prototype motor section view.

Figure 5.1: Autocad Inventor drawings of prototype traction motor.

assemblies. The bushing increases rigidity and serves as a spacer between the core and outer end-plate for winding purposes. The rotor core is press-fitted onto the shaft and kept fixed via a key-way between the shaft shoulder and a circlip. For testing purposes, one or both outer end-plates can be bolted onto a vertical frame. With extra holes on the outer end plates, flanges can also be bolted to the motor for mountings on horizontal surfaces. For the remainder of this sub-section the construction of the motor will be presented.

5.2.2 Stator core construction

The stator core construction is depicted in Figure 5.2. Each sub-figure represents a step during the construction process. The purposefully created jig

for stacking alignment is depicted in Figure 5.2a. The jig was designed to accommodate the core and extended rods. With the rods being kept stationary vertically, the insertion of the inner end plate and laminations could commence. The rods prevented any skewing while laminations were stacked. Figure 5.2b depicts the stacking process during the early stages. Laminations were iteratively added and compressed until the correct stack length was achieved as depicted in Figure 5.2c. Figure 5.2d shows how the jig was pressed out of the core. The complete stator core before and after winding is depicted in Figures 5.2e and 5.2f respectively. More winding details are given in Section 5.2.3.

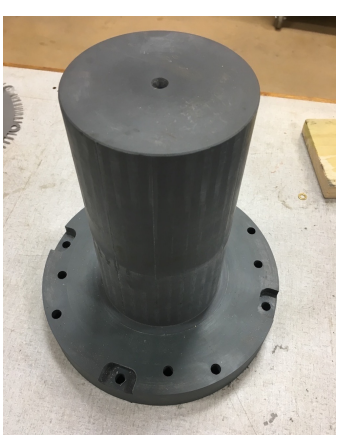

(a) Jig.

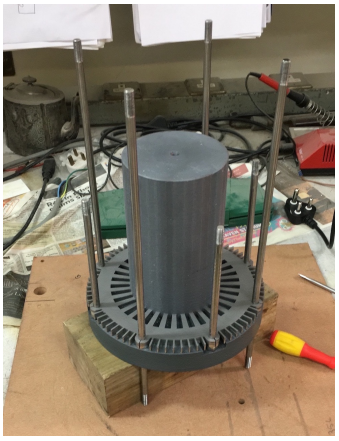

(b) Stacking.

(c) Compression.

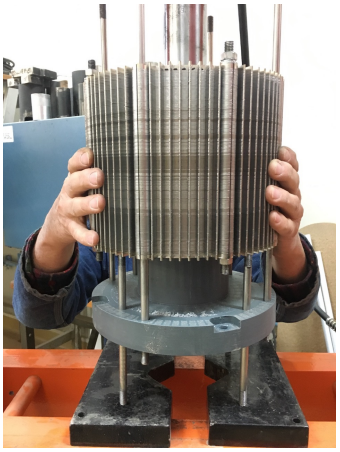

(d) Jig removal.

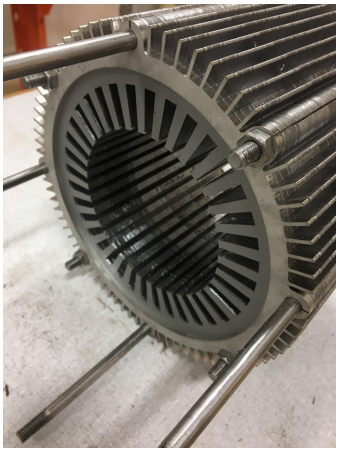

(e) Stack.

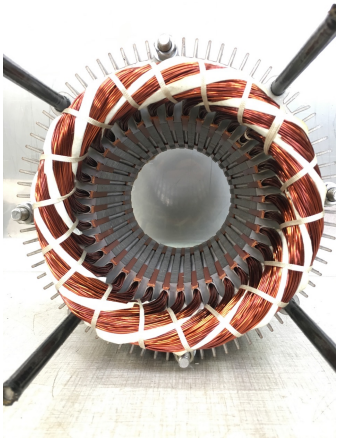

(f) Windings.

Figure 5.2: Stator core assembly.

5.2.3 Winding

Details regarding the stator winding configuration of the prototype motor will be presented in this section.

5.2.3.1 Three-phase connection

The motor was wound in such a manner that 6 coil ends were available. This allows for wye or delta three-phase winding configurations. For the developed prototype motor a wye winding configuration is implemented. Figure 5.3a indicates how the wire ends are labelled. Figure 5.3b shows wire connections with $L1, L2$ and $L3$ representing terminal connections To realize the wye configuration, wire ends 4, 5 and 6 are connected forming the neutral of the winding. Figure 5.3c displays a simplified diagram of the wye-configuration.

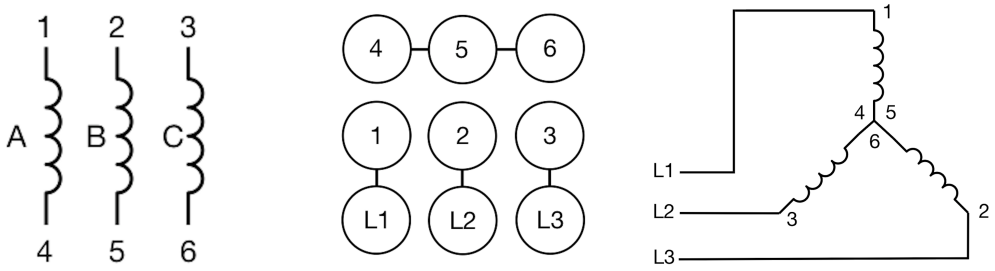

(a) Wire set-up. (b) Wire connections. (c) Wye connection.

Figure 5.3: Winding configuration.

5.2.3.2 Phase distribution

The winding phase distribution is given in Table 5.1. The table only represents half the stator due to symmetry. For the 3-phase, 4-pole, 36-slot traction motor a double-layer winding with a coil pitch of 8 was used. In addition, 34 conductors per slot were used to reach the required fill factor of 37.4%.

Table 5.1: Phase distribution of stator windings.

Slot	1	2	3	4	5	6	7	8	9	10	11	12	13	14	15	16	17	18	19/1
Top	A	A	A	-C	-C-	-C	B	B	B	-A	-A	-A	C	C	C	-B	-B	-B	A
Bottom	A	A	-C	-C	-C	B	B	B	-A	-A	-A	C	C	C	-B	-B	-B	A	A

5.2.3.3 Phase resistance

To ensure that the three phases are balanced, the stator phase resistance should be identical or reasonably close to calculated values in ANSYS RMxprt. The analytically calculated stator phase resistance across terminals from ANSYS RMxprt is $R_1 = 1.98\,\Omega$. A DC test was completed to measure each phase resistance respectively. The terminal resistance across each phase is given in Table 5.2.

Table 5.2: Winding phase terminal resistances.

Phase A	Phase B	Phase C
2.030 Ω	1.998 Ω	1.953 Ω

From Table 5.2 it can be seen that the stator phase resistances are reasonably close to the target resistance with an average value of $R_1 = 1.99\,\Omega$ as mentioned in Table 4.8. Thus, the windings are deemed correct and balanced.

5.2.4 Rotor core

The construction of the rotor core is presented in Figure 5.4. Similar to the stator, the rotor construction started by creating a jig to keep the shaft upright for stacking purposes as seen in Figure 5.4a. With the shaft upright a shaft-spacer was inserted before the stacking commenced. Once the stacking was completed, the stack was compressed with the addition of a second shaft spacer and a circlip. The rotor bars were carefully inserted into the stack as seen in Figure 5.4c with an end ring inserted and aligned below the stack. With the first end ring already in position and all the rotor bars inserted, the second end ring was pressed onto the bars to complete the rotor core assembly as seen in Figures 5.4d and 5.4e. The rotor core was then placed on a lathe as seen in Figure 5.2f to ensure complete alignment of end rings for balanced centrifugal forces. The end rings were then welded to the rotor bars to ensure conductivity and rigidity. Finally, the rotor was placed inside the stator and positioned between the two outer end plates.

5.2.5 Rotor and stator assembly

The final phase of the prototype motor assembly commenced with press-fitting the bearings onto either end of the shaft where-after the rotor was placed inside the stator. Bushings were placed over the outer rods which extends from the stator. The outer end plates were aligned with the four extending outer rods and shaft at either end of the motor, where-after it was tightly bolted compressing the core. The complete prototype motor assembly can be seen in Figure 5.5.

5.3 Deflection analysis

For experimental testing of the traction motor where only either end of the motor is bolted to a vertical frame, deflection becomes extremely important due to the small air-gap length of 0.65 mm. Any deflection that would result in a non-uniform air-gap length would hamper with machine operation. To ensure smooth motor operation, strong materials and an inherent rigid design

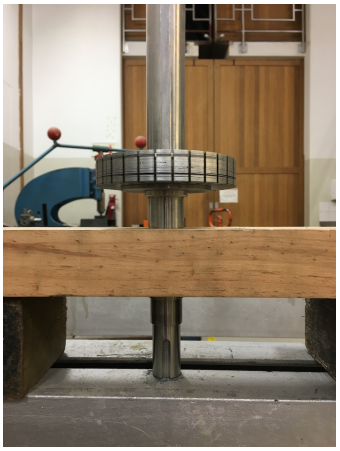

(a) Jig.

(b) Stacking.

(c) Bars.

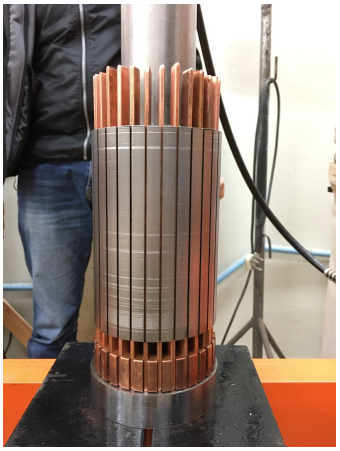

(d) End Ring.

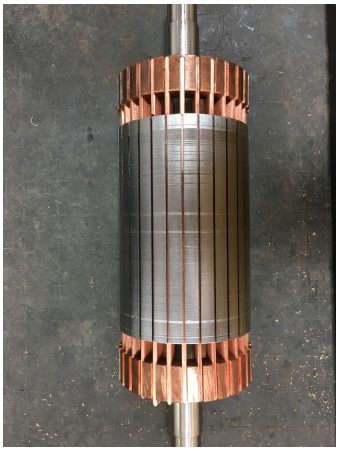

(e) Rotor.

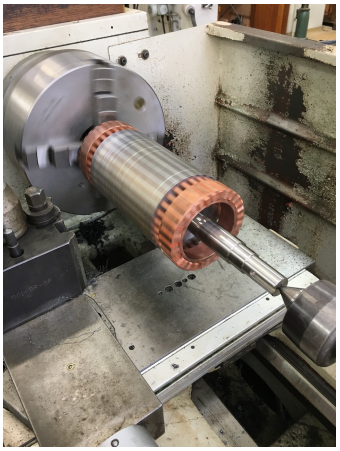

(f) Turned.

Figure 5.4: Rotor core assembly.

was implemented. A deflection test was completed to verify the design. The weight of the motor alone is 32 kg, with a total assembly weight of 43.3 kg. For this analysis, the total assembly weight was considered. To compensate for the stator windings which were not included in the Autocad model, an external point force was added to compensate for the reduction of 5 kg in total weight.

The stress analysis reveals a deflection in the vertical direction in the centre of the stack of approximately 0.02 mm. The biggest displacement of 0.03 mm is naturally furthest away from the mounting plate. This analysis verifies an acceptable design regarding mechanical rigidity for vertical mountings.

5.4 Fin experimental set-up

The available space around the circumference of the stator made heat transfer fins an interesting addition to the project. The fin length was restricted in

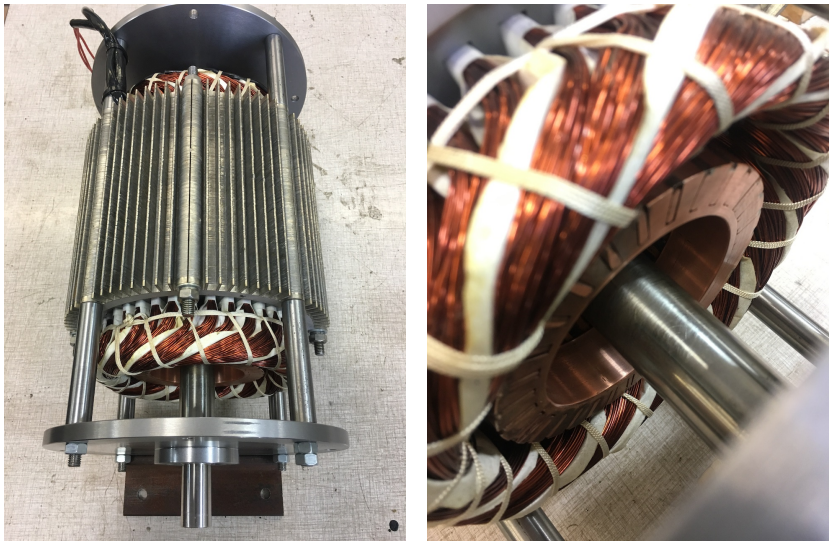

(a) General view of assembly. (b) Close-up view of assembly.

Figure 5.5: Complete prototype assembly.

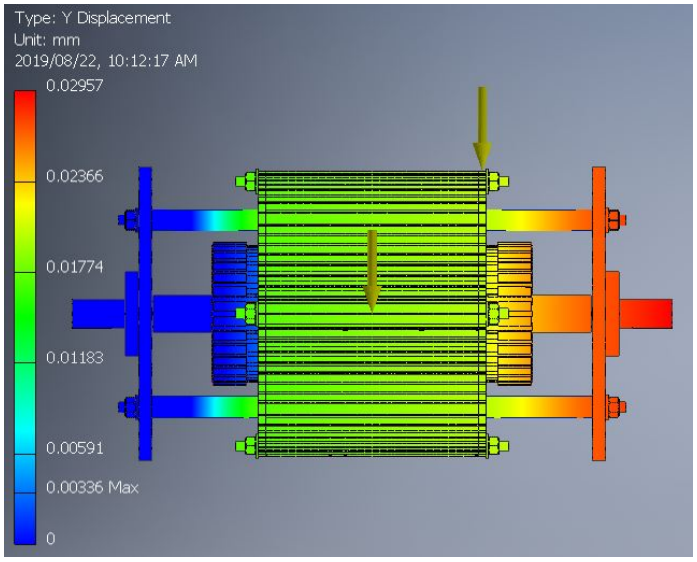

Figure 5.6: Rigidity test of motor assembly.

a radial direction to be within the outer circumference of the axial core rod slots. This allowed the addition of heat transfer fins at no additional manufacturing cost. The minimum thickness was chosen to ensure stiffness of the fin. This avoided the deformation of a fin under compression of the core rods. It should be noted that there was no formal optimization completed to achieve an optimal fin shape due to being beyond the scope of the work.

5.4.1 Fin performance calculation

Similar to Ohm's law, electrical circuits can be used as an analogy for heat transfer calculations. The temperature at any point in a thermal circuit represents the electrical voltage, heat flow is represented by current and thermal resistance by resistors [26]. The heat transfer calculation was simplified by taking the Matlab analytical model's estimated winding temperature of 80 °C, ambient temperature of 40 °C and creating a thermal circuit between the two temperatures in a radial direction as seen in Figure 5.7.

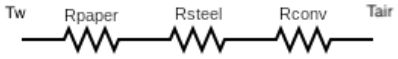

Figure 5.7: Simplified thermal circuit.

With T_w and T_{air} representing the winding and ambient air temperatures respectively. The heat transfer characteristics can be determined once the thermal resistances are known. The detailed results can be viewed in Appendix E. The Nomex paper thermal resistance R_{paper}, steel thermal resistance R_{steel} and convectional thermal resistance R_{conv} are calculated as follows:

$$R_{paper} = \frac{l_p}{k_p A_p} \tag{5.1}$$

$$R_{steel} = \frac{l_s}{k_s A_s} \tag{5.2}$$

$$R_{conv} = \frac{1}{h_{air} A_{sur}} \tag{5.3}$$

where variables $l_{p,s}$ represent the radial length through which heat is transferred per material, $k_{p,s}$ represent the thermal conductivity coefficients per material, $A_{p,s,sur}$ the cross sectional area through which heat is transferred and h_{air} is the convectional heat transfer coefficient. The initial rate of heat transfer from the windings to the ambient air was calculated as:

$$\dot{Q}_1 = \frac{T_w - T_{air}}{R_{paper} + R_{steel} + R_{conv}} = 37.0 \text{ W} \tag{5.4}$$

Seeing that the rate of heat transfer is constant, the temperature at the stator surface T_{sur} can be calculated with:

$$T_{sur} = \dot{Q}_1 R_{conv} + T_{air} = 78.7\,^{\circ}\text{C} \tag{5.5}$$

As can be seen from Eq. (5.5), the reduction in heat from the winding to the stator surface is not significant. For enhanced heat transfer, the model was

designed as a frame-less machine with a finned outer surface. A detailed view of the fin dimensions can be seen in Fig. 5.8.

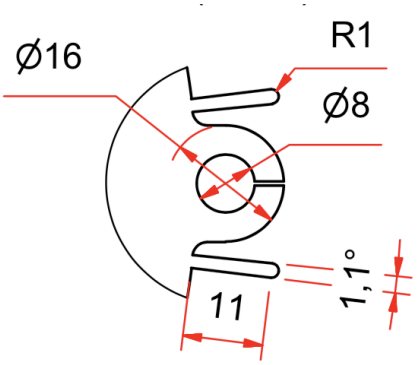

Figure 5.8: Added fins on stator surface.

To determine the heat transfer efficiency of the proposed fin design, the following calculations were made:

$$m = \sqrt{\frac{2h}{k_s t}} \tag{5.6}$$

with m being a fin shape-specific variable, h the height of the fin and t representing the thickness of the fin. After assuming convection from the fin tip, the equivalent fin length l_c with an insulated tip is calculated with:

$$l_c = l + t/2 \tag{5.7}$$

where l is the actual fin length and t is the fin thickness. Finally, the fin efficiency can be calculated as:

$$\eta_{fin} = \frac{tanh(ml_c)}{ml_c} = 99\,\% \tag{5.8}$$

With a fin efficiency of 99 % and a reasonable number of $n_{fin} = 64$ evenly distributed fins, the fin effectiveness can be calculated as follows:

$$\varepsilon_{fin} = \frac{A_{unfin} + \eta_{fin} A_{fin}}{A_{nofin}} = 3.34 \tag{5.9}$$

where A_{unfin} is the total surface area between fins, A_{fin} is the total surface area of fins and A_{nofin} is the original total stator outer surface area without added fins. From Eq. (5.9) it was calculated that the total outer surface area was increased by a factor of 3.34. Finally, the increased heat transfer from the stator surface through the fins to the ambient air can be calculated with:

$$\dot{Q}_2 = \eta_{fin} h_{air} A_{fin} n_{fin} (T_{sur} - T_{air}) = 94.4 \text{ W} \tag{5.10}$$

Therefore, it can be inferred that the addition of the fins significantly increases the heat dissipation and cooling of the traction motor.

5.5 Equivalent circuit parameters

The equivalent circuit parameters were measured and calculated after no-load and locked-rotor tests performed. The no-load test was completed at rated frequency, while the breakdown torque measurements were taken at 50 Hz. The effect testing at 50 Hz has on equivalent circuit reactance parameters are accounted for by including a ratio of f_{rated}/f_{test} into related calculations. A diagram representing the set-up for both the experiments can be viewed in Figure 5.9. The two-watt-meter method was used to measure three-phase input power. A Voltmeter was connected between two phases and an ammeter was connected to a phase. Flanges were bolted on the outer end plates of the prototype motor where after the motor was bolted on a test bench. For the locked-rotor test, a wrench was tightly clamped against the shaft to ensure zero rotation. The measurements of the no-load and locked-rotor tests are presented in Table 5.3.

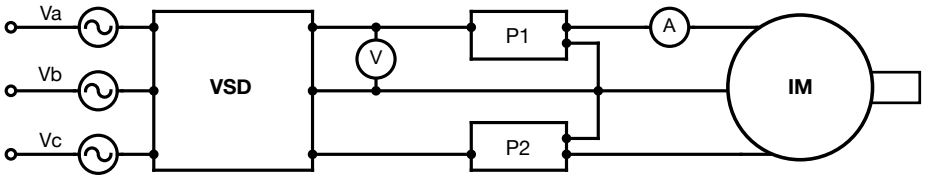

Figure 5.9: Set-up for equivalent circuit parameter measurements.

Table 5.3: No-load and locked-rotor measurements.

Parameter	No-Load	Locked-Rotor
V_L [V]	380	90
I_L [A]	5.2	7.55
P1 [W]	-720	40
P2 [W]	1000	600
P_{in} [W]	280	640

5.5.1 Calculation of equivalent circuit parameters

From the measurements taken in Table 5.3, the circuit parameters can be calculated as follows:

$$V\phi_{nl} = \frac{V_L}{\sqrt{3}} \tag{5.11}$$

with $V\phi_{nl}$ being the phase no-load voltage and V_L the measured line to line voltage. The no-load impedance can now be calculated as follows:

$$|Z_{nl}| = \frac{V\phi_{nl}}{I_L} \tag{5.12}$$

$$= X_m + X_1 \tag{5.13}$$

When X_1 is calculated from the locked-rotor measurements, X_m can be calculated. The locked-rotor impedance is calculated with:

$$|Z_{lr}| = \frac{V\phi_{lr}}{I_L} \tag{5.14}$$

$$= \frac{V_L}{\sqrt{3}I_L} \tag{5.15}$$

with $V\phi_{lr}$ being the locked-rotor phase voltage. The power factor angle can be calculated with:

$$\theta = cos^{-1}\frac{P_{in}}{\sqrt{3}V_L I_L} \tag{5.16}$$

The locked-rotor resistance can be calculated as follow:

$$R_{lr} = |Z_{lr}|cos\theta \tag{5.17}$$

$$= R_1 + R_2 \tag{5.18}$$

Thus, with R_1 known, R_2 can easily be calculated. Due to the test being conducted at 50 Hz and the rated frequency being 34.7 Hz the frequency ratio will be implemented in the formula as follows:

$$X_{lr} = \frac{f_{rated}}{f_{test}} \cdot |Z_{lr}|sin\theta \tag{5.19}$$

$$= X_1 + X_2 \tag{5.20}$$

5.5.2 Results

A relationship exists between how X_{lr} is divided between X_1 and X_2 according to the rotor design. For the prototype motor X_{lr} is divided as $0.35X_1$ and $0.65X_2$. The chosen reactance ratio is an average between the National Electrical Manufacturers Association (NEMA) class B and class C rotor designs. These two classes were most similar to that of the prototype motor rotor slots. These results, as well as the calculated values from ANSYS RMxprt and the Danfoss VSD are presented in Table 5.4. It can be seen that all three sets of circuit parameters are in good agreement. The leakage inductance of the Danfoss VSD measurements are slightly higher and will have a negative influence on the expected breakdown torque. This difference in leakage reactance can be due to the method in which the Danfoss VSD determines the circuit parameters.

Table 5.4: Circuit parameter comparison.

Parameter	RMxprt	Danfoss	Measured
R1 [Ω]	1.98	2.26	1.99
X1 [Ω]	1.50	2.84	1.41
R2 [Ω]	1.57	1.87	1.80
X2 [Ω]	2.75	3.42	2.61
Xm [Ω]	40.25	40.51	40.53

5.5.3 Estimated torque production

From the measured circuit parameters, the estimated torque-speed characteristics can easily be determined once the primary side of the equivalent circuit is converted to the Thevenin equivalent circuit as seen in Figure 5.10.

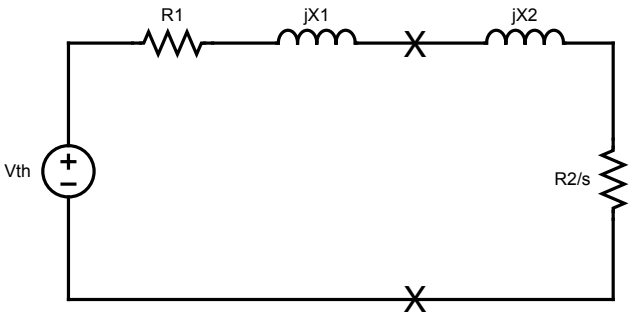

Figure 5.10: Thevenin equivalent circuit.

The conversion and torque calculation can be completed as follows:

$$V_{th} = V_{\phi}\frac{X_m}{\sqrt{R_1^2 + (X_1 + X_m)^2}} \tag{5.21}$$

where V_{th} is the Thevenin voltage. The Thevenin impedance can be calculated as:

$$Z_{th} = \frac{jX_m(R_1 + jX_1)}{R_1 + j(X_1 + X_m)} \tag{5.22}$$

$$= R_{th} + jX_{th} \tag{5.23}$$

with R_{th} and X_{th} being the real and imaginary components of Z_{th} respectively. The produced torque at specific slip can be calculated with:

$$T_{ind} = \frac{3V_{th}\frac{R_2}{s}}{\omega_{sync}[(R_{th} + \frac{R_2}{s})^2 + (X_{th} + X_2)^2]} \tag{5.24}$$

From Eq. (5.24) the torque-speed curves were calculated for the circuit parameters as measured in Table 5.4. The results are presented in Figure 5.11. The torque-speed curve is very sensitive to changes in rotor resistance R_2 and rotor reactance X_2. For example:

- A decrease in R_2 shifts the torque-speed curve towards the right (maximum speed) reducing the starting torque while keeping the breakdown torque constant.
- An increase in R_2 shifts the torque-speed curve towards the left (zero speed) increasing the starting torque while keeping the breakdown torque constant.
- An increase in X_2 shifts the entire torque-speed curve downward, reducing starting and breakdown torque by roughly the same magnitude.
- A decrease in X_2 shifts the entire torque-speed curve upward, increasing starting and breakdown torque by roughly the same magnitude.

When combing changes for both these variables in addition to stator side parameters in the torque-speed equation, breakdown torque at different speeds is possible. Although all three sets of circuit parameters are similar, their respective effect on the torque-speed curve will be of notice. At rated speed the output torque is identical for all sets of measurements. The breakdown torque is similar for the ANSYS RMxprt and the measured circuit parameters. As expected, the breakdown torque of the Danfoss measured circuit parameters are lower due to the higher measured leakage inductances.

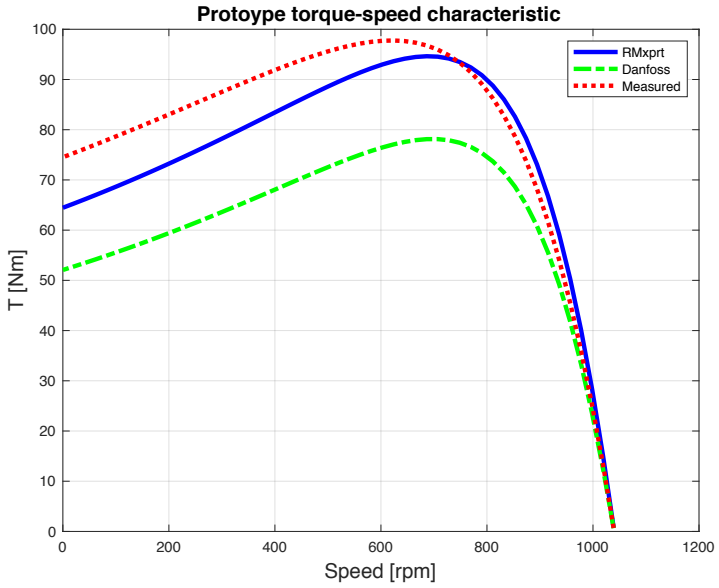

Figure 5.11: Estimated torque production from circuit parameters.

5.6 Experimental set-up and test procedures

A diagram representing the the test bench set-up can be viewed in Figure 5.12. The set-up is similar to that of the no-load and locked-rotor configuration. Two additional ammeters where added to measure the remaining phase currents. A torque sensor is connected between the shaft of the IM and a dynamometer load cell which will serve as the load. The load of the dynamometer can be adjusted with the aid of a DC current source. Additionally, the dynamometer is connected to a DC motor. From this test set-up, the following tests will be completed:

1. Load tests between 500 rpm and 3000 rpm with 500 rpm increments between measurements. The measurements taken at each increment will give insight regarding the power and torque characteristics. With the output torque, output power and speed given by the torque sensor, input power, phase currents and line to line voltage will be measured with instrumentation as depicted in Figure 5.12a. With the input and output power known, efficiency and PF can be calculated with the following equations respectively:

$$\eta_f = \frac{P_{out}}{P_{in}} \tag{5.25}$$

$$PF = \frac{P_{in}}{\sqrt{3}V_L I_{avg}} \tag{5.26}$$

2. Externally driven test between 500 rpm and 3000 rpm with 500 rpm increments between measurements. For this test the IM will be disconnected

from a power source and be driven through the DC motor. This allows the measurement of mechanical losses, which is the only form of energy dissipated, through the torque sensor.

3. Breakdown torque measurement test. The measurements will be at a fixed frequency and voltage, from where the load of the dynamo will gradually be increased until the breakdown torque is reached. The torque sensor will be used to record the breakdown torque measurements.

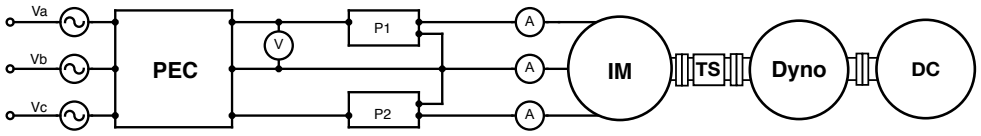

(a) Test set-up diagram.

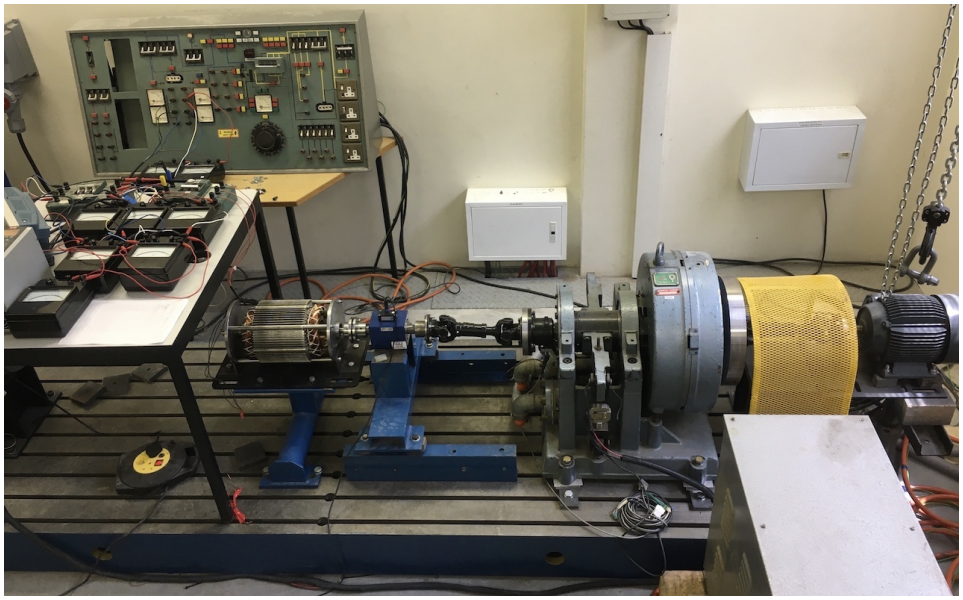

(b) Actual test set-up.

Figure 5.12: Test bench set-up for prototype motor.

5.7 Test results

The measurements of the various tests as mentioned in Section 5.6 will be presented in this section.

5.7.1 Load tests

The output torque, power and speed measured by the torque sensor during each speed increment can be seen in Figure 5.13. The sampling period during the measurements were different, therefore, the torque ripple will be more evident during shorter samples. The electrical measurements, as well as the performance of the traction motor is grouped in Table 5.5. It should be noted that each performance characteristic presented in Table 5.5 is the average value measured during test samples. An oscilloscope was used to measure the sinusoidal output voltage and current from the PEC. A FFT was completed for the current signal to investigate harmonic content. As expected, there were 3^{rd} and 5^{th} order harmonics visible at speeds of 1500 rpm and above. The frequency domain of the supplied current at each measurement is visible in Figure 5.14. The original oscilloscope measured signals are given in Appendix F. For each measurement, the fundamental frequency was close to the expected supply frequency.

Further, for maximum speed, the measurements were taken at 2909.25 rpm. This was due to excessive vibrations which led to inaccurate readings at higher speeds. These vibrations could possibly be the result of a slightly unbalanced rotor, rigidity of the design or a resonant frequency being entered. This measurement speed is within 3 % of the desired 3000 rpm and deemed expectable.

Table 5.5: Full-load test measurements.

Increment [rpm]	500	1000	1500	2000	2500	3000
Speed [rpm]	506.11	1002.74	1502.99	1998.74	2485.15	2909.25
P_{out} [kW]	1.60	3.05	3.07	2.89	3.12	3.12
T_{out} [Nm]	30.18	29.00	19.54	13.81	12.01	10.25
Efficiency [%]	71.52	81.41	80.92	80.31	73.68	58.75
Power factor [%]	79.67	74.19	81.02	81.25	89.55	83.80
V_L [V]	210.00	380.00	400.00	408.00	408.00	408.00
I_a [A]	7.60	7.60	6.80	6.20	6.70	7.50
I_b [A]	7.90	7.90	6.90	6.30	6.90	7.50
I_c [A]	7.70	7.50	6.60	6.30	6.50	7.30
I_{avg} [A]	7.73	7.67	6.77	6.27	6.70	7.43
P1 [kW]	1.60	2.74	2.60	2.44	2.64	3.04
P2 [kW]	0.64	1.00	1.20	1.16	1.60	1.36
P_{in} [kW]	2.24	3.74	3.80	3.60	4.24	4.40
I_{dyno} [A]	1.88	1.68	1.17	0.92	0.83	0.78
V_{dyno} [V]	5.40	4.90	3.30	2.50	2.40	2.30

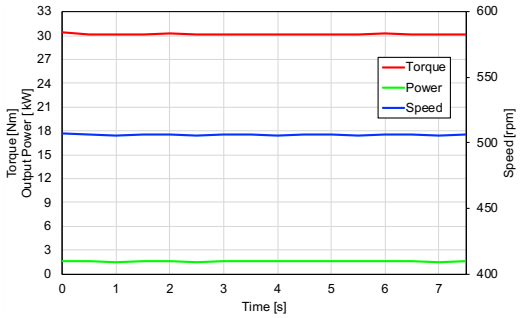

(a) 500 rpm.

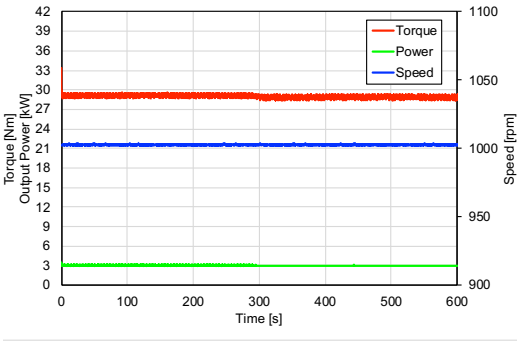

(b) 1000 rpm.

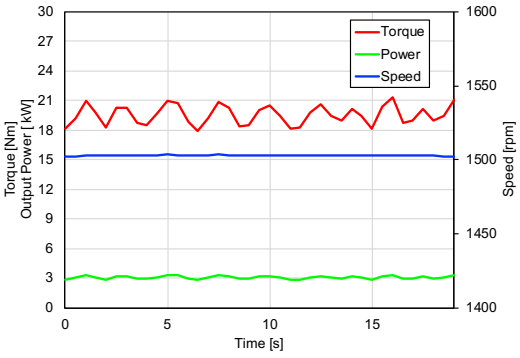

(c) 1500 rpm.

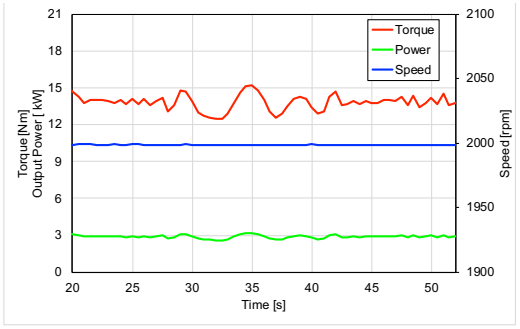

(d) 2000 rpm.

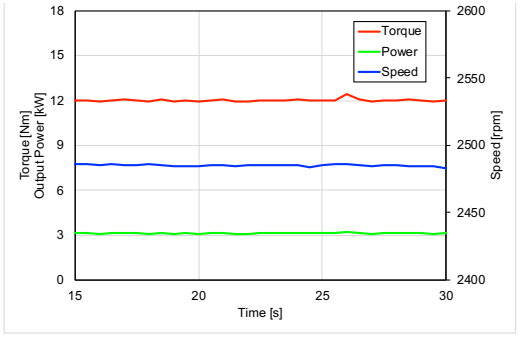

(e) 2500 rpm.

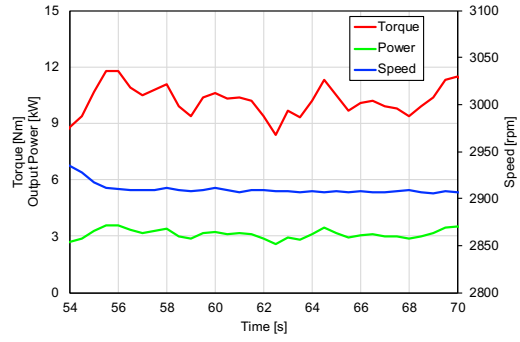

(f) 3000 rpm.

Figure 5.13: Torque sensor measurements during rated load tests at various speeds.

5.7.2 Power and torque characteristics

From the measurements recorded in Table 5.5, it was possible to plot discrete points over power-speed and torque speed curves generated in ANSYS RMxprt in Sections 4.14 and 4.12. This comparison between analytical and measured performance is presented in Figure 5.15. From the figure, it can be seen that the discrete points fit the expected curves reasonably well throughout the flux weakening range. The stable measurement taken at 2909.3 rpm was within 2 % of the maximum predicted speed of 2961.2 rpm.

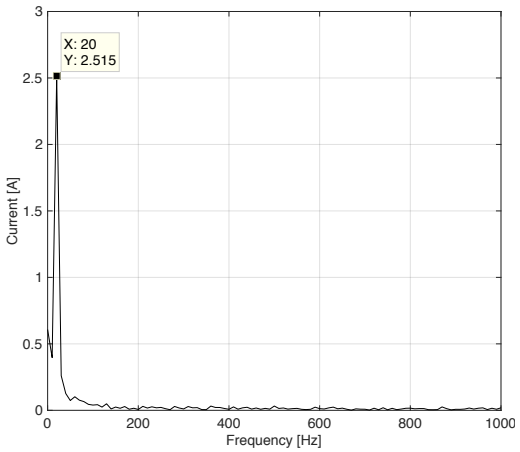

(a) 500 rpm.

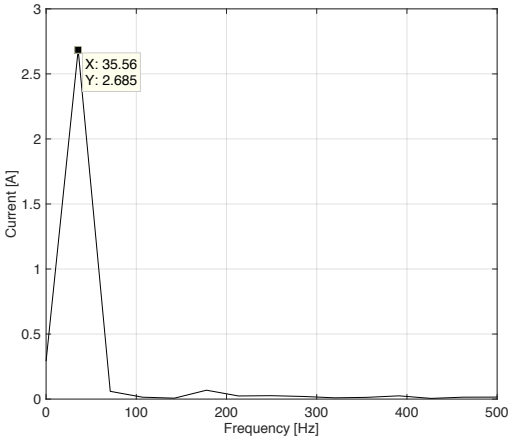

(b) 1000 rpm.

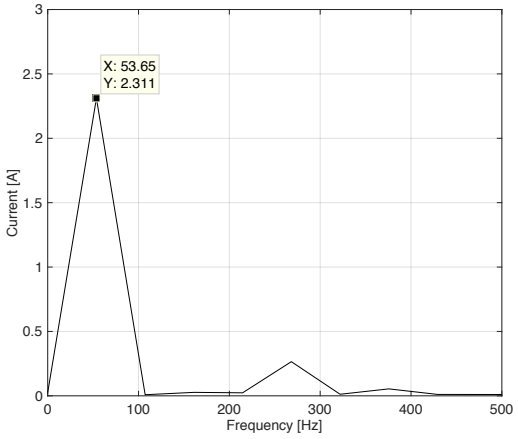

(c) 1500 rpm.

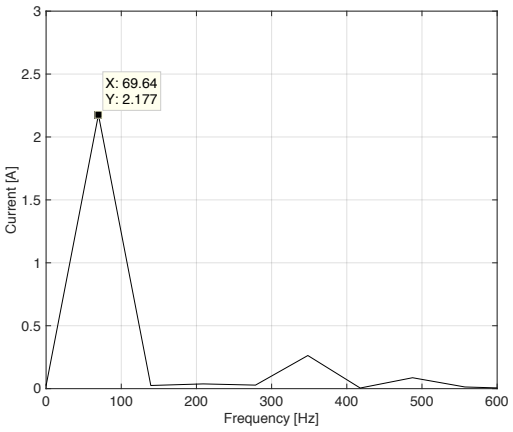

(d) 2000 rpm.

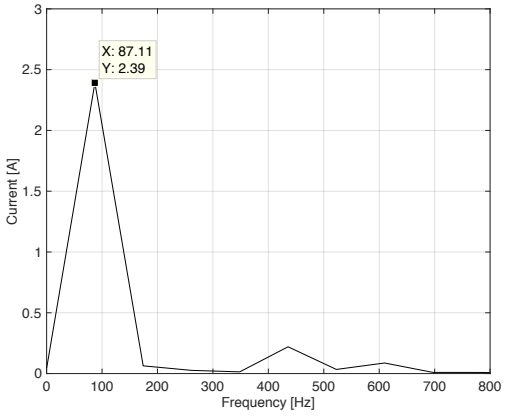

(e) 2500 rpm.

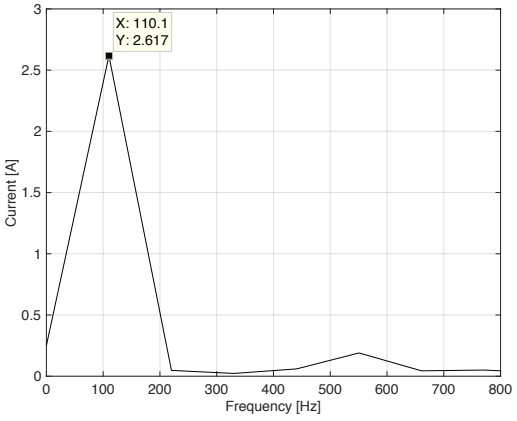

(f) 3000 rpm.

Figure 5.14: Fast Fourier transformations of supplied current through PEC at various speeds.

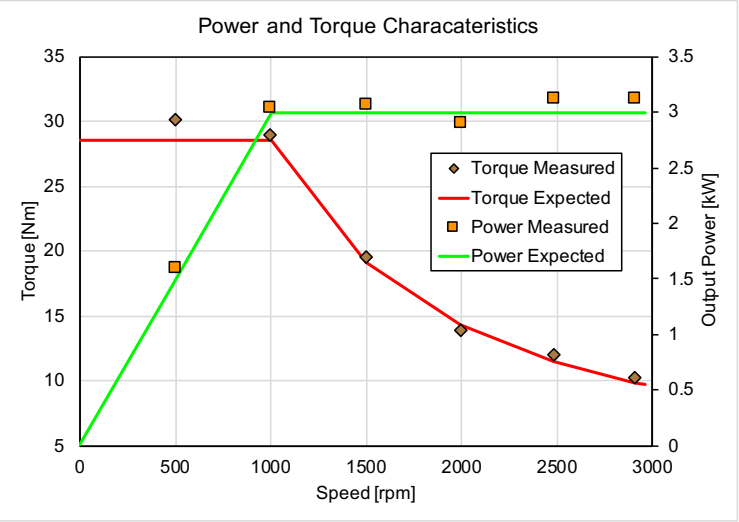

Figure 5.15: Power and torque characteristics during the flux weakening range.

5.7.3 Mechanical losses

The electrical measurements in Table 5.3 taken during the no-load test gave insight of the stator-copper-losses, as well as the rotational losses. With the input power known, the stator copper losses and rotational losses can be determined. The mechanical loss measurements taken during the externally driven tests are presented in Figure 5.16. From the figure it can be seen that the mechanical loss P_{mech} at rated speed is approximately 70 W. With rotational and mechanical losses known, the core loss at rated speed could be determined. This is summarized in Table 5.6. The predicted ANSYS RMxprt no-load core loss and rated speed core loss values are 56.7 W and 51.3 W respectively. The measured value of 46.7 W is reasonably close to the expected values.

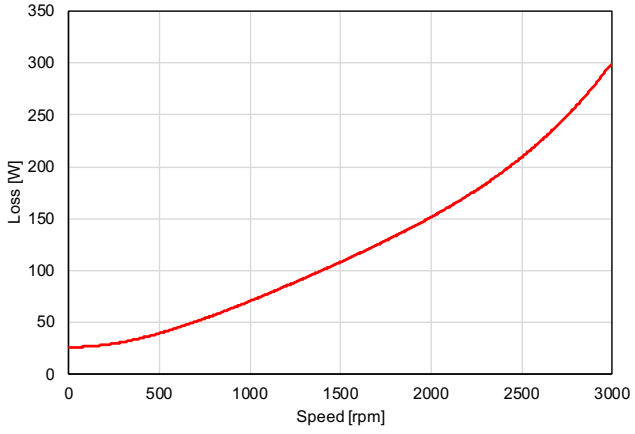

Figure 5.16: Measured mechanical losses.

Table 5.6: Calculation of core loss at rated speed.

No-load	Equation	Value
P_{in}	P1 + P2	280.0 W
P_{scl}	$3I^2R_1$	163.3 W
P_{rot}	P_{in} - P_{scl}	116.7
Mechanical losses	Equation	Value
P_{core}	P_{rot} - P_{mech}	46.7 W

5.7.4 Breakdown torque

The breakdown torque measurement is important to verify with FEM predicted values. According to ANSYS RMxprt, the phase current required for a rated frequency of 34.7 Hz at breakdown torque is 31.1 A. This exceeds the maximum output current from the Danfoss VSD. To overcome this, the prototype motor was connected to the grid. As a result, the motor could be applied with the required current at 380 V, but at a frequency of 50 Hz. This implies the achievable breakdown torque is now 52.75 Nm. The measured results compared with discrete Maxwell 2D torque values can be seen in Figure 5.17.

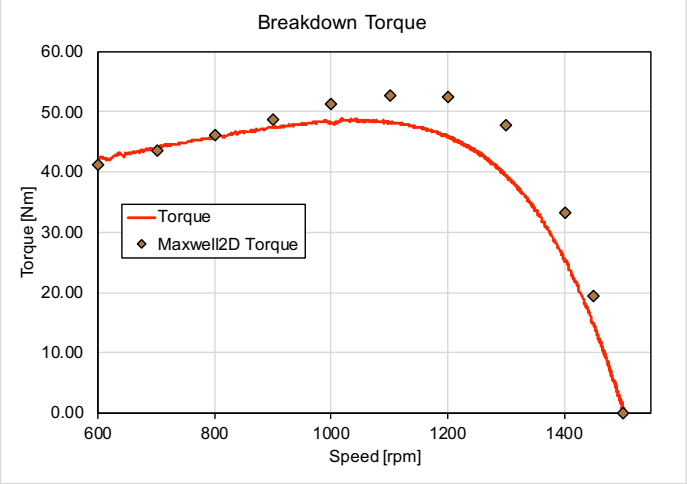

Figure 5.17: Breakdown torque measurement.

The maximum measured breakdown toque achieved is 48.70 Nm, which is approximately 10 % less than the expected value. This is satisfactory and further validates the expected motor performance.

5.8 FEM comparison

A comparison at rated speed and maximum speed between Maxwell 2D results and the measured results of the prototype motor is given in Table 5.7.

Table 5.7: Comparison between FEM model and measured performance of prototype motor.

Characteristic at 1000 rpm	Maxwell 2D	Measured	Difference
Output power [kW]	3.01	3.05	1.67 %
Efficiency %	84.90	81.41	-3.49 %
Power factor %	74.06	74.19	0.13 %
Output torque [Nm]	28.70	29.00	1.05 %
Characteristic at 2909.3 rpm	**Maxwell 2D**	**Measured**	**Difference**
Output power [kW]	3.12	3.12	0 %
Output torque [Nm]	10.24	10.25	< 0.01 %

Since the maximum speed measurement taken at 2909.3 rpm within the CPSR, the Maxwell 2D simulation was completed at the same speed. From Table 5.7 it can be concluded that the prototype motor performed as expected, which is an indication of a well designed motor.

5.9 Test summary

The Chapter documented the mechanical design, construction and testing procedures of the prototype motor. The assembly process of both the stator and rotor was given in detail. A deflection analysis was completed within Autocad Inventor and confirmed that the motor could be vertically mounted for test procedures. An experimental fin set-up was discussed which mathematically increased heat dissipation by approximately 100 W.

For the testing, the measured equivalent circuit parameters were similar to that of ANSYS RMxprt. Load tests were conducted discretely at 500 rpm increments. The measurements matched the expected torque-speed and power-speed curves from ANSYS RMxprt. At rated speed, measured performance was very similar to that of Maxwell 2D. For maximum speed measurements, performance were reasonably close to expected performance and deemed satisfactory. Measured core losses were similar to expected losses from ANSYS RMxprt. Further, the breakdown torque test could only be completed at 50 Hz, but was within 10 % of the expected value of Maxwell 2D. Finally, FEM comparisons were made within Maxwell 2D at rated and maximum speed. From

all the tests completed throughout this Chapter it can be concluded that the motor performed as expected and thus validated the estimations of ANSYS RMxprt and Maxwell 2D.

Chapter 6

Design of a large prototype motor

6.1 Introduction

Leading up to this chapter, a design approach was developed and implemented in the design of a 3 kW prototype traction motor. The measured performance compare reasonably well to the predicted results. The aim of this chapter is to test the effectiveness of this design approach for a large traction motor for locomotive applications. Additionally, an adapted version of the design strategy that incorporates voltage management will be tested.

6.2 Specifications

The design specifications for the larger traction motor are listed as follows:

- Rated power: $P_n = 500$ kW;
- Base speed: $n_b = 1500$ rpm;
- Line supply voltage: $V_l = 3300$ V;
- Number of phases: $m = 3$;
- Phase connection: wye;
- Target power factor: PF $= 0.85$;
- Target efficiency: $\eta_n \geq 0.90$ and;
- Constant power speed range of $\geq= 3.0$.

6.3 Initial design

Similar to Chapter 3, the analytical model was used, but slightly adjusted to generate an initial design for optimization. The detailed results can be viewed

in Appendix A.2. For this section, an initial design with its performance will be given, as well as electric and magnetic loading values towards the end.

6.3.1 Chosen slot and winding configuration

The slot and winding details for both the rotor and the stator are given in Table 6.1. With a required CPSR of 3, the maximum speed is thus 4500 rpm. Typically, traction induction motors have 2 - 4 pole-pairs. For simplicity, the same pole and slot combinations of the 3 kW induction motor are used for the large traction motor design study. With this slot combination the effect of torque ripple and noisy operation is mitigated. This was verified with the testing of the prototype motor. Double layer windings were used with a fractional winding factor of 8/9 to reduce harmonic distortion and high frequency losses.

Table 6.1: Stator and rotor slot information.

Stator	Value
Slots	36
Connection	Wye
Phases	3
Poles	4
Slots/pole/phase	3
Winding layers	2
Winding pitch	8
Type of winding	Form wound
Rotor	**Value**
Slots	30
Type of winding	Squirrel cage

With rectangular open stator slots, form-wound coils can be used for increased fill factor and uniform temperature distribution. The implemented stator and rotor slots, as well as their defining variables are shown in Figure 6.1.

6.3.2 Initial set of geometrical dimensions

The initial design geometry produced by the analytical model is given in Table 6.2. These are the required variables for optimization in the following section. The initial design is visually represented in Figure 6.2.

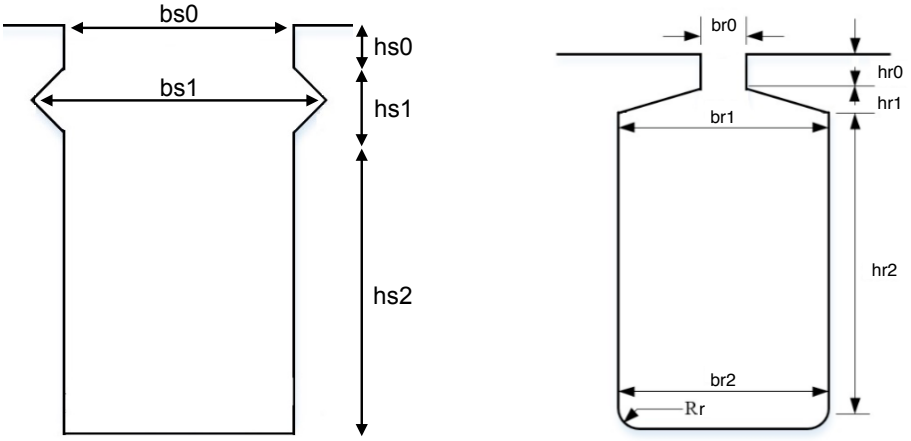

(a) Stator slot

(b) Rotor slot

Figure 6.1: Defining variables of stator and rotor slots for the 500 kW motor.

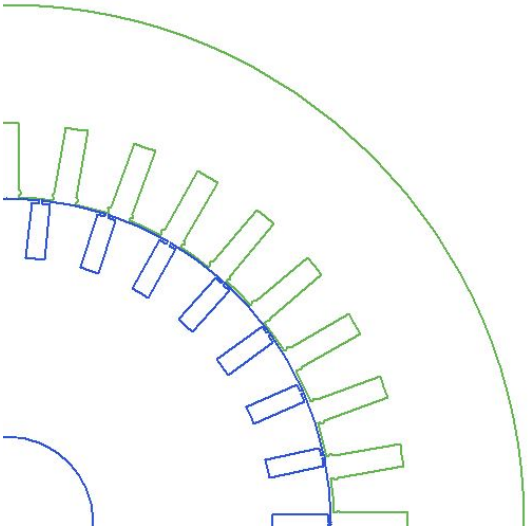

Figure 6.2: Initial design generated through analytical model.

6.3.3 Performance

The traction motor was designed for a rated power of 500 kW at 1500 rpm. The generated Matlab model was simulated within ANSYS RMxprt for verification. The original and verified results are compared to target performance specifications in Table 6.3. The analytical model was developed for low to medium voltage induction motors with random wound coils. Therefore, there exists minor discrepancies for leakage inductance calculations between results. However, the verified performance within ANSYS RMxprt proved that the design satisfied all target performance specifications. The torque-speed and power-speed curves of the initial design can be viewed in Figure 6.3, which

Table 6.2: Initial set of geometrical dimensions for the large traction motor.

General	Description	Value [mm]
L	Stack length	488.1
g	Air-gap length	1.1
D_{shaft}	Shaft diameter	110.0
Stator	**Description**	**Value [mm]**
D_{out}	Outer diameter	657.6
D_{is}	Inner diameter	414.3
h_{s0}	Slot opening height	1.0
h_{s1}	Wedge height	3.0
h_{s2}	Slot height	42.8
b_{s0}	Slot width	14.3
b_{s1}	Wedge width	17.1
h_{cs}	Yoke height	68.3
Rotor	**Description**	**Value [mm]**
h_{r0}	Rotor slot opening height	2.0
h_{r2}	Slot height	35.3
b_{r0}	Slot opening width	2.0
b_{r1}	Slot upper width	11.8
b_{r2}	Slot lower width	11.8
h_{cr}	Yoke height	113.8
l_{er}	End bar length	38.9
b_{er}	End ring width	35.7
h_{er}	End ring height	37.2

shows a CPSR of only 2 is achieved and thus, the motor enters the slip-limited region after 3000 rpm. Therefore, the breakdown torque can be optimized for further improvements.

Table 6.3: Comparison between target and achieved specifications.

Characteristic	Target	RMxprt	Matlab
Power [kW]	500	500	500
Efficiency [%]	90.00	95.6	94.6
Power factor [%]	85.00	91.2	81.0
Breakdown/Rated Torque ratio	3.00	3.3	1.3

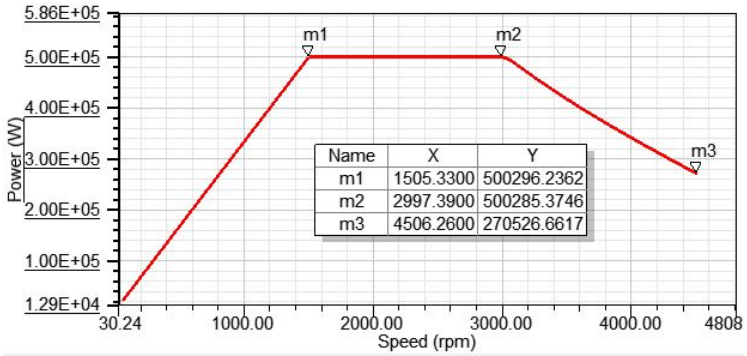

(a) Power-speed curve.

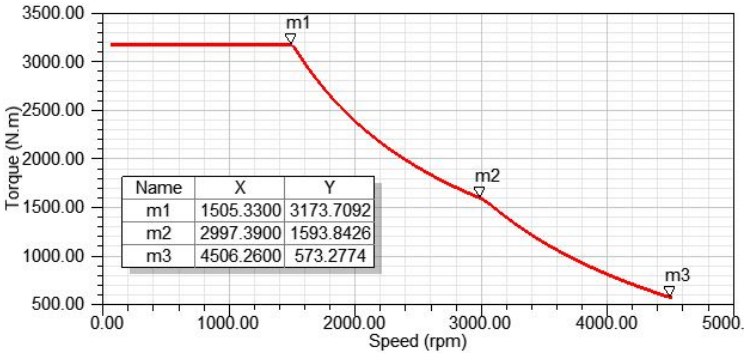

(b) Torque-speed curve.

Figure 6.3: CPSR of initial design.

6.3.4 Electric and magnetic loading

Table 6.4 gives a rough indication of the electric and magnetic loading values generated though the analytical model. These values were initially assumed, but iteratively adjusted until stator tooth and rotor tooth MMF values converged. All the design values are within the recommend ranges as discussed in Sections 2.6.6 and 2.6.7.

6.4 Optimization

The optimization formulation for the large traction motor is discussed with the associated constraints and boundaries in this section.

6.4.1 Optimization formulation

Similar slot sizing constraints and variable mapping techniques as discussed in Sections 4.3.1 and 4.3.2 were used for the optimization of the large traction motor. However, with regards to variable mapping, the outer diameter of the

Table 6.4: Analytical model electrical and magnetic loading

Flux density [T]	Design value	Recommended
Stator teeth	1.3	1.4 - 2.1
Stator yoke	1.0	1.4 - 1.7
Air-gap	0.7	0.7 - 0.9
Rotor teeth	1.3	1.5 - 2.2
Rotor yoke	1.5	1.0 - 1.6
Current density [A/mm^2]	Design value	Recommended
Stator slot	5.0	< 6
Rotor bar	5.5	< 7

stator was not a fixed value. This allowed the stator outer diameter to be calculated as the sum of the radially defined variables. It should be noted that the shaft diameter, air-gap length and wedge height remained fixed. Variable mapping can be viewed in Table 6.5. In addition, the objective function for the optimization algorithm involves minimizing deviation from optimization constraints as discussed in Section 4.4 and is given by Eq. (4.6).

6.4.2 Optimization constraints

The constraints considered at a base speed of 1500 rpm for the design of the large traction motor:

$$P_{\text{out}} = 500\,\text{kW} \tag{6.1}$$

$$\eta \geq 90\,\% \tag{6.2}$$

$$\text{PF} \geq 85\,\% \tag{6.3}$$

$$\frac{T_{\text{bk}}}{T_{\text{n}}} \geq 3.0 \tag{6.4}$$

where P_{out} is the output power, η is the efficiency, PF is the power factor, T_{bk} is the breakdown torque and T_n is the rated torque.

6.4.3 Optimization boundaries

The boundaries of geometrical variables can be seen in Table 6.6. With only the shaft diameter, air-gap length, wedge height and wedge/slot width ratio being constants, the optimization had significantly more freedom than the optimization of the smaller 3 kW traction motor. The upper and lower boundary for each of the radially defined variables, as well as the stack length were chosen

Table 6.5: Geometric variable mapping of 500 kW traction motor.

Dimensions	Defining Variable(s)
Stack length	L
Air-gap length	g (Fixed)
Shaft diameter	D_{shaft} (Fixed)
Stator	**Defining Variable(s)**
Outer diameter	$D_{shaft} + 2(h_{cr} + h_{r2} + h_{r0} + g + h_{s0} + h_{s1} + h_{s2} + h_{cs})$
Inner diameter	$D_{shaft} + 2(h_{cr} + h_{r2} + h_{r0} + g)$
Slot opening height	h_{s0}
Slot height	h_{s2}
Wedge height	h_{s1} (Fixed)
Slot opening width	$k_{bs}b_{s1}$
Wedge width	$2\tan\left(\frac{\tau_{ts}}{2}\right)\left(\frac{D_{shaft}}{2} + h_{cr} + h_{r2} + h_{r0} + g + h_{s0}\right)$
Yoke height	h_{cs}
Rotor	**Defining Variable(s)**
Outer diameter	$D_{shaft} + 2(h_{cr} + h_{r2} + h_{r0})$
Slot opening height	h_{r0}
Slot height	h_{r2}
Slot opening width	$k_{br}b_{r2}$
Slot upper width	b_{r2}
Slot lower width	$2\tan\left(\frac{\tau_{tr}}{2}\right)\left(\frac{D_{shaft}}{2} + h_{cr}\right)$
Yoke height	h_{cr}

as 25 % of the original value. The only exception is for slot opening heights, which was set to 50 % of the original value. The width ratios were chosen from experience. Minimizing or maximizing width ratios result in invalid solutions.

6.5 Optimized design

This section contains details regarding the geometry and winding information of the optimized design. Figure 6.4 serves as a visual comparison between the original and optimized model. The optimized geometry variables are given in Table 6.7. The winding information is given in Table 6.8 and will be imported into Maxwell 2D for FEM verification of the design.

After viewing Table 6.7 it can be noted that the stack length increased significantly. This will increase the breakdown torque and improve the CPSR. In addition, the rotor slot opening width had a large increase. This will re-

Table 6.6: The Matlab generated set of geometrical dimensions with optimization boundaries.

General	Description	Lower [mm]	Initial [mm]	Upper [mm]
L	Stack length	366.1	488.1	610.1
g	Air-gap length	-	1.1	-
D_{shaft}	Shaft diameter	-	110.0	-
Stator	Description	Lower [mm]	Initial [mm]	Upper [mm]
h_{s0}	Slot opening height	0.5	1	1.5
h_{s1}	Wedge height	-	3	-
h_{s2}	Slot height	32.1	42.8	53.5
k_s	Pitch ratio	0.3	0.4	0.5
k_{bs}	Wedge width ratio	-	0.85	-
b_{s0}	Slot opening width	9.3	14.3	16.7
b_{s1}	Wedge width	10.9	17.1	19.6
h_{cs}	Yoke height	57.7	74.9	96.1
Rotor	Description	Lower [mm]	Initial [mm]	Upper [mm]
h_{r0}	Slot opening height	1.0	2.0	3.0
h_{r2}	Slot height	26.5	35.3	44.1
k_r	Pitch ratio	0.1	0.4	0.9
k_{br}	Slot width ratio	0.2	0.3	4
b_{r0}	Slot opening width	0.8	2.0	23.8
b_{r1}	Slot upper width	7.1	11.8	14.1
b_{r2}	Slot lower width	7.1	11.8	14.1
h_{cr}	Yoke height	85.4	113.8.0	142.3

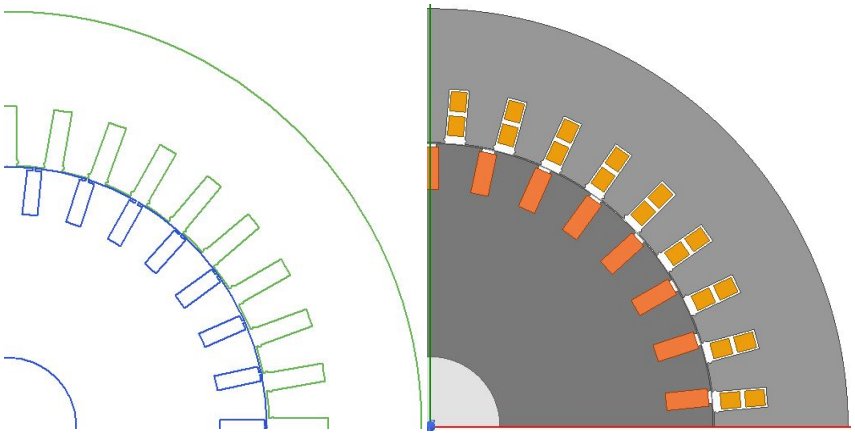

(a) Intial design. (b) Optimized design.

Figure 6.4: Visual comparison between the original and optimized design.

Table 6.7: Comparison between the optimized and initial geometry of the large traction motor.

General	Description	Initial [mm]	Optimized [mm]
L	Stack length	488.1	401.4
g	Air-gap length	1.1	1.1
D_{shaft}	Shaft diameter	110.0	110.0
Stator	Description	Initial [mm]	Optimized [mm]
D_{out}	Outer diameter	657.0	657.9
D_{is}	Inner diameter	414.3	447.4
h_{s0}	Slot opening height	1.0	1.0
h_{s1}	Wedge height	3.0	3.0
h_{s2}	Slot height	42.8	38.6
b_{s0}	Slot opening width	14.3	15.7
b_{s1}	Wedge width	17.1	18.5
h_{cs}	Yoke height	68.3	62.7
Rotor	Description	Initial [mm]	Optimized [mm]
h_{r0}	Slot opening height	2.0	2.6
h_{r2}	Slot height	35.3	33.3
b_{r0}	Slot opening width	2.0	10.0
b_{r1}	Slot upper width	11.8	13.8
b_{r2}	Slot lower width	11.8	13.8
h_{cr}	Yoke height	113.8	131.8

duce leakage flux and further increase the breakdown torque. The stator outer diameter and slot sizes remained similar.

6.6 Performance

The provisional results of the optimized model can be viewed in Table 6.9. The detailed design sheet can be viewed in Appendix B.2. These results will be verified within Maxwell 2D in Section 6.6.1. From Table 6.9, the following can be noted. Firstly, the efficiency and power factor remained similar, but the breakdown/rated torque ratio increased from 3.4 to 4.8. As a result, the CPSR increased from 2.0 to approximately 2.8 between 1500 rpm and 4345 rpm. Although this is an improved CPSR, it still struggles to reach the desired CPSR of 3. It is clear that a design with a wide CPSR will inevitably lead to an over-sized induction machine. Therefore, an adapted strategy will be tested in Section 6.7 to reduce motor size and increase the CPSR. The performance will be verified for a comparison between the original and adapted strategy. The torque-speed and power-speed curves of the optimized design can be viewed

Table 6.8: General stator and rotor winding data.

Stator winding	Value
Terminal resistance per phase	0.209 Ω
End leakage inductance per phase	0.970 mH
Turns per phase	108
Number of parallel branches	1
Number of conductors per slot	18
Coil pitch	8
Fill factor	71.09 %
Rotor winding	**Value**
End resistance between adjacent conductors	0.936 $\mu\Omega$
End inductance between adjacent conductors	0.001 μH
End length of bar	34.02 mm
Height of end ring	41.32 mm
Width of end ring	37.35 mm

in Figures 6.5 and 6.7 in the following Section.

Table 6.9: Provisional performance results of 500 kW motor.

Characteristic at 1500 rpm	Initial	Optimized
Output power [kW]	500.0	500.0
Efficiency %	95.6	95.3
Power factor %	91.2	90.9
Output torque [kNm]	3.2	3.1
Breakdown torque [kNm]	10.1	14.6
Breakdown/Rated Torque ratio	3.4	4.8
Characteristic at 4345 rpm	**Initial**	**Optimized**
Output power [kW]	270.5	500.0
Output torque [kNm]	0.6	1.1

6.6.1 Maxwell verification

For FEM verification of the optimized model performance, the design will be simulated in Maxwell 2D. Similar as to the 3 kW motor, a comparison will be made regarding output power, torque, efficiency and power factor.

6.6.1.1 Power

The power characteristics for the RMxprt Optimetrics design are given in Figures 6.5 and 6.6 respectively. It can be observed that the output power at 1500 rpm and 4345 rpm reflect the expected results.

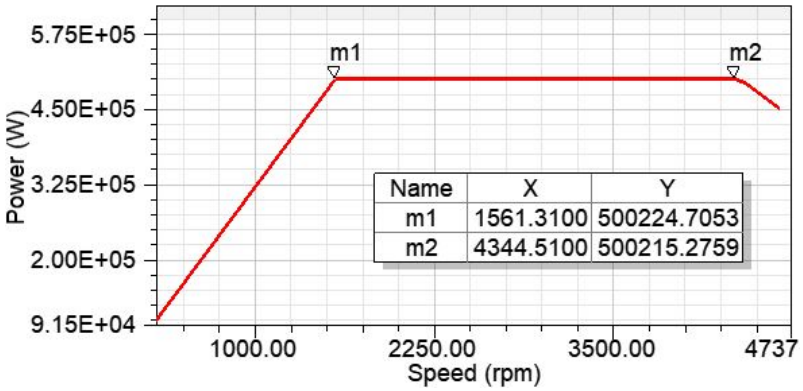

Figure 6.5: RMxprt power-speed curve.

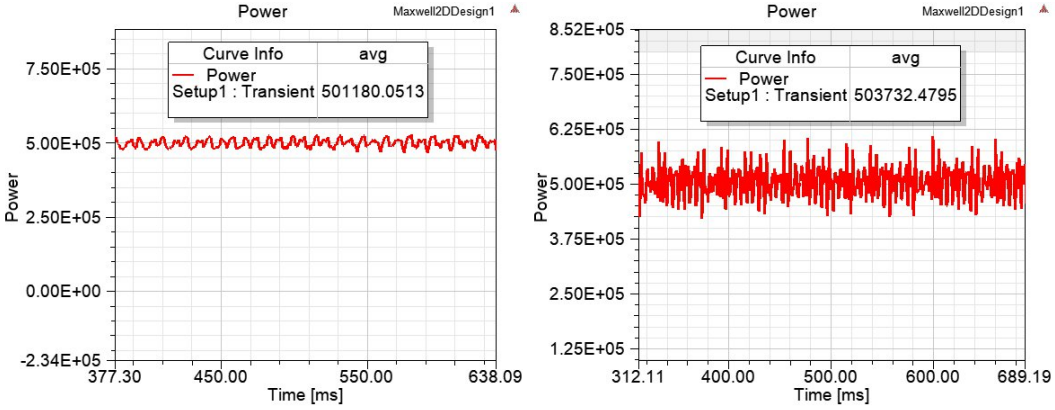

(a) Output power at 1500 rpm (b) Output power at 4345 rpm

Figure 6.6: Maxwell 2D transient power analysis of the 500 kW motor.

6.6.1.2 Torque

The torque characteristics for the designed motor are given in Figure 6.7. Torque results at 1500 rpm and 4345 rpm look reasonable and similar to what is expected.

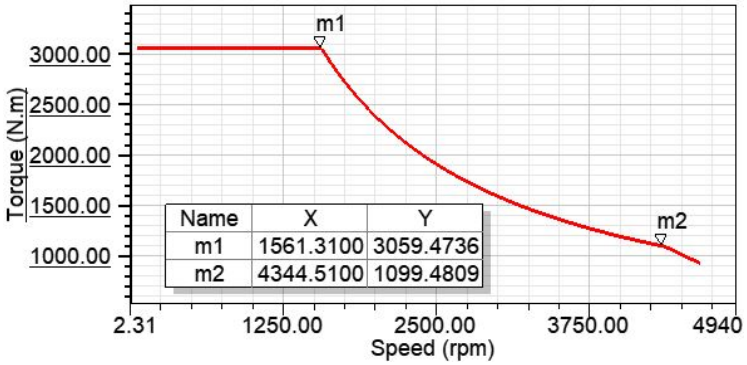

Figure 6.7: RMxprt torque-speed curve.

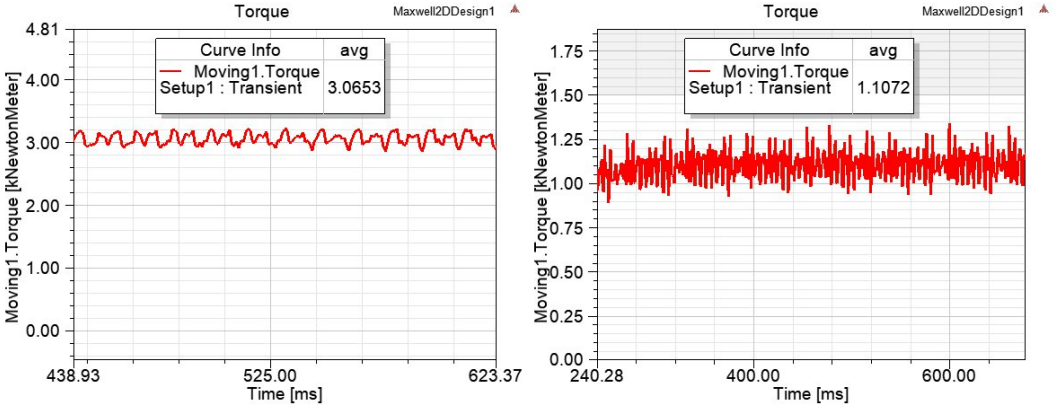

(a) Output torque at 1500 rpm. (b) Output torque at 4345 rpm.

Figure 6.8: Maxwell 2D transient torque analysis of the 500 kW motor.

6.6.1.3 Efficiency and power factor

The efficiency and power factor are given in Figure 6.9. The FEM efficiency is 2.7 % higher than the expected value from Table 6.9. This is due to Maxwell 2D not accounting for friction, stray and windage losses. The power factor in Maxwell 2D is 0.2 % higher than the expected value. These results resemble the expected performance reasonably accurate.

6.6.2 Electric and magnetic loading

Finally, the electrical and magnetic loading values are presented in Table 6.10. The presented electric and magnetic loading values are very close to or within recommended ranges. The flux lines and flux density of the optimized design during transient analysis can be viewed in Figures 6.10a and 6.10b respectively.

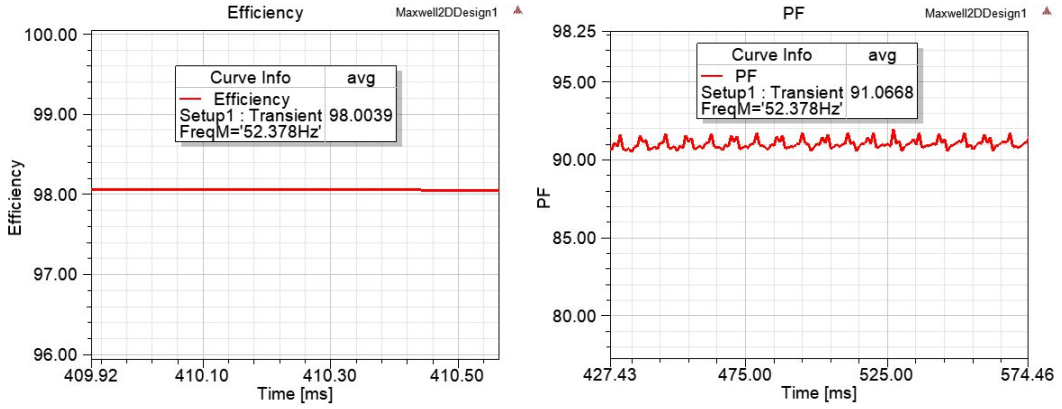

(a) Efficiency at 1500 rpm.

(b) PF at 1500 rpm.

Figure 6.9: Maxwell 2D transient analysis of efficiency and power factor of the 500 kW motor.

Table 6.10: Electrical and magnetic loading values of the 500 kW motor.

Flux density [T]	Design value	Recommended
Stator teeth	1.3	1.4 - 2.1
Stator yoke	1.6	1.4 - 1.7
Air-gap	0.9	0.7 - 0.9
Rotor teeth	1.4	1.5 - 2.2
Rotor yoke	0.8	1.0 - 1.6
Current density [A/mm^2]	Design value	Recommended
Stator slot	5.3	< 6
Rotor bar	4.1	< 7

6.7 Adapted approach

Although the verified design of the 500 kW motor presented earlier is theoretically valid for traction applications, the physical size is quite large and therefore expensive to manufacture. An adapted approach through voltage management is tested to achieve similar performance, but at reduced size. The implemented approach leading up to this section is described by Eq. (2.12) and repeated here for convenience:

$$k_b \omega_b = k_m \omega_m \tag{2.12}$$

where k_b and k_m are the the ratio's between maximum and rated torque at base speed ω_b and maximum speed ω_m within the CPSR. For the adapted approach, the base point of operation is moved from 1500 rpm to 2250 rpm, but at the same rated voltage of $V_b = 3300$ V and output power of $P_{out} = 500$ kW.

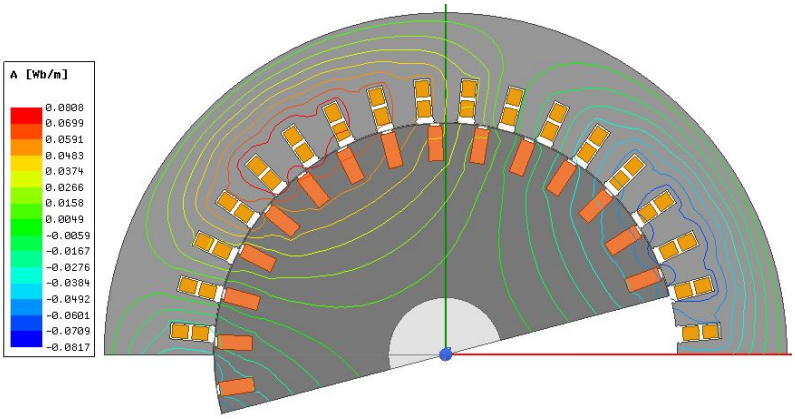

(a) Flux lines

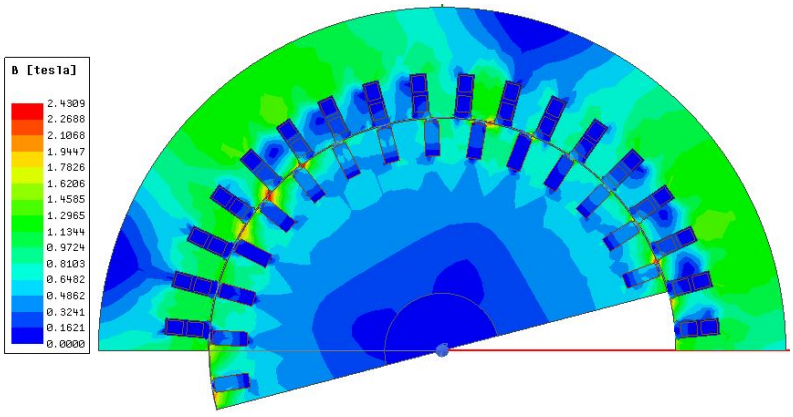

(b) Flux density

Figure 6.10: Magnetic characteristics during transient analysis of RMxprt Optimetrics design.

The goal of achieving a CPSR of 3 between 1500 rpm and 4500 rpm has remained the same. By designing for a base point within the original CPSR, a smaller overloading capability is required and thus reduces the motor size. Figure 6.11 can be used to aid in understanding the derivation.

From the base point of and within the CPSR at fixed voltage, Eq. (2.12) can be implemented. Assuming $k_m = 1$ at a maximum speed of 4500 rpm, k_b can be calculated as follows:

$$\begin{aligned} k_b &= k_m \frac{\omega_m}{\omega_b} \\ k_b &= \frac{4500}{2250} \\ &= 2 \end{aligned} \tag{6.5}$$

which translates to the minimum required breakdown torque at the base point.

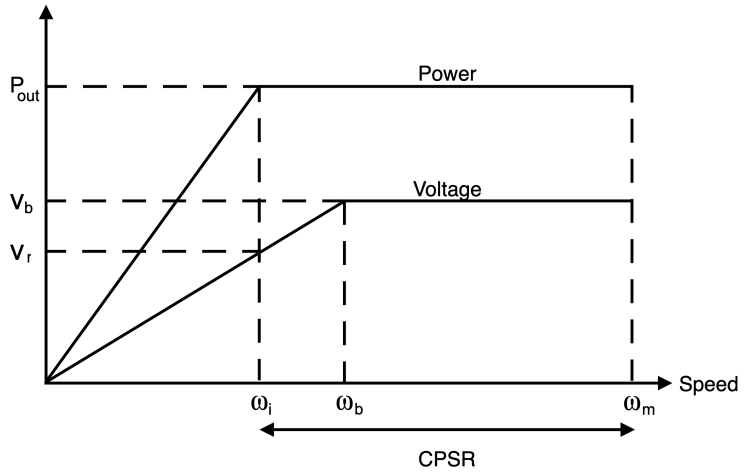

Figure 6.11: Adapted design approach.

To achieve an output power of 500 kW at 1500 rpm, the ratio k_{bi} between maximum and rated torque at 1500 rpm has to be determined. This can be done by implementing Eq. (2.12) between the initial base speed ω_i and new base speed ω_b, but accommodating the linear voltage difference between the two points as follows:

$$\begin{aligned} k_{bi} &= k_b \frac{\omega_b}{\omega_i} \left(\frac{V_b}{V_r}\right)^2 \\ &= 2 \cdot \frac{2250}{1500} \cdot \left(\frac{2200}{3300}\right)^2 \\ &= 1.3 \end{aligned} \tag{6.6}$$

It can be seen that the required overload capability for the design becomes more reasonable. The aim of this strategy is to reduce the overall manufacturing cost, which is proportional to the physical machine size, but without sacrificing performance. A new model was generated through the analytical model for an output power of $P_{out} = 500$ kW and line voltage of $V_l = 3300$ V at a base speed of $n_b = 2250$ rpm. This design is presented in the following section.

6.7.1 Initial design for adapted approach

The initial geometry for the adapted design approach of the 500 kW motor is given in Table 6.11. The slot and winding configuration presented for the original design in Table 6.1 is implemented here as well for consistency. The design can be viewed in Figure 6.12. Similar to previous designs generated through the analytical model, detailed design information can be viewed in Appendix A.3. The geometrical dimensions presented in Table 6.11 will serve as starting point for the optimization.

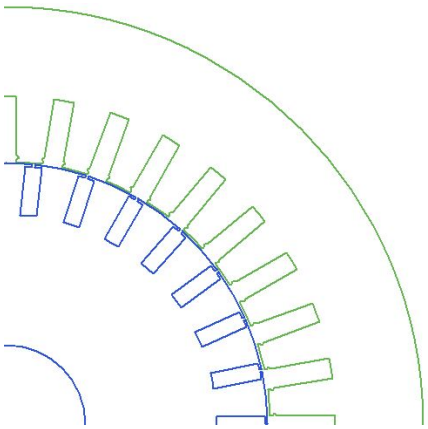

Figure 6.12: Initial design generated through analytical model.

Table 6.11: Initial set of geometrical dimensions for the adapted design of the large traction motor.

General	Description	Value [mm]
L	Stack length	426.6
g	Air-gap length	1.1
D_{shaft}	Shaft diameter	110.0
Stator	Description	Value [mm]
D_{out}	Outer diameter	574.8
D_{is}	Inner diameter	362.1
h_{s0}	Slot opening height	1.0
h_{s1}	Wedge height	3.0
h_{s2}	Slot height	40.6
b_{s0}	Slot width	13.5
b_{s1}	Wedge width	17.0
h_{cs}	Yoke height	61.8
Rotor	Description	Value [mm]
h_{r0}	Rotor slot opening height	2.0
h_{r2}	Slot height	33.5
b_{r0}	Slot opening width	2.0
b_{r1}	Slot upper width	11.2
b_{r2}	Slot lower width	11.2
h_{cr}	Yoke height	89.5
l_{er}	End bar length	33.7
b_{er}	End ring width	33.8
h_{er}	End ring height	35.5

6.7.2 Performance

The generated design was simulated in RMxprt to verify performance. As mentioned in Section 6.3.3, the analytical model was developed for low to medium voltage induction motors with random wound coils. As a result, there are some discrepancies regarding leakage inductance calculations that can influence power factor and breakdown torque. However, the RMxprt verified performance of the generated design proved that the analytical model was capable of producing a design that meets desired performance targets. The performance can be viewed in Table 6.12.

Table 6.12: Comparison between target and achieved specifications.

Characteristic	Target	RMxprt	Matlab
Power [kW]	500	500	500
Efficiency [%]	90.00	96.03	94.96
Power factor [%]	85.00	90.1	80.56
Breakdown/Rated Torque ratio	3.00	4.48	1.34

From Table 6.12 it can be concluded that a successful initial design is generated. The design will be optimized for further improvements.

6.7.3 Electric and magnetic loading

Electric and magnetic loading values are given in Table 6.13. All the values are reasonable, thus the design process can continue.

Table 6.13: Analytical model electrical and magnetic loading values of the adapted 500 kW motor.

Flux density [T]	Design value	Recommended
Stator teeth	1.3	1.4 - 2.1
Stator yoke	1.4	1.4 - 1.7
Air-gap	0.9	0.7 - 0.9
Rotor teeth	1.5	1.5 - 2.2
Rotor yoke	0.9	1.0 - 1.6
Current density [A/mm^2]	Design value	Recommended
Stator slot	4.7	< 6
Rotor bar	3.9	< 7

6.8 Optimization of adapted design

For the optimization of the adapted 500 kW motor design, identical formulation techniques were implemented as for the original design discussed in Section 6.4.1. However, changes were made regarding constraints and boundary conditions. These changes will be briefly discussed in the following sub-sections.

6.8.1 Optimization constraints for adapted design

The constraints considered at a new base speed of 2250 rpm for the adapted design of the traction motor are as follows:

$$P_{\text{out}} = 500\,\text{kW} \tag{6.7}$$
$$\eta \geq 90\,\% \tag{6.8}$$
$$\text{PF} \geq 85\,\% \tag{6.9}$$
$$\frac{T_{\text{bk}}}{T_{\text{n}}} \geq 2.0 \tag{6.10}$$

where the only difference between the original and adapted constraints is the reduced breakdown torque ratio. Seeing that the new base speed is at 2250 rpm and 500 kW is required at 4500 rpm, the minimum required breakdown torque ratio constraint is set at $T_{\text{BK}} \geq 2.0$. This increases the possibility of a reduced motor size.

6.8.2 Optimization boundaries for adapted design

Similar to the original design, the shaft diameter, air-gap length, wedge height and wedge/slot width ratio remained fixed for the optimization. The upper and lower boundary for radially defined variables were 25 % of the original value, except for slot opening heights which were set to 50 %. The stack length variable was given more freedom with boundaries being set to 40 % of the original value. This was in an attempt reduce the stack length. Slot width ratio's were chosen with experience gained to avoid invalid solutions during optimization iterations. The boundaries are given in Table 6.14.

6.9 Optimized design with adapted approach

The optimized geometry and winding information are given in this section, with the optimized performance presented in the following section. A visual comparison between the initial and optimized design is given in Figure 6.13.

Table 6.14: The Matlab generated set of geometrical dimensions with optimization boundaries for adapted design strategy.

General	Description	Lower [mm]	Initial [mm]	Upper [mm]
L	Stack length	255.6	426.6	596.4
g	Air-gap length	-	1.1	-
D_{shaft}	Shaft diameter	-	110.0	-
Stator	Description	Lower [mm]	Initial [mm]	Upper [mm]
h_{s0}	Slot opening height	0.5	1	1.5
h_{s1}	Wedge height	-	3	-
h_{s2}	Slot height	30.5	40.6	50.8
k_s	Pitch ratio	0.35	0.5	0.9
k_{bs}	Wedge width ratio	-	0.85	-
b_{s0}	Slot opening width	9.4	13.5	24.4
b_{s1}	Wedge width	11.1	16.2	28.7
h_{cs}	Yoke height	46.4	61.8	77.3
Rotor	Description	Lower [mm]	Initial [mm]	Upper [mm]
h_{r0}	Slot opening height	1	2.0	3
h_{r2}	Slot height	25.1	33.5	41.9
k_r	Pitch ratio	0.3	0.4	0.9
k_{br}	Slot width ratio	0.1	0.2	0.9
b_{r0}	Slot opening width	1.1	2.0	1.8
b_{r1}	Slot upper width	9.1	11.1	27.3
b_{r2}	Slot lower width	9.1	11.1	27.3
h_{cr}	Yoke height	67.1	89.5	111.9

The optimized geometry variables are given in Table 6.15. From these results, It can be noted that the majority of the optimized variables are reasonably close to the initial values. This is a good indication that the initial model was close to an optimal design. The generated stator and rotor winding details for the optimized motor is given in Table 6.16. This information will be used for the FEM verification of the optimized performance.

6.10 Performance of adapted design

The torque curves for various frequencies throughout the flux weakening range, as well as the torque-speed and power-speed curves of the optimized design can be viewed in Figures 6.14. The overloading capability at 1500 rpm is sufficient to produce the required 500 kW output power. Although the minimum CPSR requirement was 2 from the 2250 rpm base point, a CPSR of 2.6 was achieved. Thus, if the output power of 500 kW can be verified at 1500 rpm and

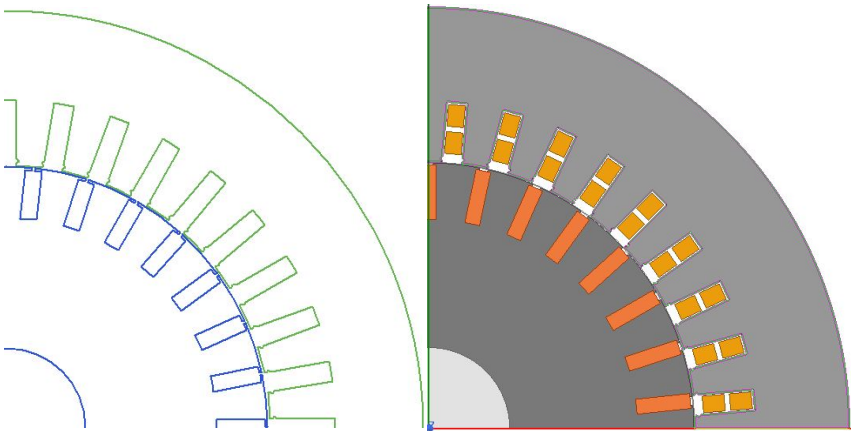

(a) Intial design. (b) Optimized design.

Figure 6.13: Visual comparison between the original and optimized design for the adapted design strategy.

Table 6.15: Geometry of the RMxprt optimetrics model for the adapted design strategy.

General	Description	Initial [mm]	Optimized [mm]
L	Stack length	426.6	468.1
g	Air-gap length	1.1	1.1
D_{shaft}	Shaft diameter	110.0	110.0
Stator	Description	Initial [mm]	Optimized [mm]
D_{out}	Outer diameter	574.8	571.7
D_{is}	Inner diameter	362.1	362.6
h_{s0}	Slot opening height	1.0	0.9
h_{s1}	Wedge height	3.0	3.0
h_{s2}	Slot height	40.6	37.1
b_{s0}	Slot opening width	13.5	14.1
b_{s1}	Wedge width	17.0	16.6
h_{cs}	Yoke height	61.8	63.5
Rotor	Description	Initial [mm]	Optimized [mm]
h_{r0}	Slot opening height	2.0	1.5
h_{r2}	Slot height	33.5	36.8
b_{r0}	Slot opening width	2.0	5.8
b_{r1}	Slot upper width	11.1	10.1
b_{r2}	Slot lower width	11.2	10.1
h_{cr}	Yoke height	89.5	87.0

Table 6.16: General stator and rotor winding data for adapted motor.

Stator winding	Value
Terminal resistance per phase	0.146 Ω
End leakage inductance per phase	0.510 mH
Turns per phase	84
Number of parallel branches	1
Number of conductors per slot	14
Coil pitch	8
Fill factor %	72.1
Rotor winding	**Value**
End resistance between adjacent conductors	0.943 $\mu\Omega$
End inductance between adjacent conductors	0.011 μH
End length of bar	41.4 mm
Height of end ring	48.2 mm
Width of end ring	32.1 mm

5817 rpm, a CPSR of 3.9 is possible. The provisional performance characteristics at 1500 rpm, 2250 rpm and 5817 rpm are given in Table 6.17.

Table 6.17: Provisional performance results of 500 kW motor.

Characteristic	1500 rpm	2250 rpm	5817 rpm
Output power [kW]	500.0	500	500
Output torque [kNm]	3.2	2.1	0.8
Line voltage [kV]	2.2	3.3	3.3
Efficiency %	94.5	95.9	-
Power factor %	91.4	90.9	-

From the results in Table 6.17, the adapted design strategy is partially validated. With the designed overload capability, the motor was capable of producing the required torque at 1500 rpm to achieve the desired output power of 500 kW. Marginal improvements were made for performance at 1500 rpm with the PF increasing by 0.85%, while the efficiency reduced by 0.13%. These results will be verified in Maxwell 2D in the following sections.

6.10.1 Power

A FEM simulation was completed at 1500 rpm, 2250 rpm and 5817 rpm to verify the analytical performance given in Table 6.17. These results are given in

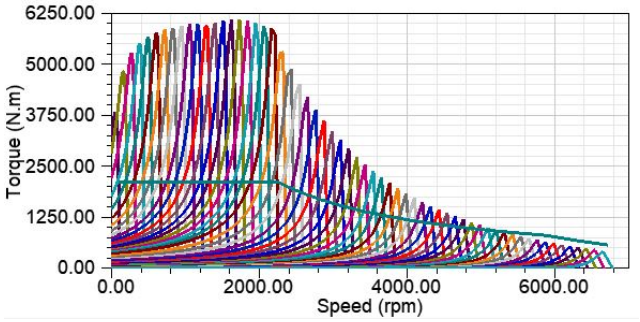

(a) Overloading capability.

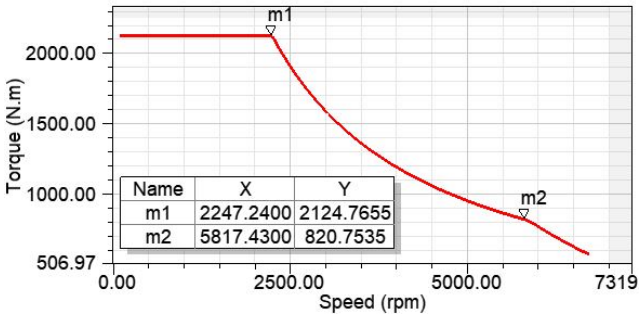

(b) Torque-speed curve.

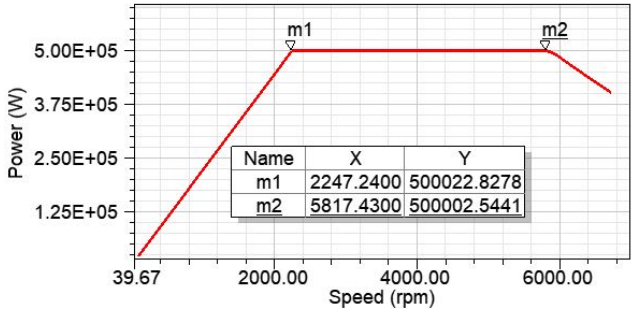

(c) Power-speed curve.

Figure 6.14: The CPSR of the adapted design at 2250 rpm.

Figure 6.15. It can be seen that an output power of 500 kW was achieved at all the operating points of interest. As a result, an effective CPSR of 3.9 was achieved through voltage management.

6.10.2 Torque

The FEM results of the output torque at the various operation points of interest are given in Figure 6.16. From these results, the adapted design strategy is verified. With a rated torque of 2.1 kN at 2250 rpm, the motor was capable of producing an output torque of 3.2 kN at 1500 rpm with a reduced voltage

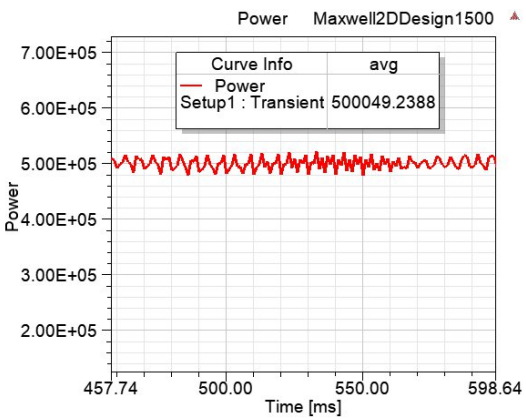

(a) Power at 1500 rpm.

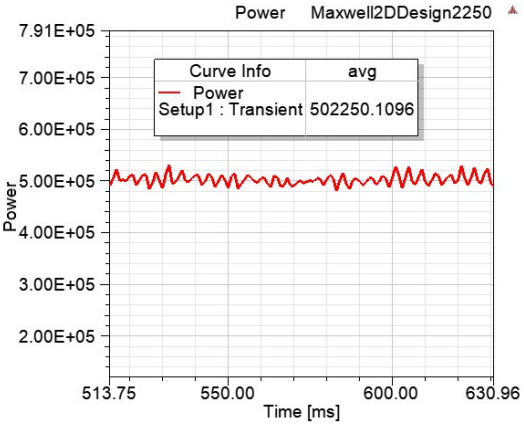

(b) Power at 2250 rpm.

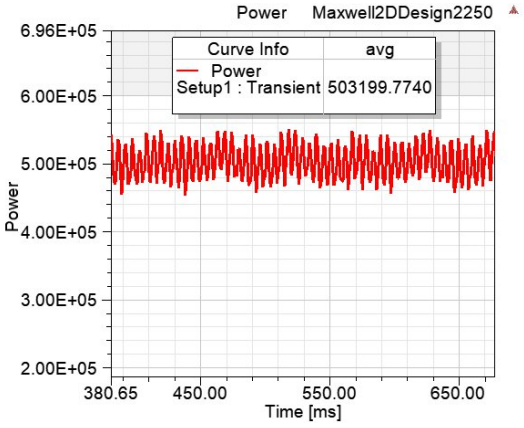

(c) Power at 5817 rpm.

Figure 6.15: Maxwell 2D verification of power characteristics for the adapted design through the CPSR.

of 2200 V due to its overloading capabilities.

6.10.3 Efficiency and power factor

The FEM efficiency and power factor at 1500 rpm and 2250 rpm are given in Figure 6.17. At both speeds, the efficiency is approximately 2.5 % higher than the expected values. As has been mentioned for previous efficiency calculations in Maxwell 2D, the friction, stray and windage losses are not accounted for. For the power factor calculation, the achieved performance is reasonably close to the expected results.

6.10.4 Electric and magnetic loading

The electrical and magnetic loading values of the adapted design are presented in Table 6.18 and are very close to or within recommended ranges. The flux

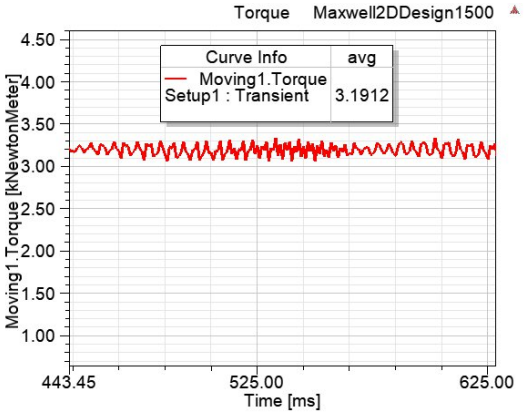

(a) Torque at 1500 rpm.

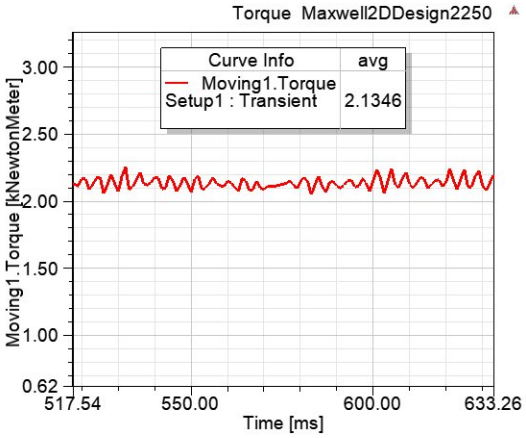

(b) Torque at 2250 rpm.

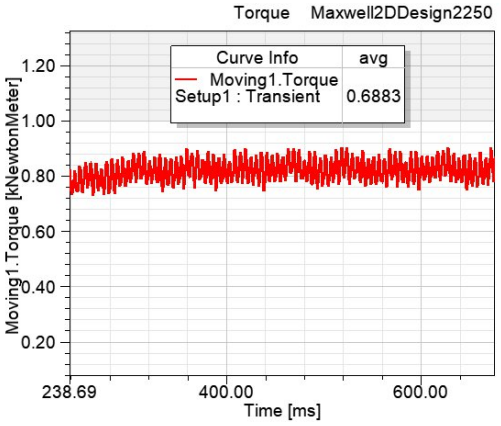

(c) Torque at 5817 rpm.

Figure 6.16: Maxwell 2D verification of torque characteristics for the adapted design.

lines and flux density during operation at 1500 rpm can be seen in Figures 6.18a and 6.18b respectively.

6.11 Design comparison

With the original and adapted design approach, 2 reasonable 500 kW designs were generated. A brief comparison will be made regarding these designs followed by a discussion. The comparison is given in Table 6.19.

From Table 6.19 it can be concluded that a smaller motor with better performance was achieved through the adapted design approach. The output power, efficiency, power factor and torque are similar at a rated speed of 1500 rpm. However, the CPSR is increased from 2.8 to 3.9 through voltage management. This was achieved with a design that is approximately 145 kg lighter. With

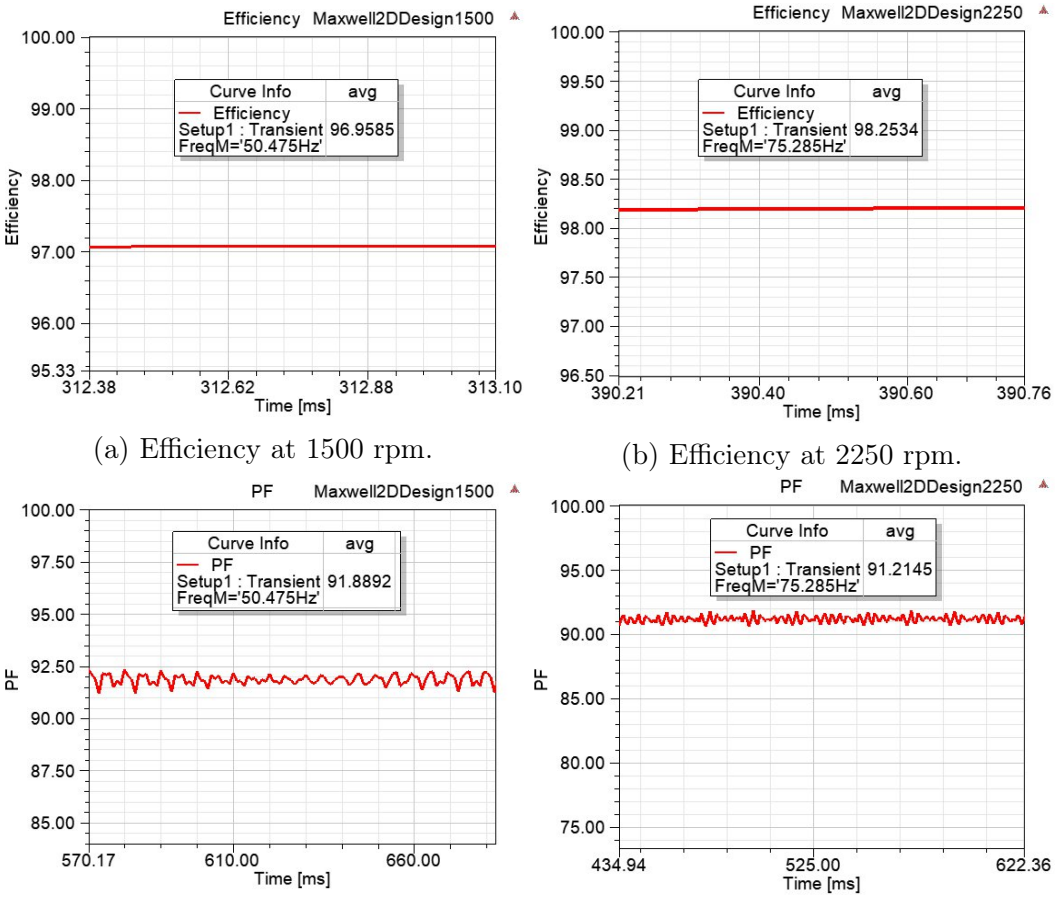

(a) Efficiency at 1500 rpm.

(b) Efficiency at 2250 rpm.

(c) Power factor at 1500 rpm.

(d) Power factor at 2250 rpm.

Figure 6.17: Maxwell 2D verification of efficiency and power factor for the adapted design.

Table 6.18: Electrical and magnetic loading values of the adapted 500 kW motor

Flux density [T]	Design value	Recommended
Stator teeth	1.3	1.4 - 2.1
Stator yoke	1.2	1.4 - 1.7
Air-gap	0.8	0.7 - 0.9
Rotor teeth	1.4	1.5 - 2.2
Rotor yoke	0.9	1.0 - 1.6
Current density [A/mm^2]	Design value	Recommended
Stator slot	4.7	< 6
Rotor bar	3.9	< 7

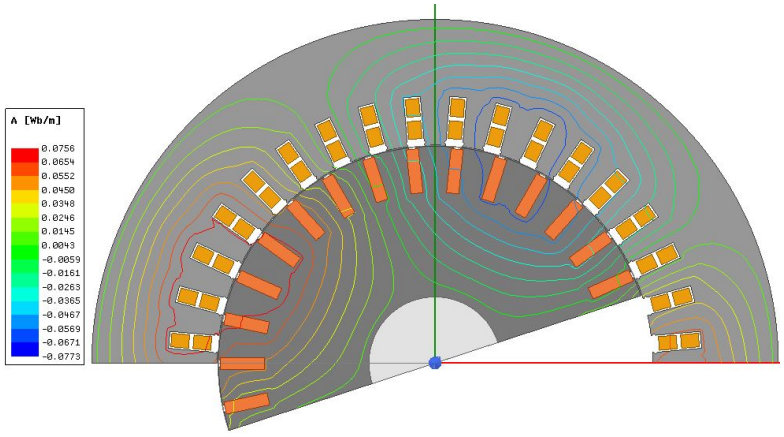

(a) Flux lines

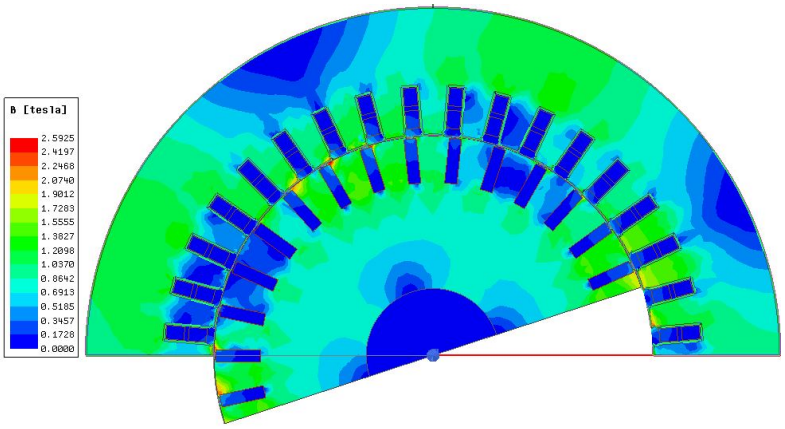

(b) Flux density

Figure 6.18: Magnetic characteristics during transient analysis of RMxprt Optimetrics design.

the adapted design being lighter, less material is required for manufacturing and it is a more cost-effective design.

6.12 Design summary

The knowledge and experience gained through the design of the 3 kW motor was used to theoretically design a 500 kW traction motor. The analytical model was used to generate an initial design for optimization. The optimized design was FEM verified within Maxwell 2D. The performance of the traction motor was satisfactory with relatively high efficiency and power factor values achieved. In addition, a CPSR of 2.8 was achieved. However, this design seemed fairly large and an adapted design strategy was derived to reduce the motor size and possibly increase the CPSR. The adapted strategy made use of effective voltage management to reduce machine size. FEM verified results

Table 6.19: Comparison between designs developed through the original and adapted design strategy of the 500 kW motor.

Performance at 1500 rpm	Original	Adapted
Output power [kW]	500.0	500
Efficiency %	98.0	97.0
Power factor %	91.1	91.9
Output torque [kNm]	3.1	3.2
CPSR	2.8	3.9
Line voltage [kV]	3.3	2.2
Size	**Original**	**Adapted**
Stator outer diameter [mm]	657.9	571.7
Stack length [mm]	401.4	468.1
Weight [kg]	1043.9	899.1

proved the effectiveness of the adapted approach with improved performance at reduced cost. Thus, the adapted approach can be implemented for large traction motors as a less expensive alternative. For smaller traction motors, the benefit of implementing voltage management will be marginal due to limited reduction in size. However, it can be implemented for a wider CPSR at increased PEC cost.

Chapter 7

Conclusions and recommendations

7.1 Introduction

This chapter contains conclusions for the design and testing of the prototype motor, as well as for the design of the large traction motor. In addition, recommendations regarding future research will be discussed.

7.2 Conclusions

The aim of this project was to formulate a design strategy for traction induction motors. The developed strategy builds on conventional induction motor literature, but prioritizes key differentiating traits such as a wide flux weakening range and high frequency losses. Further, the goal was to research and apply motor design principles in general and the application thereof. This section contains conclusions reached during the machine design process, mechanical design and testing procedures.

7.2.1 Machine design of prototype motor

The first step in this process was researching and applying all the design considerations of a traction motor. With the comprehension of traction motor operation principles, an analytical model was devised. This model gave insights regarding magnetic and electrical characteristics of a traction motor, as well as motor performance.

The second step was to determine the design specifications. This was followed by choosing an initial set of electric and magnetic loading values for the design. As a result, every geometrical aspect of the design could be calculated. This includes information regarding motor size, minimum shaft thickness, airgap length, yoke heights, slot details, etc. For the generated design, electric and magnetic loading values are calculated and compared to the initial set. If

the respective loading values are reasonably close to the initial set, the model reached convergence and the design can continue. If not, the electric and magnetic loading values are iteratively adjusted until convergence is reached. In the next step, the magnetisation current and equivalent circuit parameters are calculated. This leads to the calculation of various performance characteristics such as efficiency, power factor, torque, breakdown torque, etc. Lastly, the temperature rise during rated conditions are estimated. The accuracy of the model was in good agreement with commercial software packages such as ANSYS RMxprt. This generated design would be used as a base from which optimization would commence.

The optimization process commenced with choosing an optimization algorithm within the Optimetrics package of ANSYS RMxprt. The algorithm of choice was a non-gradient based Genetic Algorithm. The main advantage is that it searches in parallel with a population of points. This avoids being trapped in a local optimal solution, unlike conventional algorithms that search from single point. Additionally, it can accommodate a large set of parameters. The optimization formulation involved the setting-up of slot sizing constraints, as well as variable mapping. A dynamic solution which combines trigonometry with pitch ratio's prevented invalid solutions during each iteration through the optimization. Fixed parameters during optimization included the shaft diameter, air-gap length and stator outer diameter. The shaft diameter remained fixed for safety reasons, while the air-gap length had to be fixed for manufacturability. The stator outer diameter remained fixed to fit into standard frame sizes if needed. The objective function consisted of minimizing deviation from a set of constraints, where the weighting of each constraint was chosen as unity. Amongst other constraints such as for PF and efficiency, a wide CPSR was realized by setting a breakdown/rated torque ratio constraint of 3 more. Upper and lower boundaries were chosen as 25 % of the original design generated in Matlab. Optimized design performance was verified in FEM packages such as Maxwell 2D or SEMFEM. The design was then refined and moderately adapted for manufacturability and reduction of harmonic copper losses in the rotor. A performance comparison between the optimized and refined model ensured there was no significant deviation from the optimal performance.

7.2.2 Mechanical design of prototype motor

The mechanical design commenced with a decision whether or not to implement the prototype design into a frame. Due to reduced weight and torsional losses a frame-less design was chosen. This decision led to the experimental addition of fins to the outer diameter of the stator for increased heat transfer. The added fins increased the outer surface area of the stator by a ratio of 3.34. In addition, the added fins theoretically proved to increase heat transfer from the coils in a radial direction with natural convection. Naturally, the effective

heat transfer from the fin increases with forced convection. The prototype motor, with all its components were 3D modelled in Autocad Inventor. Each component had its own drawing which was dispatched to a supplier for manufacturing. Assembly of the motor took place systematically as components were received at various times during the period of the project. Custom jigs were made for both the stator and the rotor to ensure accurate alignment during stacking of the laminations. Upon completion of the stator windings, a DC test was done to verify that the phase resistance is accurate. Before testing commenced, a deflection analysis was completed. This was to ensure the rigidity of the design for test applications where a one-sided vertical mount is required.

7.2.3 Testing of prototype motor

Testing commenced by determining the equivalent circuit parameters. This was achieved through a no-load and locked-rotor test. The measured results were in correlation with that of ANSYS RMxprt. From the determined circuit parameters a Thevenin conversion was made and a torque profile estimate was created. To determine all the essential performance characteristics of the prototype motor, three sets of tests were conducted. These were load tests, externally driven tests and a breakdown torque test.

Load tests were completed from 500 rpm to 3000 rpm with 500 rpm increments. These measurements taken at discrete points gave insight regarding output power, output torque, efficiency and power factor throughout the flux weakening range. A CPSR close to 3 was achieved and the measured output power and output torque aligned well with the expected power and torque profiles. In addition, reasonably high efficiency and power factor was achieved throughout the flux weakening range. Additionally, a FFT was performed on the current measurement to investigate harmonics in the supply current from the PEC. Harmonics of the 3^{rd} and 5^{th} order were visible at speeds of 1500 rpm and higher. However, these harmonics were marginal compared to the fundamental frequency at each measurement.

Mechanical losses were measured through externally driven tests from 500 rpm to 3000 rpm with 500 rpm increments. This gave insight regarding rotational losses and allowed the calculation of core losses. The results were in good agreement with the expected analytical values.

The PEC had a current limit below the required breakdown current at rated voltage and frequency. To resolve this, the prototype motor was connected to grid supply which is capable of supplying such current. This implied that the breakdown torque test could be conducted, but at 50 Hz which naturally reduces the maximum achievable breakdown torque. The measured torque re-

sults were somewhat less than the expected values.

Considering all the results from the various tests, it can be concluded that a reasonable design of a traction motor was achieved by meeting desired performance targets. This proved that the suggested strategy followed is successful.

7.2.4 Design of large traction motor.

Initially, the same approach used for the design of the 3 kW motor was implemented for the theoretical design of a 500 kW motor. The same sequence of steps were used in the analytical model. This involved specifying motor specifications and supplying electric and magnetic loading values for a initial design. If convergence is not reached within the model, the process underwent another iteration. If an initial design was generated with satisfactory performance, optimization could commence.

The initial design had a relatively high efficiency and power factor, but only achieved a CPSR of 2.0 with the voltage remaining fixed throughout the flux weakening range. With the efficiency and power factor remaining similar, the CPSR increased to 2.8 after optimization. With the optimized design failing to achieve a CPSR of 3 and being over-sized, an adapted design strategy was derived.

In an attempt to reduce the general size of the motor and improve the CPSR, the design strategy was adapted to incorporate voltage management. This allowed the maximum rated voltage to be reached at a higher base speed. The adapted approach was verified with an improved CPSR of 3.8 at reduced manufacturing cost.

For smaller traction motors, the approach used to maximize the breakdown/rated torque ratio during optimization is sufficient to achieve a CPSR of 3 or more by not over-sizing the design. From the design process of the large motor, it was concluded that an adapted approach that incorporates voltage management in combination with an optimal breakdown torque ratio is a more efficient strategy.

7.3 Recommendations

Recommendations regarding multiple aspects of this project will be discussed in this section. These recommendations are related possible future research or similar projects.

7.3.1 Analytical model

The aim of the analytical model was to thoroughly understand the design principles of induction motors. Although the model was accurate, it was a systematic process to change between different designs. These changes included slot shapes or winding configurations. This was due to various assumed coefficients, factors, electric and magnetic loading values throughout the model. Each of these characteristics were iteratively changed until the model reached convergence and performance deemed satisfactory. Although this ensured an understanding of design principles and motor operation, the process was time consuming. For scenarios where time is restricted and various designs are to be produced, this process can be automated and a graphic user interface can be added for an improved overall experience.

The model was developed for low to medium voltage motors with random wound coils. Although the verified performance of the initial 500 kW design reached all target specifications, performance inaccuracies existed for the power factor and breakdown torque. For future work, the analytical model can be improved to incorporate high voltage designs with a winding configuration as desired.

7.3.2 Mechanical construction

For increased rigidity, an extra four outer rods can be used to replace the core rods. With the core being kept in position by bushings, it will be supported by an additional four rods. Also, the rod lengths were chosen conservatively to allow enough space for end windings. The length of these supporting rods can be reduced to further add extra rigidity.

7.3.3 Testing

In order to measure the breakdown torque at rated frequency and voltage, a PEC capable of delivering breakdown current is required. Although the breakdown torque measurement was accurate with the adapted test at 50 Hz, the test could not be completed at rated frequency. The adapted test gave strong evidence that the motor could deliver the rated breakdown torque, but it could not be confirmed.

7.4 Future work

It has been noted throughout the industry that PEC driven motors can lead to premature bearing failure [34]. Circulating currents though the motor and ultimately through the bearing leads to premature failure. With the frameless design of the prototype motor, an important study can be completed on

bearing currents and its affect on bearing reliability.

Lastly, the designed 500 kW motor described in Chapter 6 can be built and tested. This will give insight whether the adapted design approach produces accurate results for larger traction motors.

Appendices

Appendix A

Matlab analytical model results

The results from the analytical model discussed in Chapter 3 used to design the 3 kW prototype motor, 500 kW motor and adapted 500 kW motor are presented here.

A.1 Prototype traction motor

A.1.1 Main dimensions of stator core

```
MAIN DIMENSIONS OF STATOR CORE
Pole pairs: 2
Apparent Airgap Power: 4564.71 VA
Stator inner diameter: 0.108300 m
Initial stator outer diameter: 0.190000 m. TBC
Core length: 0.153106 m
Pole pitch: 0.085059 m
Slot pitch: 0.009451 m
Airgap: 0.000650 m
```

A.1.2 Stator winding

```
THE STATOR WINDING
Number of stator slots: 36
Two layer winding with chorderd coils were chosen:
Zone factor: 0.959795
Chording factor: 0.984808
Stator winding factor: 0.945214
Initial airgap flux density: 0.750000 T. TBC
Tooth saturation factor Kst + 1: 1.160000
Pole spanning coefficient: 0.681059
```

```
Pole flux: 0.006652 Wb
Number of conductors per slot (Even): 36.000000
Actual number of turns per phase: 216.000000 turns/phase
Actual airgap flux density: 0.786732 T
Rated current: 7.149849 A
Current density (chosen estimate): 5.600000 A/mm^2
Magnetic wire cross section: 1.276759 mm^2
Actual conductors in parallel: 1.000000
Wire guage diameter: 1.27 mm
Wire insulated diameter: 1.33 mm
```

A.1.3 Stator slot sizing

```
STATOR SLOT SIZING:
Slot fill factor: 0.40
Useful slot area: 114.91 mm^2
Assumed stator tooth flux density: 1.400000 T
b_ts: 0.005532 m
b_s0: 0.003500 m
b_s1: 0.004093 m
b_s2: 0.006140 m
h_s0: 0.001000 m
h_s1: 0.000000 m
h_s2: 0.022458 m
h_cs: 0.017392 m
Assumed carters coefficient: 1.200000
Airgap mmf F_mg: 488.575739 A turns
Stator tooth mmf F_mts: 39.235344 A turns
Rotor tooth mmf F_mtr: 38.936774 A turns
Stator outer diameter: 0.190000 m
Stator back core flux density B_cs: 1.249084 T
```

A.1.4 Rotor slots

```
ROTOR SLOT:
Chosen number of rotor teeth from Table 15.5: 30
Rotor bar current is: 233.561123 A
Assumed current density in rotor bar: 5.800000 A/mm^2
Rotor slot area: 0.000040 m^2
End ring current: 561.683477 A
End ring curent density: 4350000.000000 A/m^2
End ring cross section: 0.000129 m^2
```

```
h_r0: 0.002500 m
rHs01: 0 m
b_r0: 0.001000 m
Rotor slot pitch: 0.011205 m
Assumed rotor tooth flux density: 1.520000 T
b_tr: 0.006041 m
Rotor outer diameter: 0.107000 m
b_r1: 0.003664 m
b_r2: 0.003664 m
h_r1: 0.000000 m
h_r2: 0.010991 m
H_tr: 3117.052666 A/m
Rotor tooth mmf F_mtr: 42.052923 A turns
Assumed rotor back core flux density: 0.900000 T
Rotor back core height: 0.024137 m
Maximum shaft diameter: 0.031743 m
Mimimum shaft diameter: 0.010997 m
Approximate rated torque: 28.659353 Nm
End ring width: 0.009571
End ring height: 0.013491
```

A.1.5 Magnetization current

```
Magnitization Current:
Carters coefficient confirmed as: 1.497058
Stator back core mmf F_mcs: 31.994430 A turns
Rotor back core mmf F_mcr: 2.196314 A turns
Magnitization mmf F_1m: 1450.001318
Total saturation factor K_s: 0.483906
Magnitization current I_u: 5.258941 A
Relative (p.u.) value of I_mu: 73.553179 %
```

A.1.6 Resistances and inductances

```
RESISTANCES AND INDUCTANCES:
Assumed copper temperatuur: 75.000000 degrees
Stator resistance R_s: 2.057382 ohm
End ring length segment: 0.009478 m
Skin resistance coefficent K_r: 0.954215
Rotor bar end resistance R_be: 0.000096 ohm
Rotor cage resistance reduced to stator: 1.596421 ohm
Stator phase reactance X_sl: 2.006840 ohm
```

```
Rotor slot coefficient for square slots: 3.500000
Equivelant rotor bar leakage reactance X_bes1: 0.000292 ohm
Rotor leakage reactance X_rls1: 4.868465 ohm
Rotor bar end resistance at rated speed R_be: 0.000099 ohm
Rotor resistance at rated speed: 1.658494 ohm
Rotor bar leakage reactance at rated speed X_be: 0.000210 ohm
Rotor leakage reactance at rated speed X_rl: 3.497234 ohm
```

A.1.7 Losses and efficiency

```
LOSSES AND EFFICIENCY:
Stator winding losses: 315.522090 W
Rotor cage losses: 162.782920 W
Mechanical/Ventilation losses: 36.000000 W
Stray loss factor: 0.010000
Stray losses: 30.000000 W
Fundamental iron losses: 48.038935 W
Total core losses: 54.112509 W
Total losses: 598.417519 W
Motor efficiency: 83.369981 %
```

A.1.8 Operating characteristics

```
OPERATION CHARACTERISTCICS:
Active no-load current: 0.396263 A
Rated slip S_n: 0.050416
Rated shaft torque T_n: 29.577343 Nm
Breakdown torque T_bk: 85.201799 Nm
Starting current I_LR: 34.212828 A
Starting torque T_LR: 52.482904 NM

Final design values compared to original constaints:
Efficiency.  target: 85.000000   Achieved: 83.369981
Power factor.  target: 0.750000   Achieved: 0.764664
Breakdown/Rated Torque ratio.  target: 3.000000   Achieved: 2.880644
Locked/Rated Torque ratio.  target: 2.000000   Achieved: 1.774429
Locked/Rated current ratio.  target: 6.000000   Achieved: 4.785112
```

A.1.9 Temperature rise

```
TEMPERATURES RISE:
```

```
If ambient temperature is 40 degC, winding temperature is 83.76 degC
```

A.2 Large traction motor

A.2.1 Main dimensions of stator core

```
MAIN DIMENSIONS OF STATOR CORE
Pole pairs: 2
Apparent Airgap Power: 633986.93 VA
Stator inner diameter: 0.414313 m
Core length: 0.488102 m
Pole pitch: 0.325401 m
Slot pitch: 0.036156 m
Initial stator outer diameter: 0.657640 m. TBC
Airgap: 0.001052 m
```

A.2.2 Stator winding

```
THE STATOR WINDING
Number of stator slots: 36
Two layer winding with chorderd coils were chosen:
Zone factor: 0.959795
Chording factor: 0.984808
Stator winding factor: 0.945214
Initial airgap flux density: 0.700000 T. TBC
Tooth saturation factor Kst + 1: 1.070000
Pole spanning coefficient: 0.660386
Pole flux: 0.073422 Wb
Number of conductors per slot (Even): 20.000000
Actual number of turns per phase: 120.000000 turns/phase
Actual airgap flux density: 0.689727 T
Rated current: 114.349429 A
Current density (chosen estimate): 5.000000 A/mm^2
Magnetic wire cross section: 22.869886 mm^2
Actual conductors in parallel: 1.000000
```

A.2.3 Stator slot sizing

```
STATOR SLOT SIZING:
Slot fill factor: 0.75
```

```
Useful slot area: 609.86 mm^2
Assumed stator tooth flux density: 1.300000 T
b_ts: 0.019982 m
b_s0: 0.014258 m
b_s1: 0.017109 m
h_s0: 0.001000 m
h_s1: 0.003000 m
h_s2: 0.042774 m
h_cs: 0.074890 m
Assumed carters coefficient: 1.200000
Airgap mmf F_mg: 693.531783 A turns
Stator tooth mmf F_mts: 25.240937 A turns
Rotor tooth mmf F_mtr: 23.306288 A turns
Stator outer diameter: 0.657640 m
Stator back core flux density B_cs: 1.004298 T
```

A.2.4 Rotor slots

```
ROTOR SLOT:
Chosen number of rotor teeth from Table 15.5: 30
Rotor bar current is: 2282.747598 A
Assumed current density in rotor bar: 5.500000 A/mm^2
Rotor slot area: 0.000415 m^2
End ring current: 5489.704760 A
End ring curent density: 4125000.000000 A/m^2
End ring cross section: 0.001331 m^2
h_r0: 0.002000 m
rHs01: 0 m
b_r0: 0.002000 m
Rotor slot pitch: 0.043166 m
Assumed rotor tooth flux density: 1.300000 T
b_tr: 0.023857 m
Rotor outer diameter: 0.412209 m
b_r1: 0.011762 m
b_r2: 0.011762 m
h_r1: 0.000000 m
h_r2: 0.035286 m
H_tr: 539.639322 A/m
Rotor tooth mmf F_mtr: 20.121246 A turns
Assumed rotor back core flux density: 1.500000 T
Rotor back core height: 0.050141 m
Maximum shaft diameter: 0.237353 m
Mimimum shaft diameter: 0.076251 m
```

```
Chosen shaft diameter: 0.110000 m
Rotor yoke height: 0.113818 m
Approximate rated torque: 3141.102324 Nm
End ring width: 0.035692
End ring height: 0.037286
```

A.2.5 Magnetization current

```
Magnitization Current:
Carters coefficient confirmed as: 1.422727
Stator back core mmf F_mcs: 45.085024 A turns
Rotor back core mmf F_mcr: 246.627620 A turns
Magnitization mmf F_1m: 2318.660423
Total saturation factor K_s: 0.671632
Magnitization current I_u: 15.136991 A
Relative (p.u.) value of I_mu: 13.237487 %
```

A.2.6 Resistances and inductances

```
RESISTANCES AND INDUCTANCES:
Assumed copper temperatuur: 80.000000 degrees
Stator resistance R_s: 0.238466 ohm
End ring length segment: 0.038948 mm
Skin resistance coefficent K_r: 3.751916
Rotor bar end resistance R_be: 0.000103 ohm
Rotor cage resistance reduced to stator: 0.530829 ohm
Stator phase reactance X_sl: 2.838038 ohm
Rotor slot coefficient for square slots: 2.000000
Equivelant rotor bar leakage reactance X_bes1: 0.000781 ohm
Rotor leakage reactance X_rls1: 4.017131 ohm
Rotor bar end resistance at rated speed R_be: 0.000033 ohm
Rotor resistance at rated speed: 0.169224 ohm
Rotor bar leakage reactance at rated speed X_be: 0.001016 ohm
Rotor leakage reactance at rated speed X_rl: 5.230691 ohm
```

A.2.7 Losses and efficiency

```
LOSSES AND EFFICIENCY:
Stator winding losses: 9354.393434 W
Rotor cage losses: 5140.624778 W
Mechanical/Ventilation losses: 6000.000000 W
```

```
Stray loss factor: 0.010000
Stray losses: 5000.000000 W
Fundamental iron losses: 2928.110575 W
Total core losses: 3304.743077 W
Total losses: 28799.761289 W
Motor efficiency: 94.553749 %
```

A.2.8 Operating characteristics

```
OPERATION CHARACTERISTCICS:
Active no-load current: 1.656586 A
Rated slip S_n: 0.009960
Rated shaft torque T_n: 3152.079036 Nm
Breakdown torque T_bk: 4089.208922 Nm
Starting current I_LR: 386.544235 A
Starting torque T_LR: 1485.093692 Nm

Final design values compared to original constaints:
Efficiency.  target: 90.000000   Achieved: 94.553749
Power factor.  target: 0.850000   Achieved: 0.809064
Breakdown/Rated Torque ratio.  target: 3.000000   Achieved: 1.297305
```

A.2.9 Temperature rise

```
TEMPERATURES RISE:
If ambient temperature is 40 degC, winding temperature is 228.91 degC
```

A.3 Adapted design for large traction motor

A.3.1 Main dimensions of stator core

```
MAIN DIMENSIONS OF STATOR CORE
Pole pairs: 2
Apparent Airgap Power: 633986.93 VA
Stator inner diameter: 0.362094 m
Core length: 0.426582 m
Pole pitch: 0.284388 m
Slot pitch: 0.031599 m
Initial stator outer diameter: 0.574752 m. TBC
Airgap: 0.001052 m
```

A.3.2 Stator winding

```
THE STATOR WINDING
Number of stator slots: 36
Two layer winding with chorderd coils were chosen:
Zone factor: 0.959795
Chording factor: 0.984808
Stator winding factor: 0.945214
Initial airgap flux density: 0.700000 T. TBC
Tooth saturation factor Kst + 1: 1.070000
Pole spanning coefficient: 0.660386
Pole flux: 0.056080 Wb
Number of conductors per slot (Even): 18.000000
Actual number of turns per phase: 108.000000 turns/phase
Actual airgap flux density: 0.669772 T
Rated current: 114.349429 A
Current density (chosen estimate): 5.000000 A/mm^2
Magnetic wire cross section: 22.869886 mm^2
Actual conductors in parallel: 1.000000
```

A.3.3 Stator slot sizing

```
STATOR SLOT SIZING:
Slot fill factor: 0.75
Useful slot area: 548.88 mm^2
Assumed stator tooth flux density: 1.300000 T
b_ts: 0.016958 m
b_s0: 0.013526 m
b_s1: 0.016231 m
h_s0: 0.001000 m
h_s1: 0.003000 m
h_s2: 0.040579 m
h_cs: 0.061750 m
Assumed carters coefficient: 1.200000
Airgap mmf F_mg: 673.466708 A turns
Stator tooth mmf F_mts: 24.056425 A turns
Rotor tooth mmf F_mtr: 23.086244 A turns
Stator outer diameter: 0.574752 m
Stator back core flux density B_cs: 1.064479 T
```

A.3.4 Rotor slots

```
ROTOR SLOT:
Chosen number of rotor teeth from Table 15.5: 30
Rotor bar current is: 2054.472838 A
Assumed current density in rotor bar: 5.500000 A/mm^2
Rotor slot area: 0.000374 m^2
End ring current: 4940.734284 A
End ring curent density: 4125000.000000 A/m^2
End ring cross section: 0.001198 m^2
h_r0: 0.002000 m
rHs01: 0 m
b_r0: 0.002000 m
Rotor slot pitch: 0.037698 m
Assumed rotor tooth flux density: 1.300000 T
b_tr: 0.020232 m
Rotor outer diameter: 0.359989 m
b_r1: 0.011159 m
b_r2: 0.011159 m
h_r1: 0.000000 m
h_r2: 0.033476 m
H_tr: 539.639322 A/m
Rotor tooth mmf F_mtr: 19.144075 A turns
Assumed rotor back core flux density: 1.500000 T
Rotor back core height: 0.043821 m
Maximum shaft diameter: 0.201395 m
Mimimum shaft diameter: 0.066611 m
Chosen shaft diameter: 0.110000 m
Rotor yoke height: 0.089519 m
Approximate rated torque: 2096.809143 Nm
End ring width: 0.033763
End ring height: 0.035476
```

A.3.5 Magnetization current

```
Magnitization Current:
Carters coefficient confirmed as: 1.466880
Stator back core mmf F_mcs: 45.659000 A turns
Rotor back core mmf F_mcr: 219.852307 A turns
Magnitization mmf F_1m: 2263.915353
Total saturation factor K_s: 0.680792
Magnitization current I_u: 16.421774 A
```

```
Relative (p.u.) value of I_mu: 14.361046 %
```

A.3.6 Resistances and inductances

```
RESISTANCES AND INDUCTANCES:
Assumed copper temperatuur: 80.000000 degrees
Stator resistance R_s: 0.187052 ohm
End ring length segment: 0.033669 mm
Skin resistance coefficent K_r: 4.356482
Rotor bar end resistance R_be: 0.000115 ohm
Rotor cage resistance reduced to stator: 0.479693 ohm
Stator phase reactance X_sl: 2.781602 ohm
Rotor slot coefficient for square slots: 2.000000
Equivelant rotor bar leakage reactance X_bes1: 0.000891 ohm
Rotor leakage reactance X_rls1: 3.715045 ohm
Rotor bar end resistance at rated speed R_be: 0.000032 ohm
Rotor resistance at rated speed: 0.132782 ohm
Rotor bar leakage reactance at rated speed X_be: 0.001229 ohm
Rotor leakage reactance at rated speed X_rl: 5.120958 ohm
```

A.3.7 Losses and efficiency

```
LOSSES AND EFFICIENCY:
Stator winding losses: 7337.563774 W
Rotor cage losses: 4033.616477 W
Mechanical/Ventilation losses: 6000.000000 W
Stray loss factor: 0.010000
Stray losses: 5000.000000 W
Fundamental iron losses: 3477.359270 W
Total core losses: 4156.776281 W
Total losses: 26527.956532 W
Motor efficiency: 94.961719 %
```

A.3.8 Operating characteristics

```
OPERATION CHARACTERISTCICS:
Active no-load current: 1.803451 A
Rated slip S_n: 0.007832
Rated shaft torque T_n: 2099.623619 Nm
Breakdown torque T_bk: 2803.549058 Nm
Starting current I_LR: 414.355143 A
```

```
Starting torque T_LR: 1029.407028 Nm

Final design values compared to original constaints:
Efficiency.  target: 90.000000   Achieved: 94.961719
Power factor.  target: 0.850000   Achieved: 0.805588
Breakdown/Rated Torque ratio.  target: 3.000000   Achieved: 1.335263
```

A.3.9 Temperature rise

```
TEMPERATURES RISE:
If ambient temperature is 40 degC, winding temperature is 248.41 degC
```

Appendix B

ANSYS RMxprt analysis

The complete design sheet comparisons for the 3 kW and 500 kW motors discussed in Chapter 4 and 6 are presented in this appendix.

B.1 Design sheets of the optimized and fine tuned prototype 3 kW motor

OPTIMIZED DESIGN SHEET:

GENERAL DATA:

Given Output Power (kW): 3
Rated Voltage (V): 380
Winding Connection: Wye
Number of Poles: 4
Given Speed (rpm): 1000
Frequency (Hz): 34.8523
Stray Loss (W): 30
Frictional Loss (W): 18
Windage Loss (W): 18
Operation Mode: Motor
Type of Load: Constant Power
Operating Temperature (C): 75

STATOR DATA

Number of Stator Slots: 36
Outer Diameter of Stator (mm): 190
Inner Diameter of Stator (mm): 111.515
Type of Stator Slot: 3
Stator Slot
hs0 (mm): 0.953593
hs1 (mm): 0
hs2 (mm): 20.8679
bs0 (mm): 2.45544
bs1 (mm): 4.78539
bs2 (mm): 7.4396
rs (mm): 0

Top Tooth Width (mm): 5.11585
Bottom Tooth Width (mm): 6.10925

Length of Stator Core (mm): 168.204
Stacking Factor of Stator Core: 0.97
Type of Steel: M19_26G
Number of lamination sectors 1
Press board thickness (mm): 0
Magnetic press board No
Number of Parallel Branches: 1
Type of Coils: 21
Coil Pitch: 8
Number of Conductors per Slot: 32
Number of Wires per Conductor: 1
Wire Diameter (mm): 1.219

PROTOTYPE DESIGN SHEET:

GENERAL DATA:

Given Output Power (kW): 3
Rated Voltage (V): 380
Winding Connection: Wye
Number of Poles: 4
Given Speed (rpm): 1000
Frequency (Hz): 34.67
Stray Loss (W): 30
Frictional Loss (W): 18
Windage Loss (W): 18
Operation Mode: Motor
Type of Load: Constant Power
Operating Temperature (C): 75

STATOR DATA

Number of Stator Slots: 36
Outer Diameter of Stator (mm): 190
Inner Diameter of Stator (mm): 108.58
Type of Stator Slot: 3
Stator Slot
hs0 (mm): 1
hs1 (mm): 0
hs2 (mm): 22.5
bs0 (mm): 4
bs1 (mm): 5
bs2 (mm): 7
rs (mm): 0

Top Tooth Width (mm): 4.65028
Bottom Tooth Width (mm): 6.5799

Length of Stator Core (mm): 160
Stacking Factor of Stator Core: 0.95
Type of Steel: M19_26G
Number of lamination sectors 1
Press board thickness (mm): 0
Magnetic press board No
Number of Parallel Branches: 1
Type of Coils: 21
Coil Pitch: 8
Number of Conductors per Slot: 34
Number of Wires per Conductor: 1
Wire Diameter (mm): 1.219

Wire Wrap Thickness (mm): 0

Wedge Thickness (mm): 0
Slot Liner Thickness (mm): 0
Layer Insulation (mm): 0
Slot Area (mm^2): 129.896
Net Slot Area (mm^2): 127.555

Slot Fill Factor (%): 37.2787
Limited Slot Fill Factor (%): 40
Wire Resistivity (ohm.mm^2/m): 0.0217
Conductor Length Adjustment (mm): 0
End Length Correction Factor 1
End Leakage Reactance Correction Factor 1

ROTOR DATA

Number of Rotor Slots: 30
Air Gap (mm): 0.65
Inner Diameter of Rotor (mm): 30
Type of Rotor Slot: 4
Rotor Slot
hs0 (mm): 2.30342
hs1 (mm): 0
hs2 (mm): 11.0981
bs0 (mm): 1.13454
bs1 (mm): 3.89543
bs2 (mm): 3.89543
rs (mm): 0

Cast Rotor: No
Half Slot: No

Length of Rotor (mm): 168.204
Stacking Factor of Rotor Core: 0.97
Type of Steel: M19_26G
Skew Width: 0
End Length of Bar (mm): 10
Height of End Ring (mm): 17.4219
Width of End Ring (mm): 10.3
Resistivity of Rotor Bar
at 75 Centigrade (ohm.mm^2/m): 0.0217391
Resistivity of Rotor Ring
at 75 Centigrade (ohm.mm^2/m): 0.0217391
Magnetic Shaft: No

MATERIAL CONSUMPTION

Wire Wrap Thickness (mm): 0

Wedge Thickness (mm): 0
Slot Liner Thickness (mm): 0
Layer Insulation (mm): 0
Slot Area (mm^2): 139
Net Slot Area (mm^2): 135

Slot Fill Factor (%): 37.4242
Limited Slot Fill Factor (%): 40
Wire Resistivity (ohm.mm^2/m): 0.0217
Conductor Length Adjustment (mm): 0
End Length Correction Factor 1
End Leakage Reactance Correction Factor 1

ROTOR DATA

Number of Rotor Slots: 30
Air Gap (mm): 0.65
Inner Diameter of Rotor (mm): 30
Type of Rotor Slot: 4
Rotor Slot
hs0 (mm): 2.5
hs1 (mm): 0
hs2 (mm): 10
bs0 (mm): 1.2
bs1 (mm): 3.5
bs2 (mm): 3.5
rs (mm): 0

Cast Rotor: No
Half Slot: No

Length of Rotor (mm): 160
Stacking Factor of Rotor Core: 0.95
Type of Steel: M19_26G
Skew Width: 0
End Length of Bar (mm): 15
Height of End Ring (mm): 16.25
Width of End Ring (mm): 10
Resistivity of Rotor Bar
at 75 Centigrade (ohm.mm^2/m): 0.0172414
Resistivity of Rotor Ring
at 75 Centigrade (ohm.mm^2/m): 0.0172414
Magnetic Shaft: Yes

MATERIAL CONSUMPTION

Armature Copper Density (kg/m^3): 8900
Rotor Bar Material Density (kg/m^3): 8900
Rotor Ring Material Density (kg/m^3): 8900
Armature Core Steel Density (kg/m^3): 7650
Rotor Core Steel Density (kg/m^3): 7650

Armature Copper Weight (kg): 3.22735
Rotor Bar Material Weight (kg): 2.30374
Rotor Ring Material Weight (kg): 0.884918
Armature Core Steel Weight (kg): 17.3616
Rotor Core Steel Weight (kg): 9.30913
Total Net Weight (kg): 33.0867

Armature Core Steel Consumption (kg): 34.3021
Rotor Core Steel Consumption (kg):12.1906

RATED-LOAD OPERATION

Stator Resistance R1 (ohm): 1.92575
Stator Resistance at 20C (ohm): 1.58408
Stator Leakage Reactance X1 (ohm): 1.52782
Slot Leakage Reactance Xs1 (ohm): 0.955734
End Leakage Reactance Xe1 (ohm): 0.317463
Harmonic Leakage Reactance Xd1 (ohm): 0.254622
Rotor Resistance R2 (ohm): 1.42189
Rotor Leakage Reactance X2 (ohm): 2.64486
Resistance Corresponding to Iron-Core Loss Rfe (ohm): 2339
Magnetizing Reactance Xm (ohm): 45.9491

Stator Phase Current (A): 7.11056
Current Corresponding to Iron-Core Loss (A): 0.0863377
Magnetizing Current (A): 4.39495
Rotor Phase Current (A): 5.21598

Copper Loss of Stator Winding (W): 292.098
Copper Loss of Rotor Winding (W): 116.054
Iron-Core Loss (W): 52.3062
Frictional and Windage Loss (W): 36.5125
Stray Loss (W): 30
Total Loss (W): 526.97
Input Power (kW): 3.52703
Output Power (kW): 3.00006

Armature Copper Density (kg/m^3): 8900
Rotor Bar Material Density (kg/m^3): 8933
Rotor Ring Material Density (kg/m^3): 8933
Armature Core Steel Density (kg/m^3): 7650
Rotor Core Steel Density (kg/m^3): 7650

Armature Copper Weight (kg): 3.317
Rotor Bar Material Weight (kg): 1.93489
Rotor Ring Material Weight (kg): 0.784658
Armature Core Steel Weight (kg): 16.3831
Rotor Core Steel Weight (kg): 8.36319
Total Net Weight (kg): 30.7828

Armature Core Steel Consumption (kg): 32.5461
Rotor Core Steel Consumption (kg): 10.767

RATED-LOAD OPERATION

Stator Resistance R1 (ohm): 1.97924
Stator Resistance at 20C (ohm): 1.62809
Stator Leakage Reactance X1 (ohm): 1.49493
Slot Leakage Reactance Xs1 (ohm): 0.979488
End Leakage Reactance Xe1 (ohm): 0.365404
Harmonic Leakage Reactance Xd1 (ohm): 0.150033
Rotor Resistance R2 (ohm): 1.5668
Rotor Leakage Reactance X2 (ohm): 2.7519
Resistance Corresponding to Iron-Core Loss Rfe (ohm): 2356.89
Magnetizing Reactance Xm (ohm): 40.249

Stator Phase Current (A): 7.5506
Current Corresponding to Iron-Core Loss (A): 0.0852145
Magnetizing Current (A): 4.98997
Rotor Phase Current (A): 5.24012

Copper Loss of Stator Winding (W): 338.519
Copper Loss of Rotor Winding (W): 129.068
Iron-Core Loss (W): 51.3437
Frictional and Windage Loss (W): 19.8991
Stray Loss (W): 30
Total Loss (W): 568.829
Input Power (kW): 3.56901
Output Power (kW): 3.00018

Mechanical Shaft Torque (N.m): 28.447
Efficiency (%): 85.0591
Power Factor: 0.747224
Rated Slip: 0.0368118
Rated Shaft Speed (rpm): 1007.08

NO-LOAD OPERATION

No-Load Stator Resistance (ohm): 1.92575
No-Load Stator Leakage Reactance (ohm): 1.52868
No-Load Rotor Resistance (ohm): 1.42184
No-Load Rotor Leakage Reactance (ohm): 2.65566

No-Load Stator Phase Current (A): 4.61375
No-Load Iron-Core Loss (W): 57.5788
No-Load Input Power (W): 250.567
No-Load Power Factor: 0.0726344
No-Load Slip: 0.000422401
No-Load Shaft Speed (rpm): 1045.13

BREAK-DOWN OPERATION

Break-Down Slip: 0.35
Break-Down Torque (N.m): 100.214
Break-Down Torque Ratio: 3.52284
Break-Down Phase Current (A): 31.7204

LOCKED-ROTOR OPERATION

Locked-Rotor Torque (N.m): 80.9536
Locked-Rotor Phase Current (A): 46.9534
Locked-Rotor Torque Ratio: 2.84577
Locked-Rotor Current Ratio: 6.60334

Locked-Rotor Stator Resistance (ohm): 1.92575
Locked-Rotor Stator Leakage Reactance (ohm): 1.44773
Locked-Rotor Rotor Resistance (ohm): 1.46111
Locked-Rotor Rotor Leakage Reactance (ohm): 1.92764

DETAILED DATA AT RATED OPERATION

Mechanical Shaft Torque (N.m): 28.7223
Efficiency (%): 84.062
Power Factor: 0.712126
Rated Slip: 0.0409849
Rated Shaft Speed (rpm): 997.472

NO-LOAD OPERATION

No-Load Stator Resistance (ohm): 1.97924
No-Load Stator Leakage Reactance (ohm): 1.49526
No-Load Rotor Resistance (ohm): 1.56673
No-Load Rotor Leakage Reactance (ohm): 2.76243

No-Load Stator Phase Current (A): 5.24557
No-Load Iron-Core Loss (W): 56.7065
No-Load Input Power (W): 271.855
No-Load Power Factor: 0.0700517
No-Load Slip: 0.000255155
No-Load Shaft Speed (rpm): 1039.83

BREAK-DOWN OPERATION

Break-Down Slip: 0.38
Break-Down Torque (N.m): 98.1198
Break-Down Torque Ratio: 3.41616
Break-Down Phase Current (A): 31.37

LOCKED-ROTOR OPERATION

Locked-Rotor Torque (N.m): 82.302
Locked-Rotor Phase Current (A): 45.3542
Locked-Rotor Torque Ratio: 2.86544
Locked-Rotor Current Ratio: 6.0067

Locked-Rotor Stator Resistance (ohm): 1.97924
Locked-Rotor Stator Leakage Reactance (ohm): 1.45635
Locked-Rotor Rotor Resistance (ohm): 1.60593
Locked-Rotor Rotor Leakage Reactance (ohm): 1.98924

DETAILED DATA AT RATED OPERATION

Stator Slot Leakage Reactance (ohm): 0.955734
Stator End-Winding Leakage Reactance (ohm): 0.317463
Stator Differential Leakage Reactance (ohm): 0.254622
Rotor Slot Leakage Reactance (ohm):1.78562
Rotor End-Winding Leakage Reactance (ohm): 0.102782
Rotor Differential Leakage Reactance (ohm): 0.75645
Skewing Leakage Reactance (ohm): 0

Stator Winding Factor: 0.945214

Stator-Teeth Flux Density (Tesla): 1.34657
Rotor-Teeth Flux Density (Tesla): 1.52569
Stator-Yoke Flux Density (Tesla): 1.28114
Rotor-Yoke Flux Density (Tesla): 0.832097
Air-Gap Flux Density (Tesla): 0.751353

Stator-Teeth Ampere Turns (A.T): 15.0616
Rotor-Teeth Ampere Turns (A.T): 36.1928
Stator-Yoke Ampere Turns (A.T): 18.6795
Rotor-Yoke Ampere Turns (A.T): 1.9047
Air-Gap Ampere Turns (A.T): 463.946

Correction Factor for Magnetic Circuit Length of Stator Yoke: 0.572675
Correction Factor for Magnetic Circuit Length of Rotor Yoke: 0.7
Saturation Factor for Teeth: 1.11048
Saturation Factor for Teeth & Yoke: 1.15484
Induced-Voltage Factor: 0.920466

Stator Current Density (A/mm^2): 6.09265
Specific Electric Loading (A/mm): 23.3816
Stator Thermal Load (A^2/mm^3): 142.456

Rotor Bar Current Density (A/mm^2): 4.39525
Rotor Ring Current Density (A/mm^2): 2.5372

Half-Turn Length of Stator Winding (mm): 269.715

Stator Slot Leakage Reactance (ohm): 0.979488
Stator End-Winding Leakage Reactance (ohm): 0.365404
Stator Differential Leakage Reactance (ohm): 0.150032
Rotor Slot Leakage Reactance (ohm):1.94356
Rotor End-Winding Leakage Reactance (ohm): 0.145938
Rotor Differential Leakage Reactance (ohm): 0.662377
Skewing Leakage Reactance (ohm): 0

Stator Winding Factor: 0.945214

Stator-Teeth Flux Density (Tesla): 1.37534
Rotor-Teeth Flux Density (Tesla): 1.50295
Stator-Yoke Flux Density (Tesla): 1.30556
Rotor-Yoke Flux Density (Tesla): 0.544822
Air-Gap Flux Density (Tesla): 0.766589

Stator-Teeth Ampere Turns (A.T): 21.0804
Rotor-Teeth Ampere Turns (A.T): 28.0197
Stator-Yoke Ampere Turns (A.T): 21.214
Rotor-Yoke Ampere Turns (A.T): 0.727816
Air-Gap Ampere Turns (A.T): 579.754

Correction Factor for Magnetic Circuit Length of Stator Yoke: 0.559336
Correction Factor for Magnetic Circuit Length of Rotor Yoke: 0.7
Saturation Factor for Teeth: 1.08469
Saturation Factor for Teeth & Yoke: 1.12254
Induced-Voltage Factor: 0.91544

Stator Current Density (A/mm^2): 6.4697
Specific Electric Loading (A/mm): 27.0934
Stator Thermal Load (A^2/mm^3): 175.286

Rotor Bar Current Density (A/mm^2): 5.81656
Rotor Ring Current Density (A/mm^2): 2.99068

Half-Turn Length of Stator Winding (mm): 260.901

WINDING ARRANGEMENT

The 3-phase, 2-layer winding can be arranged in 9 slots as below:

AAAZZZBBB

Angle per slot (elec. degrees): 20
Phase-A axis (elec. degrees): 100
First slot center (elec. degrees): 0

TRANSIENT FEA INPUT DATA

For one phase of the Stator Winding:
Number of Turns: 192
Parallel Branches: 1
Terminal Resistance (ohm): 1.92575
End Leakage Inductance (H):0.00144971
For Rotor End Ring Between Two Bars of One Side:
Equivalent Ring Resistance (ohm): 1.99143e-06
Equivalent Ring Inductance (H): 3.08016e-09
2D Equivalent Value:
Equivalent Model Depth (mm): 168.204
Equivalent Stator Stacking Factor: 0.97
Equivalent Rotor Stacking Factor: 0.97

WINDING ARRANGEMENT

The 3-phase, 2-layer winding can be arranged in 9 slots as below:

AAAZZZBBB

Angle per slot (elec. degrees): 20
Phase-A axis (elec. degrees): 100
First slot center (elec. degrees): 0

TRANSIENT FEA INPUT DATA

For one phase of the Stator Winding:
Number of Turns: 204
Parallel Branches: 1
Terminal Resistance (ohm): 1.97924
End Leakage Inductance (H):0.00167741
For Rotor End Ring Between Two Bars of One Side:
Equivalent Ring Resistance (ohm): 2.24298e-06
Equivalent Ring Inductance (H): 3.89442e-09
2D Equivalent Value:
Equivalent Model Depth (mm): 160
Equivalent Stator Stacking Factor: 0.95
Equivalent Rotor Stacking Factor: 0.95

B.2 Design sheets of the original and adapted 500 kW motor

ORIGINAL 500 kW DESIGN:

GENERAL DATA

Given Output Power (kW): 500
Rated Voltage (V): 3300
Winding Connection: Wye
Number of Poles: 4
Given Speed (rpm): 1500
Frequency (Hz): 52.391
Stray Loss (W): 5000
Frictional Loss (W): 3000
Windage Loss (W): 3000
Operation Mode: Motor
Type of Load: Constant Power
Operating Temperature (C): 100

STATOR DATA

Number of Stator Slots: 36
Outer Diameter of Stator (mm): 657.861
Inner Diameter of Stator (mm): 447.415
Type of Stator Slot: Edited
Symmetric Slot

	Type	Info	(mm)
1	End Width:		15.7347
	Line Edge:	0	
2	Height:		0.957625
	Parallel Slot Width:		0
2	Height:		1.5
	End Width:		18.5114
2	Height:		1.5
	End Width:		15.7347
2	Height:		38.5905
	Parallel Slot Width:		0
1	End Width:		0
	Line Edge:	0	

Top Tooth Width (mm): 26.6498
Bottom Tooth Width (mm): 26.6498

Length of Stator Core (mm): 401.367
Stacking Factor of Stator Core: 0.97
Type of Steel: M19_26G
Number of lamination sectors 1
Press board thickness (mm): 0
Magnetic press board No
Number of Parallel Branches: 1
Type of Coils: 21
Coil Pitch: 8
Number of Conductors per Slot: 18
Number of Wires per Conductor: 1

ADAPTED 500 kW DESIGN:

GENERAL DATA

Given Output Power (kW): 500
Rated Voltage (V): 3300
Winding Connection: Wye
Number of Poles: 4
Given Speed (rpm): 2250
Frequency (Hz): 75.2953
Stray Loss (W): 5000
Frictional Loss (W): 3000
Windage Loss (W): 3000
Operation Mode: Motor
Type of Load: Constant Power
Operating Temperature (C): 100

STATOR DATA

Number of Stator Slots: 36
Outer Diameter of Stator (mm): 571.686
Inner Diameter of Stator (mm): 362.641
Type of Stator Slot: Edited
Symmetric Slot

	Type	Info	(mm)
1	End Width:		14.107
	Line Edge:	0	
2	Height:		0.926222
	Parallel Slot Width:		0
2	Height:		1.5
	End Width:		16.5965
2	Height:		1.5
	End Width:		14.107
2	Height:		37.0521
	Parallel Slot Width:		0
1	End Width:		0
	Line Edge:	0	

Top Tooth Width (mm): 20.7243
Bottom Tooth Width (mm): 20.7243

Length of Stator Core (mm): 468.055
Stacking Factor of Stator Core: 0.97
Type of Steel: M19_26G
Number of lamination sectors 1
Press board thickness (mm): 0
Magnetic press board No
Number of Parallel Branches: 1
Type of Coils: 21
Coil Pitch: 8
Number of Conductors per Slot: 14
Number of Wires per Conductor: 1

Wire Diameter (mm): 4.897
Wire Wrap Thickness (mm): 0

Wedge Thickness (mm): 3
Slot Liner Thickness (mm): 0
Layer Insulation (mm): 0
Slot Area (mm^2): 673.645
Net Slot Area (mm^2): 607.208

Slot Fill Factor (%): 71.0878
Limited Slot Fill Factor (%): 75
Wire Resistivity (ohm.mm^2/m): 0.0217
Conductor Length Adjustment (mm): 0
End Length Correction Factor 1
End Leakage Reactance Correction Factor 1

ROTOR DATA

Number of Rotor Slots: 30
Air Gap (mm): 1.05
Inner Diameter of Rotor (mm): 110
Type of Rotor Slot: 4
Rotor Slot
hs0 (mm): 2.55113
hs1 (mm): 0
hs2 (mm): 33.3038
bs0 (mm): 9.99148
bs1 (mm): 13.8463
bs2 (mm): 13.8463
rs (mm): 0

Cast Rotor: No
Half Slot: No

Length of Rotor (mm): 401.367
Stacking Factor of Rotor Core: 0.97
Type of Steel: M19_26G
Skew Width: 0
End Length of Bar (mm): 34.0188
Height of End Ring (mm): 41.3236
Width of End Ring (mm): 37.3549
Resistivity of Rotor Bar
at 75 Centigrade (ohm.mm^2/m): 0.0217391
Resistivity of Rotor Ring
at 75 Centigrade (ohm.mm^2/m): 0.0217391
Magnetic Shaft: No

MATERIAL CONSUMPTION

Armature Copper Density (kg/m^3): 8900
Rotor Bar Material Density (kg/m^3): 8900
Rotor Ring Material Density (kg/m^3): 8900

Wire Diameter (mm): 5.189
Wire Wrap Thickness (mm): 0

Wedge Thickness (mm): 3
Slot Liner Thickness (mm): 0
Layer Insulation (mm): 0
Slot Area (mm^2): 581.816
Net Slot Area (mm^2): 522.695

Slot Fill Factor (%): 72.1186
Limited Slot Fill Factor (%): 75
Wire Resistivity (ohm.mm^2/m): 0.0217
Conductor Length Adjustment (mm): 0
End Length Correction Factor 1
End Leakage Reactance Correction Factor 1

ROTOR DATA

Number of Rotor Slots: 30
Air Gap (mm): 1.05
Inner Diameter of Rotor (mm): 110
Type of Rotor Slot: 4
Rotor Slot
hs0 (mm): 1.46968
hs1 (mm): 0
hs2 (mm): 36.798
bs0 (mm): 5.77002
bs1 (mm): 10.1361
bs2 (mm): 10.1361
rs (mm): 0

Cast Rotor: No
Half Slot: No

Length of Rotor (mm): 468.055
Stacking Factor of Rotor Core: 0.97
Type of Steel: M19_26G
Skew Width: 0
End Length of Bar (mm): 41.415
Height of End Ring (mm): 48.2008
Width of End Ring (mm): 32.1127
Resistivity of Rotor Bar
at 75 Centigrade (ohm.mm^2/m): 0.0217391
Resistivity of Rotor Ring
at 75 Centigrade (ohm.mm^2/m): 0.0217391
Magnetic Shaft: No

MATERIAL CONSUMPTION

Armature Copper Density (kg/m^3): 8900
Rotor Bar Material Density (kg/m^3): 8900
Rotor Ring Material Density (kg/m^3): 8900

Armature Core Steel Density (kg/m^3):	7650
Rotor Core Steel Density (kg/m^3):	7650
Armature Copper Weight (kg):	84.5298
Rotor Bar Material Weight (kg):	60.9888
Rotor Ring Material Weight (kg):	34.4325
Armature Core Steel Weight (kg):	471.867
Rotor Core Steel Weight (kg):	392.09
Total Net Weight (kg):	1043.91
Armature Core Steel Consumption (kg):	832.494
Rotor Core Steel Consumption (kg):	468.259

RATED-LOAD OPERATION

Stator Resistance R1 (ohm):	0.209287
Stator Resistance at 20C (ohm):	0.159308
Stator Leakage Reactance X1 (ohm):	1.18775
Slot Leakage Reactance Xs1 (ohm):	0.631576
End Leakage Reactance Xe1 (ohm):	0.319201
Harmonic Leakage Reactance Xd1 (ohm):	0.236971
Rotor Resistance R2 (ohm):	0.130658
Rotor Leakage Reactance X2 (ohm):	1.87578
Resistance Corresponding to Iron-Core Loss Rfe (ohm):	3139.99
Magnetizing Reactance Xm (ohm):	65.5881
Stator Phase Current (A):	100.062
Current Corresponding to Iron-Core Loss (A):	0.585751
Magnetizing Current (A):	28.0425
Rotor Phase Current (A):	92.8659
Copper Loss of Stator Winding (W):	6286.37
Copper Loss of Rotor Winding (W):	3380.4
Iron-Core Loss (W):	3232.04
Frictional and Windage Loss (W):	6505.76
Stray Loss (W):	5000
Total Loss (W):	24404.6
Input Power (kW):	524.627
Output Power (kW):	500.223
Mechanical Shaft Torque (N.m):	3059.46
Efficiency (%):	95.3482
Power Factor:	0.90855
Rated Slip:	0.00662682
Rated Shaft Speed (rpm):	1561.31

Armature Core Steel Density (kg/m^3):	7650
Rotor Core Steel Density (kg/m^3):	7650
Armature Copper Weight (kg):	74.2894
Rotor Bar Material Weight (kg):	56.109
Rotor Ring Material Weight (kg):	26.7807
Armature Core Steel Weight (kg):	460.045
Rotor Core Steel Weight (kg):	281.838
Total Net Weight (kg):	899.062
Armature Core Steel Consumption (kg):	788.339
Rotor Core Steel Consumption (kg):	358.735

RATED-LOAD OPERATION

Stator Resistance R1 (ohm):	0.145896
Stator Resistance at 20C (ohm):	0.111055
Stator Leakage Reactance X1 (ohm):	1.18607
Slot Leakage Reactance Xs1 (ohm):	0.69283
End Leakage Reactance Xe1 (ohm):	0.241307
Harmonic Leakage Reactance Xd1 (ohm):	0.251935
Rotor Resistance R2 (ohm):	0.101912
Rotor Leakage Reactance X2 (ohm):	2.29884
Resistance Corresponding to Iron-Core Loss Rfe (ohm):	3071.08
Magnetizing Reactance Xm (ohm):	71.3528
Stator Phase Current (A):	99.4102
Current Corresponding to Iron-Core Loss (A):	0.60096
Magnetizing Current (A):	25.8658
Rotor Phase Current (A):	92.4746
Copper Loss of Stator Winding (W):	4325.41
Copper Loss of Rotor Winding (W):	2614.53
Iron-Core Loss (W):	3327.39
Frictional and Windage Loss (W):	5985.32
Stray Loss (W):	5000
Total Loss (W):	21252.6
Input Power (kW):	521.257
Output Power (kW):	500.004
Mechanical Shaft Torque (N.m):	2124.68
Efficiency (%):	95.9228
Power Factor:	0.908574
Rated Slip:	0.00514059
Rated Shaft Speed (rpm):	2247.25

NO-LOAD OPERATION

No-Load Stator Resistance (ohm): 0.209287
No-Load Stator Leakage Reactance (ohm): 1.20541
No-Load Rotor Resistance (ohm): 0.130638
No-Load Rotor Leakage Reactance (ohm): 1.97074

No-Load Stator Phase Current (A): 28.5771
No-Load Iron-Core Loss (W): 3342.77
No-Load Input Power (W): 15615
No-Load Power Factor: 0.0649871
No-Load Slip: 8.41296e-05
No-Load Shaft Speed (rpm): 1571.6

BREAK-DOWN OPERATION

Break-Down Slip: 0.07
Break-Down Torque (N.m): 14629.9
Break-Down Torque Ratio: 4.78187
Break-Down Phase Current (A): 661.671

LOCKED-ROTOR OPERATION

Locked-Rotor Torque (N.m): 7228.05
Locked-Rotor Phase Current (A): 1113.49
Locked-Rotor Torque Ratio: 2.36253
Locked-Rotor Current Ratio: 11.128

Locked-Rotor Stator Resistance (ohm): 0.209287
Locked-Rotor Stator Leakage Reactance (ohm): 0.965564
Locked-Rotor Rotor Resistance (ohm):0.327311
Locked-Rotor Rotor Leakage Reactance (ohm): 0.666559

DETAILED DATA AT RATED OPERATION

Stator Slot Leakage Reactance (ohm): 0.631589
Stator End-Winding Leakage Reactance (ohm): 0.319201
Stator Differential Leakage Reactance (ohm): 0.237044
Rotor Slot Leakage Reactance (ohm):0.699279
Rotor End-Winding Leakage Reactance (ohm): 0.162335
Rotor Differential Leakage Reactance (ohm): 1.01461
Skewing Leakage Reactance (ohm): 0

NO-LOAD OPERATION

No-Load Stator Resistance (ohm): 0.145896
No-Load Stator Leakage Reactance (ohm): 1.19303
No-Load Rotor Resistance (ohm): 0.10188
No-Load Rotor Leakage Reactance (ohm): 2.34541

No-Load Stator Phase Current (A): 26.311
No-Load Iron-Core Loss (W): 3429.45
No-Load Input Power (W): 14441.1
No-Load Power Factor: 0.0627782
No-Load Slip: 5.52212e-05
No-Load Shaft Speed (rpm): 2258.73

BREAK-DOWN OPERATION

Break-Down Slip: 0.05
Break-Down Torque (N.m): 8806.65
Break-Down Torque Ratio: 4.14492
Break-Down Phase Current (A): 587.902

LOCKED-ROTOR OPERATION

Locked-Rotor Torque (N.m): 5044.26
Locked-Rotor Phase Current (A): 1069.11
Locked-Rotor Torque Ratio: 2.37412
Locked-Rotor Current Ratio: 10.7545

Locked-Rotor Stator Resistance (ohm): 0.145896
Locked-Rotor Stator Leakage Reactance (ohm): 0.965032
Locked-Rotor Rotor Resistance (ohm):0.356349
Locked-Rotor Rotor Leakage Reactance (ohm): 0.753261

DETAILED DATA AT RATED OPERATION

Stator Slot Leakage Reactance (ohm): 0.69283
Stator End-Winding Leakage Reactance (ohm): 0.241307
Stator Differential Leakage Reactance (ohm): 0.251935
Rotor Slot Leakage Reactance (ohm):1.00541
Rotor End-Winding Leakage Reactance (ohm): 0.146022
Rotor Differential Leakage Reactance (ohm): 1.14741
Skewing Leakage Reactance (ohm): 0

Stator Winding Factor: 0.945214

Stator-Teeth Flux Density (Tesla): 1.29063
Rotor-Teeth Flux Density (Tesla): 1.44262
Stator-Yoke Flux Density (Tesla): 1.59047
Rotor-Yoke Flux Density (Tesla): 0.757503
Air-Gap Flux Density (Tesla): 0.854495

Stator-Teeth Ampere Turns (A.T): 21.6507
Rotor-Teeth Ampere Turns (A.T): 54.0699
Stator-Yoke Ampere Turns (A.T): 443.117
Rotor-Yoke Ampere Turns (A.T): 6.96144
Air-Gap Ampere Turns (A.T): 1420.3

Correction Factor for Magnetic
Circuit Length of Stator Yoke: 0.371356
Correction Factor for Magnetic
Circuit Length of Rotor Yoke: 0.7
Saturation Factor for Teeth: 1.05331
Saturation Factor for Teeth & Yoke: 1.3702
Induced-Voltage Factor: 0.965356

Stator Current Density (A/mm^2): 5.31274
Specific Electric Loading (A/mm): 46.1299
Stator Thermal Load (A^2/mm^3): 245.076

Rotor Bar Current Density (A/mm^2):
4.12421
Rotor Ring Current Density (A/mm^2):
2.95381

Half-Turn Length of
Stator Winding (mm): 778.206

WINDING ARRANGEMENT

The 3-phase, 2-layer winding can be arranged in 9 slots as below:

AAAZZZBBB

Angle per slot (elec. degrees): 20
Phase-A axis (elec. degrees): 100
First slot center (elec. degrees): 0

TRANSIENT FEA INPUT DATA

For one phase of the Stator Winding:
Number of Turns: 108

Stator Winding Factor: 0.945214

Stator-Teeth Flux Density (Tesla): 1.28411
Rotor-Teeth Flux Density (Tesla): 1.37438
Stator-Yoke Flux Density (Tesla): 1.21032
Rotor-Yoke Flux Density (Tesla): 0.885369
Air-Gap Flux Density (Tesla): 0.8157

Stator-Teeth Ampere Turns (A.T): 19.9961
Rotor-Teeth Ampere Turns (A.T): 34.354
Stator-Yoke Ampere Turns (A.T): 42.8603
Rotor-Yoke Ampere Turns (A.T): 7.02692
Air-Gap Ampere Turns (A.T): 1296.45

Correction Factor for Magnetic
Circuit Length of Stator Yoke: 0.634045
Correction Factor for Magnetic
Circuit Length of Rotor Yoke: 0.674519
Saturation Factor for Teeth: 1.04192
Saturation Factor for Teeth & Yoke: 1.0804
Induced-Voltage Factor: 0.968686

Stator Current Density (A/mm^2): 4.70082
Specific Electric Loading (A/mm): 43.9779
Stator Thermal Load (A^2/mm^3): 206.732

Rotor Bar Current Density (A/mm^2):
3.93903
Rotor Ring Current Density (A/mm^2):
2.28151

Half-Turn Length of
Stator Winding (mm): 783.158

WINDING ARRANGEMENT

The 3-phase, 2-layer winding can be arranged in 9 slots as below:

AAAZZZBBB

Angle per slot (elec. degrees): 20
Phase-A axis (elec. degrees): 100
First slot center (elec. degrees): 0

TRANSIENT FEA INPUT DATA

For one phase of the Stator Winding:
Number of Turns: 84

Parallel Branches:	1
Terminal Resistance (ohm):	0.209287
End Leakage Inductance (H):	0.00096968
For Rotor End Ring Between Two Bars of One Side:	
Equivalent Ring Resistance (ohm):	9.36296e-07
Equivalent Ring Inductance (H):	1.02282e-08
2D Equivalent Value:	
Equivalent Model Depth (mm):	401.367
Equivalent Stator Stacking Factor:	0.97
Equivalent Rotor Stacking Factor:	0.97

Parallel Branches:	1
Terminal Resistance (ohm):	0.145896
End Leakage Inductance (H):	0.000510061
For Rotor End Ring Between Two Bars of One Side:	
Equivalent Ring Resistance (ohm):	9.43012e-07
Equivalent Ring Inductance (H):	1.05823e-08
2D Equivalent Value:	
Equivalent Model Depth (mm):	468.055
Equivalent Stator Stacking Factor:	0.97
Equivalent Rotor Stacking Factor:	0.97

Appendix C

FEM analysis

The electric and magnetic characteristics of Maxwell 2D and SEMFEM for the optimized 3 kW motor is presented in this appendix.

C.1 Magnetic loading of Maxwell 2D

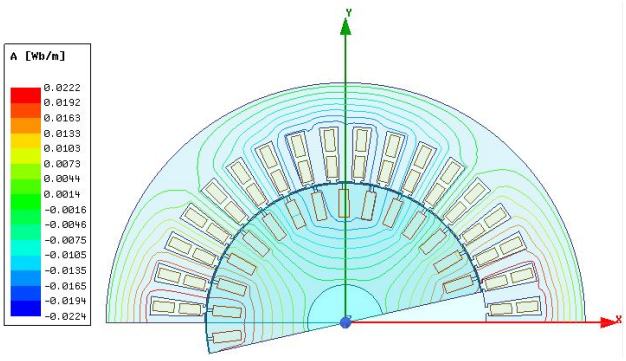

(a) Flux lines.

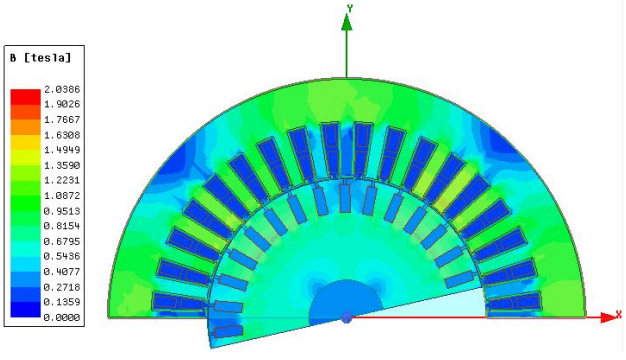

(b) Flux density.

Figure C.1: Magnetic characteristics at 1000 rpm, time = 0.3s, position = 12.7 deg.

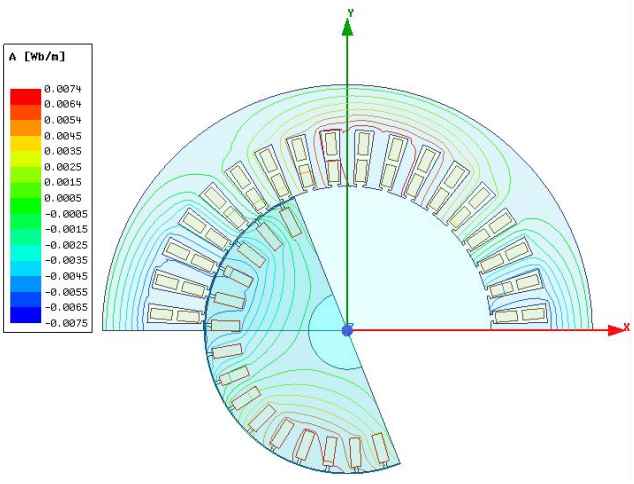

(a) Flux lines.

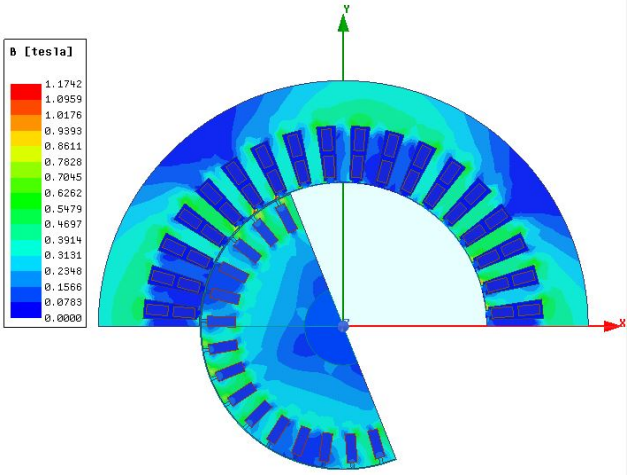

(b) Flux density.

Figure C.2: Magnetic characteristics at 3000 rpm.

C.2 Magnetic loading of SEMFEM

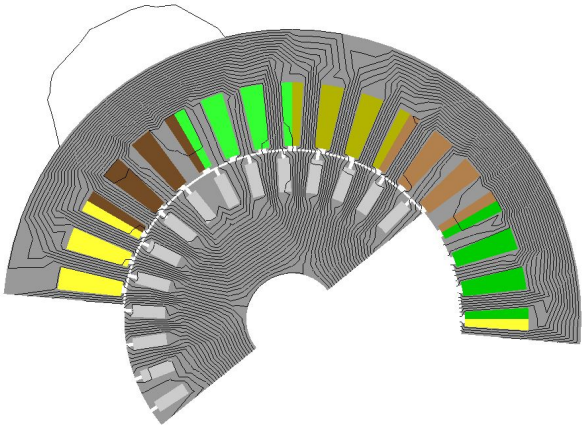

(a) Flux lines

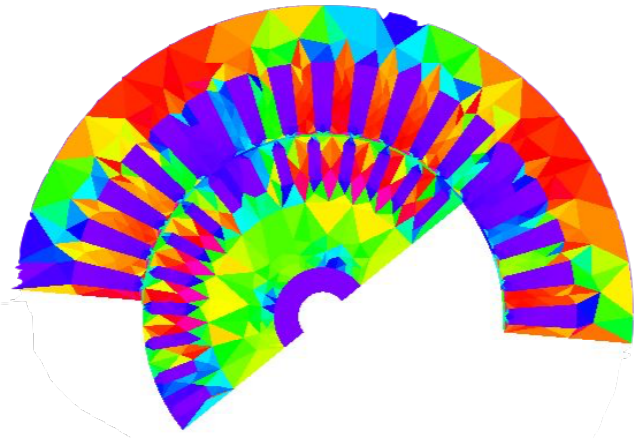

(b) Flux density

Figure C.3: Magnetic characteristics at 1000.

Appendix D

Protoype motor mechanical drawings

A complete drawing set of the mechanical components designed for the testing of the prototype motor is presented in this appendix.

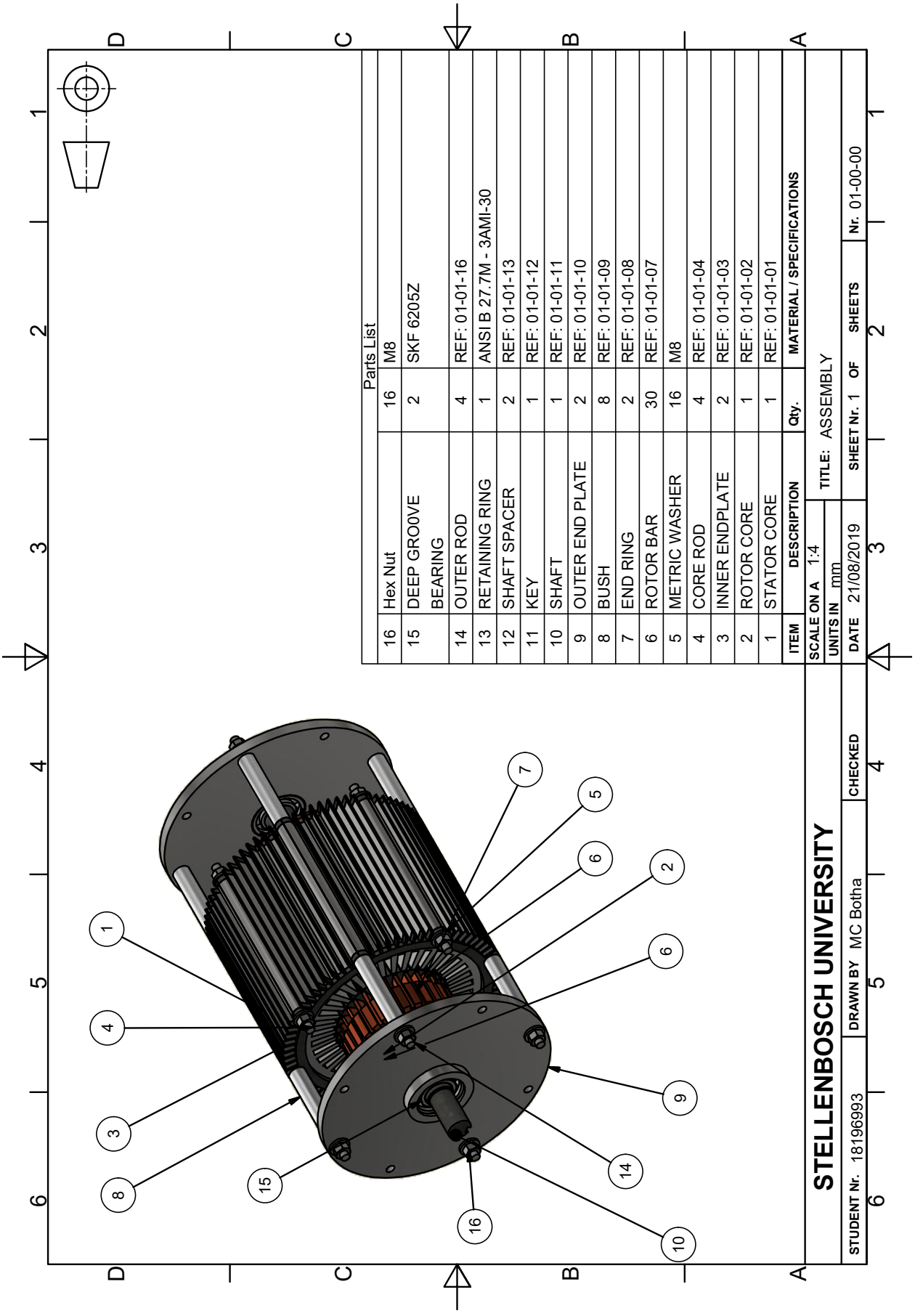

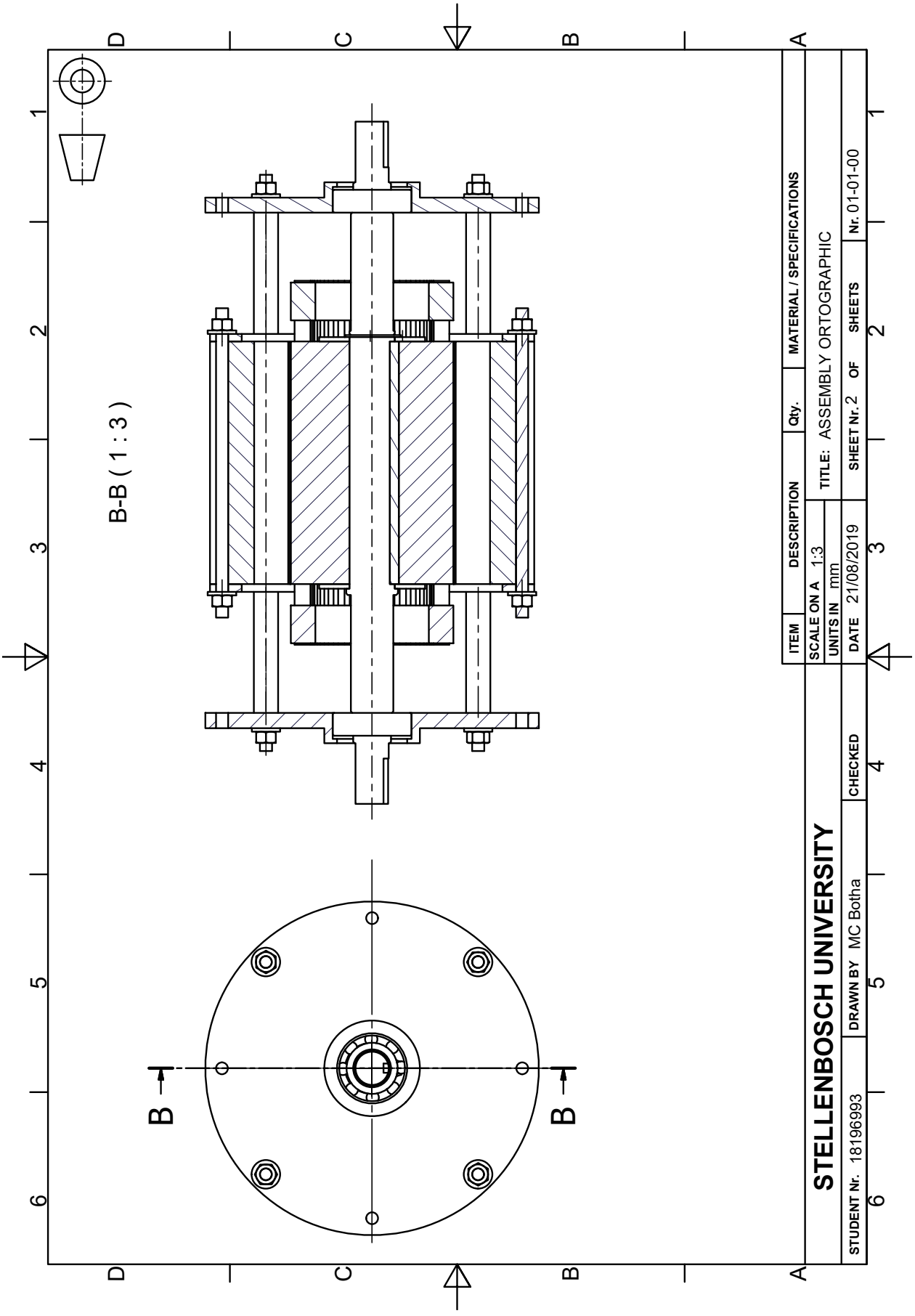

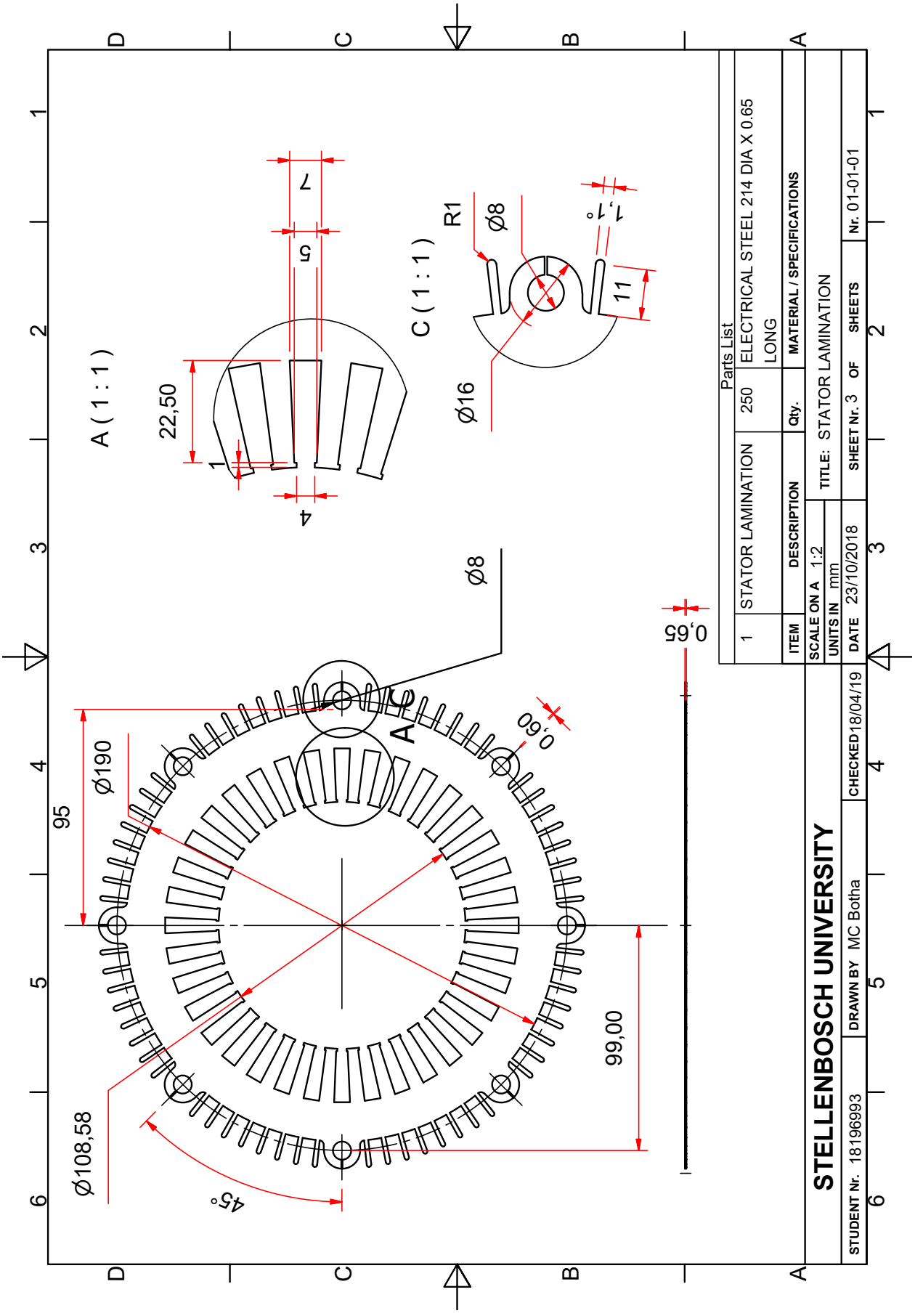

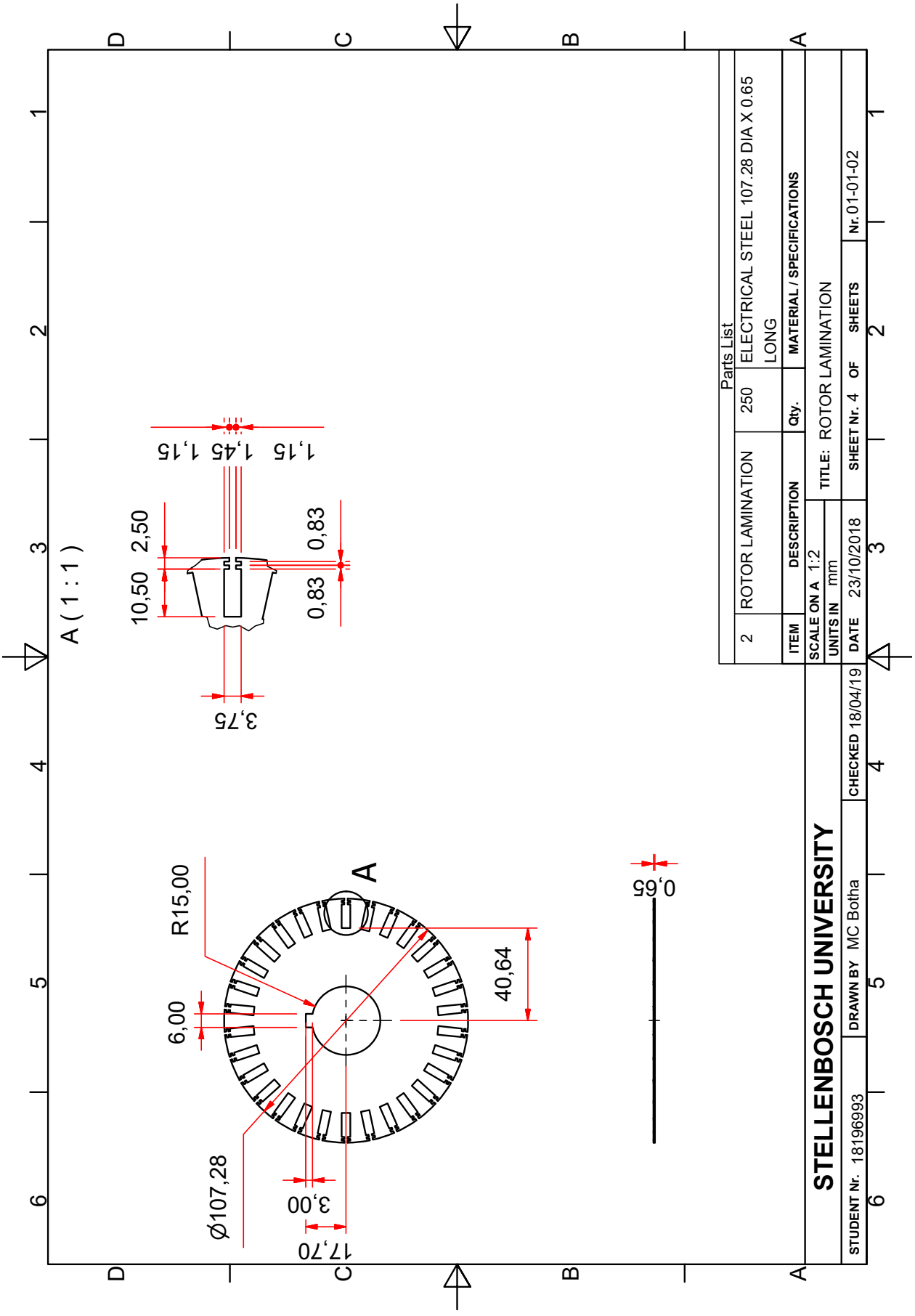

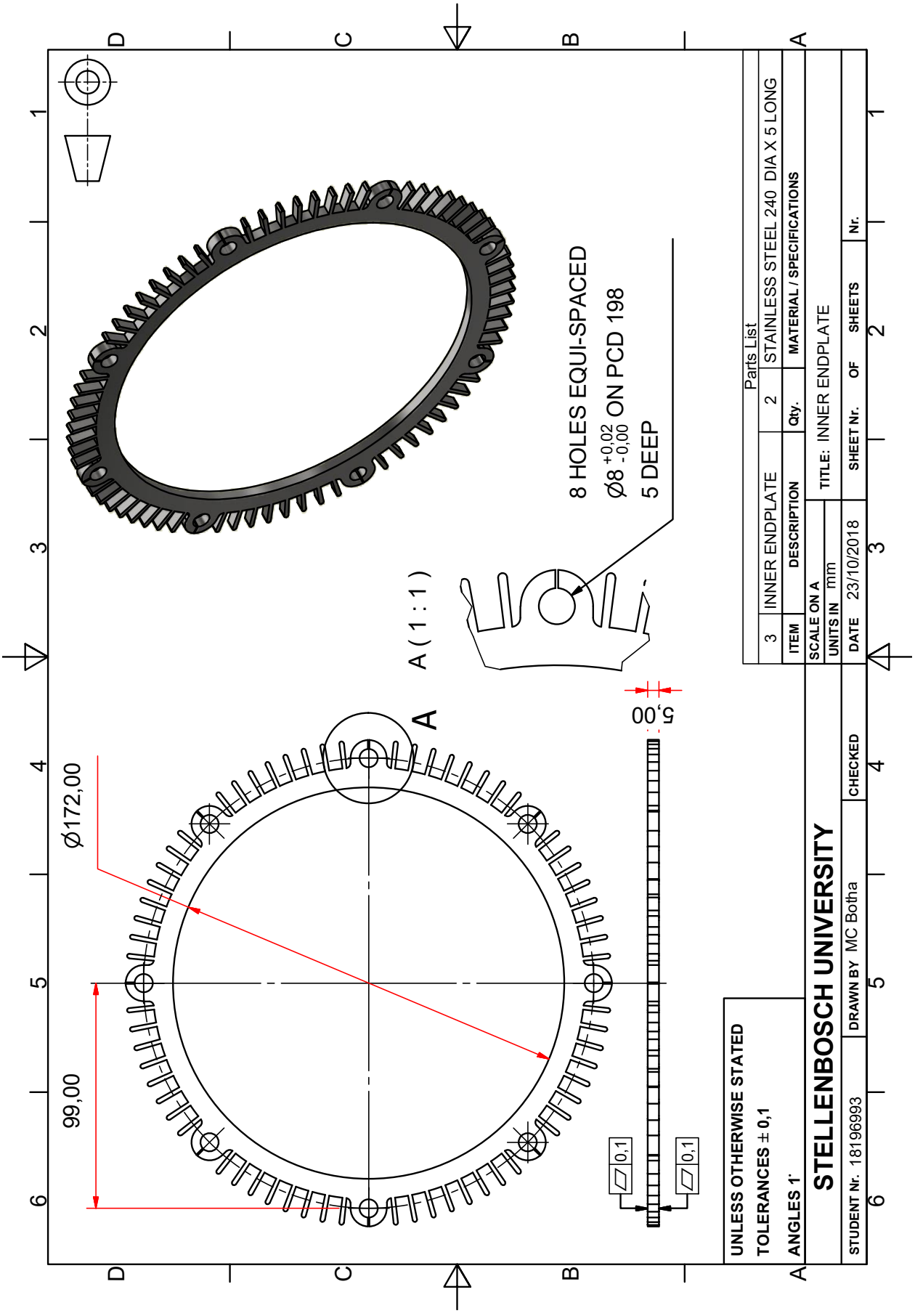

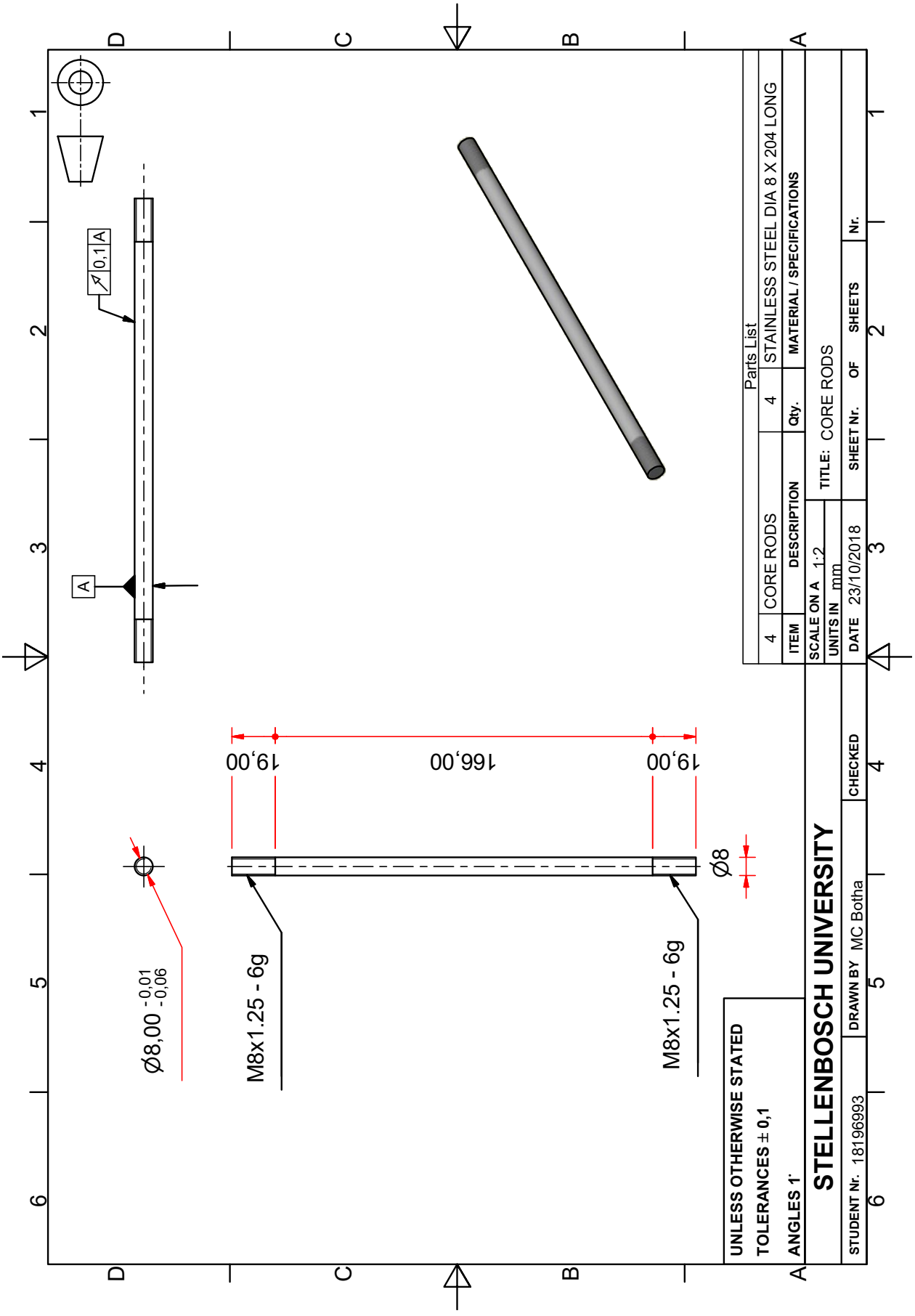

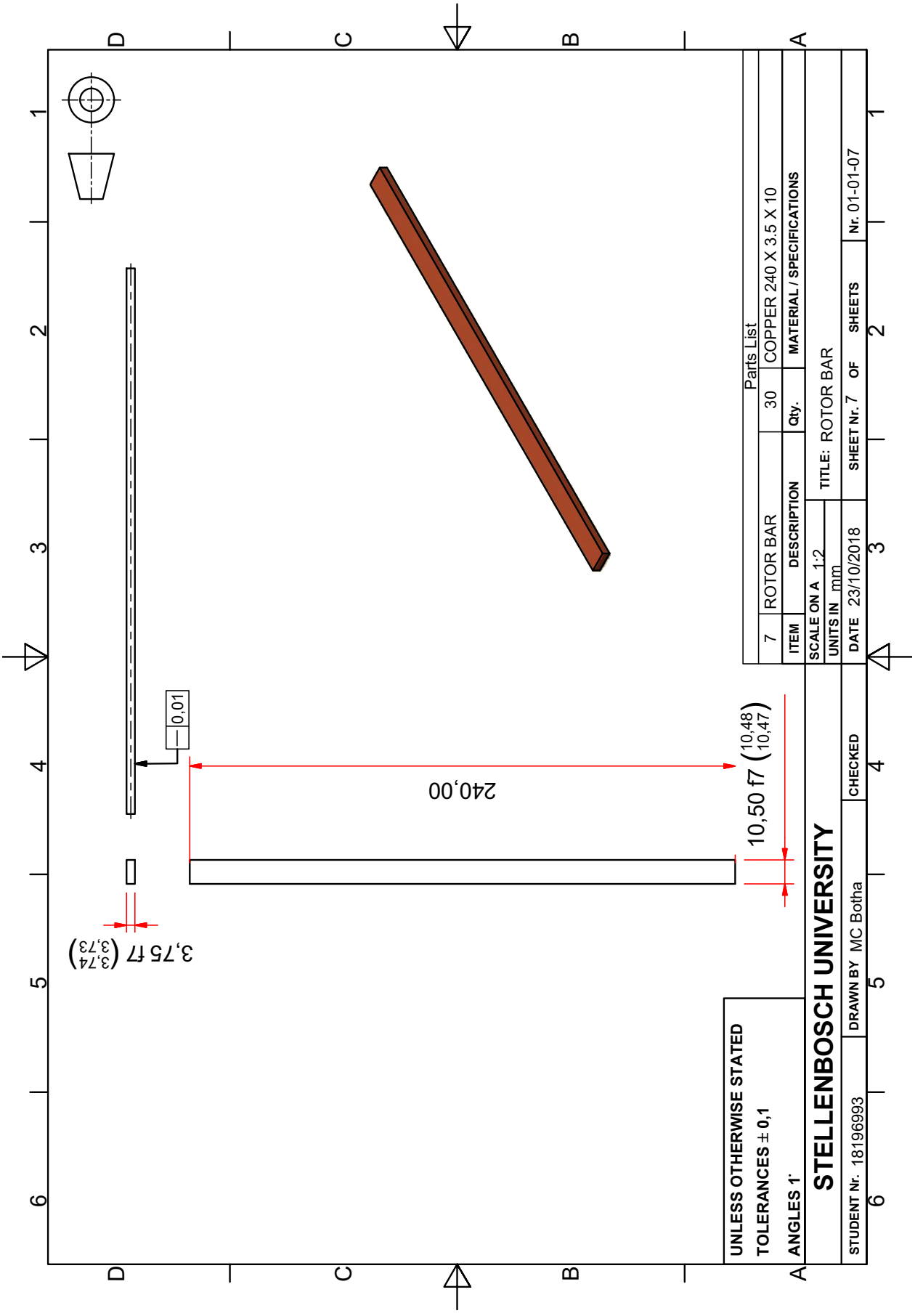

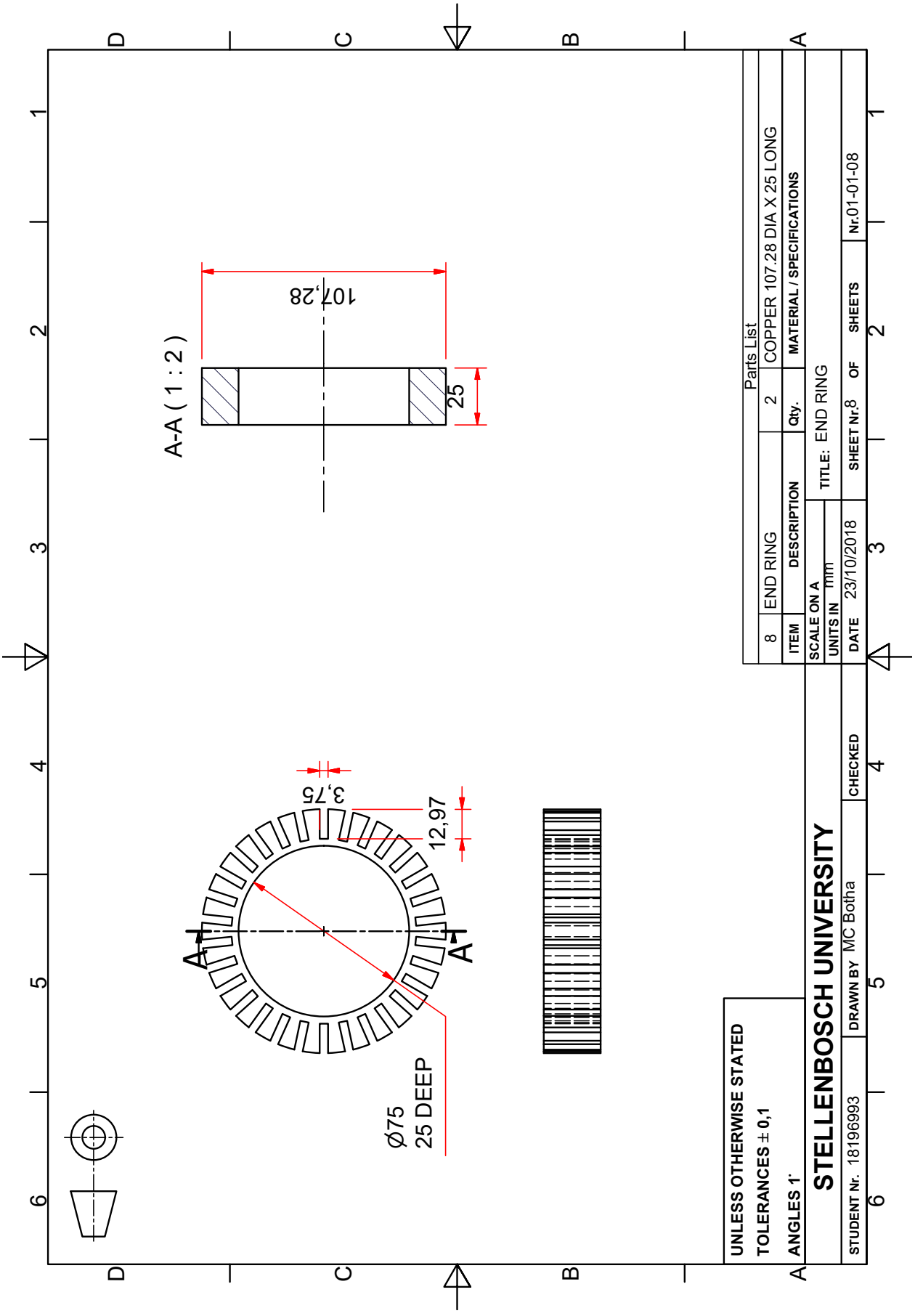

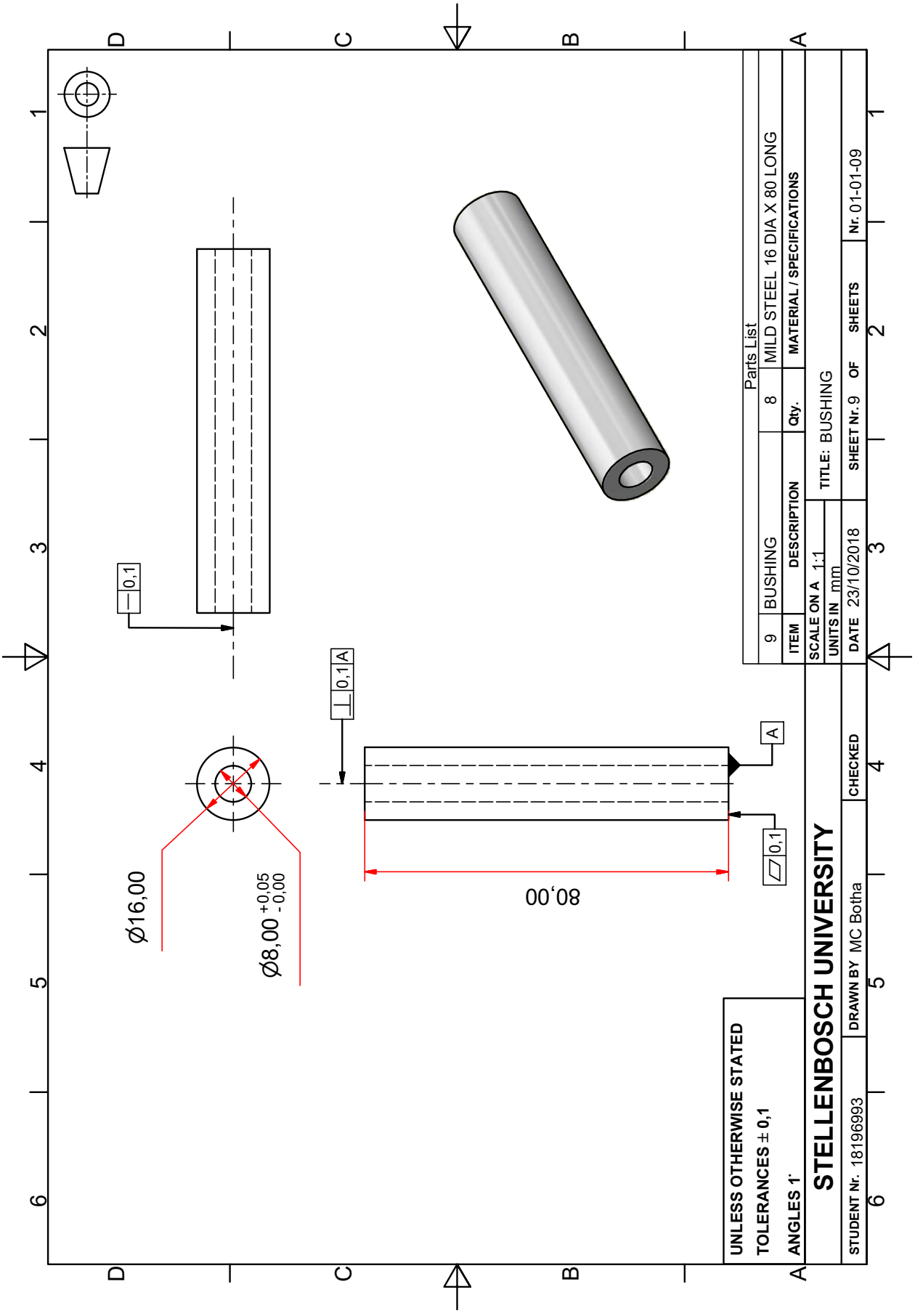

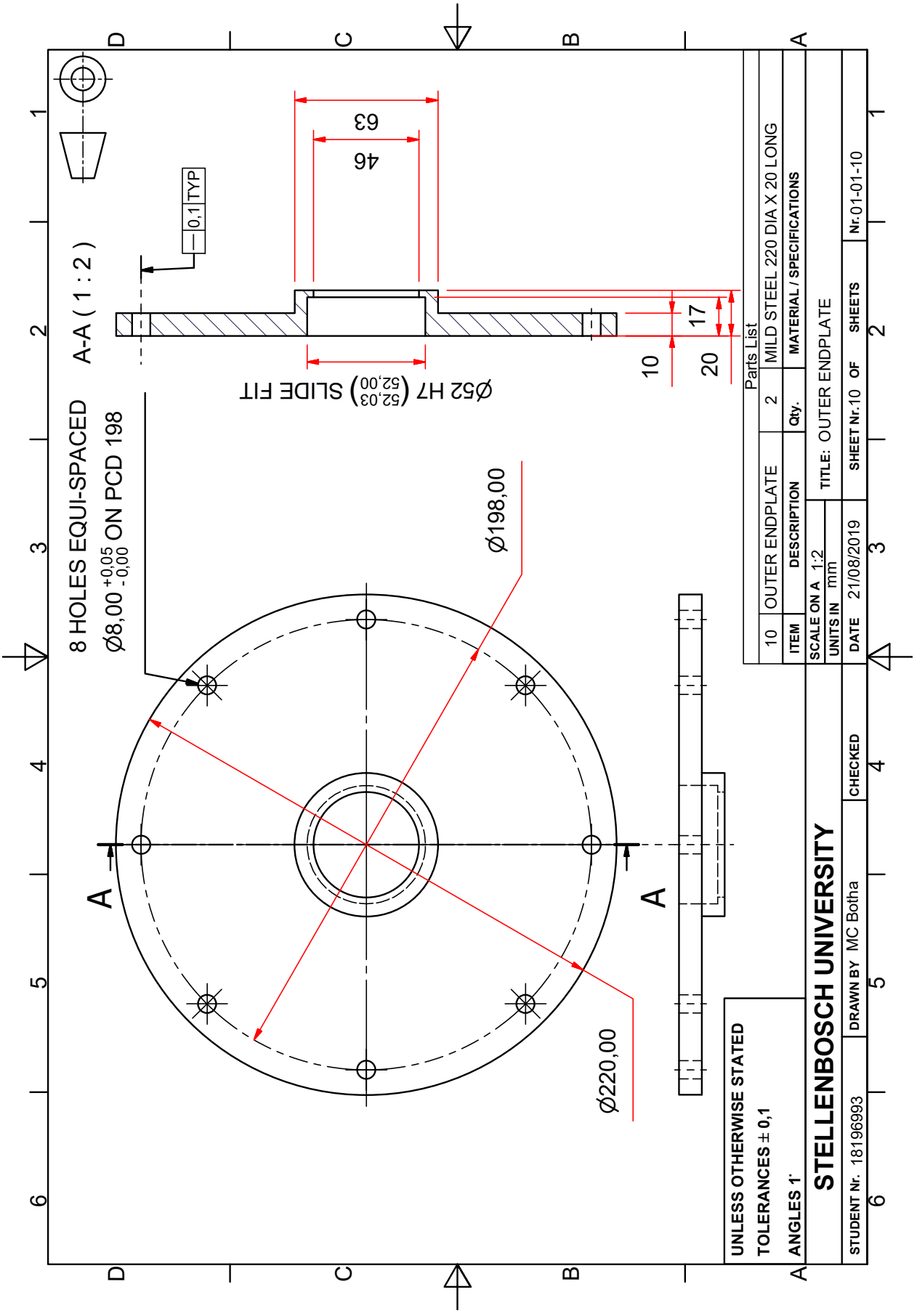

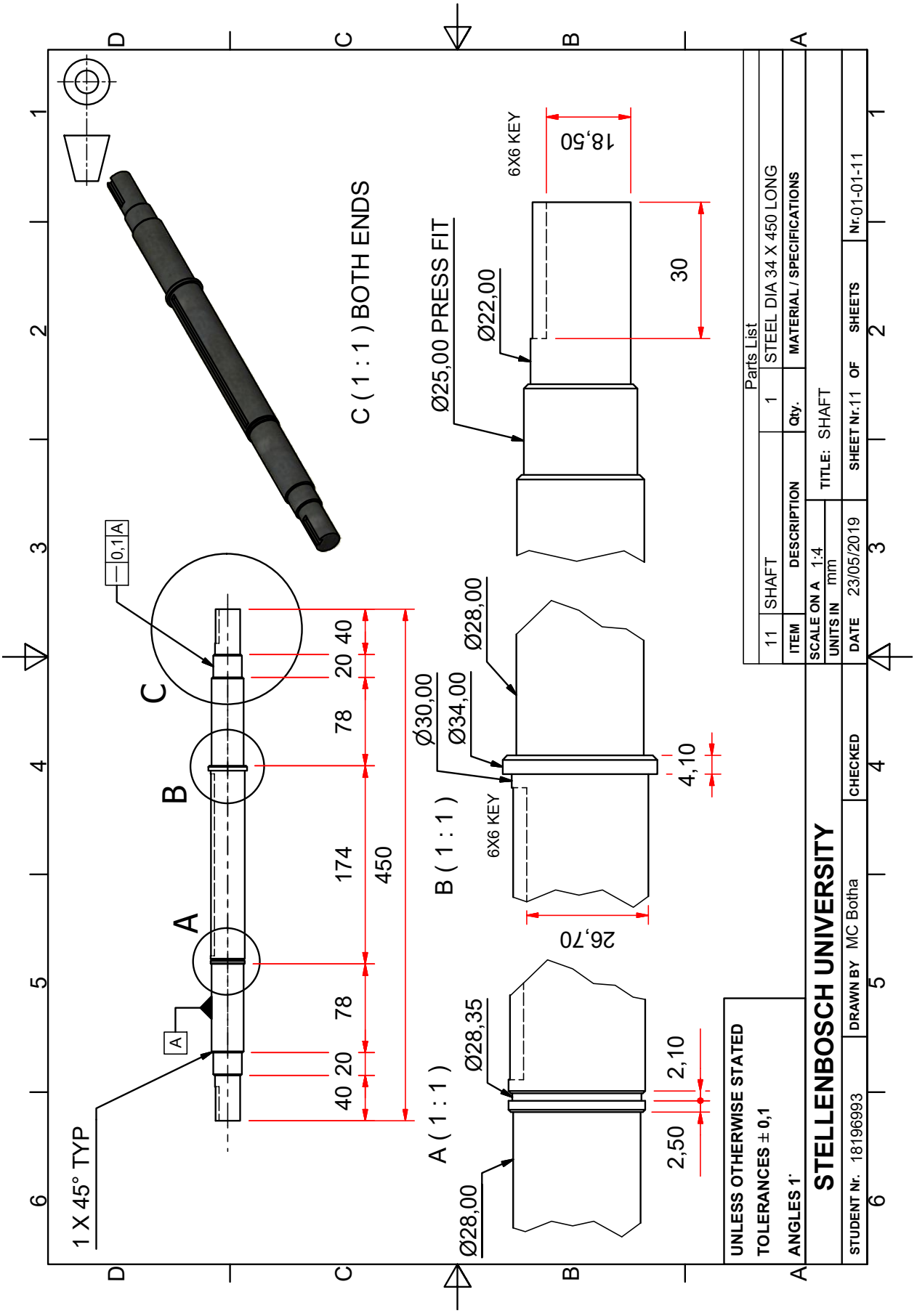

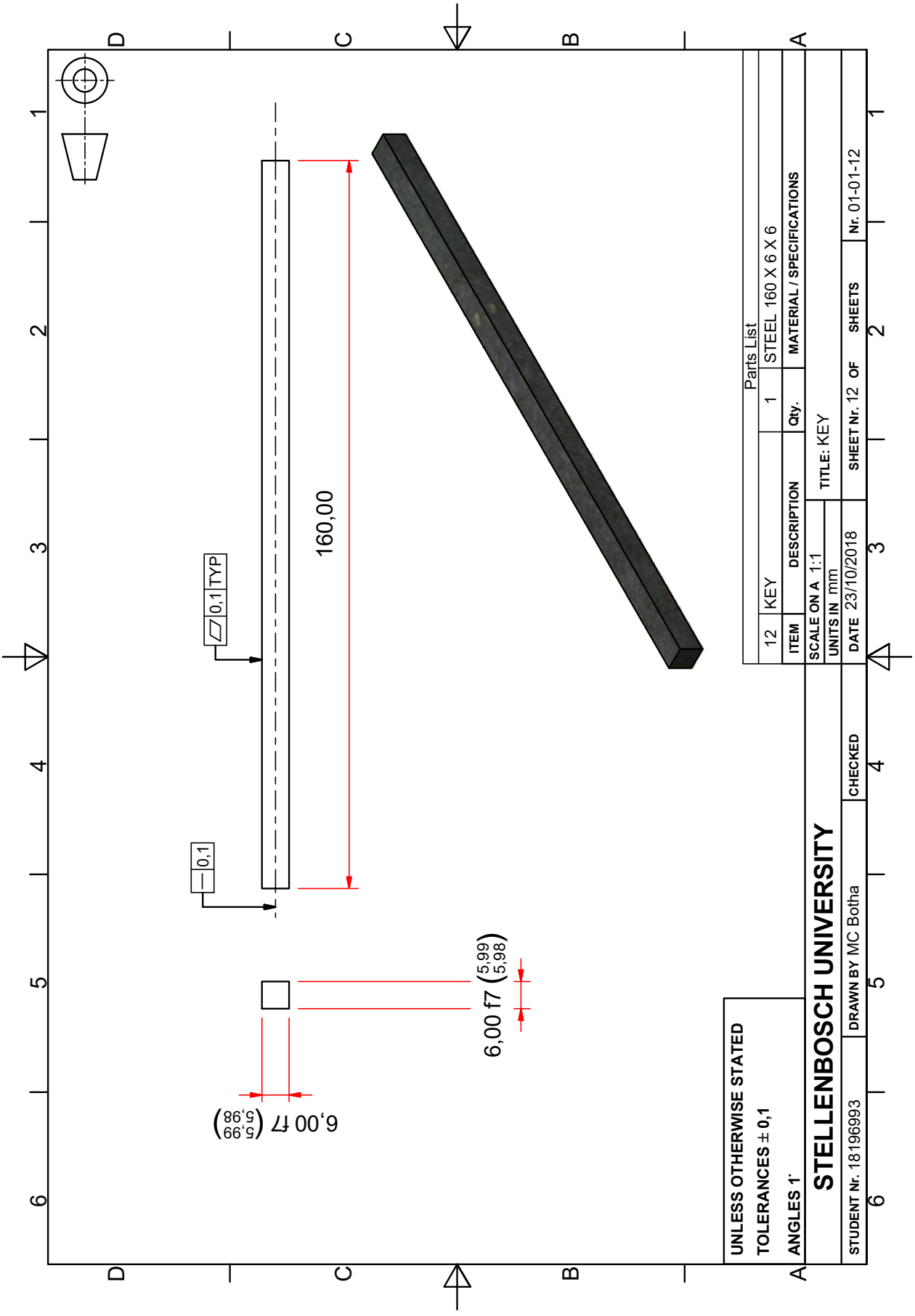

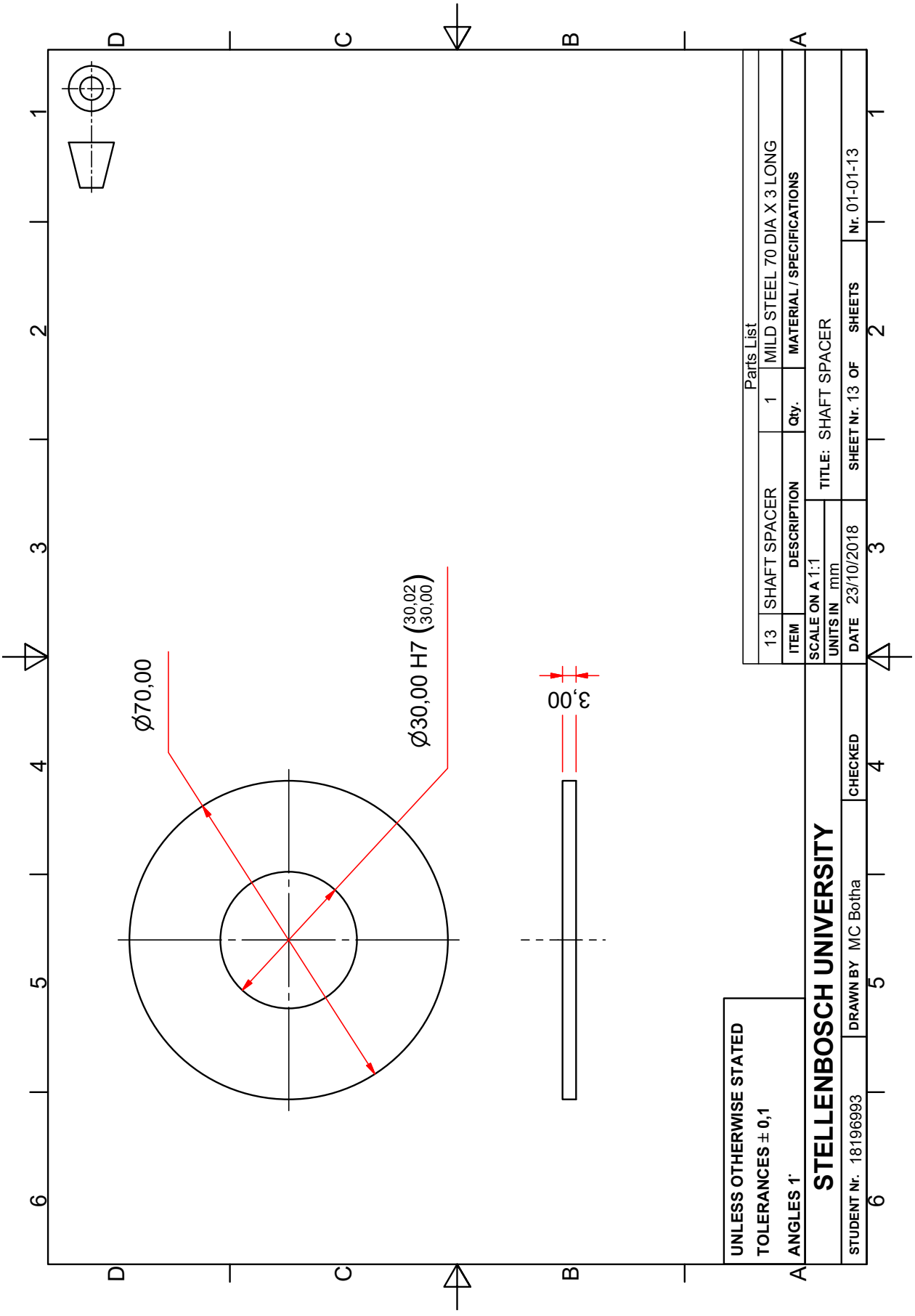

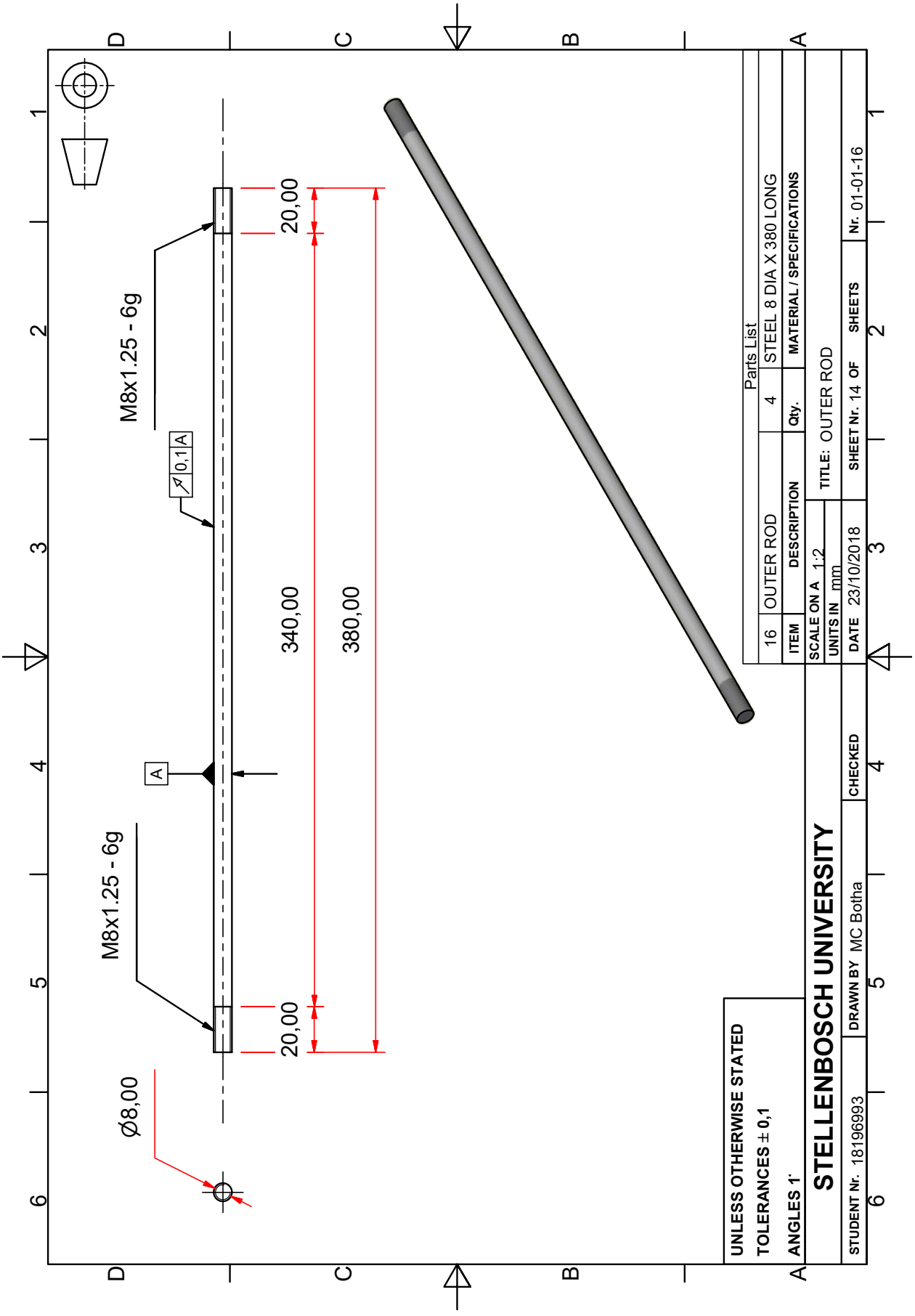

Appendix E

Heat transfer results

```
Winding Temperature: 80.000000 deg
Air Temperature: 40.000000 deg
Paper thermal conductivity coef: 0.400000 W/mK
Steel thermal conductivity coef: 79.500000 W/mK
Air convection coef: 10.000000 W/m^2K
Number of fins on stator surface: 64.000000
Insulation paper thermal resistace: 0.032296 deg/W
Steel thermal resistace: 0.002727 deg/W
Convection thermal resistance: 1.047072 deg/W
Total thermal resistance: 1.082095 deg/W
Rate of heat transfer to stator surface: 36.965329 W
Stator surface temperature: 78.705361 deg
Fin efficiency: 0.992974
Fin effectiveness: 3.340763
Rate of heat transfer from fins: 94.453945 W
```

Appendix F

Oscilloscope measurements

The oscilloscope signals at each speed increment measurement during loaded tests are given in Figure F.1. These signals were used for FFT transformations.

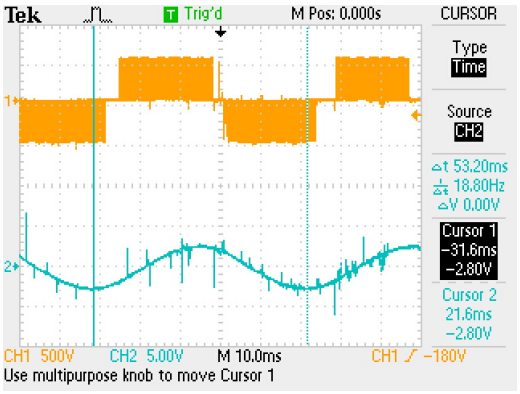

(a) 500 rpm.

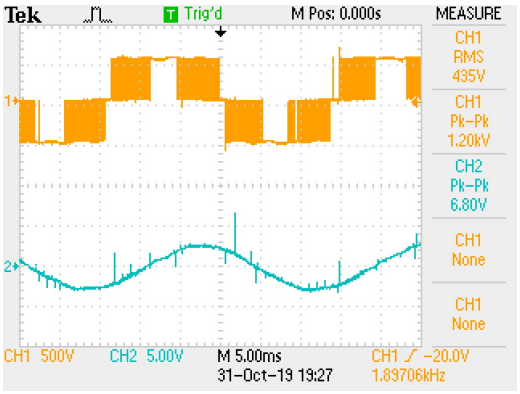

(b) 1000 rpm.

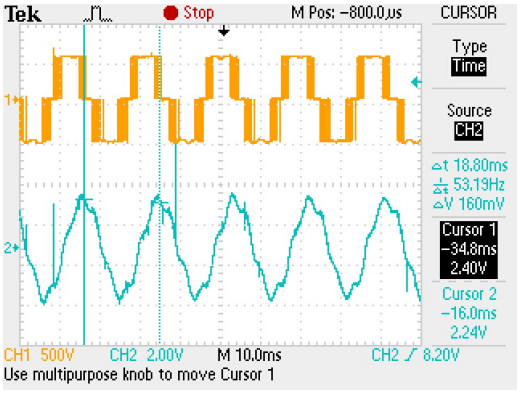

(c) 1500 rpm.

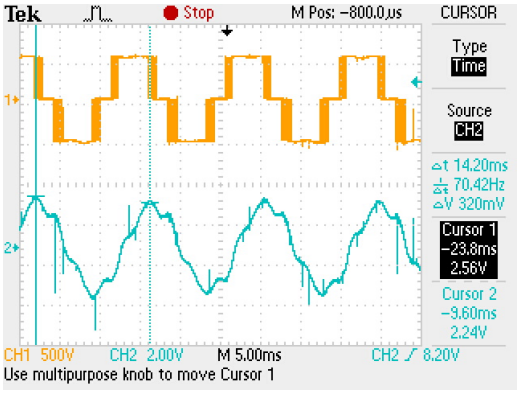

(d) 2000 rpm.

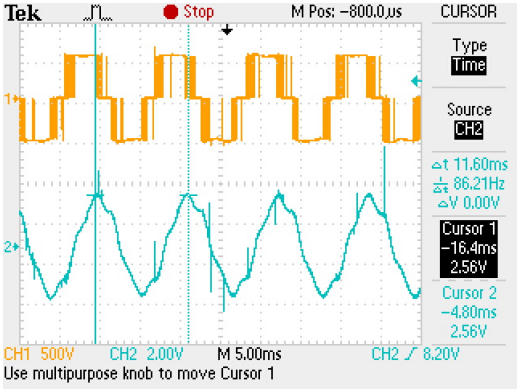

(e) 2500 rpm.

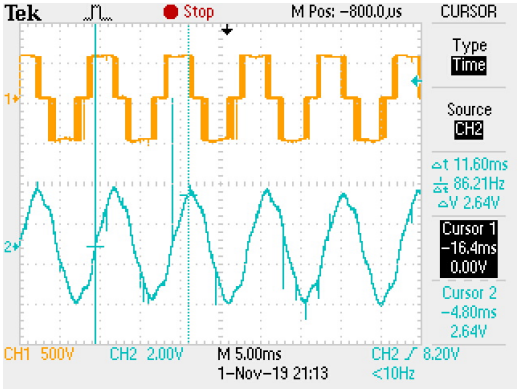

(f) 3000 rpm.

Figure F.1: Oscilloscope signals taken at each measurement.

Appendix G

Published article

The following article was published and presented at the 27th Southern African Universities Power Engineering Conference, (SAUPEC) in Bloemfontein.

2019 SAUPEC/RobMech/PRASA Conference
Bloemfontein, South Africa, January 28-30, 2019

Design Strategy of Traction Induction Motors

T. M. Masuku, R-J. Wang*, M. C. Botha and S. Gerber
Dept. of Electrical and Electronic Engineering
Stellenbosch University
Stellenbosch, 7600
South Africa
Corresponding author: rwang@sun.ac.za*

***Abstract*—In this paper, a strategy for designing induction motors for traction applications is proposed. The proposed strategy builds on the conventional design of induction motors, but makes emphasis on the differentiating characteristics, which are the constant power speed ratio and overloading capability. A design procedure, which breaks up the motor design into different parts and phases was formulated. The formulated design strategy was then validated by the design of a 3 kW traction induction motor using the ANSYS Electronics packages. ANSYS RMxprt was used in conjunction with ANSYS Optimetrics optimization module to create an initial optimum design, which was then verified by using ANSYS Maxwell 2D finite element analysis. The proposed design strategy has been shown to work well.**

***Index Terms*—Design optimization, finite element analysis, induction motors, traction motors, flux weakening**

I. Introduction

Induction motors are widely used in traction applications because of their high efficiency, good overload capability and wide constant power speed range. The design strategy of an induction motor for traction applications is significantly different from that of the conventional induction motor [1]. For an induction motor to be deemed suitable for traction drives a set of requirements have to be met [2]–[4]: high power density, overload capability, high torque at low speeds, fast torque response, high reliability, high efficiency over wide torque and speed ranges, high durability and low cost. The aim of this paper is to formulate a design strategy that conforms to these requirements. The suggested approach will be implemented in the design of a traction induction machine.

A. Power and Torque Characteristics

The power and torque characteristics of a traction motor determine the vehicle's running performance, including the vehicle's acceleration, grade-ability and maximum speed [3], [4]. Typically, the output power and torque of a traction motor are broken down into three operating regions: constant torque, constant power and slip limited, as shown in Fig. 1.

In the constant torque region, the machine's rated torque is maintained by keeping a constant voltage-frequency ratio. This ratio maintains the flux level and the currents in the machine to the given rated values. The output power of the motor increases linearly with an increase of the supply voltage. The constant power region is entered when the supply frequency continues increasing while the voltage is at maximum breaking the constant voltage-frequency ratio. The machine current is constant but the air-gap flux reduces inversely to the supply frequency. This decreases the output torque inversely to the angular velocity and the output power remains constant. For the slip limited region the machine operates at breakdown slip to maximize the output torque, which results in the reduction of output power.

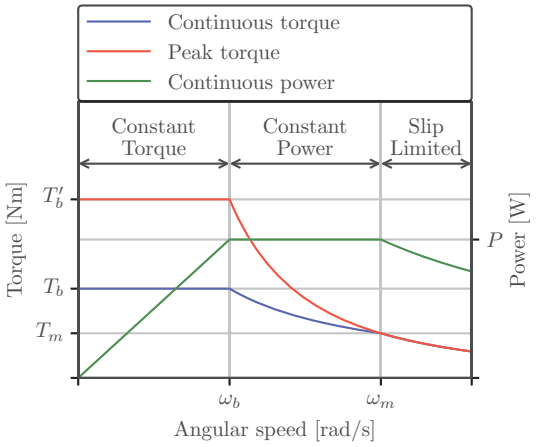

Fig. 1. Induction machine torque power characteristics [4]

B. Realizing Wide Constant Power Speed Range

For the design to be considered suitable for traction drives the Constant Power Speed Range (CPSR), which is defined as ω_m/ω_b as illustrated in Fig. 1, should be 3 or greater [3]. In other words, the maximum speed ω_m achieved in the constant power region should be a minimum of 3 times greater than the base speed ω_b. Since the design point is usually set at the base speed ω_b and the maximum constant power speed ω_m is a consequence thereof, it is essential to establish the relation between the two so that the design specifications at both speeds can be satisfied. Since the maximum torque of an $m-$phase, $p-$pole pair induction motor can be expressed as [3], [5]:

$$T' = \frac{p}{2\pi f} \cdot \frac{mV_{1eq}^2}{2\left(R_{1eq} + \sqrt{R_{1eq}^2 + (X_{1eq} + X_2)^2}\right)} \quad (1)$$

978-1-7281-0369-3/19/$31.00 ©2019 IEEE

where V_{1eq}, R_{1eq}, X_{1eq} and X_2 are equivalent stator voltage, resistances, leakage reactance and referred rotor leakage reactance, respectively.

Assuming R_{1eq} is negligible and V_{1eq} is constant under flux weakening operation, eqn. (1) can be written as:

$$T' = K \cdot \left(\frac{V_{1eq}}{f}\right)^2 \tag{2}$$

where $K = mp/[8\pi^2(L_{1eq}+L_2)]$ and L_{1eq} and L_2 are equivalent stator leakage and referred rotor leakage inductances.

Since $f \propto \omega$ (electrical angular speed) and V_{1eq} is constant:

$$T' \approx K_1 \frac{1}{\omega^2} \tag{3}$$

where K_1 is a constant. The relation between the maximum torques at the base and maximum speeds, ω_b and ω_m, is thus:

$$T'_b \cdot \omega_b^2 = T'_m \cdot \omega_m^2 \tag{4}$$

Under constant power P, the rated operational torques at the base and maximum speed, T_b and T_m, are related by:

$$P = \omega_b T_b = \omega_m T_m \tag{5}$$

At the maximum speed, the maximum torque must exceed the rated operating torque by a factor κ_m, such that:

$$T'_m = \kappa_m T_m \tag{6}$$

For example, in Fig. 1, $\kappa_m = 1$ and $T'_m = T_m$. From (4) – (6), the ratio between the maximum torque and the rated operational torque at the base speed, κ_b, can be derived:

$$T'_b = \kappa_b T_b \tag{7}$$

$$T'_b = \frac{\omega_m}{\omega_b}\kappa_m T_b \tag{8}$$

$$\implies \kappa_b = \frac{\omega_m}{\omega_b}\kappa_m \tag{9}$$

Eqn. (9) can be incorporated into the initial design steps to optimize a suitable maximum torque in order to realize the required CPSR for the induction motor.

C. Mitigation of Harmonic Losses

Traction induction motors are usually fed from voltage source inverters. The time harmonic content of the supply voltages cause additional copper and core losses resulting in high machine temperature. Often the motor rating has to be reduced somewhat to maintain the rated temperature [3], [6]. Another contributor for efficiency loss of a traction induction motor is the harmonic secondary copper losses in the rotor bars. These harmonic secondary copper losses occur in the conductor near the rotor surface and are produced by the harmonic component of the air-gap flux density due to the stator slots. To counter this problem and improve the efficiency of the traction induction motor, new rotor slot designs proposed in [7] as shown in Fig. 2 were considered. Taking the slot profile in Fig. 2A (A-type) as a base design, the configuration shown in Fig. 2B (B-type) involved only reducing the conductor size and without changing the slot shape. Although the results

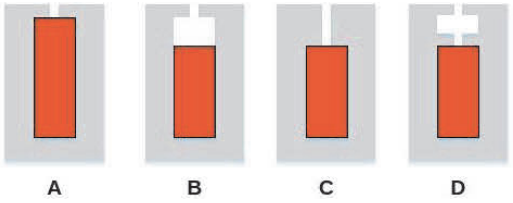

Fig. 2. Candidate rotor slot designs [7].

are promising, the conductor can shift from its position due to centrifugal force during operation. An alternative design as in Fig. 2C (C-type) is to place the conductor deeper in the rotor. Harmonic secondary copper losses are expected to reduce, however there is a chance that leakage inductance would increase in the upper portion of the rotor slots leading to reduced stalling torque. Fig. 2D (D-type) gives an interesting design, which was devised to withstand centrifugal forces as well as reduce the harmonic secondary copper losses without significantly increasing rotor leakage inductance.

II. Design Procedure

A. Design Specifications

The validation of the design procedure will be executed by the design of an induction motor with the following specifications:

TABLE I
KEY IM DESIGN SPECIFICATIONS

Description	Values
Rated power (kW)	3
Rated voltage (V)	380
Number of phases	3
Number of poles	4
Rated speed (rpm)	1000
Maximum speed (rpm)	3000
Overload ratio at maximum speed κ_m	≥ 1
Rated efficiency	$\geq 80\%$
Rated power factor	≥ 0.7
Winding configuration	Delta
Core material	M19-26Ga
Rotor bar material	Copper
Allowable stator outer diameter (mm)	190

In addition to these specifications, the motor should have ideal electric and magnetic loading values to avoid oversaturation and overheating.

B. Selection of Number of Slots

In an induction motor design, the selection of number of stator and rotor slots needs careful consideration. To reduce the leakage reactance, the number of stator slots per pole per phase should generally greater than two [8]. For a 4-pole small induction motor, 24/36/48 slots can be viable options.

In order to avoid disturbances in the operation of an induction motor, the rotor slots have to be carefully selected with respect to the stator slots. Common problems which arise

due to the incorrect selection of rotor and stator slot number combinations are cogging and crawling defined as follows:

- *Cogging:* Also known as *magnetic locking*, is when the motor refuses to start up and remains stationary. This normally occurs when the number of stator slots equal the number of rotor slots. When the rotor and stator slots face each other, the reluctance of the magnetic path is minimum so the rotor position tends to remain fixed [9], [10].
- *Crawling:* The rotating magnetic field in the air-gap of the motor is normally non-sinusoidal and generally contains odd harmonics of the 3^{rd}, 5^{th} and 7^{th} order. The presence of harmonics in the flux wave affects the torque speed characteristics. A motor with a presence of 7^{th} order harmonics will have a tendency to run at one seventh of its normal speed [9], [10].

The following guidelines can be used in conjunction with Fig. 3 to better define the selection of rotor slots:

- To avoid cogging and crawling $Q_s \neq Q_r$ and $(Q_s - Q_r) \neq \pm 3p$
- To avoid synchronous hooks and cusps in torque speed characteristics $Q_r \neq \pm p, \pm 2p, \pm 5p$
- To avoid noisy operation $(Q_s - Q_r) \neq \pm 1, \pm 2, (\pm p \pm 1), (\pm p \pm 2)$

The combinations without symbols shown in Fig. 3 are safe choices. For the 3 kW IM design, the number of slots for stator and rotor are chosen as 36 and 30, respectively.

		Number of pole pairs $p = 1$									Number of pole pairs $p = 2$								
		Ones of rotor slot number Q_r									Ones of rotor slot number Q_r								
Q_s	Tens of rotor slot number	0	1	2	3	4	5	6	7	8	9	0	1	2	3	4	5	6	7	8	9
24	1	−	×	○	×	+	×	−	×	○	×	−	×	○	×	+	×	+	×		×
	2	+	×	−	×	○	×	+	×	−	×	−	×	−	×	○	×	+	×	+	×
	3	○	×	+	×	−	×	○	×	+	×		×	−	×		×	○	×		×
36	1	−	×	○	×	+	×	−	×	○	×		×	○	×		×	∓	×	○	×
	2	+	×	−	×	○	×	+	×	−	×	±	×		×	○	×		×	+	×
	3	○	×	+	×	−	×	○	×	+	×		×	−	×	−	×	○	×	+	×
	4	−	×	○	×	+	×	−	×	○	×	+	×		×	−	×		×	○	×
	5	+	×	−	×	○	×	+	×	−	×		×	+	×		×	−	×		×
48	1	−	×	○	×	+	×	−	×	○	×		×	○	×		×	+	×		×
	2	+	×	−	×	○	×	+	×	−	×	−	×	−	×	○	×	+	×	+	×
	3	○	×	+	×	−	×	○	×	+	×		×	−	×		×	○	×		×
	4	−	×	○	×	+	×	−	×	○	×	+	×		×	−	×	−	×	○	×
	5	+	×	−	×	○	×	+	×	−	×	+	×	+	×		×	−	×		×
	6	○	×	+	×	−	×	○	×	+	×	○	×		×	+	×		×	−	×

Fig. 3. Rotor and stator slot safe combinations [10], where "−" stands for harmful torques in counter-current braking, "+" stands for harmful torques at positive speeds, "×" represents harmful mechanical vibrations, and "○" refers to harmful synchronous torques at standstill.

C. Design Steps

Fig. 4 shows a high level flow diagram of the complete design procedure.

- Step 1: Selection of the initial diameter and core lengths based on sizing equation.
- Step 2: The design of the stator, which includes selection of the number of slots and winding types.
- Step 3: The design of the rotor, which includes the selection of the number of rotor slots, rotor slot type, air-gap length and the rotor shaft diameter.
- Step 4: The performance evaluation of the initial design is conducted, which includes efficiency, power factor, torque-speed curve during flux weakening, magnetic loading, electric loading etc.
- Step 5: The optimization of the design.
- Step 6: If the optimization results are the desired characteristics then proceed to Step 7. Otherwise it will loop back into Step 5 after redesigning the constraints.
- Step 7: Finite Element Analysis of the analytical design is conducted.
- Step 8: If the results are validated in all cases the design can proceed to Step 9. Otherwise it will loop back to Step 5, to re-design and re-optimize the motor.
- Step 9: The final optimized and verified design can be manufactured. The electromagnetic design process is complete.

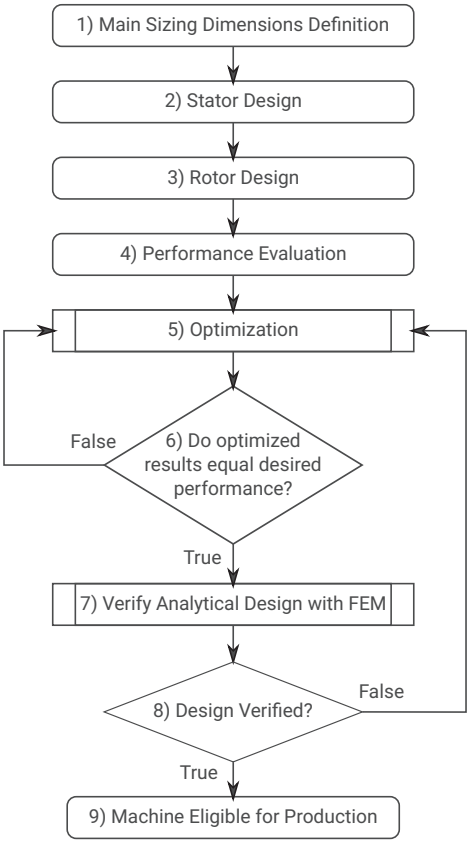

Fig. 4. Design flow diagram.

The optimization of the design, conducted in step 5, can generally be approached in several different ways. Different types of optimization algorithms may be employed. Further-

more, there are many different ways in which the optimization problem may be formulated, depending on the specific requirements of the application, the capabilities of the analysis function and the nature of the optimization algorithm.

In this study, the optimization was conducted using RMxprt analyses together with ANSYS' built-in optimization tool. The genetic algorithm was employed. Using these tools, the optimization problem was formulated as an unconstrained problem:

$$\text{Minimize:} \quad F(\mathbf{X}) = \sum_i [w_i G_i(X)] \tag{10}$$

where F is the objective function, X is the set of design variables, w_i is a set of weighting functions and G_i is a set of penalty functions for constraints. The constraints considered in this process were:

$$\eta \geq 80\,\% \tag{11}$$
$$\text{PF} \geq 70\,\% \tag{12}$$
$$P_{\text{out}} = 3\,\text{kW} \tag{13}$$
$$T_b' \geq 100\,\text{Nm} \tag{14}$$

where η is the efficiency, PF is the power factor, P_{out} is the rated continuous output power and T_b' is the breakdown torque. The weighting functions in (10) were all chosen as unity.

III. Analysis of Results

To verify the traction induction motor design strategy, results of both the analytical design model and finite element analysis are compared. Table I shows the design specifications of the traction induction motor, which is to be modeled and validated. In addition, a stator outer diameter constraint of 190 mm is put in place to limit the size of the machine to standard frame sizes. Although better performance can be expected with a bigger size machine the results summarized in this section are within reasonable margins.

The analytical design cross section is shown in Fig. 5a. The experimental rotor slot profile discussed in Section I-C is implemented in 2D Maxwell using the draw tool and is shown in Fig. 5b.

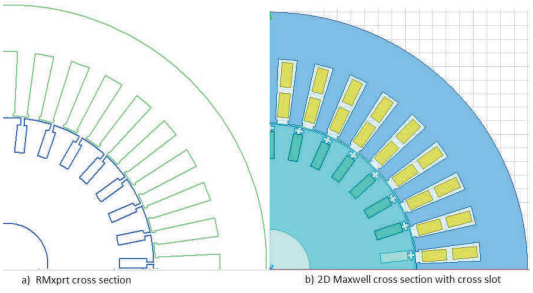

Fig. 5. The cross-sections of the optimum induction motor: (a) with C-type rotor slots, and (b) with D-type rotor slots.

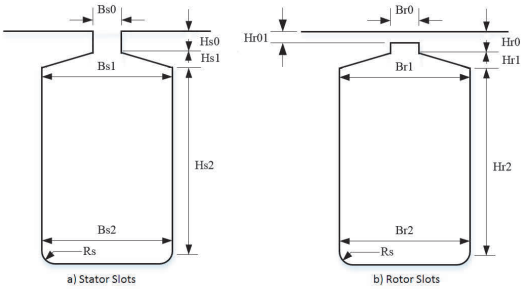

Fig. 6. Definition of slot dimensions for (a) stator slots, and (b) rotor slots.

The optimized slot and sizing dimensions of the machine are summarized in Table II with their definitions shown in Fig 6. The rated performance is summarized on Table III together with the calculated circuit parameters. These results are obtained from the analytical model (RMxprt) and need to be verified by using more accurate numeric modeling method like Finite Element Method (FEM).

TABLE II
INDUCTION MOTOR OPTIMIZED DIMENSIONS

Stator (36 slots)	Initial [mm]	Optimum [mm]
Hs0	0.8	1
Hs1	0	0
Hs2	28	22.5
Bs0	5	4
Bs1	6	5
Bs2	8.5	7
Rs	0	0
Rotor (30 slots)	**Initial [mm]**	**Optimum [mm]**
Hr0	5	2.5
Hr1	0	0
Hr2	15	10
Br0	2.5	1.2
Br1	5.5	3.5
Br2	5.5	3.5
Hr01	0	0
Rs	0	0
General	**Initial [mm]**	**Optimum [mm]**
Core length	105	160
Outer diameter	220	190
Inner diameter	120	108
Shaft diameter	40	30
Air-gap length	0.3	0.65

A. Performance Characteristics

The torque-speed characteristics of the designed traction induction motor obtained using ANSYS analytical design tool RMxprt is shown in Fig. 7. The corresponding power-speed curve is given in Fig. 8, which shows a constant power speed range close to 3. For validation purpose, ANSYS Maxwell 2D FEM is used to compute the output power at both base speed and maximum speed points. The 2D Maxwell results shown in Fig. 9 gives an output power of 3010 W at 1000 rpm and 2949 W at 3000 rpm, which is in a good agreement with that

TABLE III
RATED PERFORMANCE OF THE OPTIMUM INDUCTION MOTOR

Performance parameters	Values	Units
Input power	3558,14	W
Total losses	558,085	W
Output power	3000	W
Rated efficiency	84.31%	-
Power factor	0.712	-
Rated torque	28.6	Nm
Rated speed	1000.29	rpm
Rated slip	0.0383	-
Source frequency	34.67	Hz
Calculated circuit parameters	Values	Units
Stator resistance (R_s)	1.979	Ω
Rotor resistance (R_r)	1.567	Ω
Stator leakage reactance (X_{ls})	1.495	Ω
Rotor leakage reactance (X_{lr})	2.752	Ω
Magnetizing reactance (X_m)	40.249	Ω
Core loss resistance (R_c)	2356.890	Ω

of RMxprt. The power at the maximum speed is slightly less than the specified 3 kW.

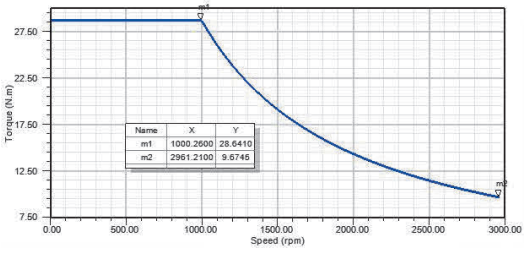

Fig. 7. Torque-speed characteristics of the optimum induction motor design obtained from RMxprt.

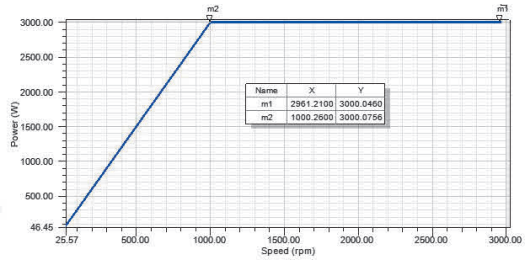

Fig. 8. Power-speed characteristics of the optimum induction motor design obtained from RMxprt.

B. Magnetic and Electric Loading

In a well designed induction machine, the highest flux density occurs in the teeth. As a further review of the design, the average magnetic and electric loadings obtained in the ANSYS RMxprt analytical design are summarized on Table IV together with the recommended value range set out as design guidance in [3], [11]. Generally, the design values correspond to desired characteristics and show a quality design.

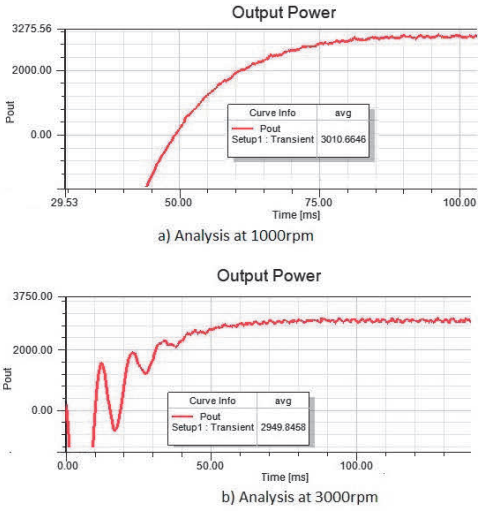

Fig. 9. Transient power analysis using 2D Maxwell.

TABLE IV
MAGNETIC AND ELECTRIC LOADING

Flux density (T)	Design value	Recommended values
Stator teeth	1.375	1.4 - 1.7
Rotor teeth	1.503	1.5 - 1.8
Stator yoke	1.306	1.4 - 1.7
Rotor yoke	0.545	1.0 - 1.6
Air-gap	0.767	0.7 - 0.9
Current density (A/mm^2)		
Stator slot	6.470	5.0 - 6.5
Rotor bar	5.817	5.5 - 7.5

C. Harmonic Loss Reduction Analysis

The rotor slot types (A and D) shown in Fig. 2 were simulated using FEM in order to compare their harmonic secondary copper losses. The simulation involved modeling the exact same machine with the only difference being the rotor slots and simultaneously running them at synchronous speed to mimic true no-load conditions. The results of the experiment are summarized on Fig. 10. At 1000 rpm, the rotor eddy current loss and core loss in the machine with A-type rotor slots were 3.77 W and 29.53 W, respectively. For the D-type rotor slots, the eddy current loss and core loss were 0.00115 W and 29.72 W. This shows the effectiveness of reducing the secondary rotor eddy current losses just from altering the rotor slot. The core losses for both slot types are practically the same.

IV. MECHANICAL DESIGN

The mechanical design of the induction traction motor prototype is described in this section. Fig. 11 depicts a 3D model of the 3 kW induction motor created in AutoCad Inventor. For enhanced heat transfer, the model was designed as a frameless machine with a finned core outer surface. Each fin was

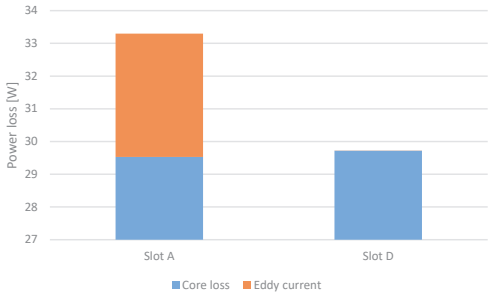

Fig. 10. Slot A and slot D loss comparison

designed with a heat transfer efficiency of 99 %. With 64 evenly distributed fins, a fin effectiveness of 3.34 was achieved. A detailed view of the fin dimensions can be seen in Fig. 12. With a winding temperature of 120 °C, ambient temperature at 40 °C and an assumed convective heat transfer coefficient of $h = 10$ W/m^{2}K, the rate of heat transfer from the induction machine was estimated as 189 W, which means that forced air cooling will be required.

The core consists of eight slots tangent to the outer surface of the stator as seen in Fig. 12. Manufacturing costs were further reduced by the inclusion of the rectangular cutaway for continuous laser cutting motion. The stator core laminations are compressed between two inner end-plates via four threaded rod and nut assemblies. Its further held stationary between two outer end-plates via four threaded rod, nut and bush assemblies. The bushing additionally serves as a spacer between the core and outer end-plate for winding purposes. The rotor is press-fitted onto the shaft and locked via a keyway and two circlips. A countersunk hole was created for each bushing on each outer end-plate for an embedded fit. Thus, increasing the overall rigidity of the machine.

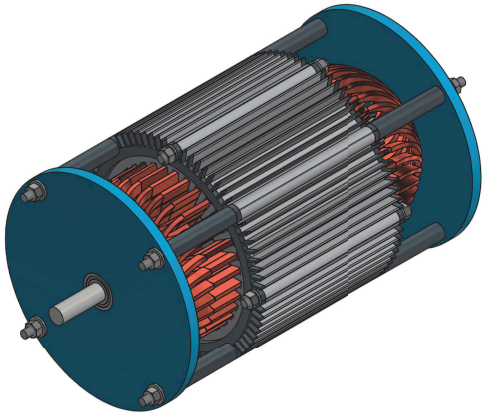

Fig. 11. 3D model of the designed 3 kW traction induction machine.

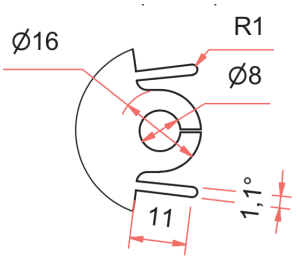

Fig. 12. Detailed view of finned lamination

V. Conclusion

The primary objective of formulating a design strategy for traction induction motors was met. Literature research on the motor technology was conducted and a high level flow diagram was created to summarize the applied design approach. Validation of the design approach was conducted using RMxprt and 2D FEM, which shows that the optimized traction motor has a good efficiency (84%) and power factor (0.71) even though a physical dimension restriction was put in place on the outer diameter. The designed induction traction motor had a CPSR of approximately 3 and the magnetic and electric loadings were within the desired ranges. These results give proof that the designed machine using the formulated approach is suitable for traction drive systems.

Acknowledgment

This work was supported in part by the Eskom Tertiary Education Support Program (TESP), National Research Foundation (NRF) and Stellenbosch University, all of South Africa.

References

[1] J. H. Lee, J. W. Kim, and Y. H. Kim, "Optimum design criteria for premium performance of traction induction motor," in *9th IET International Conference on Computation in Electromagnetics (CEM 2014)*, March 2014, pp. 1–2.
[2] J. F. Gieras and N. Bianchi, "Electric motors for light traction," *EPE Journal*, vol. 14, pp. 12–23, 2004.
[3] I. Boldea and S. Nasar, *The Induction Machines Design Handbook*. CRC Press, 2009.
[4] N. Zhao and N. Schofield, "An improved induction machine design procedure for electric vehicle traction," in *8th IET International Conference on Power Electronics, Machines and Drives (PEMD 2016)*, April 2016, pp. 1–6.
[5] C. Kingsley and S. D. Umans, *Fitzgerald and Kingsley's Electric Machinery*. McGraw Hill, 2003.
[6] P. K. Sen and H. Landa, "Derating of induction motors due to waveform distortion," *IEEE Transactions on Industry Applications*, vol. 26, no. 6, pp. 1102–1107, 1990.
[7] M. Kondo, M. Miyabe, and R. Ebizuka, "Design and efficiency evaluation of a high-efficiency induction motor for railway traction," *Electrical Engineering in Japanl*, vol. 194, no. 2, pp. 15–23, 2016.
[8] V. Mittle, *Design of Electrical Machines*. Standard Publishers Distributors, 2005.
[9] T. Lipo, *Introduction to AC machine design*. Wiley, 2017.
[10] J. Pyrhonen, T. Jokinen, and V. Hrabovcova, *Design of rotating electrical machines*, 2nd ed. Wiley, 2014.
[11] R. G. Harley and Y. Duan, "Traditional design of cage rotor induction motors," Grainger CEME, Seminars, 2009.

List of References

[1] Timeline: History of the Electric Car | Department of Energy. URL https://www.energy.gov/timeline/timeline-history-electric-car.

[2] Brian Wang. Electric car domination in 2025-2030, 2018. URL https://www.nextbigfuture.com/2018/10/electric-car-domination-in-2025-2030.html.

[3] Jacek F Gieras and East Hartford. Electric Motors for Light Traction. *EPE Journal*, Volume 14(February):12–23, 2004.

[4] N. Schofield and N. Zhao. An Improved Induction Machine Design Procedure for Electric Vehicle Traction. *8th IET International Conference on Power Electronics, Machines and Drives (PEMD 2016)*, 2016. URL http://digital-library.theiet.org/content/conferences/10.1049/cp.2016.0127.

[5] Ion Boldea and Sayed A Nasar. *The Induction Machines Design Handbook*. CRC Press, New York, second edition, 2009.

[6] Hashem Oraee Mirzamani and Azim Lotfjou Choobari. Study of Harmonics Effects on Performance of Induction Motors. In *WSEAS international conference on Applications of electrical engineering*, volume 2, 2004.

[7] Cole Ferguson. How Induction Machines Work, 2016. URL https://jmkengineering.com/induction-machines-work/.

[8] Electrical4U. Induction Motor | Working Principle | Types of Induction Motor |. *https://www.electrical4u.com/*. URL https://www.electrical4u.com/induction-motor-types-of-induction-motor/.

[9] Stephen Chapman. *Electric machinery fundamentals*. McGraw Hill Education, fifth edition, 2005. ISBN 0072465239.

[10] Difference Between Slip Ring and Squirrel Cage Induction Motor, 2018. URL https://circuitglobe.com/difference-between-slip-ring-and-squirrel-cage-induction-motor.html.

[11] William R Finley and Mark M Hodowanec. Selection of Copper vs. Aluminum Rotors for Induction Motors. *IEEE Transactions on Industry Applications*, 37 (Issue 6):1563–1573, 2001.

[12] Alan Goodrich. Selection of Rotor Material for Industrial Induction Motors. The Case for Copper. 2012. URL https://pdfs.semanticscholar.org/b3c3/55ad74319f1160de02835c272128c4a7d5a4.pdf?{_}ga=2.158219962.1458287867.1582385590-1803432062.1582385590.

[13] Mehmet Murat Tezcan, Asim Gokhan Yetgin, Ali Ihsan Canakoglu, Baris Cevher, Mustafa Turan, and Murat Ayaz. Investigation of the effects of the equivalent circuit parameters on induction motor torque. *MATEC Web of Conferences*, Voloume 15, 2018.

[14] S J Rind, Y Ren, Y Hu, J Wang, and L Jiang. Configurations and control of traction motors for electric vehicles: A review. *Chinese Journal of Electrical Engineering*, 3(3):1–17, 2017. ISSN 2096-1529. doi: 10.23919/CJEE.2017.8250419. URL http://ieeexplore.ieee.org/document/8250419/.

[15] Checking For Motor Overload. URL https://www.fluke.com/en-us/learn/best-practices/motors-and-drives/checking-for-motor-overload.

[16] Markus Lienkamp. Status Electromobility 2016 Or How Tesla Will Not Win, 2016. URL https://books.google.co.za/books/about/STATUS{_}ELECTROMOBILITY{_}2016.html?id=b-j1DAAAQBAJ{&}redir{_}esc=y.

[17] V.N. Mittle. *Design of Electrical Machines*. Standard Publishers, New Delhi, India, 1st edition, 2009. ISBN 8180141268.

[18] Circuit Globe. Difference Between Star and Delta Connection. URL https://circuitglobe.com/difference-between-star-and-delta-connection.html.

[19] Thomas A Lipo. *Introduction to AC Machine Design*. Wiley, 2017. ISBN 978-1-119-35216-7.

[20] Juha Pyrhonen, Tapani Jokinen, and Valeria Hrabovcova. *Design of Rotating Electrical Machines*. Wiley, 2nd edition, 2013. ISBN 9780470740095.

[21] One by Zero Electronics. What are Random wound and Form wound Coils in Electric Motor? How they influence the Motor? URL https://onebyzeroelectronics.blogspot.com/2017/03/what-are-random-wound-and-form-wound.html.

[22] Electrical Concepts. Advantages and Disadvantages of Short-Pitch Winding, 2016. URL https://electricalbaba.com/advantages-and-disadvantages-of-short-pitch-winding/.

[23] Ahmed Farahat. Short-pitch Winding : Pitch factor/chording factor. URL http://machineryequipmentonline.com/electric-equipment/alternatorsshort-pitch-winding-pitch-factorchording-factor-2/.

[24] Jonas Oberg, Henry Ryffel, Holbrook L Horton, and Christopher J Mccauley. *Machinery's Handbook*. Industrial Press Inc, 2016. ISBN 9780831130978.

[25] Austin. Hughes. *Electric motors and drives: Fundamentals, Types, and Applications*. Elsevier/Newnes, 2006. ISBN 9780750647182.

[26] Yunus Cengel and Ghajar Afshin. *Heat and Mass Transfer: Fundamentals & Applications*. Fith edition, 2015. ISBN 978-0-07-339818-1.

[27] S.L. Nau and H.G.G. Mello. Acoustic noise in induction motors: causes and solutions. *Petroleum and Chemical Industry Technical Conference*, pages 253–263, 2000.

[28] A Fitzgerald, Charles Kingsley, and Stephen Umans. *Electric Machinery*. McGraw-Hill, 6th edition, 2003. ISBN 978-0071230100.

[29] T.M. Masuku, R-J. Wang, M. C. Botha, and S. Gerber. Design Strategy of Traction Induction Motors. *SAUPEC*, (27th):316–321, 2019.

[30] Minoru Kondo, Minoru Miyabe, Ryuji Ebizuka, and Koji Hanaoka. Design and efficiency evaluation of a high-efficiency induction motor for railway traction. *Electrical Engineering in Japan (English translation of Denki Gakkai Ronbunshi)*, 194(2):15–23, 2016. ISSN 15206416. doi: 10.1002/eej.22771.

[31] Eugene Ossipov. Genetic Algorithms: Search and Optimization by Natural Selection. URL `https://www.toptal.com/algorithms/genetic-algorithms`.

[32] Jeff Nazarro. What You Should Know About Frameless Motors. URL `http://blog.parker.com/what-you-should-know-about-frameless-motors`.

[33] Kollmorgen Experts. Why Choose a Frameless Motor for Your Machine? URL `https://www.kollmorgen.com/en-us/blogs/{_}blog-in-motion/articles/melanie-cavalieri/why-are-frameless-motors-ideal-choice-your-machine/`.

[34] Marcus Westerlund. Bearing currents - IEC Low voltage motors | ABB. URL `https://new.abb.com/motors-generators/iec-low-voltage-motors/articles/bearing-currents`.